UNIVERSITY OF SOUTHAMPTON

The use of geometric uncertainty data in aero engine structural analysis and design

by

Aditya S. Deshpande

A thesis submitted in partial fulfillment for the
degree of Doctor of Philosophy

in the
FACULTY OF ENGINEERING AND THE ENVIRONMENT

August 2013

UNIVERSITY OF SOUTHAMPTON

ABSTRACT

FACULTY OF ENGINEERING AND THE ENVIRONMENT
AERONAUTICS, ASTRONAUTICS AND COMPUTATIONAL ENGINEERING

Doctor of Philosophy

THE USE OF GEOMETRIC UNCERTAINTY DATA IN AERO ENGINE STRUCTURAL ANALYSIS AND DESIGN

by Aditya S. Deshpande

A gas turbine disc has three critical regions for which lifing calculations are essential: the assembly holes or weld areas, the hub region, and the blade-disc attachment area. Typically, a firtree joint is used to attach the blades to the turbine disc instead of a dove-tail joint, which is commonly used for compressor discs. A firtree joint involves contact between two surfaces at more than one location which makes the joint more difficult to design. Large loads generated due to the centrifugal action of the disc and associated blades are distributed over multiple areas of contact within the joint. All of the contacts in a firtree joint are required to be engaged simultaneously when the blades are loaded. However, slight variations in the manufacture of these components can have an impact on this loading. It is observed that small changes in the geometric entities representing contact between the two bodies can result in variations in the stress distribution near contact edges and the notch regions. Even though manufacturing processes have advanced considerably in the last few decades, the variations in geometry due to these processes cannot be completely eliminated. Hence, it is necessary to design such components in the presence of uncertainties in order to minimise the variation observed in their performance.

In this work, the variations in geometry due to the manufacturing processes used to produce firtree joints between a gas turbine blade and the disc are evaluated. These variations are represented in two different ways using measurement data of firtree joints obtained from a coordinate measuring machine (CMM): (i) the variation for the pressure angle in the firtree joint is extracted from a simple curve fit and (ii) using the same measurement data, the unevenness of the pressure surfaces is represented using a Fourier series after filtering noise components. A parametric computer aided design (CAD) model which represents the manufacturing variability is implemented using Siemens NX. Non-smooth surfaces are also numerically generated by assuming the surface profile to be a random process. Two- and three-dimensional elastic stress analysis is carried out on the firtree joint using the finite element code, Abaqus and the variations observed in the notch stresses with changing pressure angle are extracted.

A surrogate assisted multiobjective optimisation is performed on the firtree joint based on the robustness principles. Kriging based models are used to build a surrogate for notch stresses and the non-dominated sorting genetic algorithm-II (NSGA-II) is implemented to perform a multiobjective optimisation in order to minimise the mean and standard deviation of the notch stresses. An iterative search algorithm that updates the Kriging models with equally spaced infill points from the predicted Pareto front is adopted. Finally, a new design of the firtree joint is obtained which has better performance with respect to the variation in the notch stresses due to manufacturing uncertainties.

Contents

List of Figures

List of Tables

Declaration of Authorship

I, Aditya S. Deshpande , declare that the thesis entitled 'The use of geometric uncertainty data in aero engine structural analysis and design' and the work presented in the thesis are both my own, and have been generated by me as the result of my own original research. I confirm that:

- this work was done wholly or mainly while in candidature for a research degree at this University;
- where any part of this thesis has previously been submitted for a degree or any other qualification at this University or any other institution, this has been clearly stated;
- where I have consulted the published work of others, this is always clearly attributed;
- where I have quoted from the work of others, the source is always given. With the exception of such quotations, this thesis is entirely my own work;
- I have acknowledged all main sources of help;
- where the thesis is based on work done by myself jointly with others, I have made clear exactly what was done by others and what I have contributed myself;
- parts of this work have been published as:

    1. Deshpande, A. S., Keane, A. J., Sóbester, A., Toal, D. J. J. "Geometric parameterisation of firtree joints in gas turbine discs considering manufacturing variability." *Proceedings of 3rd Aircraft Structural Design Conference, Delft (2012).*

Signed:.....

Date:.....

Acknowledgements

I would like to thank my supervisor, Prof. Andy Keane, for giving me the opportunity to work on this project. His constant support and guidance have been useful to keep the motivation going through the course of this PhD. I feel privileged to have worked under his guidance and to get a chance to learn from his vast experience and in-depth knowledge. Thanks is due to Dr. Andras Sóbester and Dr. David Toal for giving their comments while preparing this thesis. I am grateful to Rolls-Royce plc and the University of Southampton for providing the financial support required for this PhD. The contribution from the rest of the members of the Computational Engineering and Design group for creating a healthy working environment is appreciated. I am also grateful to Rosalind Mizen, Alicja Ash, Tracey Staddon, and Jackie Allen for providing the administrative support required.

I owe a special thanks to Dr. David Toal for the numerous discussions I have had with him for the last three years. I have benefited immensely from his expertise in the fields of surrogate modelling and design optimisation. Every discussion I have had with him has managed to instill enthusiasm and motivation in me.

The extended discussions I have had with Sanjay Pant and Joshua Jeeson Daniel, during the coffee breaks, have been enjoyable especially on those, otherwise, dull days. The conversations, related to music and sports, with Sanjay have been insightful and fun. Thanks is also due to Jie Zhou, Aditya Karnik, Moresh Wankhede, Athanasios Makrodimopoulos (and his coffee!), Alkin Nasuf, and Amrith Surendra. Having house-mates, Robert Hanzal and Pin-Ru Huang, sailing in the same boat certainly helped in having conversations that lit up the boring evenings.

The telephonic conversations, on various non-academic topics, I have had with Ohmkar during the course of this PhD have helped keep my mind fresh all the time.

Finally, special thanks should go to my mother, father, and sister, Dnyaneshwari. Without their support and encouragement this thesis would not have been possible.

Chapter 1

Introduction

Over the years, the gas turbine engine has developed into a complex machine involving multiple stages of compressor-turbines, inlet, combustor, afterburner, etc. The design of every component of a gas turbine engine needs to be approached with minimal pre-conceptions regarding its importance to the whole engine. The increasing demands on the aircraft industry, and hence on aero engines, have pushed the engine manufacturers to minimise the cost and weight of the engine while delivering the required efficiency. Integration between different fields involved is a vital activity at all stages of design and development of an engine. Multiple solutions often exist while designing machines like aero engines where no one solution can be identified as an optimum solution [1]. The design of the engine is coupled through optimum performance-based parameters obtained through several disciplines such as aerodynamics, thermodynamics, structures, and control. A considerable level of judgement and compromise is required to decide upon the values of design parameters for the final solution.

The design process of a gas turbine engine can be broadly divided into two sections: (i) engine cycle design and (ii) engine components design [1]. The engine cycle design involves decision making with respect to the thermodynamic cycles, number of compression stages, bypass ratios, etc. Once the basic layout of the engine is obtained from the engine cycle design, each component needs to be carefully designed to satisfy the thermal, aerodynamic, and structural performance to achieve the required efficiency. In this thesis, the structural design of one of the rotatory components in a gas turbine engine is considered.

Rotatory components operate at high tangential velocities imposing stringent constraints on the design of the turbomachinery involved in a gas turbine engine. The high-pressure turbine components are amongst the hottest parts of the engine, with temperatures reaching up to 1600° C, exceeding the melting point of the material used for casting them [2]. Such constraints need to be assessed carefully before performing the design study. One of the structural requirements in designing is to reduce the weight of the

components and hence that of an engine. While achieving this goal, the geometries of these components are often optimised to an extent that the least possible material is used to deliver the required structural performance. In addition to this, the durability margins of the engine parts have to be minimised so that every part is certain to last its intended design lifetime [1]. The design of heavy rotating and highly pressurised parts in an engine are of primary concern since in the event of a failure of any of these parts, large pieces of metal can be ejected which may harm the parent aircraft. Most of the rotating components in a gas turbine engine, such as the long first-stage compressor fan blades, blades and discs of high-pressure turbines and non-rotating components such as the outer cases of combustors are classified as the critical parts in an engine and accurate evaluation of their structural life is one of the major steps in the engine development process [1].

Iterative process for structural design require accurate estimation of the stresses that every part experiences. These stresses are then related to the primary response in terms of the life expectancy of the part. If the estimated life of the given part is found to be insufficient, the design parameters are varied and the same process is repeated until a satisfactory design is reached. The stresses and strains emerge due to the exposure of the part to its working environment and can be regarded as the forcing functions which consume the available life. The centrifugal force is generally the main source of stresses in rotating parts [1, 3]. Blade aerofoil bending moments due to the pressure differences, self-induced vibrations of aerofoils, thermal differential stresses leading to low-cycle fatigue problems, local stress concentrations and foreign and domestic object damage are a few other factors that reduce the available life of an engine part. Due to the high rotating speeds ($\approx 10,000$ revolutions per minute [2]) and fluctuating temperatures[1], the stresses often exceed the elastic stress levels causing plastic flows and permanent deformations. Hence, suitable selection of material compositions is of utmost importance to avoid material damage due to erosion, corrosion and creep during the service life of the engine.

Advances made in the field of computational methods for analysis such as computational fluid dynamics (CFD) and computational structural mechanics (CSM) have helped engineers to perform optimisation on large and complex assemblies by combining objectives from multiple disciplines. In the case of the CFD tools, detailed definition of the external geometric entities is required whereas CSM tools require definition of both internal and external geometric entities. Although a relatively coarse grid or mesh is sufficient for the CSM as compared to the CFD, often the geometries involved are complex [4]. Such complex geometries have to be parametrised appropriately for performing optimisation studies.

[1] In this work, only the structural analysis is considered and the thermal analysis is omitted since they do not affect the optimisation process even if they may affect the result.

1.1 Geometry parametrisation

Geometric design of machine components essentially involves deciding upon the values of the parameters defining their geometry based on various objectives and constraints. Engineers may consider either single or multiple objectives when designing a component, with the final geometry obtained either by minimising or maximising these objective functions. The parameters that define the geometry play a significant role when performing such optimisation. The parametrisation scheme should be such that the design parameters allow the search domain to be sufficiently large to find better designs while the solution time should be affordable. The geometry parametrisation should ideally be able to eliminate geometrically infeasible solutions from the search space. The selection of the components defining the geometry (like lines, arcs, splines, etc.) which build the required shape has a significant impact on the formulation of any shape optimisation problem. It is possible to construct a part geometry with a large number of geometric entities, however, the number of parameters involved in the optimisation may then be so large as to make the optimisation computationally expensive. While dealing with high-fidelity computations in optimisation, selecting entities which build the required geometry with a minimum number of parameters is generally desirable.

Due to the importance of the parametrisation techniques, many researchers have investigated the effect of their choice on the results of design optimisation, especially in the aerospace applications. Song and Keane [5] compared the use of B-splines with orthogonal basis functions while performing aerofoil optimisation in assessing their ability to represent three dimensional aerofoil shapes. The B-spline approach gave more accurate results as compared to the basis function approach but with higher computational effort. Castonguay and Nadarajah [6] studied the effect of shape parametrisation by comparing four different techniques – Hicks-Henne bump functions [7], B-spline curves, mesh points, and PARSEC [8] on automatic aerodynamic shape optimisation. In another work, Mousavi et al. [9] attempted to quantify the effect of shape parametrisation on aerodynamic shape optimisation while using three different parametrisation schemes – mesh points, B-spline surfaces and Class function/Shape function Transformation. The selection of an appropriate parametrisation scheme is an important pre-requisite for conducting any design optimisation study.

1.2 Computer Aided Design

For modelling purposes, the computer aided design (CAD) approach is commonly used by industry today. The CAD approach for geometric modelling makes use of higher class curves such as B-splines in conjunction with curve fitting tools. Modelling the parametrised geometry using modern CAD systems provides the user with the flexibility of generating a large number of possible geometries, that can then be considered to

assess their performance while at the same time it is possible to constrain the geometry so that the generated model is geometrically feasible. Due to its simplicity in use and the possibility of generating models with complex geometric entities (such as B-splines), CAD tools such as Siemens NX, Dassault Systémes' Solidworks and CATIA, etc. have become popular in engineering design companies. Since their introduction in the design industry, CAD systems have advanced to a large extent. Today they are capable of handling the complex geometries required for engineering applications with an intuitive user interface. Tasks such as creating lofts, extrusions, sweeps and revolves are performed seamlessly within the CAD environment. In the recent past, CAD software providers have given much importance to parametric feature-based solid modelling functionality [10]. Automatic generation of parametrised geometries through user scripts has proved to be useful in performing shape optimisation. The growing need for efficient designs of minimum cost has led to the use of new and better design approaches such as multi-disciplinary design optimisation (MDO), robust design, reliability-based design, etc. A suitably parametrised geometry which can be modelled in a CAD environment is useful while performing such optimisation studies especially on complex geometries.

1.3 Design in the presence of uncertainties

Although a part is designed to deliver the desired structural performance for its service life, existence of uncertainties in different parameters may have an effect on its life expectancy. From a structural point of view, uncertainties or variations may arise due to fluctuations in loading and boundary conditions, environmental conditions, geometric parameters, or deviations in material properties such as the yield strength, Poisson's ratio, etc. Uncertainties may also result from assumptions made while modelling a real engineering problem [11]. Variations due to manufacturing may result in a final part which has deviations with respect to the nominal geometry. This uncertainty in the geometric parameters may result in a scatter in the overall efficiency, performance and hence life expectancy of the part. Recently a lot of effort has been made to include such uncertainties in the system variables while performing design studies both in academia and industry. It has become essential to understand and quantify the effects these uncertainties have on the performance of the part, while designing it, with a goal to minimise them. For this reason the two most commonly used approaches used by researchers are robust design and reliability-based design [12].

1.3.1 Reliability based design optimisation (RBDO)

To prevent catastrophic failure while designing a critical component in a structural system, reliability-based design optimisation can be adopted [11]. The constraint conditions of the optimisation problem are characterised by the probability of its structural failure.

Reliability-based design optimisation can be considered as the process of minimising the cost function under the observance of probabilistic constraints instead of the conventional deterministic constraints [13]. The inclusion of probability of failure in the reliability analysis can be achieved using various different methods. The simplest and most direct method to gather such information is to perform Monte Carlo simulation on a large amount of sampled data which can be a computationally expensive exercise. The first and second order reliability methods [14] require an additional nonlinear constrained optimisation procedure for locating the most probable point of failure making the RBDO a two-level optimisation process. Weighted regression based response surface methods have been adopted for structural reliability analysis to overcome some of these computational burdens [15]. However, the approximation methods used for the constraint functions can suffer in accuracy when the constraint functions are highly nonlinear [16].

1.3.2 Robust design optimisation

Engineering components can be designed by optimising the parameter values with respect to a single or multiple objective functions. These parameter values are then delivered to the manufacturing unit in the form of engineering drawings with tolerances on the geometric entities. However, these manufactured components are subject to variations due to the processes used for producing them. Variations in designed parameters may also occur during the operation period. Robust design is the field of research that aims to tackle such problems by minimising the effect, of variations in the design parameters, on the performance of the component. The optimum design is sought without eliminating the source of uncertainty or variation [17, 18]. Instead of designing a component based just on the nominal performance, the variations occurring because of the inaccuracies in modelling, variations due to manufacturing tolerances and operating conditions are given due consideration. Often robust designs have slightly worse nominal performance as compared to an optimisation on nominal performance alone. Some designs can show improvements in both nominal performance as well as the extent of variation in performance, however these are typically not properly optimised to begin with. In their survey, Beyer and Sendhoff [19] have given a comprehensive list of different approaches to perform robust design optimisation. Taguchi's [20] work on developing a design methodology that accounts for the uncertainties in the framework of quality engineering has been regarded as one of the earliest works on robust design.

McAllister and Simpson [21] used the robust design approach on the combustion chamber of an internal combustion engine. The uncertainties which arise due to the manufacturing in the cylinder bore, intake and exhaust valve diameters were introduced while performing the robust design optimisation. Kumar et al. [22] illustrated an efficient methodology to design compressor blades by considering the aerodynamic performance

of the blades in the presence of manufacturing uncertainties. A geometric parametrisation technique was developed to represent the variations in blade geometry due to the manufacturing process. The design obtained using this method showed less sensitivity to manufacturing variations as compared to the conventional deterministic design. The application of surrogate models, which replaced the high fidelity CFD simulations resulted in significant reductions in computational time.

Thakur et al. [18, 23] performed similar studies on turbine blades. One of the difficulties that arises while representing variations due to manufacturing in the parametrisation scheme is the elimination of noise from the measurement data. Thakur et al. [23] used principal component analysis for filtering the noise from the measurement data in conjunction with a dimensionality reduction method. It was reported that 82% of the variation in the geometry was accounted for by the manufacturing process and 18% of the variation represented the noise in the measurement data. A lifing study on a turbine blade showed that the mean life of the manufactured blades showed a reduction of 1.7% as compared to the designed blade life. Using the robust design approach, an improvement of up to 3% in the mean life of the blade was observed with approximately 57% reduction in the standard deviation [18]. Hence, it is observed that using the robust design principles, for designing engineering components, can reduce the variations observed in the service life of components due to manufacturing uncertainty.

Du and Chen [24] highlighted that while achieving a robust design it is also important to control the robustness in the design feasibility due to the effect of uncertainties. It was reported that the approaches available for existing robust design may lead to infeasible design solutions. Du and Chen examined several feasibility modelling techniques while evaluating the robust design. It was concluded that the probability feasibility formulation is an ideal method to use when evaluating robustness in the feasibility of the design solution [24].

1.4 Disc blade attachments

The design of gas turbine engines has received a lot of attention in the aerospace engineering literature. The performance of an aircraft can be significantly influenced by the design of its engine. The core of a turbine design consists of the design of rotating blades and discs. Rotating discs and the attached blades are the central components in a gas turbine engine, their structural integrity is vital to the engine's service life. Design of the attachments between compressor or turbine blades and their discs is critical in order to transfer the large loads generated due to centrifugal, thermo-mechanical actions and other gas loads between the two components. Several different methods have been adopted for attachments between the blades and the discs such as welded, pin, dove-tails and firtree joints [25, 26]. The more common methods used today are dove-tail

and firtree joints. Dove-tail joints are commonly used for the disc blade attachments in compressors whereas firtrees are used for the turbine disc blade attachments. In this thesis, a firtree joint between a high pressure turbine disc and the blade of a gas turbine engine is considered.

It has been reported by Kanth [26] that due to the cyclic application of severe thermal loads together with the high centrifugal loads, high stress intensification is observed at the bore of the rotating turbine disc. Large centrifugal loads that are transferred through the disc blade attachments impose severe design requirements on the attachment. In addition to this, these joints have to position the blades at precise locations along the disc rim so that the torque on the blades is efficiently transmitted to the drive shaft and the leakage flows are controlled. The fundamental principle in designing such joints is that they should be strong in tension and as strong in fatigue as the attached blade. In other words, it is desirable to have a longer service life for the disc blade attachments than the attached blade so that the joints do not fail before the blades [25].

Typical dove-tail and firtree joints are shown in Figure 1.1. The transmission of loads from one component to the other takes place through several *contacts* between the two parts. As illustrated in Figure 1.1, in the case of a dove-tail joint, there are two locations where contact takes place, whereas in the case of firtree joints, more than two areas of contact are used for the transmission of the centrifugal load. The surfaces which come into contact are referred to as *pressure faces* in this work. It is necessary that the corresponding pressure faces on the disc and the blade firtree come into contact at precisely defined locations along the pressure faces with the application of load. However, there will be manufacturing variations which may impact on the dimension and orientation of these pressure faces due to which there could be a shift in the location of the contact zone. The pressure distribution across the contact zone between two bodies depends on the radius of curvature of the surfaces that come in contact. If the contact zones

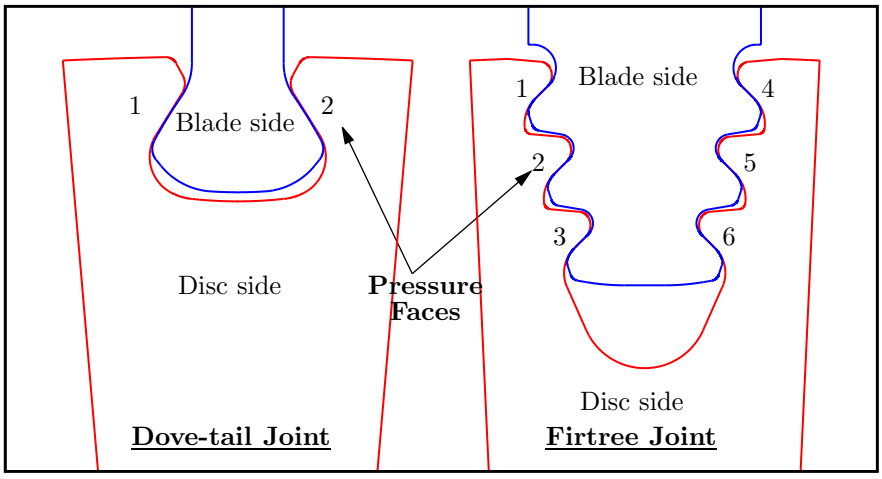

FIGURE 1.1: Schematic of dove-tail and firtree joints

shift to the adjoining regions to the pressure faces, an elevation in the contact pressures is possible. This can affect the resulting stress distribution in the joint in the region surrounding the pressure faces. For desired working of the firtree joint, it is essential that each of the six corresponding pressure faces on the disc and blade come into contact simultaneously. Variations in the orientation of these pressure faces can cause different contacts to engage at different loadings. Due to this, a redistribution of stresses could be experienced by the firtree joint resulting in higher stresses in regions surrounding some pressure faces compared to others, which may eventually affect the life of the joint. In order to assess the effect of the variations in geometry on the life of the joint it is important to investigate the possible modes of failure of a blade disc attachment.

1.4.1 Manufacturing variations in disc blade attachments

The centrifugal force that is transferred through the contacts in a blade disc attachment results in high stress region near the contacts. A slight change in the geometry of the joints can affect these stresses and hence their service life. Even though manufacturing technologies have advanced considerably, the variations due to these processes cannot be completely eliminated. Such variations in geometry can affect the contact conditions involved in dove-tail or firtree joints which may induce peak stresses near the contact edges resulting in a failure of the blade. Due to their complex geometries, it is essential to assess the effect of such manufacturing variations on the service life of the disc blade attachments.

Qin et al. [27] studied the effect of mismatch in the geometry due to manufacturing on turbine blades by considering their fundamental frequencies. The variations were introduced in the three dimensional finite element model by including gaps between different contact faces. It was observed that the first order frequency of the blades due to variations in geometry (gaps between the contact faces) was 18% lower than that of the zero gap model. Also, it was noted that any mismatch due to manufacturing in the corresponding contact faces on blade and disc affects the bending vibration modes more than the twisting modes [27]. A similar study on the disc and blade attachments based on a robust design approach was made by Singh [28]. Singh used probabilistic methods to calculate the probability of stresses given the probability distribution of the gap between the contact faces.

1.4.2 Failure of disc blade attachments

Design of joints is critical for achieving the required service life of any structure. Structural failure of joints before the failure of attached members is not desirable. The joint between a turbine blade and disc is one such joint which has to transfer a large centrifugal load while positioning the blade precisely. Failure of a blade root can have a

(A) Arrieta et al. [31]

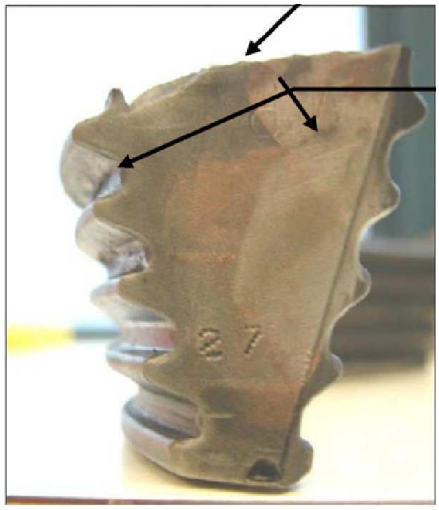

(B) James [32]

(C) Barella et al. [33]

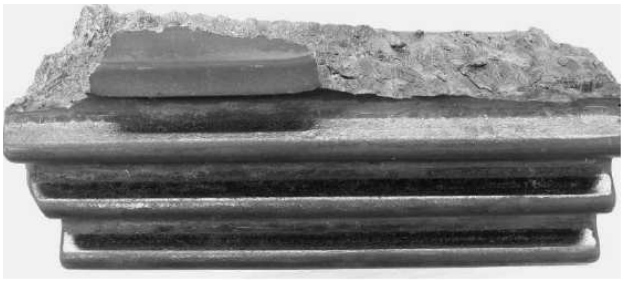

(D) Farhangi and Moghadam [34]

FIGURE 1.2: Fracture of firtree joints

catastrophic effect on the turbine. One such case of a blade root failure of the last stage steam turbine engine is reported by Rao [29], the failure in one blade root subsequently resulted in fracture of several more blades in the turbine. The fracture observed in the blade root showed three zones in which the crack had propagated since its nucleation. The critical stress intensity factor approach for simulating the crack propagation process was found to agree with the actual fracture observed in the blade root [29]. Witek [30] performed a non linear finite element analysis on a firtree joint to determine the stress state under operating conditions. High stresses were observed in the region near the lower tooth of the firtree slot where the actual blade root had fractured. Witek suggested a change to the tolerance requirements in the firtree region to unload the critical zone where high stresses are observed [30]. Arrieta et al. [31] used a fretting-fatigue model to predict the life of turbine components. In particular, blade root failure due to the fretting action between the contact faces on blade and disc was considered. Experimental studies on the firtree joint in a spin test showed cracks nucleating in the regions near the contact edges. Peak tensile stresses observed near the trailing edges of the contact zone exceed the yield limit of the material which may eventually nucleate a crack. The critical locations which are most susceptible to crack initiation are observed in the

notch regions, where the tensile stresses are high, or near the contact edges. Figures 1.2a and 1.2b show the fracture surface on a disc and blade firtree joint respectively, which joins a point in the notch region to the contact edge on the opposite side [32, 31]. The locations of cracks initiated in the notch regions of a blade firtree joint are shown in Figures 1.2c and 1.2d. Farhangi and Moghadam [34] investigated the fracture of second stage turbine blades in a 32 MW unit thermal power plant. It was reported that the high cycle fatigue fracture mechanism was the main contributing factor in the cracking of the blade root. In a similar investigation Barella et al. [33] observed similar fracture phenomenon of high cycle fatigue that caused the failure of a turbine blade root for a 150 MW unit thermal power plant.

Based on these examples, it is evident that the magnitudes of tensile stresses in the notch regions and near contact edges are the governing factors an engineer should consider while designing such a joint. Although, many factors such as environmental conditions, material properties, high temperatures, etc. contribute to the stress distribution in firtree regions, the centrifugal action is considered to be the primary forcing function that is responsible for the complex stress distribution.

1.4.3 Design of firtree joints

The effect of variation in the geometric parameters, defining a firtree joint such as the angle a pressure face makes with the vertical, or notch radii, etc., on the stress distribution needs to be assessed carefully. The manufacturing processes used to produce these joints are the primary source of variation in the geometric parameters in the manufactured joint. Design approaches which incorporate uncertainty in the system parameters can be used to minimise any substantial effects on the stress distribution, and hence the life expectancy.

In a previous study of design optimisation on the firtree joints by Song [35] and Song et al. [36], emphasis was given to the shape parametrisation while formulating a deterministic optimisation problem. The tooth profile geometry was constructed using non-uniform rational B-splines (NURBS). The design variables comprise of the control point coordinates and the related weights of these NURBS curves with several other geometric feature dimensions. The use of NURBS curves resulted to a design that showed reduction in the notch peak tensile stresses as compared to the firtree geometry created with simpler geometric entities such as lines and arcs.

Zhang et al. [37] performed a structural optimisation on the firtree joint by minimising the maximum equivalent stress in the blade root and disc rim with twelve design variables defining the geometry. A complex damping structure of the integral shroud and tie wire between three blades attached to the disc was used while performing the three dimensional finite element analysis of the assembly. The design optimisation resulted in

a firtree joint which showed a reduction by 12.26% in the maximum equivalent stress in the firtree region of the disc. However, no consideration was given to the variation in the stresses observed in the firtree region as a result of the manufacturing variations.

In a recent study, Zhou et al. [38] designed the firtree joint again by minimising the maximum equivalent stress in the joint with eight different geometric parameters as design variables by using four different optimisation algorithms: Pattern search, genetic algorithm, simulated annealing, and the Particle swarm optimisation. The variations due to the manufacturing processes were included in the optimisation process by varying the initial gap between the contacting faces. Five different cases were considered by choosing arbitrary values for these initial gaps at different flanks.

While performing a robust design optimisation on the gas turbine disc and the blade firtree root, Brujic et al. [17] used Monte Carlo simulation with 500 samples using a descriptive sampling as suggested by Saliby [39]. The blade root that was optimised, for the variation in the maximum principal stress and the contact pressure, has four contacting pressure faces. First, a deterministic design optimisation was performed for two separate objectives: meeting the rupture criteria and minimising the critical stresses, in order to reduce the design space. A reduction of up to 28% was obtained in the stress magnitudes in the blade root section. In order to achieve a robust blade root design, Brujic et al. [17] combined the structural reliability and robust design approaches with the Six Sigma concepts. Variations were incorporated in the input design variables, constraint formulation, and the objective formulation. The parameters defining the blade root geometry were perturbed with a normally distributed noise characterised with a standard deviation of 3%. However, the computational time required for this process was around 5 days since Monte Carlo simulation was used on the finite element (FE) model to evaluate the response mean and standard deviation.

1.5 Objectives of the thesis

The main objectives of the work presented in this thesis are:

1. To extract the variations in the geometric parameters of the manufactured firtree joint from the available measurement data by applying different parametrisation schemes with increasing complexities.

2. Use the measurement data to parametrise the roughness on the pressure faces to numerically generate new surfaces that belong to the same family of surfaces with respect to the surface texture.

3. To assess and quantify the effect that these manufacturing variations have on the stress distribution in the two- and three-dimensional firtree joints.

4. To propose a design methodology based on robustness principles in conjunction with response surface methods, in order to select the values of the geometric parameters that yield designs which have least variation in the performance of these joints in the presence of manufacturing uncertainties.

1.6 Thesis overview

This thesis is divided into six chapters including this chapter and the conclusions. A brief overview of each chapter is presented below.

Chapter 2 deals with the parametrisation based on the available data on real disc side firtree joints on a high-pressure turbine disc. A curve fitting method is used while minimising the root mean square error in order to fit two different substitute geometries. The variations observed in the pressure angles on the disc firtree joints are evaluated by comparing the angles from the substitute geometries to the nominal firtree geometry. The results obtained from the fitting process show that a slight drift towards the left side of the firtree joint exists either due to the manufacturing processes or measurement error. A Fourier transform is also applied to the raw measurement data on the disc firtree joints, in order to eliminate the noise.

Chapter 3 attempts to parametrise the roughness on the pressure faces by assuming the surface to be a two-dimensional random process. Two different methods are described which are used to numerically generate new rough surfaces which show the same variation in the observed heights over the mean plane on the manufactured surfaces. The autocorrelation function which represents the spatial distribution of the scanned heights, is one of the two parameters required to define a rough surface, the other being the height distribution function. In the first method a linear transformation is performed on matrices with random numbers following a given height distribution and autocorrelation function while generating new rough surfaces. Convergence issues make this method stable only for matrices with a limited number of elements ($\approx 20 \times 20$). Alternative approach suggested in the literature to tackle these issues is mentioned. In the second method digital filters based on Fourier series are used in order to generate new rough surfaces. Working with larger matrices is easier while implementing digital filters, however, the accuracy of the results is reduced when the size of matrices exceeds 64×64. The parametrisation suggested here is able to generate a large variety of Gaussian and non-Gaussian surfaces with arbitrary autocorrelation functions. In this work, only the Gaussian type of surfaces are generated since a normal distribution of heights is observed on the pressure faces of the disc firtree joints.

Chapter 4 performs elastic stress analysis on the two- and three-dimensional firtree joints in the FE environment of Abaqus. Only centrifugal loads are applied on the blades, since the stresses due to the rotatory motion of the bladed-disc govern the stress

distribution. Analysis is performed on a single sector of the disc with a blade attached at its rim with the help of a firtree joint. The geometry is created using the Open C API of Siemens NX which is capable of representing the variation in the geometry in different ways. An automated work flow is set-up using Matlab scripts, that relates the variation observed in the manufactured disc firtree joint to the stress distribution in the notch regions. Since the scanned data is available only on the disc side firtree joint, the geometry on the blade side is kept nominal throughout this thesis. It is observed that the magnitude of stresses near the bottom flank of the firtree joint are higher as compared to the other two flanks. The effect of a twist between the front and rear side geometries of a three-dimensional firtree joint on the notch stresses is extracted. It is observed that higher magnitudes of twists, results in larger variation in the notch stresses. The roughness of the pressure faces is included in the stress analysis by fitting a B-spline curve or surface through the noise-filtered scanned data in Siemens NX. An elastic stress analysis shows localised peak stresses on the pressure faces, which have an effect on the stress distribution in the notch regions. The numerically generated rough surfaces are included in the three-dimensional stress analysis, by transforming the nodal coordinates on the pressure faces to follow the generated rough surface.

Chapter 5 combines the results obtained on the variation in the pressure angles from chapter 2 within a robust design optimisation of the firtree joints. The mean and standard deviation of tensile stresses in the notch regions are used as objectives in the optimisation. Their accurate evaluation requires a number of runs of the FE code which makes it a computationally expensive exercise. To overcome this issue, the approximate response surface approach based on Gaussian process modelling is adopted in this chapter. An evolutionary multi-objective optimisation method is used on the surrogate models for the mean and standard deviation for variation in notch stresses. It is observed that reducing the pressure angle by 6% with respect to the initial geometry, results in a more robust design for the evaluated variation in pressure angles. However, any increase in the pressure angle from the starting geometry results in a design which is highly sensitive to the variation in pressure angles.

Chapter 6 lists the important conclusions that are drawn from this work with respect to the parametrisation of the firtree joints to include the geometric variations due to manufacturing processes. Important results obtained from studying the effect of geometric variations on the stress distribution are presented. Benefits of using a surrogate modelling approach in the robust design optimisation study are highlighted. The design obtained as a result of the robust optimisation study is compared with the nominal design. Finally, recommendations for further work in the aforementioned areas are made.

Chapter 2

Geometric Representation of Manufacturing Uncertainty

2.1 Introduction

Engineers prepare drawings based on the design calculations which are used to manufacture these components. While preparing these design drawings, engineers specify tolerances to restrict the variations due to manufacturing processes. As mentioned by Dowling et al. [40] "Functional requirement or assembly conditions on a manufactured part are normally translated into geometric constraints to which the part must conform". The methods used for manufacturing engineering components have to be developed enough to manufacture the components with respect to the tolerances specified by the design drawings. Geometric constraints are generally expressed in terms of standards provided by international standards institutes such as ANSI, ISO, etc. These constraints are generally specified in terms of the *envelope principle* which restricts the part to lie within two envelopes of ideal shape [40]. This envelope principle evolved from the gauging technology of *go* and *not go* gauges which check the maximum and minimum manufacturing variation, respectively. The tolerances vary directly as a function of the feature's characteristic dimension since smaller features are required to be located more precisely. For engineering components obtained in high-efficiency machines such as aero engines, the tolerances on the geometry are stringent. Variations in the geometry due to the manufacture of such components can affect the performance of the engine significantly.

Before the advent of advanced measuring instruments such as the coordinate measuring machines, hard gauges were commonly employed for inspecting manufactured parts or components. However, this method of inspection has certain disadvantages such as:

1. Design is an iterative process, hence minor changes in the design at later stages are unavoidable. This requires the design and manufacture of new gauges for every change that is made in the design, which makes hard gauging an expensive method.

2. For more complex geometries, high precision hard gauges are required which are more expensive to manufacture.

Due to these shortcomings, the hard gauges used for dimensional measurements are now generally replaced by more sophisticated measuring machines such as the coordinate measuring machine (CMM). Collecting and processing data using such measuring machines is sometimes referred to as *soft gauging* [40]. CMMs have been proved to be more flexible for dimensional measurements and tolerance evaluations. The coordinate measuring machine records the coordinates of a point, on the component being measured, from the probing device which are further transformed to a component coordinate system from the machine coordinate system. The CMM uses a pre-defined sampling rate (Λ) while scanning the coordinates of points on the component [40, 41, 42]. This data is further analysed using a suitable regression algorithm to obtain the manufacturing variations in the geometry, assuming the measured data is free of any measuring error. However, if the variations due to the measuring machine are of the same order as the manufacturing variations, the measured data have to be filtered of this unwanted variation before processing it further. The term *coordinate metrology* is used to define the study of best fit methods and regression algorithms for extracting geometric entities from such scanned data [43]. The geometry extracted from the scanned data is the manufactured representation of the nominal geometry, it is also sometimes referred to as the *substitute geometry*. The geometric parameters of the substitute geometry are compared with that of the nominal geometry to evaluate the manufacturing variation and to check if they are within the specified tolerance bounds.

The choice of sampling strategy and the fitting algorithm used for evaluating the substitute geometry are the key issues related to coordinate metrology. These issues originate from the method's divergence problem which has been the focus of much of the research in this field [43, 44, 45]. If the measuring instrument is sufficiently accurate, the evaluated manufacturing variation can originate from two sources viz., the choice of data analysis algorithms and the sampling strategies used to collect the data. It has been reported by Yan et al. [43] that using different algorithms for fitting geometric entities to the same scanned data can give different results. This emerges from the lack of a mathematical definition for geometric dimensioning and tolerancing in current standards since they were originally designed for hard gauging [43]. The second source of uncertainty comes from the fact that any sampling scheme provides data at finite discrete points on a surface which is made up of an infinite number of points. Variations in geometry due to manufacturing can originate due to the material deficiencies at the surface, machining deviations or due to the presence of particles of debris on the surface. Such variations

can vary between consecutive points, hence the variation in the manufactured geometry depends on the distribution and the number of scanned points.

2.2 Geometric Inspection Using Scanned Data

The inspection of manufactured parts involves measuring the dimension, form, and position of the geometric entities and comparing them with the nominal geometry. Traditionally, inspection for dimension, form, and position were done independently of each other [46]. But with the use of high-precision measuring machines such as a CMM, simultaneous measurement of these features has become possible. For example, the same CMM scanned data of a straight edge on a manufactured component can be used to evaluate its length, straightness of the edge and its orientation. The process of inspecting a manufactured part can be divided in three major steps [47]:

1. In the first step, the distribution and number of sampled points at which the measurements are to be taken are decided.
2. The second step consists of measuring the coordinates of the discrete points on the manufactured part using high precision machines such as a CMM. This involves mounting the part in the CMM, usually with specialised jigs.
3. In the last step, the coordinates measured from the manufactured part are analysed to evaluate best fit geometric entities of known analytical expression such as lines, arcs, cones, etc.

Although extensive research has been carried out into the algorithms used to fit geometry to discrete data points, it is difficult to select one particular algorithm which can be used in the majority of the cases. Two methods for fitting purposes that are found to have been used frequently in the literature are the minimum zone method and the least squares method. The method of least squares has been more popular than any other method for evaluating the best fit geometry. However, since these methods are used to inspect the geometry, they give very little information about the functionality of the component. Weckenmann et al. [48] suggested using functionality oriented methods for inspection of a manufactured component. Since the evaluation of variation in geometry is of interest here the minimum zone method and the least squares methods are briefly discussed in the following sections.

2.2.1 The Minimum Zone Method

The implementation of the minimum zone method is based on the envelope principle used by the standards organisations [40]. Evaluating the minimum zone essentially means

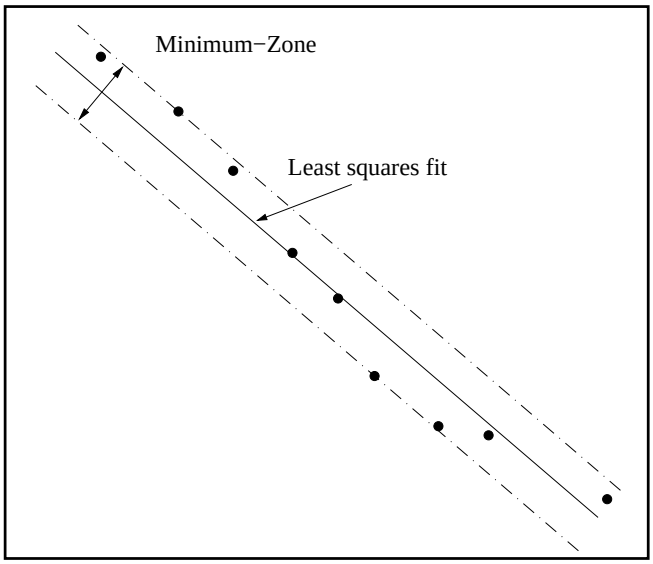

FIGURE 2.1: Minimum-Zone Method

calculating the upper and lower bounds of the geometry within which all the points on the surface of a part lie. The normal distance between these bounds is the required minimum zone. The problem of evaluating the minimum zone is formulated as an extreme fit evaluation which locates the nearest and the farthest point that characterise the zone [49]. In some cases, the minimum zone is evaluated by fitting a mean geometry to the data and then by offsetting it in both directions so that all the scanned points lie within these extremes. In these cases, the mean geometry is obtained using the least squares method [50]. An example of calculating the minimum zone for a set of scanned

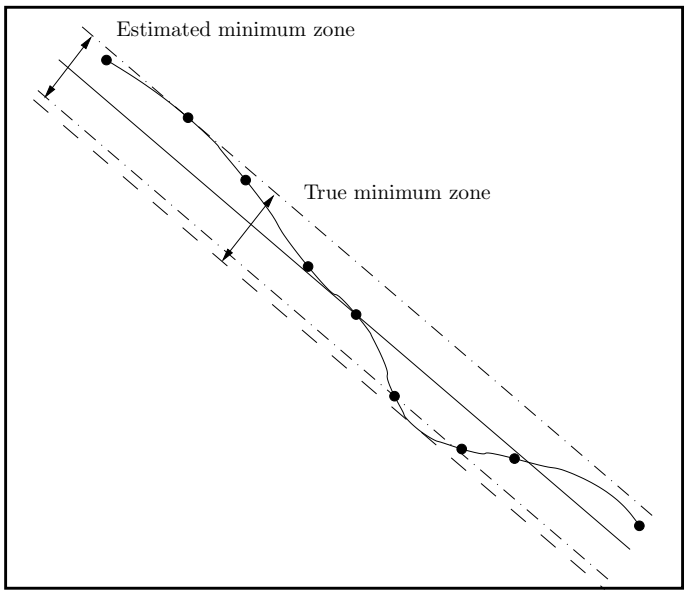

FIGURE 2.2: Estimated Minimum-Zone and True Minimum-Zone

points along a straight line is shown in Figure 2.1.

The upper and lower bounds are obtained by drawing parallel lines to the mean line, so that all the measured points lie within the zone defined by the two bounds. The perpendicular distance between these two lines is the required minimum zone which is compared with the specified tolerance. Although this method conforms with the envelope principle used by the standards, there exists a drawback to this method which is illustrated in Figure 2.2. The extreme fit surfaces are evaluated so that all the scanned points on the manufactured surface lie within the zone created by them. However, the region of the manufactured part between two consecutive points is assumed to lie within the minimum zone which may not be the case. A sufficiently large sampling rate will reduce the error in the evaluated minimum zone.

2.2.2 Least Squares Method

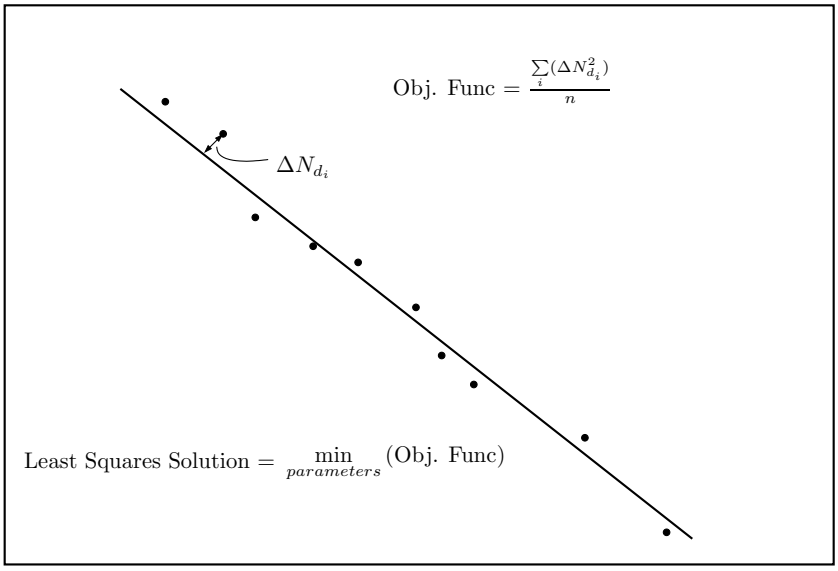

FIGURE 2.3: Least Squares Method

The least squares method of fitting curves to the discrete set of data points has been used frequently in the literature. A curve is fitted to the coordinate data by minimising the sum of squared deviations, Figure 2.3. The method is also referred to as the normal least squares method when the deviations are taken normal to the fitted curve [40].

The objective function involved in the least squares method is a nonlinear function of the parameters representing the fitted curve. The least squares method is computationally fast as compared to the minimum zone method. Also, it is shown by Dowling et al. [40] that the least squares method shows less bias towards the sampling rate, as compared to the minimum zone method. Choi et al. [49], however reported that the minimum zone method yields smaller zone value as compared with the least-squares fit. Minimum zone

method is consistent with the standard definition since it is based on the hard gauging inspection approach.

2.3 Characterisation of Geometric Variability

There could be several factors affecting the variations due to manufacturing such as a slight shift in positioning of the machining tools, drift in alignment of the manufacturing machine over a period of time if components are manufactured in batches or due to the particles of debris on the finished surface. In the current work, it is assumed that errors due to the measuring instruments are negligible as compared to the variations due to the manufacturing processes. In most manufactured components, the variation can be categorised in two distinct components, the waviness and the roughness component [43, 51]. Variation due to the waviness component is the smooth change along the surface of the part that has a functional relationship with the characteristic dimension of the surface, whereas the roughness component of manufacturing variability represents the closely spaced irregularities on the surface of the part. These irregularities have high frequencies as compared to the smooth waviness variations.

$$\mathbf{M} = \mathbf{N} + \boldsymbol{\epsilon_w} + \boldsymbol{\epsilon_r} \tag{2.1}$$

The geometry of the manufactured part, $\mathbf{M}$ can be considered as the sum of the nominal geometry, $\mathbf{N}$, and the components of manufacturing variability due to the waviness and the roughness, $\boldsymbol{\epsilon_w}$ and $\boldsymbol{\epsilon_r}$ respectively Equation 2.1, [43]. Every data point scanned using the measuring machine consists of variations due to these two components. Since there is a spatial correlation between the nominal geometry and the waviness component, it is also known as the deterministic component of the geometric variation [43]. It is essential to separate these components of variability from the raw scanned data in order to evaluate the true representation of the substitute geometry. Frequency domain methods such as Fourier transform (discrete and continuous Fourier transforms, etc.) can be useful in filtering the roughness component of the variation. However, these methods can be used efficiently when the sample size is sufficiently large, since the irregularity in geometry due to the roughness component of error can vary between two consecutive points. Hence, a larger sampling rate may result in a more realistic representation of roughness of the surface.

2.4 Extracting geometric variability from CMM scanned data of a firtree joint

In this section the manufacturing variations are extracted from the CMM scanned data of a firtree joint on a turbine disc using two methods. The firtree joint that is analysed here

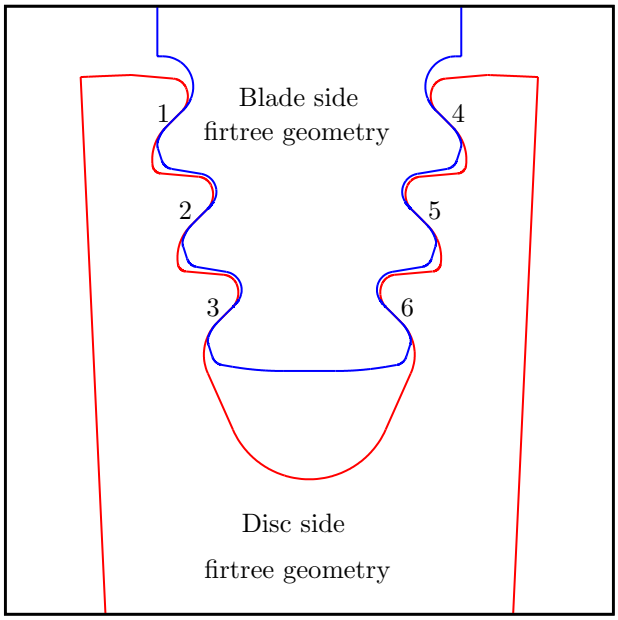

FIGURE 2.4: Firtree geometry

involves contact between the blade and disc at six different locations. High centrifugal loads acting on the blade are transferred to the disc through these firtree joints. Accurate manufacturing of these joints is essential in order to locate the engine blades in their precise positions.

The principle used to transfer high centrifugal loads from engine blades to the discs via firtree joints is the contact between the two components. Multiple contacting surfaces are useful in increasing the surface area helping in cooling of the firtree region and distributing the stresses across the joint. The lines (surfaces in 3D) along which the blades and disc come in contact are referred to as *flank lines* or the *pressure lines*[1] in this thesis. These pressure lines form the most important geometric feature in a firtree joint. A slight variation in either form, position or orientation of these pressure lines can affect the contact conditions (contact area and pressures) and may result in high localised stresses in that region. It is therefore important to extract the manufacturing variations from the CMM data of the firtree geometry, especially in the region near the pressure lines to study their effect on stresses.

The firtree geometry that is analysed in this work has three flanks on each side of the centre line as illustrated in Figure 2.4. A sector of the disc which contains just one firtree slot is shown in the figure. The geometry is symmetrical about the centre line for both the disc and blade side firtree geometries. Both geometries are made up of basic geometric entities such as lines and arcs. The firtree geometry tapers down from the rim of the disc towards the centre of the disc.

[1]The term *pressure line* is used to represent the *pressure face* on the three dimensional firtree joint in two dimensions.

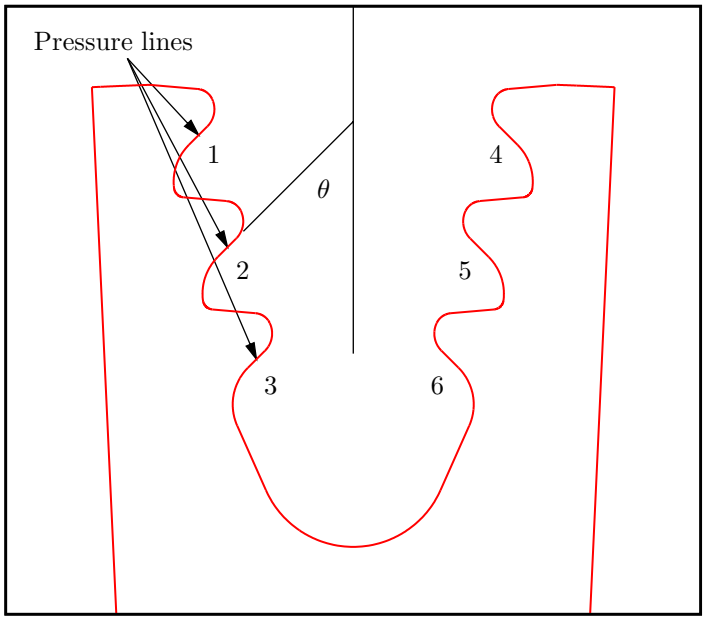

FIGURE 2.5: Disc side firtree geometry

1. **Disc side firtree geometry**: The disc side firtree geometry is as shown in Figure 2.5. It can be seen that the thickness at the flank, on the disc side firtree, that is closest from the disc axis is larger than the flank away from the disc axis. The geometry consists of six pressure lines, three on each side of the line of symmetry. These lines are inclined at an angle θ (pressure angle) with the vertical as shown in the figure. Slight variation in the orientation of these lines can vary the pressure

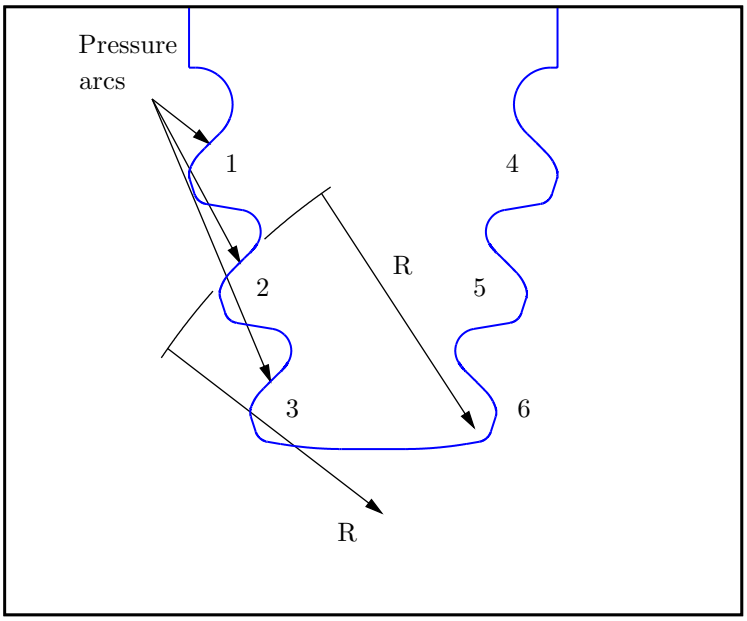

FIGURE 2.6: Blade side firtree geometry

angle θ to $(\theta \pm \Delta\theta)$ which may affect the contact conditions between the corresponding pressure faces on the firtree joints. Surface roughness on these pressure faces may also affect the stresses near the contact regions. A smooth surface over the contact zone will ensure a uniform distribution of contact pressure across the contact zone.

2. **Blade side firtree geometry**: Figure 2.6 shows the firtree geometry from the blade side of the joint. The geometric entity that comes in contact with the pressure line on the disc firtree analysed here is an arc with radius R. This method of designing the pressure faces on blade firtree as cylindrical surfaces is called *crowning* which helps in reducing the fluctuating hoop stresses at the edges of the contact zone [52].

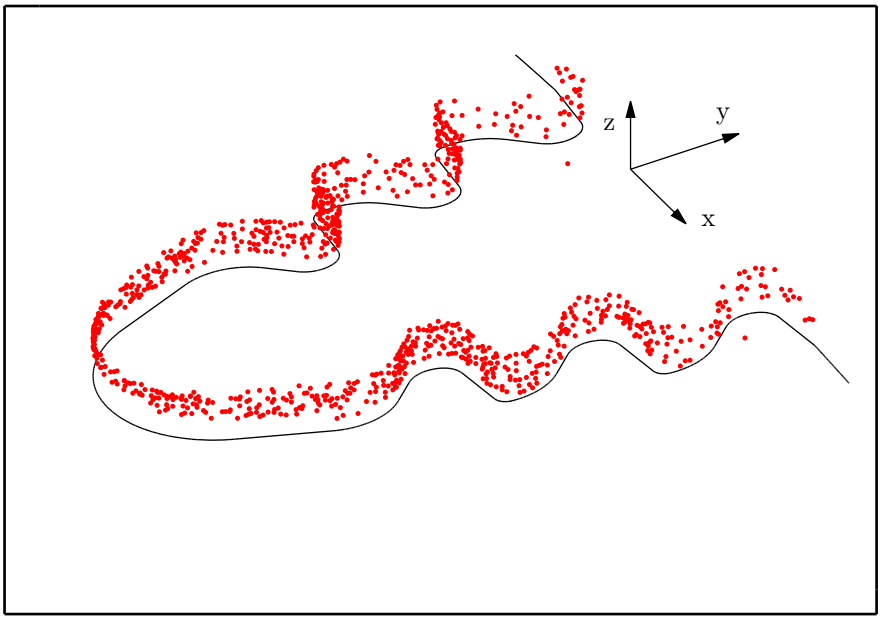

FIGURE 2.7: Scanned data of a firtree joint

The firtree slots from the real discs are scanned using the CMM on nine representative discs since these were all that were available. Data from five evenly spaced slots along the disc rim are analysed for evaluating the best fit geometry. For each firtree, the data is further divided into front and rear along the thickness of the disc at the rim. Hence, data for several individual slots, each of the same nominal geometry, are analysed using two methods, minimising the root mean square error (RMS) and fast Fourier transform (FFT). Figure 2.7 shows the cloud of points scanned using the CMM on one of the firtree slots.

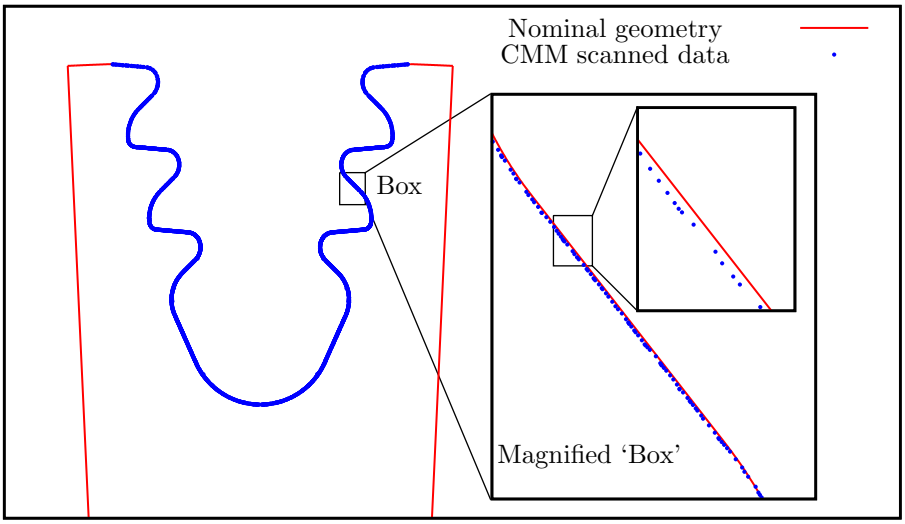

FIGURE 2.8: Scanned data vs nominal geometry

2.4.1 RMS Minimisation

The CMM scans the coordinates in three directions (x, y, z) for each point on the surface of the part. By taking the projection of the scanned data on the $x - y$ plane, we can compare the manufactured geometry (represented in two dimensions) with the nominal geometry as shown in Figure 2.8. The manufacturing variation can be seen in the magnified view of a pressure line on the disc firtree geometry. The position and the orientation of these pressure lines on the manufactured part is evaluated by minimising the root mean square value of the errors. If $y_1, y_2, y_3, \ldots, y_n$ is a set of n numbers, their RMS value is given as:

$$\text{RMS} = \sqrt{\frac{{y_1}^2 + {y_2}^2 + {y_3}^2 + \ldots + {y_n}^2}{n}}. \tag{2.2}$$

2.4.1.1 Pressure line and adjoining arcs

The parameters used while minimising the RMS error are the coefficients of the equation of curve used to fit the data. It is required to evaluate the variation in the position and orientation of the pressure lines by analysing the scanned data near the region of these lines. To do this, the scanned data for the whole firtree is divided into six data sets, with each data set representing a region surrounding one pressure line. It can be seen from the geometry of the disc firtree, Figure 2.9, that each pressure line has tangent arcs at both its ends[2]. From the nominal geometry, the end point coordinates of both arcs are known. Using these coordinates, the data for each pressure line is obtained so that each point in this data set represents either the pressure line or either of the two adjoining arcs.

[2]Firtree geometries are typically designed with circles and straight lines to facilitate manufacturing.

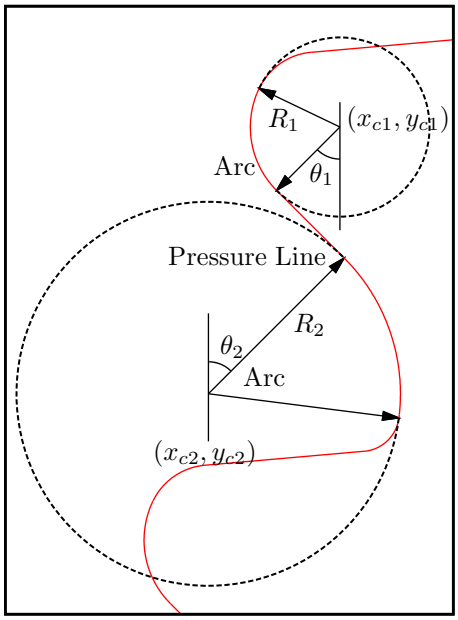

FIGURE 2.9: Pressure line and adjoining arcs ($\theta_1 = \theta_2$)

Having divided the data, the equations for the nominal pressure lines and arcs are used to evaluate the RMS error of the scanned data. This RMS error is then minimised using the `fminsearch` function available in Matlab which is based on the 'Nelder-Mead simplex direct search' algorithm [53]. Hence, the *best fit* geometry for the pressure line and adjoining arcs is obtained. Including the arcs for evaluating the best fit for pressure lines allows the location of the end points of the pressure line and hence their length and orientation. The parameters used for minimising the RMS error are the centre

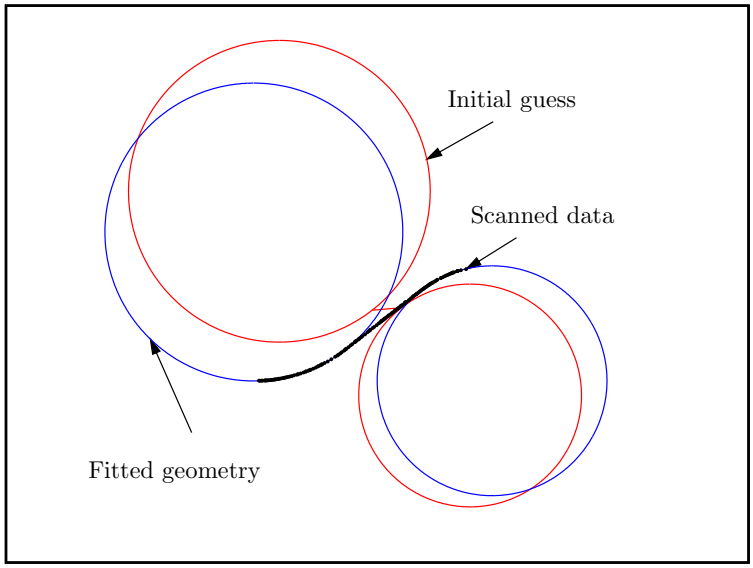

FIGURE 2.10: Best-fit geometry by minimising RMS value

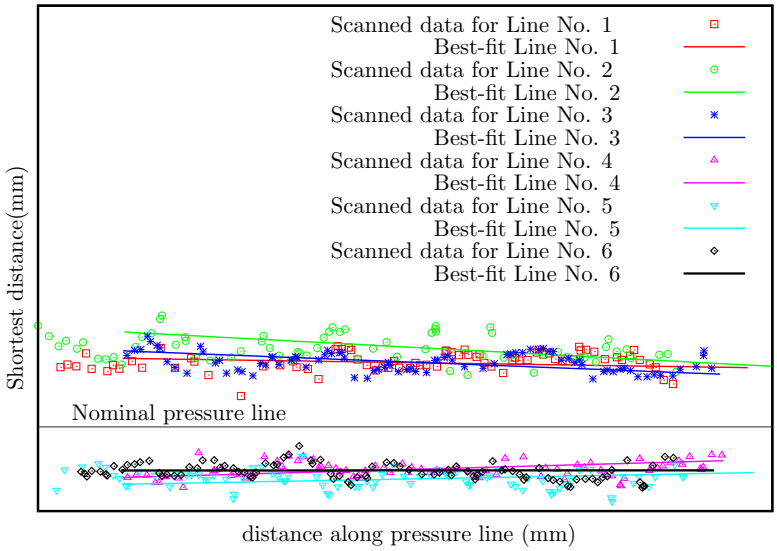

FIGURE 2.11: Best-fit for six lines in a firtree joint (Not to scale)

coordinates of the two arcs, their radii and the angle at which the pressure lines are tangent to the arcs $(x_{c1}, y_{c1}, R_1, x_{c2}, y_{c2}, R_2, \theta_1, \theta_2)$, Figure 2.9.

An example of the best fit geometry evaluated using the data set for one of the flanks is illustrated in Figure 2.10. Figure 2.11 shows the scanned data and the best fit lines for all six pressure lines in a single firtree joint. It can be seen that the best fit lines are shifted from the nominal pressure line and also they are not parallel to the nominal pressure line. Hence, the manufactured pressure lines make an angle $(\theta \pm \Delta\theta)$ with the vertical.

Figure 2.12 shows the normal distance of scanned data from the nominal geometry for all six lines in five firtrees of a single disc. It can be seen from the figure that for all firtrees, except firtree number 3, pressure lines $1, 2, 3$ and $4, 5, 6$ are on either side of the nominal pressure line. It can be therefore said that there may be a shift in the centre line of the machining tool while manufacturing the firtree slots or it could be due to the mounting error while taking the measurements. The variation in the pressure angle due to the manufacturing process is evaluated from the best fit geometries for such a set of data for each flank.

Figure 2.13 shows the histogram of the manufactured pressure angles. It is assumed that the distribution in manufactured angle follows the Gaussian probability distribution with its mean shifted by -0.07% from the nominal value of the pressure angle. It is observed that approximately 61% of the pressure lines are manufactured with a pressure angle less than the nominal value of θ. Since every firtree slot is machined with the same tool setting, it is expected that the variation in parameters at the front side of the firtree would have some correlation with the parameters representing the rear side of the firtree. Each point on the Figure 2.14 represents the angle of the same pressure line

at the front and the rear side of a firtree slot on the disc. Variation up to 0.29% of θ is observed between the front and the rear pressure angles. It is clear that there is very little correlation between the front and rear pressure lines.

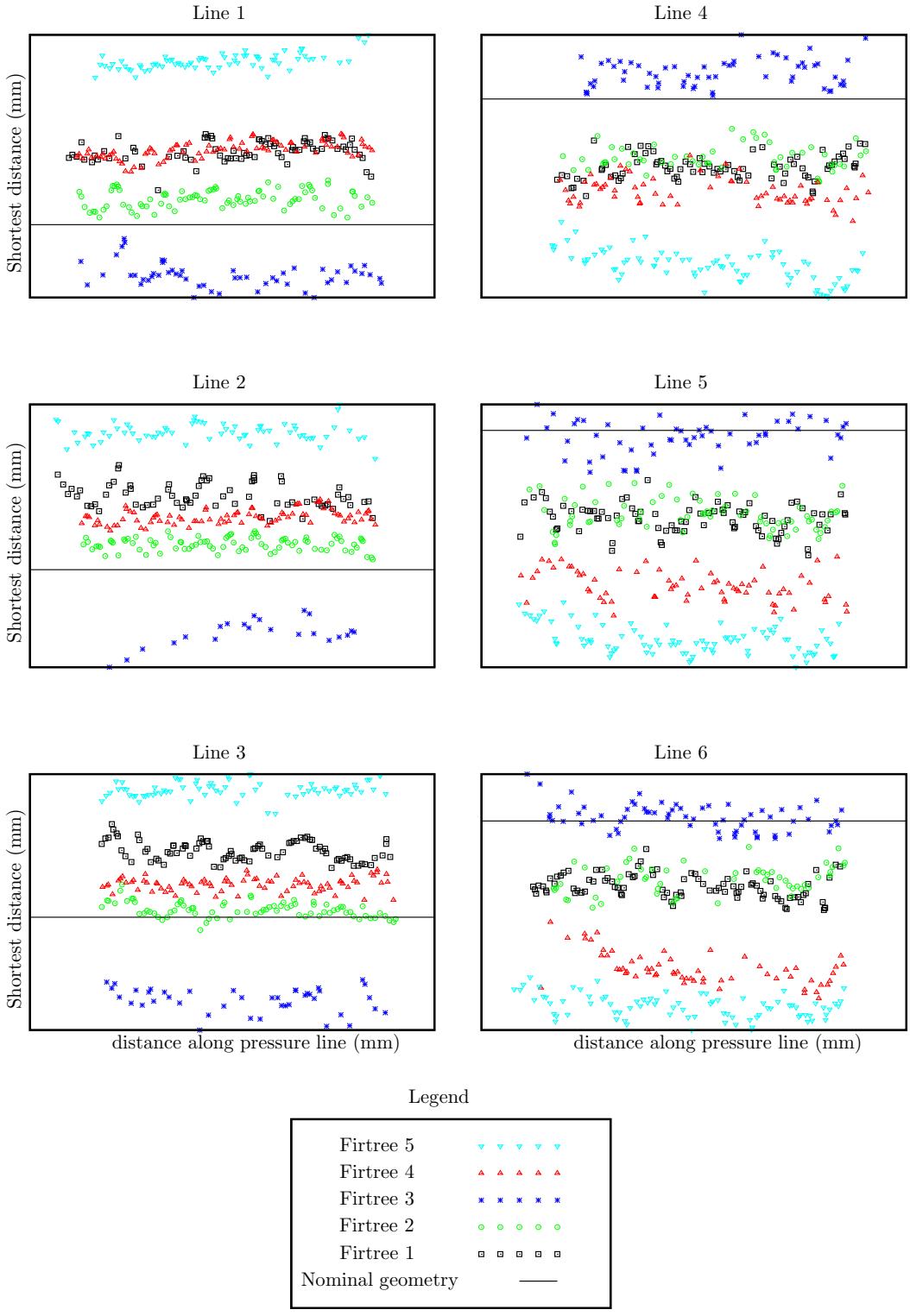

FIGURE 2.12: Shortest distance from nominal geometry (Not to scale)

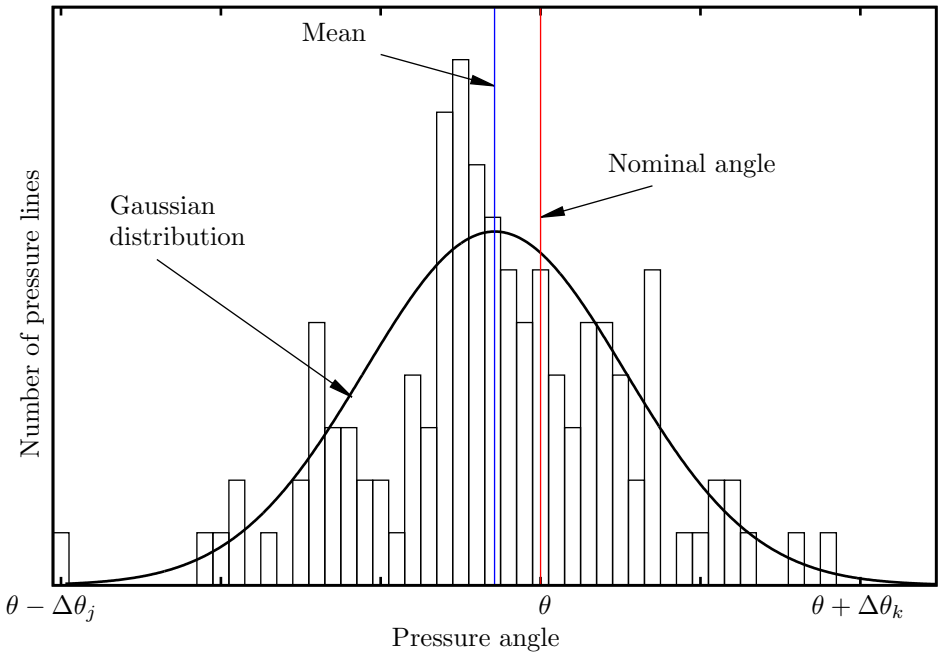

FIGURE 2.13: Histogram of number of lines with pressure angle

2.4.1.2 Included angle

To investigate whether the choice of parametrisation scheme affects the lack of correlation between the pressure angles at front and rear illustrated in Figure 2.14, an alternate substitute geometry is used next. Instead of using the pressure line and adjoining arcs,

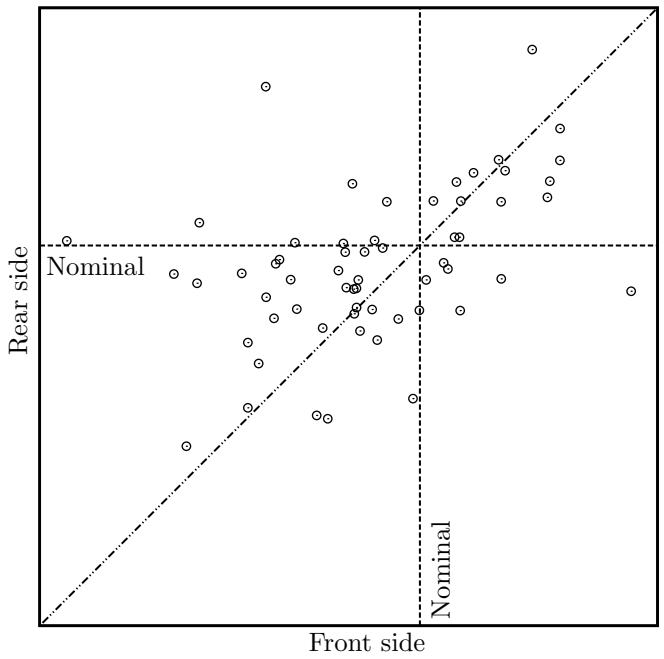

FIGURE 2.14: Correlation between front and rear pressure angles

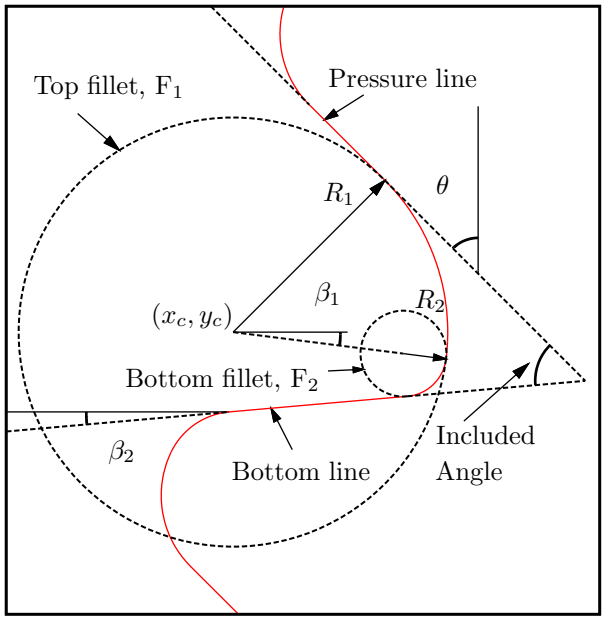

FIGURE 2.15: Substitute geometry for extracting included angle

Figure 2.9, the geometry as shown in Figure 2.15 is used. This geometry consists of the pressure line and a bottom line with two tangential arcs as shown in the figure. The parameters used for minimising the RMS error for this substitute geometry are the centre coordinates of one of the arcs, (x_c, y_c), radii of the arcs, R_1 and R_2, the angle the pressure line makes with the vertical axis, θ, the angle the line joining centres of the two arcs makes with the horizontal axis, β_1 and the angle the bottom line makes with the horizontal axis, β_2. As in the previous section, the CMM data for the whole firtree geometry is divided into six different sets so that each set represents the substitute geometry for one pressure line and adjoining geometry. The advantage of using this particular geometry as the substitute geometry is that the variation in the manufactured included angle, Figure 2.15, can be extracted from the scanned data. Matlab's `fminsearch` function is once again used to minimise the RMS error. While performing this study, data for five slots, front and rear, on nine different discs was available. Hence, 540 sets of scanned data are used to evaluate the best fit geometry.

Figure 2.16a illustrates the variation in the included angle due to the manufacturing processes. It can be seen that the mean of the variation is shifted by 0.15% from the nominal value, while the standard deviation is 0.29% of $\theta_{nominal}$. The maximum variation observed in the included angle is 1.56% of $\theta_{nominal}$. It is observed that 95% of the designs have an included angle greater than the nominal value. The variation in the pressure angle obtained by fitting this substitute geometry is shown with the help of a histogram as shown in Figure 2.16b. The mean of the variation is shifted by -0.05% from the nominal value of the pressure angle. The standard deviation of the fitted pressure angles is found to be 0.2% of $\theta_{nominal}$. It can be seen from Figures 2.16a

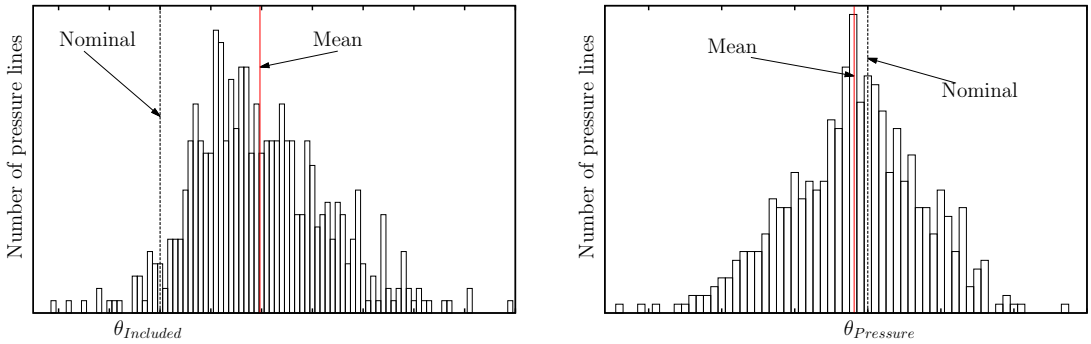

(A) Included angle (B) Pressure angle

FIGURE 2.16: Histogram for variation in included angle and pressure angle

and 2.16b that the variation in the included angle is more widely spread as compared to the variation in the pressure angle. There are 42.5% designs with pressure angle greater than the nominal pressure angle. It can be concluded that the larger shift in the mean of included angle compared with the shift in the mean of pressure angle is due to the relatively low precision in manufacturing the bottom lines as compared to the pressure

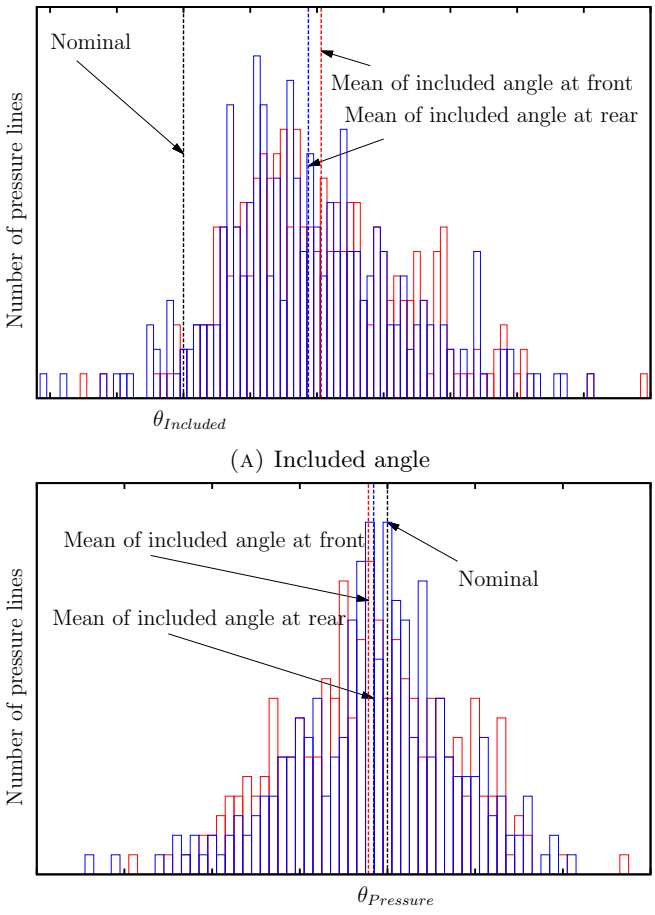

(A) Included angle

(B) Pressure angle

FIGURE 2.17: Histogram of number of lines with included angle and pressure angle at front (red) and rear (blue) of firtree slot

lines. In Figure 2.17, the histograms of variation in included angle and pressure angle, for front and rear sides of the firtree slot are plotted. The mean of the variation in included angle at front and rear is shifted by 0.15% and 0.14% of the nominal included angle, respectively, whereas the shift in the mean of variation in pressure angle at front is −0.06% and at rear −0.04% of the nominal pressure angle.

From Figures 2.17a and 2.17b, it can be seen that the trend in the variation of included angle and pressure angle at the front and rear of the firtree slot is similar. The variations in the included angle at both ends of the firtree slot are more widely spread as compared to the variations in pressure angle. Figure 2.18a shows the correlation between pressure angles at the front and rear of the firtree slot, again the correlation is limited. The histogram shown in Figure 2.18b shows that the mean of the variation in the twist angles between the front and rear is approximately 0°. However, in some slots the change in the pressure angles at front and rear is found to be ≈ 0.78% of $\theta_{nominal}$.

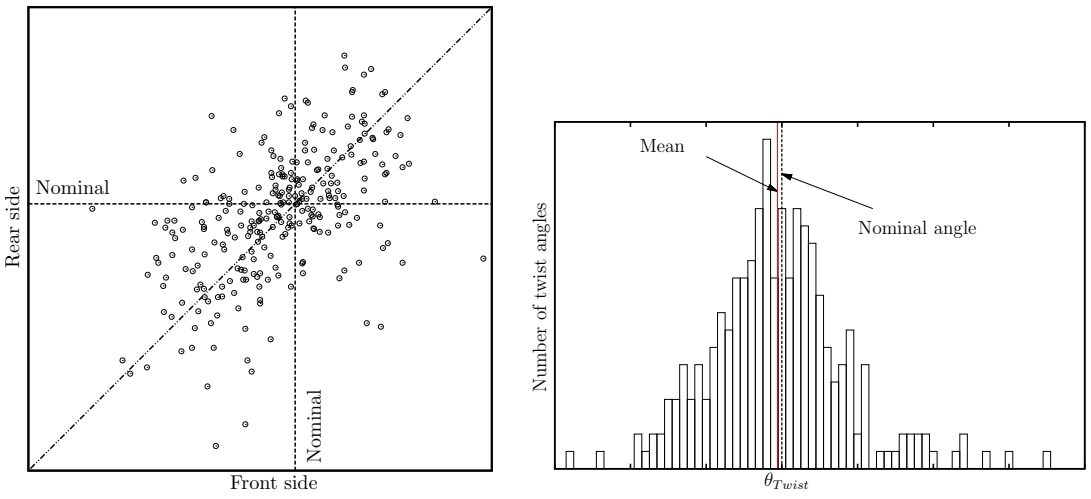

(A) Correlation between front and rear pressure angles

(B) Variation in twist angle

FIGURE 2.18: Variation in pressure angle at front and rear of the firtree slot

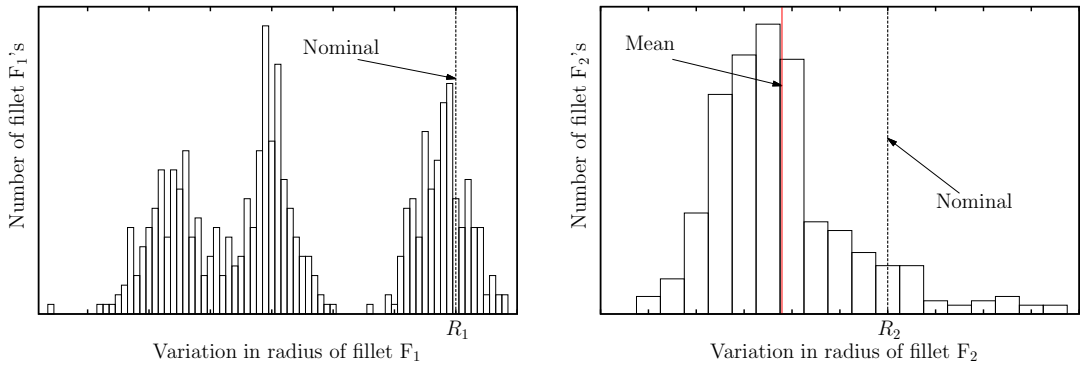

(A) R_1

(B) R_2

FIGURE 2.19: Variation in fillet radii in firtree slot

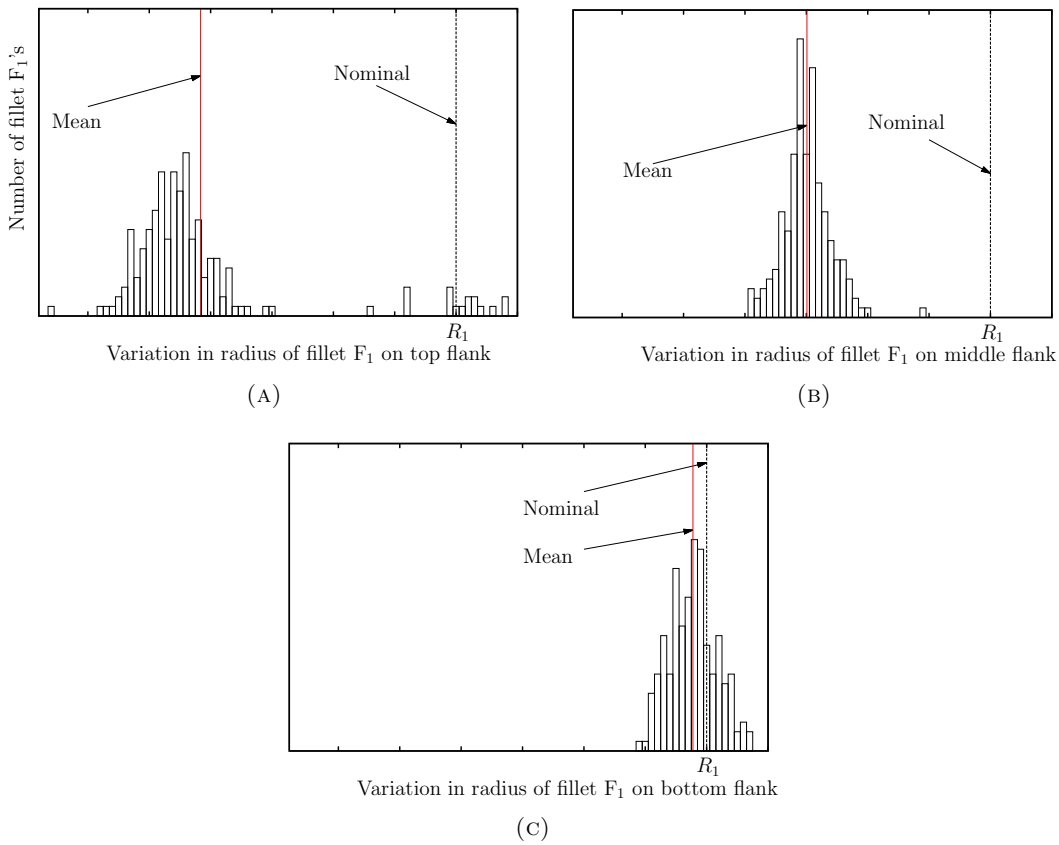

FIGURE 2.20: Variation in radius of fillet no. 1 in firtree slot at top, middle and bottom flanks

Figures 2.19a and 2.19b show the variation in the fillet radius extracted after fitting the substitute geometry in Figure 2.15. Figure 2.19 shows the variation in the radii of fillets F_1 and F_2 respectively. It can be seen that the histogram in Figure 2.19a consists of three peaks separated from each other. When the variation for fillet radii for the same fillet F_1 (Figure 2.15) but for different flanks (top, middle, and bottom) are plotted separately, the histograms look as shown in Figure 2.20. Since the nominal value of the radius for fillet F_1 is different at different flanks, the mean of the variation is different. Also, it should be noted that the mean of radius of fillet at the top flank is greater than the radius of the fillets at the middle and bottom flanks, i.e., top R_1 > middle R_1 > bottom R_1. The mean for variation in R_1 at top, middle and bottom flanks is shifted from the nominal value by -6.5%, -4.7%, and -0.35% respectively. Again, it can be seen that the fillet with smaller radius (F_1 at bottom flank) is manufactured with higher precision than the fillets with larger radii (top and middle flanks). The standard deviations are found to be 0.15%, 0.04% and 0.04% of nominal value R_1.

2.4.2 Fast Fourier Transform

As mentioned by Yan et al. [43], in coordinate metrology the scanned data is generally filtered of any noise so that the smooth component of the manufacturing variation, the *waviness* component, can be determined. The scanned data records two components of manufacturing variability, waviness and roughness. The roughness component comes from high frequency, closely spaced irregularities whereas the waviness component is the smooth variation along the characteristic dimension of the part being measured. To filter out this roughness component from the scanned measurement of points, the frequency domain approach of Fourier transform is used here. It is required that the scanned data is sufficiently dense in order to use the Fourier transform efficiently.

The fast Fourier transform is an algorithm used to calculate the discrete Fourier transform (DFT) of a sequence of N numbers efficiently [54]. DFT has often been used for noise filtering purposes in different fields of research such as acoustics, bio informatics, image processing, etc [54]. A function h of a parameter s, along the length of the pressure line $h(s)$, can also be represented as a function of its frequency f, $H(f)$, with $(-\infty < f < \infty)$. A Fourier transform can be used to represent a function in its frequency domain and an inverse Fourier transform to regenerate the original function from its frequency representation $H(f)$ [55],

$$H(f) = \int_{-\infty}^{\infty} h(s) e^{2\pi i f t} ds, \tag{2.3}$$

$$h(s) = \int_{-\infty}^{\infty} H(f) e^{-2\pi i f t} df. \tag{2.4}$$

In this case, h is a function representing the surface profile. The function $h(s)$, is sampled at finite number of points along the s-scale. Let Λ denote the sampling time interval of the scanned data with N sampled values,

$$h_k \equiv h(s_k), \quad s_k = k\Lambda, \quad \text{for } k = 0, 1, 2, \ldots, N-1. \tag{2.5}$$

A DFT produces N independent numbers of output for N independent numbers of input, [54]. Using DFT, the values of Fourier transform $H(f)$ can only be estimated at discrete values,

$$f_n \equiv \frac{n}{N\Lambda}, \quad \text{for } n = -\frac{N}{2}, \ldots, \frac{N}{2}. \tag{2.6}$$

Hence, to get the Fourier transform of such discrete data, equation 2.3 has to be approximated, using equations 2.5 and 2.6,

$$H(f_n) = \int_{-\infty}^{\infty} h(s) e^{2\pi i f_n s} ds \approx \sum_{k=0}^{N-1} h_k e^{2\pi i f_n s_k} \Lambda = \Lambda \sum_{k=0}^{N-1} h_k e^{2\pi i k n / N}. \tag{2.7}$$

Equation 2.7 is called the *discrete Fourier transform* of the N points h_k, [55]. Let H_n be defined as:

$$H_n \equiv \sum_{k=0}^{N-1} h_k e^{2\pi i k n / N}. \tag{2.8}$$

As quoted by Press et al. [55], "The discrete Fourier transform maps N complex numbers (the h_k's) into N complex numbers (the H_n's)". The Fourier transform does not depend on the sampling rate Λ. Hence, the relation between the discrete Fourier transform of a set of numbers and their continuous Fourier transform as samples of a continuous function sampled at an interval Λ is written as [55],

$$H(f_n) \approx \Lambda H_n. \tag{2.9}$$

To recover the h_k's exactly from the H_n, the discrete inverse Fourier transform can be used which is given as [55]:

$$h_k = \frac{1}{N} \sum_{n=0}^{N-1} H_n e^{-2\pi i k n/N}. \tag{2.10}$$

The discrete Fourier transform pairs are represented by:

$$h_k \Longleftrightarrow H_n.$$

The discrete Fourier transform for a given set of numbers can be obtained using the fast Fourier transform algorithm. The FFT algorithm is based on the fact that a discrete Fourier transform of N numbers can be represented as sum of two discrete Fourier transforms, each of length $N/2$. FFT gives N complex numbers for an input of N numbers. Hence, the H_k's are of the form $a(\omega) + ib(\omega)$, where ω is the frequency parameter. Representing H_k in polar form,

$$H_k = H(\omega_k) = |H(\omega_k)| \cdot e^{i\phi(\omega_k)}, \tag{2.11}$$

where,

$$|H(\omega_k)| = \sqrt{(a^2 + b^2)}$$

and,

$$\phi(\omega_k) = tan^{-1}\left(\frac{b}{a}\right).$$

The norm of the amplitude, $|H(\omega_k)|$ is called the Fourier spectrum of f, and the exponent $\phi(\omega_k)$ is the phase angle.

1. **Filtering high frequency components**: Taking a representative pressure line and the associated data set of the distances of scanned points from its nominal geometry are shown in Figure 2.21a. A discrete Fourier transform is performed on this data using Matlab's `fft` function. The frequency spectrum obtained from the FFT algorithm is shown in Figure 2.21b. The high frequency components that represent the noise are neglected from the frequency spectrum [56]. The H_k's will contain non zero coefficients for frequencies (first ten in this case, see Section 2.4.3) lower than a cut-off frequency and zero components for the higher frequencies. After performing the inverse Fourier transform on this truncated frequency spectrum a new data set can be regenerated from which the variation representing the noise is eliminated as shown in Figure 2.21a.

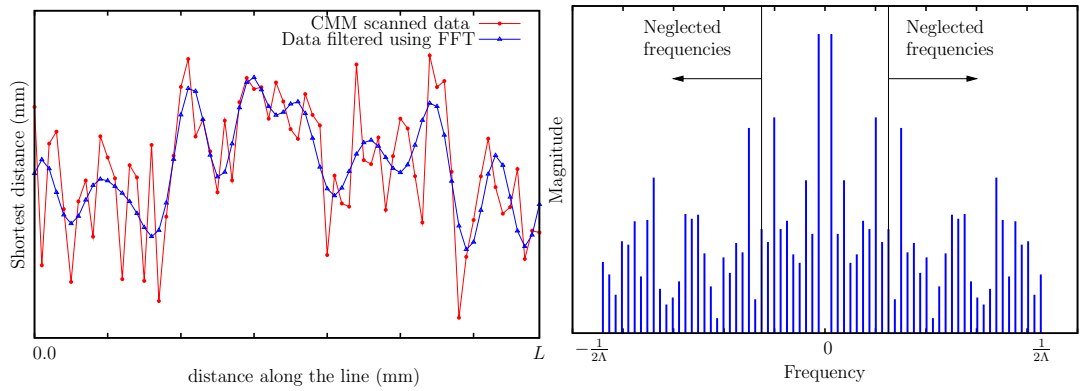

(A) Shortest Distance h_k's (NTS) (B) Frequency Spectrum $|H(\omega_k)|$'s

FIGURE 2.21: Filtering high frequency components using FFT technique

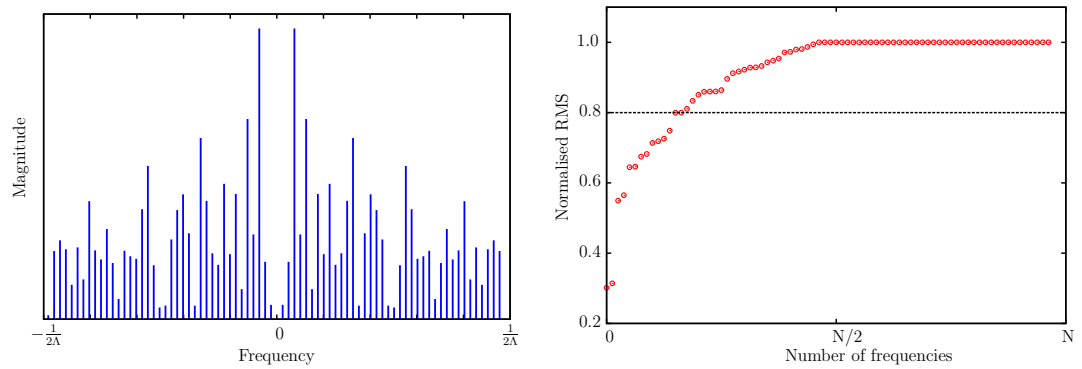

(A) Frequency spectrum (B) Root mean square

FIGURE 2.22: Change in the root mean square value with number of frequencies

2. **Observations**: It can be seen from Figure 2.21a, that the closely spaced irregularities are eliminated, maintaining the characteristic shape of the geometry.

2.4.3 Cut-off frequency

For selecting the cut-off frequency a method based on the reduction observed in the root mean square value is employed. It is observed that for a given CMM data, as the number of frequency components, that are included to regenerate the data, is increased the root mean square value of the regenerated data increases, Figure 2.22. However, it can be seen from Figure 2.22b, that the root mean square value remains constant for the number of frequencies greater than $N/2$ used to regenerate the data. It is observed that selecting a cut-off frequency when a reduction of 20% in the root mean square value provides a new set of points which manages to reflect the characteristic dimension of the geometry while removing the unwanted closely spaced irregularities. However, the choice of cut-off frequency here is still arbitrary. By measuring the same pressure surface using

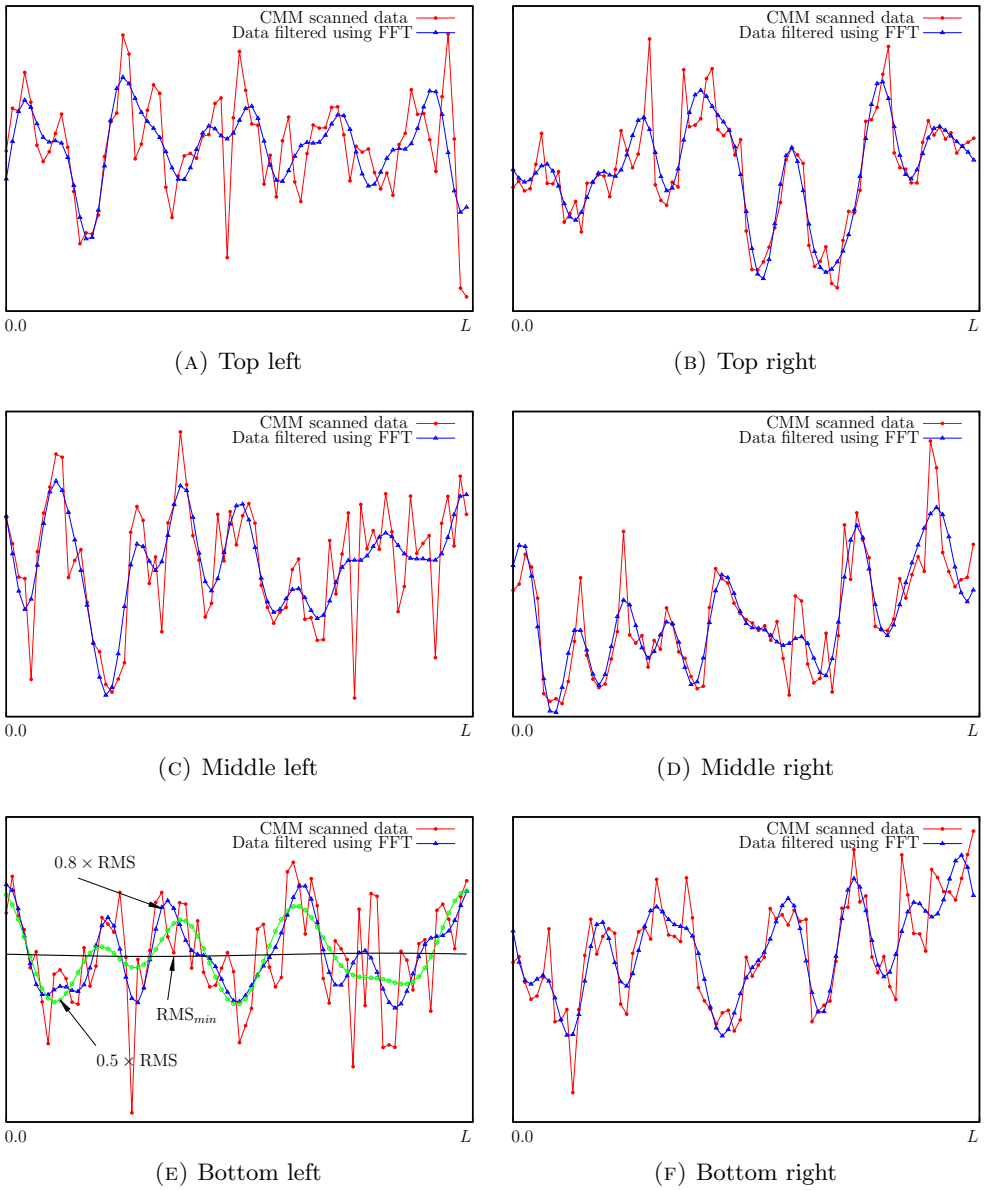

(A) Top left (B) Top right

(C) Middle left (D) Middle right

(E) Bottom left (F) Bottom right

FIGURE 2.23: Data regenerated after filtering high frequency components using FFT technique on all six flanks of a firtree

the CMM multiple times and then comparing the regenerated data for different sets of data may provide more information regarding the accuracy of the cut-off frequency.

The regenerated data, after filtering the high frequency components, for all the pressure lines of a firtree slot when a reduction of 20% in the root mean square value is obtained are shown in Figure 2.23. It can be seen that the generated data follow the characteristic dimension of the geometry but ignores the noise from the raw data.

2.5 Summary

The variation in geometry due to the manufacturing process is extracted using two different methods. In the first case, the geometric component (pressure lines) are represented using a simple curve fit by minimising the root mean square error. Two different substitute geometries are used while performing the curve fitting. The first substitute geometry consists of the pressure line and the adjoining tangential arcs while the second geometry includes the bottom line which helps in extracting the included angle in the flank. A limited correlation is observed between the front and the rear manufactured pressure angles of the firtree joint for both the substitute geometries. It is observed that approximately 61% of the designs have pressure angles less than the nominal pressure angle when the first substitute geometry is used while the second substitute geometry showed that 57% of the designs have lower pressure angles. Hence, whichever substitute geometry is used, the mean for variation in the pressure angle is similar. Eventually the variations in the pressure angle are obtained as shown in Figures 2.13 and 2.17b.

In the second case, a more sophisticated approach is used to represent the surface profile of the pressure faces with the help of a Fourier series. An FFT analysis is performed to filter the raw scanned data for high frequency components. The frequency component for which a reduction of 20% is obtained in the root mean square value is selected as the cut-off frequency. It is observed that the regenerated data manages to reflect the smooth variation in the pressure face profile while ignoring the unwanted closely spaced irregularities.

In this chapter, the variation in the surface profile is extracted from the CMM data, that is available along narrow strips near the front and the rear edge of the firtree joint, using different methods. However, these methods cannot predict the changes in the profile away from the edges of the pressure face. In the next chapter, different methods of predicting a two-dimensional surface profile are discussed which are then used to generate a new surface which is assumed to belong to the same family of surfaces as the disc side firtree pressure face based on the available CMM data.

Chapter 3

Roughness parametrisation

3.1 Introduction

Although manufacturing processes have advanced considerably, parts and components cannot be produced with perfectly smooth surfaces. When a freshly manufactured surface is viewed under a microscope, peaks and valleys with random spatial and height distributions can be seen. These asperities may take different shapes depending on the manufacturing process used to produce them. A design engineer generally assumes a perfectly smooth surface while modelling the mechanisms where two surfaces interact with each other. In situations where the interaction between two surfaces can have an important role on the intended performance, it is important to examine the effect these *real* non-smooth surfaces have. Irrespective of whether such interaction or contact between the two surfaces is dry or lubricated, surface texture is the most important parameter that determines frictional behaviour [57]. A typical machined surface is shown in Figure 3.1 with vertical magnification greatly exaggerated compared to the horizontal

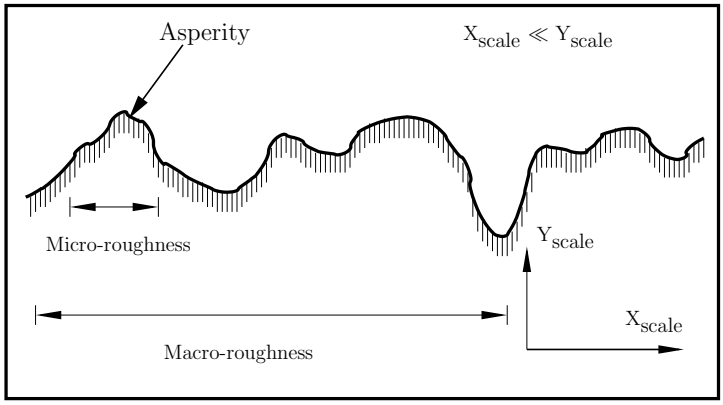

FIGURE 3.1: Surface texture terminology (Typical length scales for such surfaces are 1 : 800)

magnification for convenience. When two surfaces, as shown in the figure, come into contact, the asperities (or the peaks) on the surface profile contribute to the frictional resistance whereas the voids serve as reservoirs for the lubricants [57].

The roughness of a real machined surface can be characterised into macroscopic roughness and microscopic roughness. The irregular geometry of a typical asperity is categorised as the microscopic roughness whereas macroscopic roughness comprise of distribution of such asperities. For engineering purposes, the macroscopic representation of the roughness is considered sufficient while physicists and physical chemists require the microscopic details of the surface [57]. There is extensive literature available on the study of the effect of using rough surface models instead of a perfectly smooth surface in applications related to wear, contact, fatigue, etc. One of the early works in which a non-smooth surface is used to study the contact between two surfaces is reported by Greenwood and Williamson [58]. A Gaussian distribution is assumed for the heights of the asperities above a nominal plane. Since, the contact area between two perfectly smooth surfaces is greater than that between non-smooth surfaces, even at low loads the contact can become plastic, hence resulting in localised permanent deformations. Liu et al. [59] reviewed the existing models for simulating contact conditions between rough surfaces by considering three aspects: representing the rough surfaces, evaluating the contact pressures and surface displacements and different numerical methods to solve the contact equations. Ciulli et al. [60] reviewed different models for roughness description based on statistical approaches based on stochastic methods and deterministic approach with actual surface topography. Analytical representation of a surface profile using parabolas by maintaining the surface characteristics have been proposed. Five different parabolic approximations for measured surface profiles of several engineering surfaces were compared using two elastic and two elastic-plastic contact mechanics models [61]. It was reported that the elastic-plastic contact mechanics model in combination with the parabolic representation of the surface roughness provided satisfactory results.

Roughness of surfaces influence a large number of physical properties. In the case of friction and wear properties of a surface, in both dry and lubricated conditions, it is necessary to keep the asperity height within a prescribed limit to obtain the required minimum lubrication film thickness. It has been observed that the fatigue strength of a part component increases for polished surfaces which help to avoid stress concentrations. The life and performance of oil seals is affected by the quality of finishing of the shaft surface [62]. Liu et al. [63] developed an isothermal elasto-plastic contact model based on the contact between asperities to deal with the plastic flow of materials at micro-roughness scales. Nayak analysed the plastic contact between a rough surface and a smooth surface by modelling the rough surface as an isotropic, Gaussian random process [64, 65]. It is observed that the contact between rough surfaces depends not only on the height distribution of the asperities but also on the shape of the power spectral density of the surface. Bhushan [66] proposed models for the multiple-asperity

contacts between surfaces under dry and lubricated conditions. Analytical solutions for surfaces with specified distribution of asperity heights and numerical solutions for real surfaces with arbitrary asperity shapes and variable size and height distributions are presented. Ao et al. [67] proposed a method to extract the roughness parameters of a worn surface by connecting the wear tests with statistical analysis. Sellgren et al. [68] and Kogut and Etsion [69] demonstrated the use of finite element methods to simulate the normal contact conditions between rough surfaces under elastic and elastic-plastic material models.

Ardito et al. [70] generated Gaussian and non-Gaussian rough surfaces artificially on the basis of a priori known statistical properties of the surface to study the adhesion phenomenon in micro-electro-mechanical systems (MEMS). Modelling of rough surfaces is an important issue in the fields of rock mechanics [71, 72]. Reeves [71] presented a method to relate a parameter defining the roughness of the rock surface with the frictional strength of the discontinuities. Representation of the surface roughness in a convenient manner is an essential prerequisite for performing any study on their performance.

3.2 Roughness characterisation

Depending on the application, the surface roughness or the true machined surface need to be measured or scanned using appropriate techniques. In this work, only the macroscopic roughness is considered. The measurement of the macroscopic roughness can be classified into two groups depending on whether the entire profile of the surface is measured or only part of the profile is measured [57]. Measuring devices which involve the motion of a stylus over the surface being measured, have been commonly used to measure profiles of surface heights. For the purpose of analysis of such manufactured surfaces in engineering applications, it is necessary to represent the surface features obtained from the measured profiles in a convenient form. Thomas [73] listed some issues that need to be given importance in the characterisation of surface roughness such as the high and low-pass filtering, importance of appropriate sampling while measuring, etc. The roles of different users involved – the manufacturer, the researcher and the quality control engineer are also discussed. An extensive list of parameters, that have been used by researchers, for defining a surface are described. These roughness defining parameters can be broadly classified into three categories; height descriptors which give, in some sense, the behaviour of the surface profile in a plane normal to the surface, the extreme-value descriptors and the texture descriptors which describe the profile in the plane parallel to the surface [73]. Dong et al. [74, 75, 76, 77] published a comprehensive study in the form of four publications for characterising the three-dimensional surface topography with respect to the inherent properties in parameter variation due to the machining processes, their statistical properties, parameters to characterise the amplitude

and spatial properties. In their first paper Dong et al. [74], discussed different factors that can affect the parameters describing a surface roughness. It is reported that the theoretical models based on random data models of surfaces such as normal, non-normal, correlated and non-correlated distributions are limited in their accuracy since they are based upon many assumptions. The measurement conditions such as the accuracy of the measuring instruments, the geometry of the stylus in case of moving stylus measuring methods, the range of magnification, etc. affects the parameter estimation. Processing of the measurement data involves use of signal-processing techniques which are affected by the sampling rates and lengths, and the filtering conditions. Thomas and Rosén [78] proposed a method to determine a sampling interval for a rough surface which is defined by self-affine fractals. Dong et al. [74] reported that the type of manufacturing process used has a more profound effect on the roughness parameter variation than the measurement and signal-processing conditions. Surfaces manufactured in different ways, such as ground, end-milled and shaped surfaces are used to study the variation in the parameters such as the arithmetic mean height R_a, RMS roughness R_q, the skewness R_{sk} and kurtosis R_{ku}. If z_i's, such that $(i = 1, 2, 3, \ldots, N)$, are the heights of N points measured on a surface profile from a datum then these statistical parameters are expressed as:

$$R_a \text{ or } \mu = \frac{1}{N}\sum_{i=1}^{N} z_i,$$

$$R_q \text{ or RMS} = \left(\frac{1}{N}\sum_{i=1}^{N} {z_i}^2\right)^{1/2},$$

$$R_{sk} = \frac{1}{N(R_q)^3}\sum_{i=1}^{N} {z_i}^3 \quad \text{and}$$

$$R_{ku} = \frac{1}{N(R_q)^4}\sum_{i=1}^{N} {z_i}^4.$$

In applications where the interaction between two or more machined surfaces occurs, it is important to have a comprehensive characterisation of the surface texture. It is possible to achieve this goal with the use of statistics. Problems in design such as wear, lubrication, joints which involve contact between two bodies, dynamics of machine tools, etc., cannot be approached satisfactorily without information about the surface texture that exhibits a random character [79]. A profile of a machined surface can be modelled as a random process which can be both *stationary* and *ergodic*. A rough surface, when considered as a random process, is said to be stationary when the parameters defining the process such as its mean, standard deviation, etc., are invariant with respect to time. Box and Jenkins [80] define a stationary random process as a process which "remains in *equilibrium* about a *constant mean level*". A random process is said to be ergodic when the time average for a particular profile is the same for all other profiles on the same surface [57]. Dong et al. [75] investigated the statistical parameter variation on manufactured engineering surfaces when the assumption of ergodicity or stationarity of

the surface profile is applied. It is reported that many real engineering surfaces exhibit non-stationarity such that unexpected spikes or pits and troughs are observed on the surfaces. In case of a ground surface, it is observed that the surface possess a strong non-stationarity and hence the variation in the parameters is relatively large. Surfaces machined through shaping show less non-stationarity and hence can be regarded as weakly stationary surfaces. Electric discharge textured (EDT) surfaces are considered to have an ergodic nature [75].

The statistical properties that are significant for modelling the roughness of a surface are as follows [57]:

1. Root mean square values and the mean
2. Autocorrelation function
3. Power spectral density function
4. Cross-correlation function
5. Cross-spectral density function

Out of these, the cross-correlation function and the cross-spectral density function apply to a pair of surface profiles whereas the rest are applicable to a single surface profile. Table 3.1 gives the mathematical definition of these parameters. $Z^j(x)$ is the j^{th} profile on the surface which is of length L measured in the direction of the parameter x. Figure 3.2a shows a two dimensional surface profile along with its height distribution as shown

Statistical Property	Mathematical definition
Mean or centre-line average	$\mu = \left(\frac{1}{L}\right) \int_0^L \lvert Z^1(x)\rvert \mathrm{d}x$
Root mean square value	$\mathrm{RMS} = \left[\left(\frac{1}{L}\right) \int_0^L \left[Z^1(x)\right]^2 \mathrm{d}x\right]^{1/2}$
Autocorrelation function	$R(\Delta) = \left(\frac{1}{L}\right) \int_0^L Z^1(x) Z^1(x+\Delta) \mathrm{d}x$
Power spectral density function	$S(\omega) = \left(\frac{1}{2\pi}\right) \int_{-\infty}^{\infty} R(\Delta) e^{-i\omega t} \mathrm{d}t$
Cross-correlation function	$R_c(\Delta) = \left(\frac{1}{L}\right) \int_0^L Z^1(x) Z^2(x+\Delta) \mathrm{d}x$
Cross-spectral density function	$T(\omega) = \left(\frac{1}{2\pi}\right) \int_{-\infty}^{\infty} R_c(\Delta) e^{-i\omega t} \mathrm{d}t$

TABLE 3.1: Statistical properties of surfaces [57]

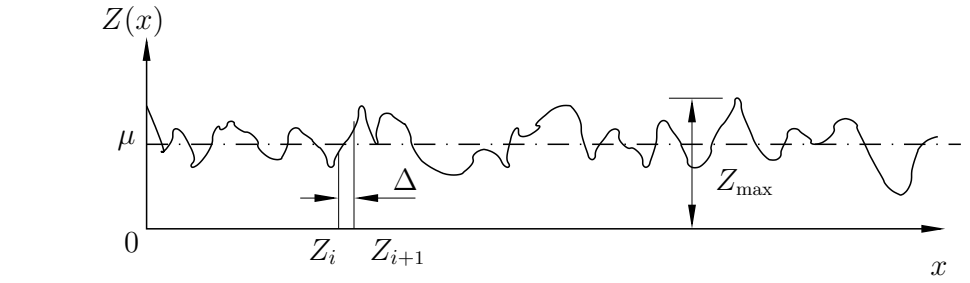

(A) Surface profile

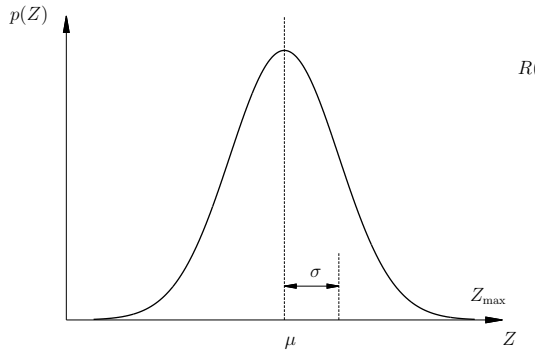

(B) Height distribution function

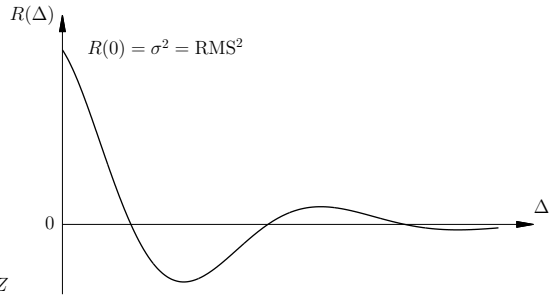

(C) Autocorrelation function

FIGURE 3.2: Statistical parameters of a surface profile

in Figure 3.2b. μ and σ are the mean and standard deviation (or RMS) of the profile. Figure 3.2c shows the autocorrelation function for the profile. It can be seen from the figure that when $\Delta = 0$, the autocorrelation function is equal to the square of the standard deviation. The autocorrelation function for a surface profile can be obtained by multiplying the original profile by a new profile which is obtained by delaying the original profile, and then taking the average. The power spectral density $S(\omega)$ for a single stationary profile is the measure of the rate of change of the mean square value with the frequency. The area under the power spectral density function from $-\infty$ to ∞ is the total mean square value in the profile. $S(\omega)$ can be obtained by taking the Fourier transform of the autocorrelation function. Similarly, the cross-spectral density function can be obtained by taking the Fourier transform of the cross-correlation function $R_c(\Delta)$. Some of these statistical properties of rough surfaces are discussed in more detail in the following sections.

3.2.1 Height distribution function

It is reported by Thomas [81] that irrespective of the sampling interval used for measuring the heights on a surface, they are rarely uncorrelated. This correlation between the heights on random locations on a surface generally follows a certain distribution. Greenwood and Williamson [58] suggested that it is not uncommon to see that such a distribution of heights is governed by the Gaussian form. Engineering surfaces are

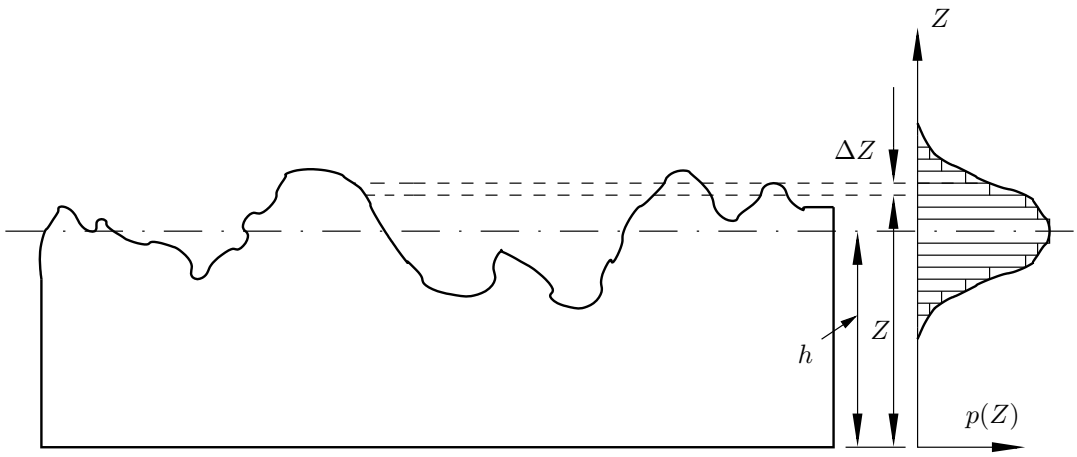

FIGURE 3.3: Height distribution of surface profile

formed as a result of many independent effects, however, it can be shown that the surface that is manufactured is subject to the central limit theorem which follows the Gaussian type of probability distribution [81]. To assess the parameters that describe the heights at different points on a surface, the mean line or the mean plane is necessary before the measurements can be made. Depending on the surface and the methods used for machining them, the mean line may not be a straight line but could follow a long-wavelength form. Such a mean line if used as a datum for the height measurement compensates for any d.c. (direct current) component of the manufacturing variation [81]. The two most commonly used methods for evaluating the mean line of the surface profile are the root mean square and the centre-line average. In the case of the RMS technique the mean line or the mean plane is obtained by minimising the root of mean of squares whereas in case of centre-line average the areas or volumes of surface-fill and void are equated to get the mean. It has been observed that both these techniques generally result in the same mean [81]. If the surface height profile measured from such a mean datum is considered as a random process, the distribution of heights is the probability density function $p(Z)$. Such distributions can be obtained by plotting the function which evaluates the proportion of surface heights lying between two specific heights as shown in Figure 3.3. The value of $p(Z)$ for heights between Z and $Z + \Delta Z$ is equal to the number of heights on the surface that lie in that range; the area under the curve $p(Z) = 1$.

3.2.2 Autocorrelation function

If the surface height, at finite number of points on the surface, is considered as a random variable then the autocorrelation function (ACF), of that random process, is the autocovariance function (ACVF) in its normalised form [81]. It is a function which correlates a random series with its spatially separated representation. Height distribution

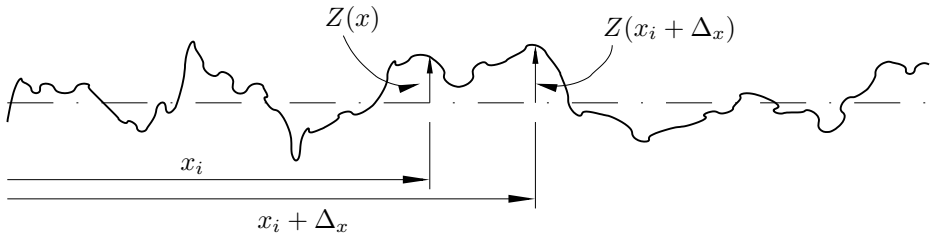

FIGURE 3.4: Evaluation of autocorrelation function

on its own, does not provide any information about the spatial variation in the random series. The autocorrelation function contains useful information regarding the spatial variation; for example, ACF can be used to extract repeating patterns in the surface profile which may be hidden by the noise. Let $Z(\mathbf{x})$ be the height of a rough surface where $\mathbf{x}$ (for 1D $\mathbf{x} = \{x\}$, for 2D $\mathbf{x} = \{x\ y\}$) is the vector defining the spatial coordinates on the surface, Figure 3.4. If an assumption is made that the surface possesses homogeneity in the sense that its statistical properties are invariant with the translation along the surface, its ACF is defined as:

$$R(\boldsymbol{\Delta}) = E\{Z(\mathbf{x})Z(\mathbf{x} + \boldsymbol{\Delta})\} \tag{3.1}$$

where $E\{\bullet\}$ is the expectancy operator or an average value of $Z(\mathbf{x})Z(\mathbf{x} + \boldsymbol{\Delta})$ and $\boldsymbol{\Delta}$ is the vector of delay lengths in the direction of $\mathbf{x}$ [82, 81]. The heights on a surface profile are available at finite number of points. There are various estimates suggested in the literature, in different fields, for the autocorrelation function of a discrete data set, for example,

$$R(\Delta_x) = \frac{1}{N-p} \sum_{i=1}^{N-p} Z(x_i)Z(x_i + \Delta_x) \ \ldots \text{ in 1D} \tag{3.2}$$

$$R(\Delta_x, \Delta_y) = \frac{1}{(N-p)(M-q)} \sum_{i=1}^{N-p} \sum_{j=1}^{M-q} Z(x_i, y_j)Z(x_i + \Delta_x, y_j + \Delta_y) \ \ldots \text{ in 2D} \tag{3.3}$$

where $\Delta_x = p\Lambda x$ and $\Delta_y = q\Lambda y$ ($p \in [0, n-1]$ and $q \in [0, m-1]$, n and m are integers) are the delay lengths in x and y directions with Λx and Λy as the sampling intervals and N and M are the number of points in data sets for x and y profiles [82, 79]. Box and Jenkins [80] defined the ACF as:

$$R(\Delta_x, \Delta_y) = \frac{1}{NM} \sum_{i=1}^{N} \sum_{j=1}^{M} Z(x_i, y_j)Z(x_i + \Delta_x, y_j + \Delta_y). \tag{3.4}$$

In this work, the definition for ACF as given in Equation 3.3 is adopted. It can be seen that when the delay lengths Δ_x and Δ_y are set to zero, the autocorrelation function is the same as the square of standard deviation of the surface height profile

$$R(0,0) = \frac{1}{NM} \sum_{i=1}^{N} \sum_{j=1}^{M} [Z(x_i, y_i)]^2 = \sigma^2.$$

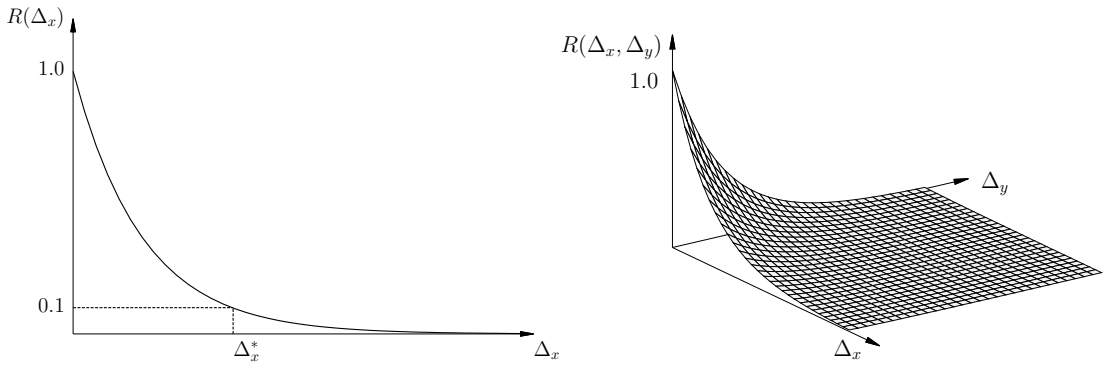

(A) ACF for 2D surface profile (B) ACF for 3D surface

FIGURE 3.5: Exponential autocorrelation function

It has been observed that ACFs for many random surfaces can be modelled as the simple exponential representation [81, 82] as shown in Figure 3.5. The standard deviation is set to unity. Δ_x^* is the correlation length defined as the delay length at which the ACF reduces to 10% of its value at the origin. Some researchers have defined the correlation length as the minimum length where the magnitude of ACF reduces to zero [79].

3.2.3 Power spectral density function

The power spectral density function (PSD) is another statistical property which provides information about the spatial variation but in different form [81]. In the field of optics, surfaces are often characterised with the help of the power spectral density function [83, 84]. Theoretically, a true PSD can be obtained by taking the Fourier transform of the ACF given in Equation 3.3 [85, 83],

$$S(\omega_x, \omega_y) = \frac{1}{(N-p)(M-q)} \sum_{p=-N/2+1}^{N/2-1} \sum_{q=-M/2+1}^{M/2-1} R(\Delta_x, \Delta_y) e^{-i\omega_x \Delta_x} e^{-i\omega_y \Delta_y} \tag{3.5}$$

where,

$$\omega_x = -N/2+1, \ldots, -1, 0, 1, \ldots, N/2-1,$$

$$\omega_y = -M/2+1, \ldots, -1, 0, 1, \ldots, M/2-1.$$

Elson and Bennett [83] investigated the problems involved in evaluating the PSD using the Fourier transformation. The surface heights measured are discrete digitised data, where each point represents the area covered by the stylus probe of the measuring instrument. A PSD evaluated from a single profile measured on a rough surface contains excessive noise and is often non reproducible. It is suggested that a true PSD can be obtained by taking an average over an ensemble of profiles scanned on the same surface at different locations [84].

Evaluation of the above mentioned properties for a rough surface provides useful information which can be used for various purposes. If the surface profile height distribution,

$p(Z)$, is stationary and has a Gaussian form, then the mean and the autocorrelation function can completely characterise the surface [57]. It has been observed that most of the statistical parameters of a rough surface can be derived from two statistical functions: the frequency density function or the height distribution function and the autocorrelation function [79, 86, 82, 87]. It is shown in the next section that it is possible to numerically generate an ensemble of surfaces which possess the required frequency density function and autocorrelation function.

3.3 Generation of random surfaces with specified statistical properties

The analysis and design process followed in industry depends a lot on the computational capabilities available. Over the last few decades, computers have become increasingly fast, allowing engineers and researchers to perform high-fidelity simulations. In applications where the precise representation of manufactured surfaces, which represent the roughness, is required for analysis or design purposes, it is necessary to generate such surfaces numerically. As discussed in the previous sections discrete data representing surface profile heights can be considered as a random process. Extracting important statistical properties for these surfaces can be useful in order to numerically generate new surfaces which belong to the same family of surfaces.

The easiest way to generate a rough surface with a normal height distribution is to add Gaussian noise to the mean plane. However, although the height distribution for the new surface confirms to be a Gaussian, it may not belong to the same family of surfaces. Figure 3.6 shows contour plots of two rough surfaces generated numerically, with contour levels $0, \pm\sigma, \pm 2\sigma,$ and $\pm 3\sigma$. Figure 3.7 shows the histograms of the height distribution for both the surfaces. It can be said that both surfaces have a Gaussian

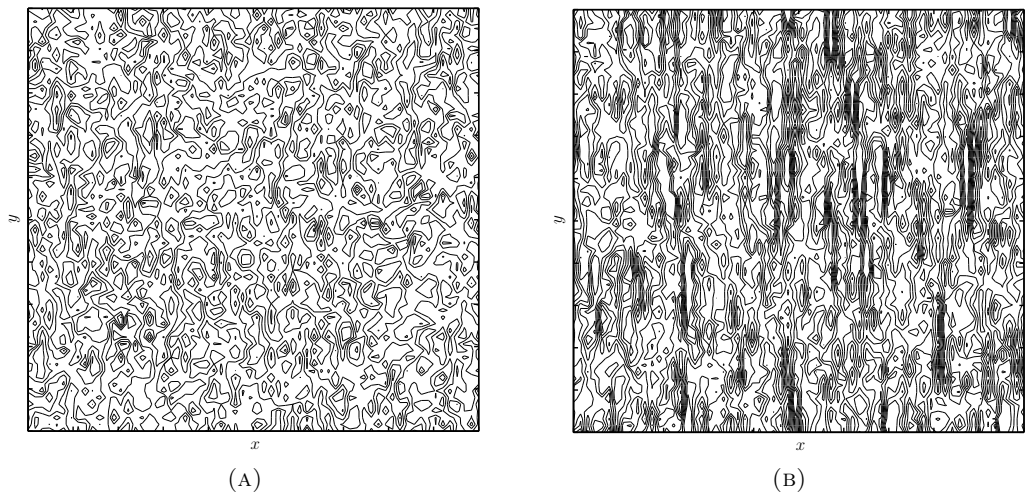

(A) (B)

FIGURE 3.6: Rough surfaces generated by adding Gaussian noise to a mean plane

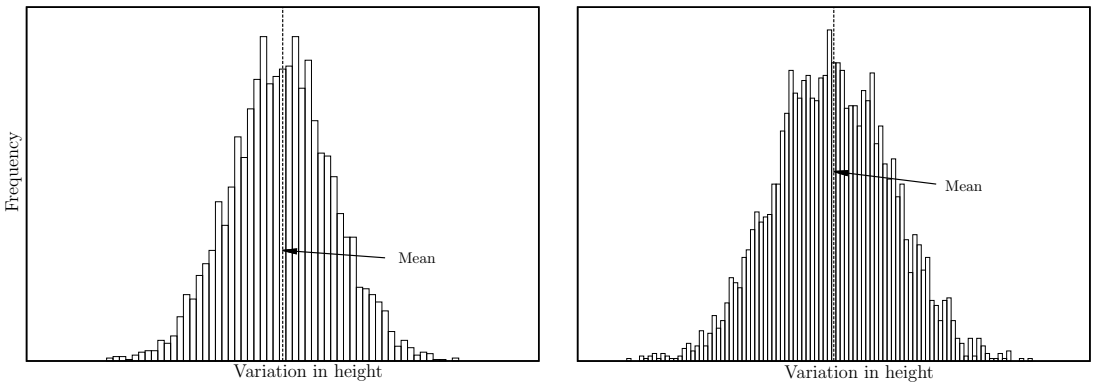

(A) (B)

FIGURE 3.7: Height distribution

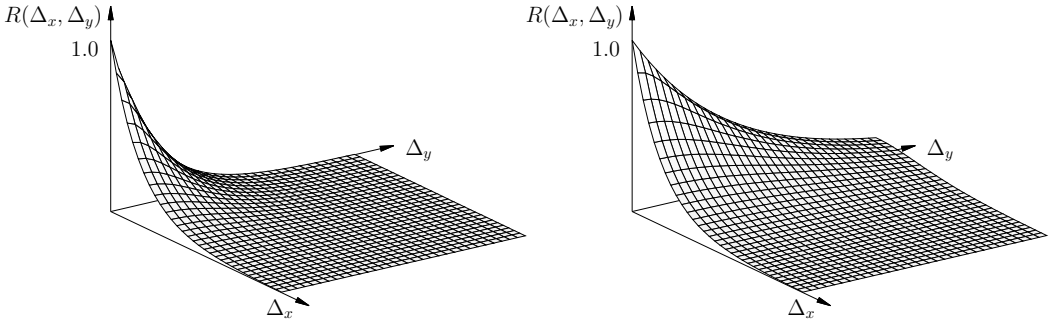

(A) (B)

FIGURE 3.8: Autocorrelation function

type of height distribution with zero mean. However, the two surfaces (Figures 3.6a and 3.6b) clearly do not belong to the same family of surfaces. The peaks and troughs are more evenly distributed on the first surface, Figure 3.6a, with respect to the x and y directions. While, the surface in Figure 3.6b shows that the peaks and troughs are more densely populated in x direction as compared to the y direction. This can be explained by plotting the autocorrelation functions for the two surfaces, Figure 3.8. For the first surface in Figure 3.6, the ACF used is of the exponential form in both directions with equal correlation lengths $\Delta_x^* = \Delta_y^*$, Figure 3.8a. While the correlation lengths for the second surface in Figure 3.6, are not equal but with a relation $\Delta_x^* \ll \Delta_y^*$, Figure 3.8b. Thus, just adding Gaussian noise to the smooth surface is not sufficient to generate a new rough surface belonging to a specific family of surfaces. The ACF of the generated surface should conform with the ACF of the family of surfaces.

The random nature of surface asperities with respect to their size, shape and spatial distribution can be expressed in statistical terms. The height distribution function of a particular type is used to describe the surface irregularities in a plane normal to the surface. The shape of an asperity is an important parameter to represent a rough surface [67]. For instance, a rough surface of the type shown in Figure 3.6a has asperities that

are approximately circular in shape, whereas the asperities on the surface in Figure 3.6b are elliptical with their major axes along the y direction while the minor axes along x direction. The ellipticity ratio,

$$\Gamma = \frac{\Delta_x^*}{\Delta_y^*}$$

defines the surface irregularities, where Δ_x^* and Δ_y^* are the 10% correlation lengths of the surface in x and y directions respectively. For $\Gamma = 1$, the asperities are circular in shape, $\Gamma < 1$ represents surfaces with asperities having elliptical shapes with major axes along y direction and surfaces with $\Gamma > 1$ have elliptical asperities with major axes along x direction.

3.3.1 Existing models for generating rough surfaces

The tribological behaviour of a surface in the case of dry or wet contact depends mainly on the roughness of the surface [88]. To analyse such problems numerically, it is essential to represent the two- or three-dimensional rough profile. For roughness when considered as a statistical measure, parameters should be chosen so as to allow the researcher to generate surfaces as per the specific requirement. Different manufacturing processes produce surfaces with different statistical behaviours. The selected parametrisation should be able to include the relevant type of surfaces. While simulating contact conditions for various applications such as rolling, repetitive impact, sliding etc., surfaces manufactured using a specific process may perform better than other methods. Therefore, it is useful if such numerical generation of a wide variety of rough surfaces is possible. Many researchers have suggested methods to artificially develop two- and three-dimensional rough surfaces. Patir [82] used the linear transformation in order to produce surfaces with specified height distribution and ACF. Box and Jenkins [80] and Watson and Spedding [89] used time series modelling to produce rough surfaces. They used an autoregressive moving average (ARMA) model to generate surface profiles with the required ACF [89]. Whitehouse [90] implemented AR time series models which take into account only the few most important terms to generate rough surfaces. Hence, the ACF of the generated surface follows the required ACF only in the region in the neighbourhood of the origin.

Hu and Tonder [85] applied Fourier transforms filters and window functions for generating Gaussian and non-Gaussian rough surfaces. Wu [91, 92] used the FFT technique to simulate rough surfaces that have a height distribution of Gaussian or non-Gaussian form and a specified ACF. It was observed that average of ACFs of the generated surfaces match the required ACF closely. As the number of points on the new surface increase, the efficiency of FFT reduces due to wrap-around errors. Watson and Spedding [89] calculated the correlation between the statistical moments of the input data set with the generated heights which help to generate non-Gaussian surfaces with specified skewness and kurtosis. Hu and Tonder [85] used these relations to numerically

generate non-Gaussian surfaces using the FFT technique. Patir's [82] method requires the solution of a system of non-linear equations which result in excessive storage space and time consuming solutions. As the range of the ACF increases, convergence issues in using Newton's method to solve the non-linear equations are observed. Bakolas [88] used the non-linear Conjugate Gradient Method (NCGM) to solve these non-linear equations for faster convergence. Manesh et al. [87] proposed an areal autocorrelation function (AACF) to generate a Gaussian surface that provides dependency between the heights of consecutive data points. Another technique of using fractal functions to simulate rough surfaces is reported by several researchers [93, 94, 95]. Fractals are useful in characterising engineering surfaces that are made by machining brittle materials, deposition of materials or solidification of liquid and fracture. Mack [96] investigated several numerical methods of generating rough edges, surfaces and volumes. It was reported that all methods result in data that have a variance close to the desired value only in the limit for large data sets and small grid sizes. This statistical bias is a consequence of describing an infinite, continuous function with a finite number of points. In his work, Mack [96] correlated the degree of bias to the roughness exponents of many model power spectral density functions. It was reported that selection of an appropriate grid size that always minimises the statistical bias is more suitable.

The work done by Patir [82] and Hu and Tonder [85] for generating three dimensional rough surfaces numerically based on statistical parameters is used widely for applications in contact mechanics and lubrication modelling [67]. In the following sections these two methods are discussed in more detail and further applied to generate a rough surface for the pressure faces on the firtree joint on the disc side[1]. Only the generation of surfaces with a Gaussian type of height distribution is considered in this work.

3.3.2 Patir's method – Linear transformation on random matrices

Patir [82] used a linear transformation on random matrices to generate Gaussian and non-Gaussian rough surfaces with a specified autocorrelation function. The height $Z(x, y)$ of a rough surface is considered as a two-dimensional random variable. Z is assumed to be measured from the mean plane of the surface. It is also assumed that the rough surface is homogeneous, i.e., the surface properties are invariant with respect to any translation along the surface. The ACF of such a surface can be calculated from Equation 3.1,

$$R(\Delta_x, \Delta_y) = E\{Z(x, y)Z(x + \Delta_x, y + \Delta_y)\}$$

where Δ_x and Δ_y are the delay lengths. The ACFs along x and y profiles are,

$$R_x(\Delta_x) = R(\Delta_x, 0), \qquad R_y(\Delta_y) = R(0, \Delta_y).$$

[1]Detailed roughness may not be an issue in the blade disc joint. This study only attempts to predict the surface texture produced by a manufacturing process based on limited data.

It is useful to adopt an index notation, since a finite number of points are generated with required heights from the mean plane. Let Z_{ij} be the roughness height at (x, y), Λx and Λy are the sampling intervals in the x and y directions respectively. Hence, the ACF in index notation is,

$$R_{pq} = R(p\Lambda x, q\Lambda y) = E\{Z_{ij} Z_{i+p,j+q}\}$$

The magnitude of R reduces to zero as the arguments, $p\Lambda x$ and $q\Lambda y$ increase beyond predefined limits. Let n and m be such that $R_{pq} = 0$ if $p \geq n$ or $q \geq m$ giving an $n \times m$ autocorrelation matrix. The selection of $n, m, \Lambda x,$ and Λy affects the ACF matrix and hence the generated rough surface.

It was shown that it is possible to generate a $N \times M$ matrix of heights $[Z_{ij}]$ on a rough surface with a Gaussian distribution and a specified $n \times m$ autocorrelation matrix $[R_{pq}]$ by linearly transforming random matrices. A random number generator is used to generate an $(N + n) \times (M + m)$ matrix $[\eta_{IJ}]$ whose components are independent and distributed with a Gaussian form with zero mean and unit standard deviation. The height on the rough surface can then be obtained through linear transformation [82],

$$Z_{ij} = \sum_{k=1}^{n} \sum_{l=1}^{m} A_{kl} \eta_{i+k,j+l} \tag{3.6}$$

where,

$$i = 1, 2, 3, \ldots, N$$

$$j = 1, 2, 3, \ldots, M$$

and A_{kl} are the coefficients derived from the given autocorrelation matrix. Since, the matrix $[\eta_{IJ}]$ have components that are independent with unit variance, the following property is used,

$$E(\eta_{ij}\eta_{kl}) = \begin{cases} 1 & \text{if } i = k,\ j = l \\ 0 & \text{otherwise.} \end{cases} \tag{3.7}$$

Using Equations 3.6 and 3.7 with the definition of ACF, R_{pq}, in Equation 3.3, it can be shown that,

$$R_{pq} = \sum_{k=1}^{n-p} \sum_{l=1}^{m-q} A_{kl} A_{k+p,l+q} \tag{3.8}$$

where,

$$p = 0, 1, 2, \ldots, n-1,$$

$$q = 0, 1, 2, \ldots, m-1.$$

Equation 3.8 represents $n \times m$ simultaneous non-linear equations in the coefficients A_{kl}. Iterative techniques such as the Newton method, non-linear Conjugate Gradient method, etc., can be used to solve these equations. In this work, the Newton method is adopted to evaluate the coefficients of the transformation matrix (Appendix A.1).

Hence, by measuring surface heights in two orthogonal directions, its ACF can be obtained by using Equation 3.3. From the solution of Equation 3.8, the coefficients of the transformation matrix are evaluated which can be further used to generate a new set of surface heights Z_{ij} which possess the same autocorrelation function as the measured surface provided the height distribution of the measured surface is of Gaussian type. This procedure is demonstrated for few standard ACFs with different n and m values. An exponential function is used to generate ACFs for the purpose of demonstration of the method. The ACF used by Patir [82] is adopted here,

$$R(\Delta_x, \Delta_y) = \sigma^2 \exp\left[-2.3\left|\left(\frac{\Delta_x}{\Delta_x^*}\right)^2 + \left(\frac{\Delta_y}{\Delta_y^*}\right)^2\right|^{1/2}\right] \tag{3.9}$$

where, σ is the standard deviation, and Δ_x^* and Δ_y^* are the 10% correlation lengths for x and y profiles respectively. The ACF in discretised form is given by,

$$R_{pq} = \exp\left[-2.3\left(\left(\frac{p}{n-1}\right)^2 + \left(\frac{q}{m-1}\right)^2\right)^{1/2}\right]$$

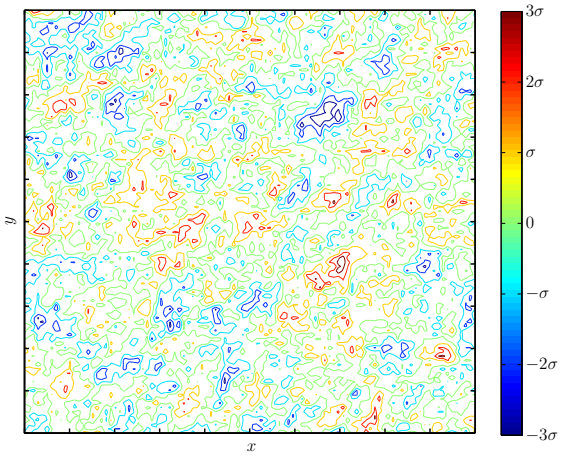

(A) Surface profile

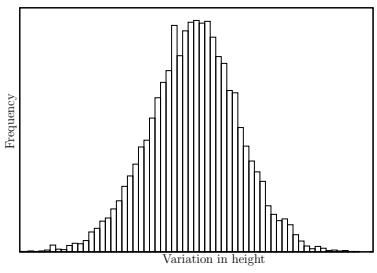

(B) Height distribution function

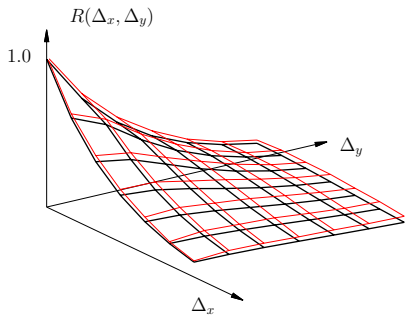

(C) Autocorrelation function: Input ACF (black), generated ACF (red)

FIGURE 3.9: Surface generated using Patir's method, $n = 7, m = 7, \Lambda x = \Lambda y$

such that, $R_{pq} = 0$ if $p \geq n$ or $q \geq m$. The correlation lengths are given by $(n-1) \times \Lambda x$ and $(m-1) \times \Lambda y$. Figure 3.9 shows a surface generated using Patir's method, with $n = m = 7$, $\Lambda x = \Lambda y$ and $N = M = 100$. Since the correlation lengths in both directions are same ($\Gamma = 1$), it can be seen from Figure 3.9a that the asperities are approximately circular in shape. The distribution of these asperities along the two orthogonal directions over the surface is uniform. Figure 3.9b shows the height distribution of the generated heights which follow the Gaussian form of distribution. Autocorrelation functions for the input and generated surfaces is compared in Figure 3.9c. The input ACF is plotted using black bold lines while the ACF for the generated surface is in red. It can be observed that the ACF of the generated surface follows the input ACF closely. However, it was reported that the ACF of the generated surface depends on how well the random number generator generates a set of mutually independent random numbers $[\eta_{IJ}]$ with unit standard deviation [82].

Two surfaces with $\Gamma = 5$ and 0.2 are plotted in Figures 3.10a and 3.10b. It can be seen that the asperities take the shape of an ellipse with their major axes along x and y direction for $\Gamma = 5$ and 0.2, respectively. The ACFs for both the surfaces are shown in Figures 3.10c and 3.10d. The ACF plotted with black lines represents the input ACF

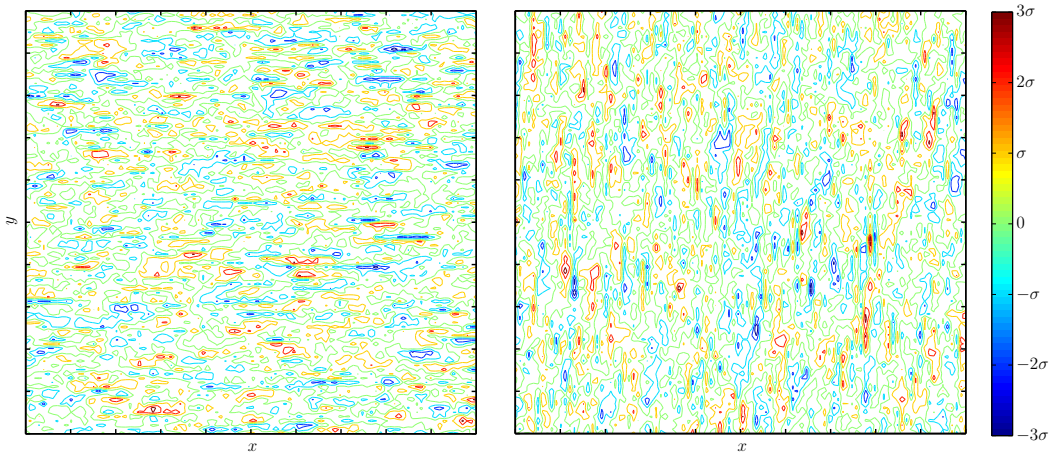

(A) Surface for $\Gamma = 5$

(B) Surface for $\Gamma = 0.2$

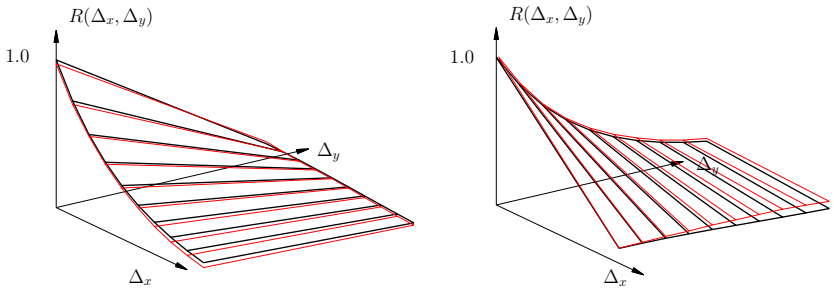

(C) ACF for $\Gamma = 5$: Input ACF (black), generated ACF (red)

(D) ACF for $\Gamma = 0.2$: Input ACF (black), generated ACF (red)

FIGURE 3.10: Surfaces generated using Patir's method

while the red is for the generated surface. The generated heights for both the surfaces follow the Gaussian type of probability distribution. Thus, it is possible to generate an ensemble of Gaussian rough surfaces with the required autocorrelation function by linearly transforming the random matrix $[\eta_{IJ}]$. However, it is observed that as the values n and m exceed certain limits, the Newton method struggles to converge.

It is shown that it is possible to generate Gaussian rough surface since linear transformation on a Gaussian set of numbers, $[\eta_{IJ}]$, results in Gaussian variables. This is not true while transforming a non-Gaussian $[\eta_{IJ}]$. Hence, to generate a non-Gaussian surface, Patir [82] suggested generating a random matrix $[\eta_{IJ}]$ that represents the desired distribution function of Z_{ij}. This involves an additional set of non-linear equations relating the frequency densities of $[\eta_{IJ}]$ and $[Z_{ij}]$.

3.3.3 Hu and Tonder's method – Fourier Transform

Hu and Tonder [85] used 2D digital filter techniques to generate 3D rough surfaces with specified height distribution and autocorrelation functions. Various methods used in digital filter designs such as spectrum analysis, Fourier transform and window functions are used which make the numerical generation of rough surfaces more efficient. In this work, the technique involving Fourier transform is used.

The power spectral density (PSD) of the rough surface is obtained by taking the Fourier transform of the autocorrelation function. If the ACF is denoted by R_{pq}, its PSD S_{zz} is obtained as [85]:

$$S_{zz} = S_{zz}(\omega_x, \omega_y) = \frac{1}{n \times m} \sum_{p=-n/2+1}^{n/2-1} \sum_{q=-m/2+1}^{m/2-1} R_{pq}\ e^{-ip\omega_x} e^{-iq\omega_y} \tag{3.10}$$

where,

$$\omega_x = -n/2+1, \ldots, -1, 0, 1, \ldots, n/2-1,$$

$$\omega_y = -m/2+1, \ldots, -1, 0, 1, \ldots, m/2-1.$$

Let $[\eta_{IJ}]$ be a random matrix (where $I = -n/2+1, \ldots, 0, \ldots, N-1+(n/2-1)$ and $J = -m/2+1, \ldots, 0, \ldots, M-1+(m/2-1)$) such that its components follow a normal distribution and are mutually independent with unit standard deviation. The PSD of this random matrix, $[\eta_{IJ}]$ is denoted as $S_{\eta\eta}$. The PSD for the input random matrix and the autocorrelation matrix are related as [85],

$$S_{zz} = |H(\omega_x, \omega_y)|^2 S_{\eta\eta} \tag{3.11}$$

where $H(\omega_x, \omega_y)$ is the frequency response of the surface height profile. Since, $[\eta_{IJ}]$ has components which are mutually independent random numbers, its PSD function is constant C,

$$S_{\eta\eta} = S_{\eta\eta}(\omega_x, \omega_y) = C.$$

Hence, the frequency response $H(\omega_x, \omega_y)$ can be obtained from S_{zz} [85],

$$H(\omega_x, \omega_y) = \left[\frac{S_{zz}(\omega_x, \omega_y)}{C}\right]^{1/2}.$$

Taking the inverse Fourier transform of the frequency response function [85],

$$h(p,q) = \frac{1}{n \times m} \sum_{\omega_x=-n/2+1}^{n/2-1} \sum_{\omega_y=-m/2+1}^{m/2-1} H(\omega_x, \omega_y)\ e^{-ip\omega_x} e^{-iq\omega_y} \tag{3.12}$$

where,

$$p = -n/2+1, \ldots, -1, 0, 1, \ldots, n/2-1,$$

$$q = -m/2+1, \ldots, -1, 0, 1, \ldots, m/2-1.$$

The surface height data can now be obtained from $h(p,q)$ and $[\eta_{IJ}]$ as follows [85],

$$Z_{ij} = \sum_{p=-n/2+1}^{n/2-1} \sum_{q=-m/2+1}^{m/2-1} h(p,q)\eta_{i+p,j+q} \tag{3.13}$$

where,

$$i = 0, 1, 2, \ldots, N-1,$$

$$j = 0, 1, 2, \ldots, M-1.$$

The surface height data obtained from the Fourier series contains an infinite number of coefficients. Hence, it is necessary to truncate the series which may lead to the Gibbs phenomenon that causes an error in the approximate frequency response function near a discontinuity [85]. Hu and Tonder proposed the use of window functions in order to minimise the effects of the Gibbs phenomenon. If a window function $w(p,q)$ is designed, the function $h(p,q)$ in Equation 3.13 is replaced by $h_w(p,q)$ given as [85],

$$h_w(p,q) = h(p,q)\ w(p,q).$$

The surface height data generated is normalised such that the standard deviation $\sigma = 1$. A surface with a specific standard deviation of heights is obtained by multiplying the heights by the desired σ value. The values for other parameters used in this work are,

$$N = M = 100 \qquad \text{and} \qquad n = m = 32.$$

Figure 3.11 shows the surface generated using Hu and Tonder's method when an exponential ACF, Figure 3.11c is used as an input ACF as before

$$R_{pq} = \exp\left[-2.3\left(\left(\frac{p\Lambda x}{\Delta_x^*}\right)^2 + \left(\frac{q\Lambda y}{\Delta_y^*}\right)^2\right)^{1/2}\right].$$

The correlation lengths used while generating this surface are $\Delta_x^* = 8\Lambda x, \Delta_y^* = 8\Lambda y$ ($\Lambda x = \Lambda y$), hence the ellipticity ratio $\Gamma = 1$. As a result, it can be seen from Figure

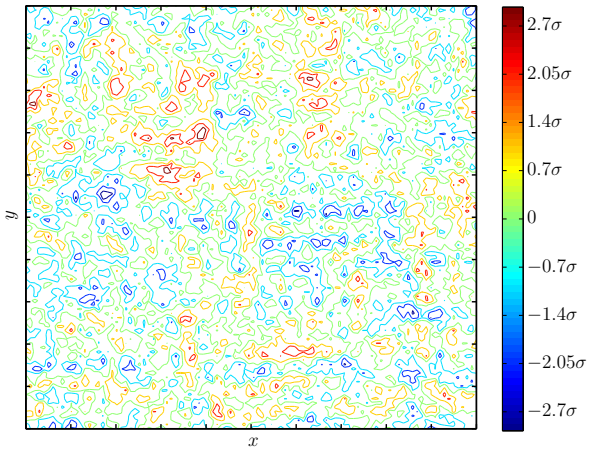

(A) Surface profile

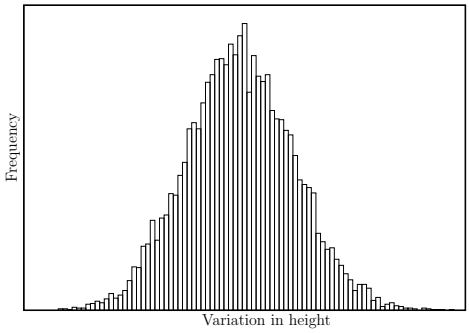

(B) Height distribution function

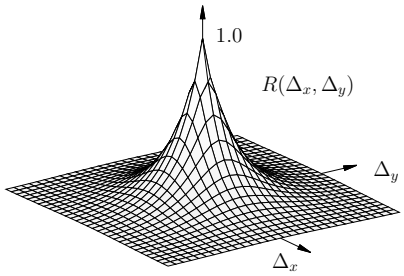

(C) Input ACF

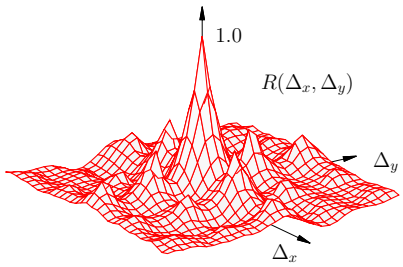

(D) ACF of generated surface

FIGURE 3.11: Surface generated using Hu and Tonder's method, $n = 32, m = 32$

3.11a, the peaks and troughs are uniformly distributed along x and y directions. Also, the asperities are approximately circular in shape. The distribution of the generated surface heights is plotted using a histogram in Figure 3.11b which follow a Gaussian distribution. ACFs for the input and the generated surfaces are compared in Figures 3.11c and 3.11d. It can be seen that the ACF for the generated surface follows the general exponential trend of the input ACF. However, there is less agreement between the two ACFs when compared with the Patir's method. As reported by Chilamakuri and Bhushan [97] and Wu [91], the average of ACFs of profiles of surfaces generated by Hu and Tonder's method is close to the desired one. It is shown by Wu [91] that, the error between the ACF for generated surface and the input ACF is small for surfaces

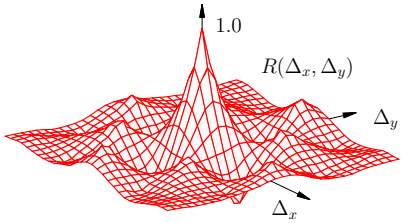

(A) $N = M = 150$

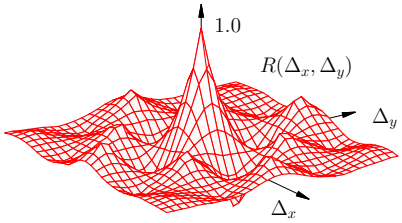

(B) $N = M = 300$

FIGURE 3.12: ACF for surfaces with different N and M

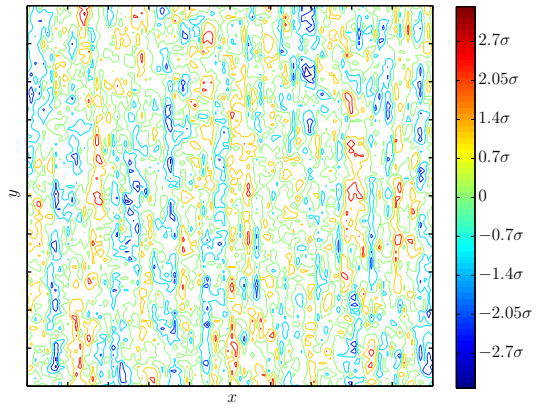

(A) Surface

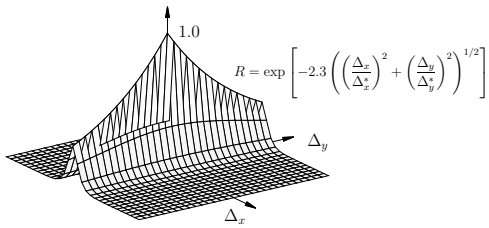

(B) Exponential ACF with $\Gamma = 0.067$

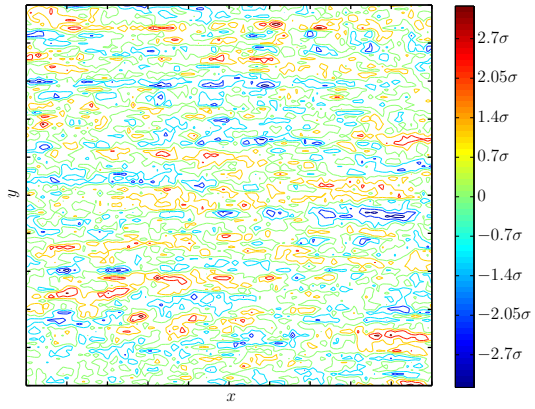

(C) Surface

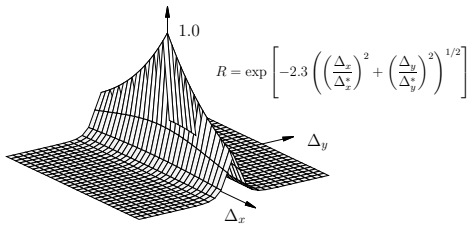

(D) Exponential ACF with $\Gamma = 15.0$

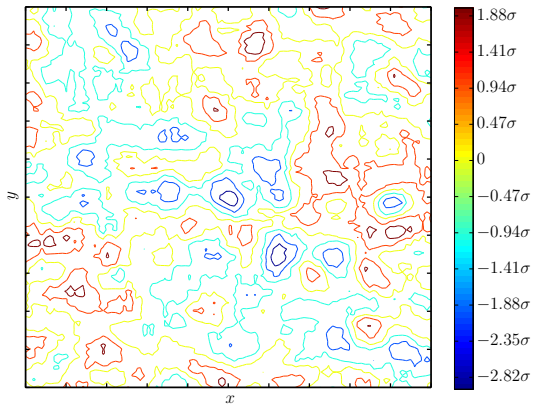

(E) Surface

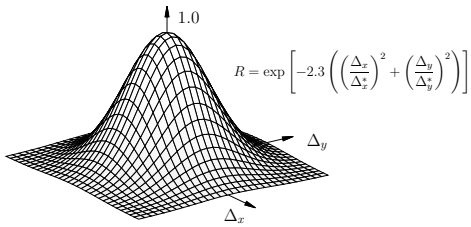

(F) Bell-shaped ACF with $\Gamma = 1$

FIGURE 3.13: Surfaces for different ACFs and Γ values

with small correlation lengths Δ_x^* and Δ_y^* and large number of points N and M. Figures 3.12a and 3.12b show that the ACF for the generated surface follow closely with the input ACF as the number of generated points are increased.

Figure 3.13 shows three surfaces generated using Hu and Tonder's method with different ACFs and Γ values. The Γ value for the surface in Figure 3.13a is 0.067 which means

$\Delta_x^* < \Delta_y^*$. Hence, the asperities take the shape of an ellipse with their major axes along y direction. Whereas for $\Gamma = 15.0$ in Figure 3.13c, the asperities have their major axes along the x direction. The surface in Figure 3.13e is generated using a bell-shaped ACF as shown in Figure 3.13f. Since the correlation lengths for surfaces in Figures 3.11a and 3.13e are same, the asperities for these two surfaces are approximately circular in shape. However, due to different ACFs for the two surfaces, there is a notable difference in the population and distribution of asperities.

3.3.4 Comparison between Patir's and Hu and Tonder's methods

In the previous sections, two-dimensional height profiles for rough Gaussian surfaces are numerically generated using two methods: (i) Patir's method and (ii) Hu and Tonder's method. Figure 3.14 show surfaces generated using the two methods with the same autocorrelation function and correlation lengths. It can be said that both these methods produce similar surfaces under the same parameters. The shape and distribution of peaks and troughs in both surfaces look similar. The generated ACFs using both Patir and Hu and Tonder's method show similar trend, however, the generated ACF using Hu and Tonder's method follows the exponential (input) ACF more closely near the origin. The height distribution function of both surfaces follows the Gaussian type of distribution.

In summary, Patir [82] used linear transformation on random matrices to generate a new matrix with normally distributed components which follow the specified autocorrelation function. A system of non-linear simultaneous equations is required to be solved to evaluate the coefficients of transformation matrix. It is observed that for ACF matrices with relatively smaller dimensions, Patir's method is more suitable with good convergence. However, as the size of the ACF matrix increases, it takes longer to attain convergence. To overcome this issue, researchers [88] have tried alternative methods, like non-linear Conjugate Gradient method, to replace the Newton method adopted by Patir [82].

Hu and Tonder [85] made use of digital filters and window functions to generate the surface heights for the given ACF. A Fourier transform of the ACF is related to the frequency response function of the surface height profile. As mentioned by Wu [91], the surface generated using Hu and Tonder's method, gave good results when the correlation lengths are small enough or if sufficiently large number of surface height points are generated.

3.4 Generating rough surface using CMM scanned data on disc side firtree pressure faces

As discussed in Chapter 2, the firtree joint that is analysed in this work consists of six pressure faces. To achieve the intended performance from such a joint, it is required

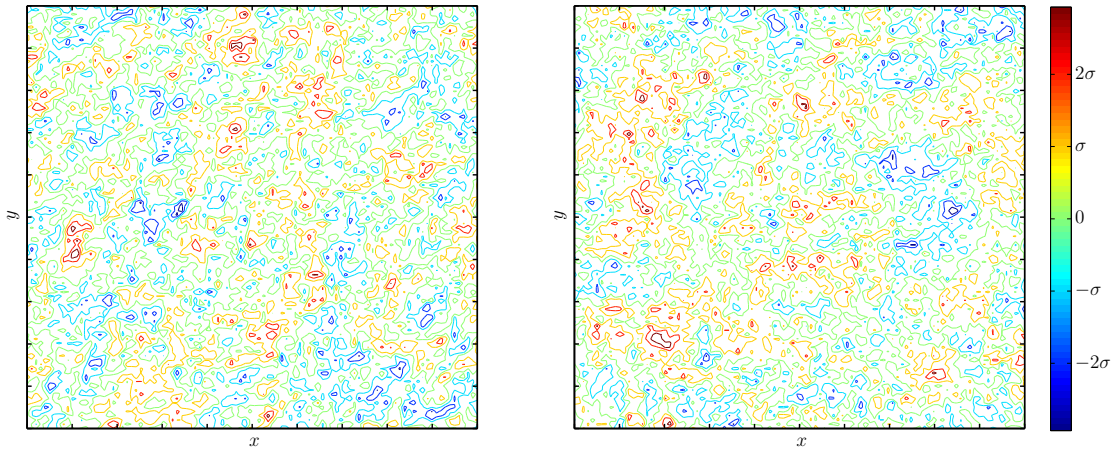

(A) Surface contour using Patir's method

(B) Surface contour using Hu and Tonder's method

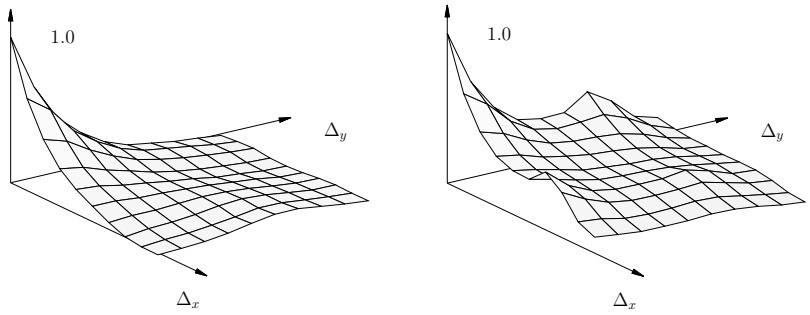

(C) Generated ACF using Patir's method

(D) Generated Hu and Tonder's method

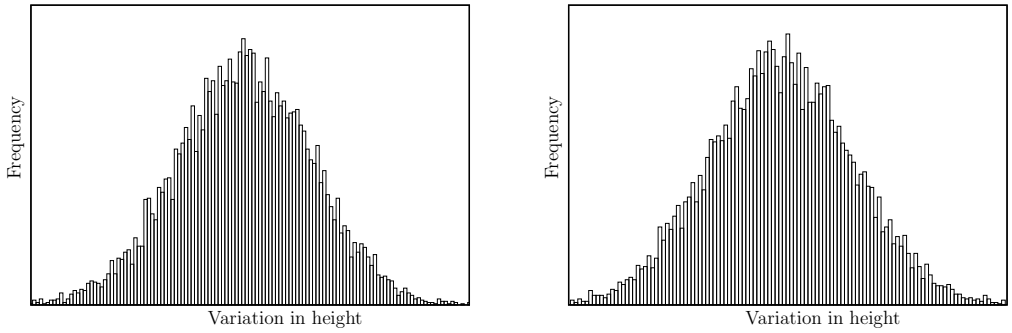

(E) Height distribution using Patir's method

(F) Height distribution Hu and Tonder's method

FIGURE 3.14: Surfaces generated using two methods with same ACF

that all six pressure faces on the disc side of the firtree joint come into contact with the respective pressure faces on the blade firtree joint simultaneously. However, due to the non-smooth pressure faces that are produced as a result of the manufacturing process, the first contact may occur between a few randomly distributed asperities on these faces. As a result, different parts of the six pressure faces may experience non uniform stress distribution, affecting the stresses in the notch regions which may alter the life of the joint. Hence, it is desirable to represent these manufactured non smooth

pressure faces in the analysis procedure in order to extract the variation in stresses in the notch regions. Accordingly, it is useful to numerically generate the surface height data spread across the pressure face that represent the same statistical properties as the real manufactured surfaces.

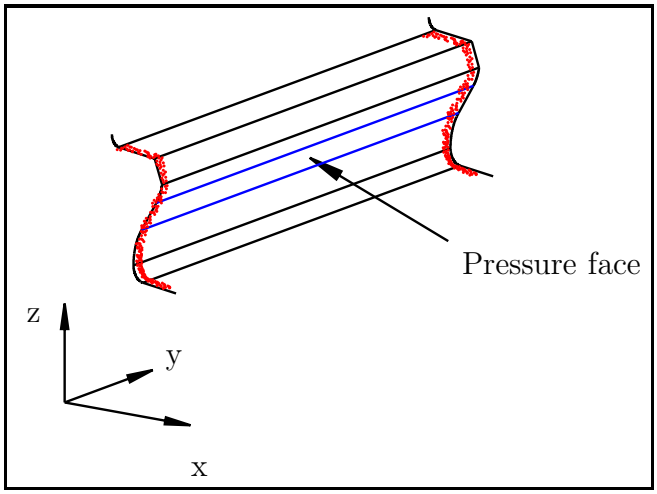

FIGURE 3.15: Disc firtree scanned using CMM

The disc side of the firtree joint used as an attachment between a high pressure turbine disc blade attachment in a gas turbine engine has been scanned using a coordinate measuring machine (CMM). Firtree slots are measured along their edges at the front and the rear sides as shown in Figure 3.15. Hence, the surface profile heights are available only in one orthogonal direction.

3.4.1 Extraction of statistical properties from the scanned data

CMM scanned data is available for nine disc side firtree joints where each slot consists of six pressure faces. As a first step, the normal distance from each scanned point to the corresponding nominal pressure face is evaluated. The function `UF_MODL_ask_minimum_dist` available in Siemens NX Open C API capability is used to evaluate these normal distances.

3.4.1.1 Height distribution function

The distribution of such normal distances, which are the heights of points on the machined pressure face above the nominal plane, is shown in Figure 3.16 using a histogram after subtracting the mean, μ. It can be said that the distribution of heights follow the Gaussian type of distribution with σ as the standard deviation. If the autocorrelation function for the machined pressure face is known it is possible to numerically generate

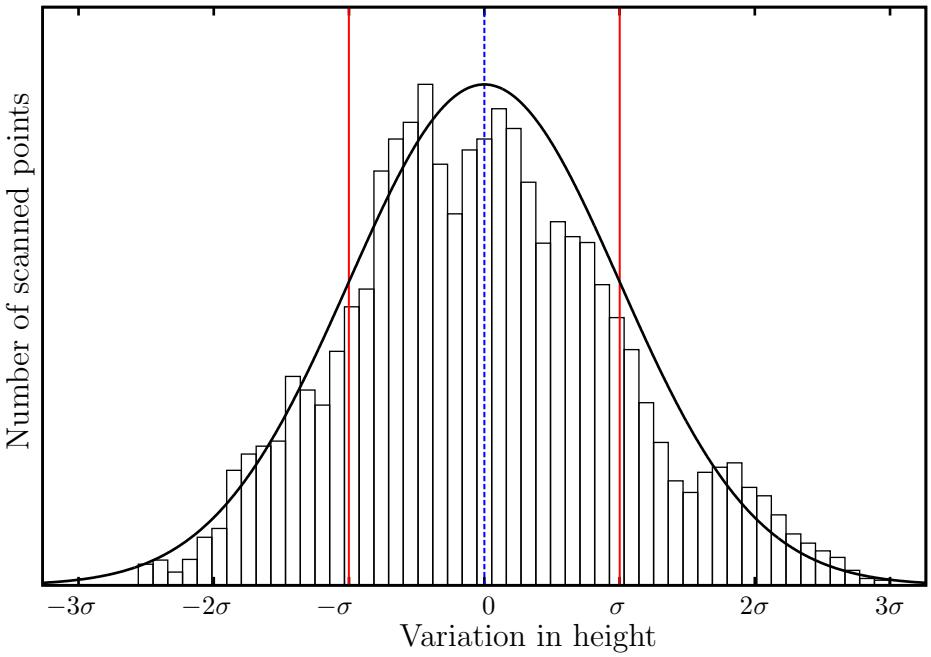

FIGURE 3.16: Histogram showing distribution of height

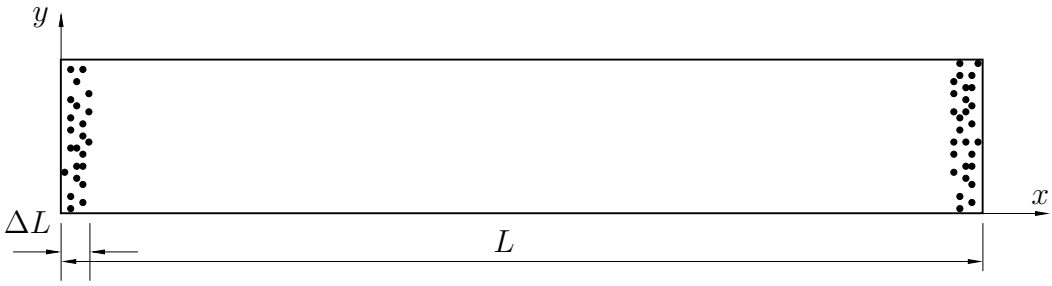

FIGURE 3.17: Pressure face

a Gaussian rough surface, belonging to the same family of manufactured surfaces as the pressure face, using either of the two methods discussed in previous sections.

3.4.1.2 Autocorrelation function

If $Z_{ij} = Z(x_i, y_j)$ is the height at point (x_i, y_j) on the surface, its autocorrelation function can be obtained from Equation 3.3 as,

$$R_{pq} = R(p,q) = \frac{1}{(N-p)(M-q)} \sum_{i=1}^{N-p} \sum_{j=1}^{M-q} Z_{ij} Z_{i+p,j+q}.$$

However, the disc side firtree joint is scanned in a very narrow strip along its edges at front and rear as shown in Figure 3.17 ($\Delta L \ll L$). There is no scanned data available along the length L of the pressure face. Hence, an exponential ACF with a higher

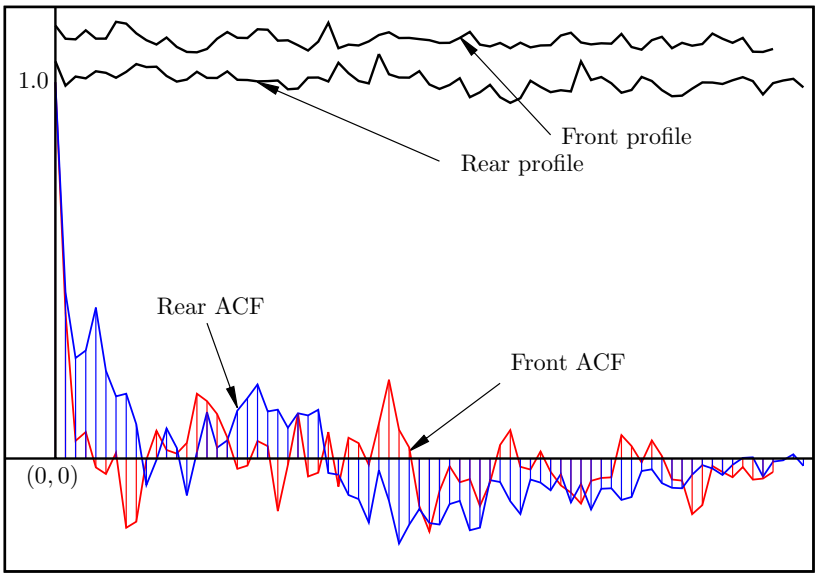

FIGURE 3.18: Front and rear profiles with their ACFs

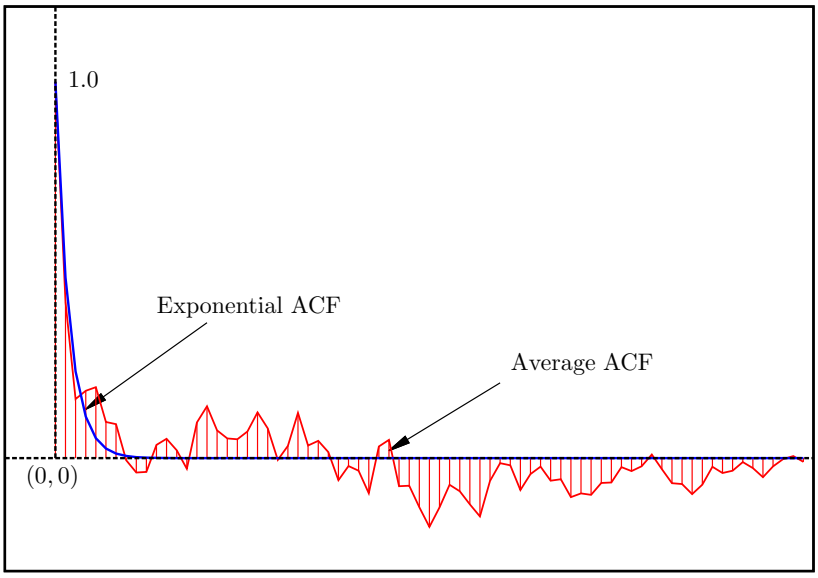

FIGURE 3.19: Average ACF

correlation length Δ_x^* is assumed. A higher correlation length reduces the number of peaks or troughs on the generated surface along the x direction. This assumption can be justified by the fact that the same cutting tool is moved from one edge to the other edge of the disc rim to produce the pressure face on the firtree slot. Hence, it is expected that the asperities have an elliptical shape, with their major axes along the x direction.

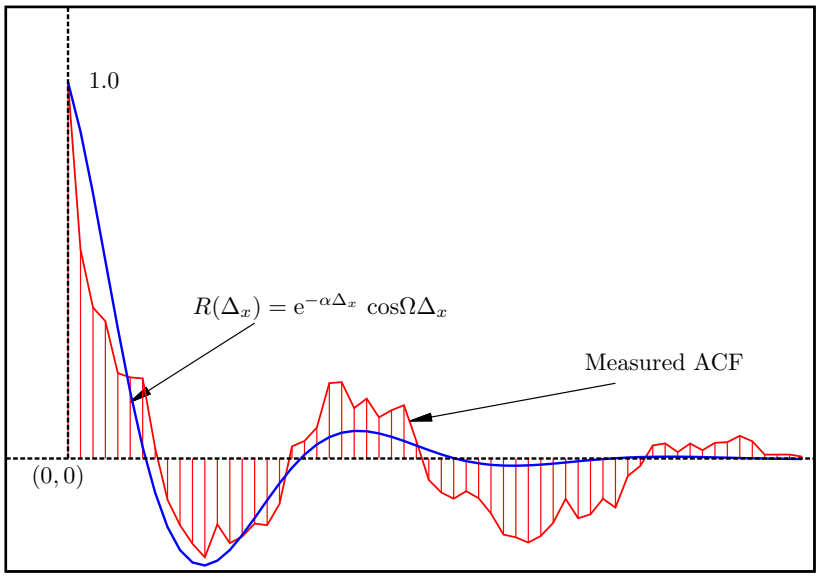

FIGURE 3.20: Measured ACF

To evaluate the ACF along y direction the following equation is used,

$$R_p = \frac{1}{(N-p)} \sum_{i=1}^{N-p} Z_i Z_{i+p}$$

It is also assumed that the scanned points are located along a straight line with a constant sampling rate although they are located in a narrow strip ΔL near the edges of the surface. Figure 3.18 shows the scanned profiles at the front and rear edges of one of the six pressure faces on a firtree slot with their ACFs. The average of the two ACFs is shown in Figure 3.19 with an exponential ACF that has the same correlation length as the average ACF.

Moore [57] and Peklenik [79] reported another form of autocorrelation function which represents a large number of engineering surfaces,

$$R(\Delta_x) = e^{-\alpha\Delta_x} \cos\Omega\Delta_x \tag{3.14}$$

where, α and Ω are constants that can be obtained by fitting the above equation to the measured ACF of a surface. Figure 3.20 shows one such measured ACF which can be used to fit the ACF of the form given in Equation 3.14. It can be seen to fit the measured data well.

Hence, the height distribution and the autocorrelation functions for the machined pressure faces are extracted from the CMM data on the disc side of the firtree joint. These properties are used to numerically generate the surface height data on the nominal pressure faces that represent these statistical properties.

3.4.2 Firtree pressure face generated using Patir's method

A rough surface is generated by linearly transforming a random matrix $[\eta_{IJ}]$ with unit standard deviation and zero mean. The ACF matrix (with dimensions $n \times m$) is created using exponential functions in x and y direction with $\Delta_x^* \gg \Delta_y^*$, Δ_y^* is taken from the exponential ACF in Figure 3.19. n and m are set equal to 10, while $N \times M$ (100×100) surface heights Z_{ij} are generated to represent the rough surface. Figure 3.21a shows the contour plot of the surface heights for the generated rough surface.

The height distribution function, Figure 3.21c, follows the Gaussian form with the mean and standard variation same as the distribution in Figure 3.16. The input ACF and the ACF of the generated surface are plotted on Figures 3.21b and 3.21d respectively. It can be seen that there is a good agreement between the generated and the input ACFs. Also, the shape of the asperities are elliptic with their major axes along the x direction.

The contour plot shown in Figure 3.22a is generated with an ACF which is of the form shown in Figure 3.20 in the y direction and exponential in x direction with $\Delta_x^* \gg \Delta_y^*$. It can be seen that although the asperities have elliptical shapes, with same Γ as in Figure 3.21b, the use of a different ACF in y direction generates surface which does not belong to the same family of surfaces as Figure 3.21a. The asperities on the surface in

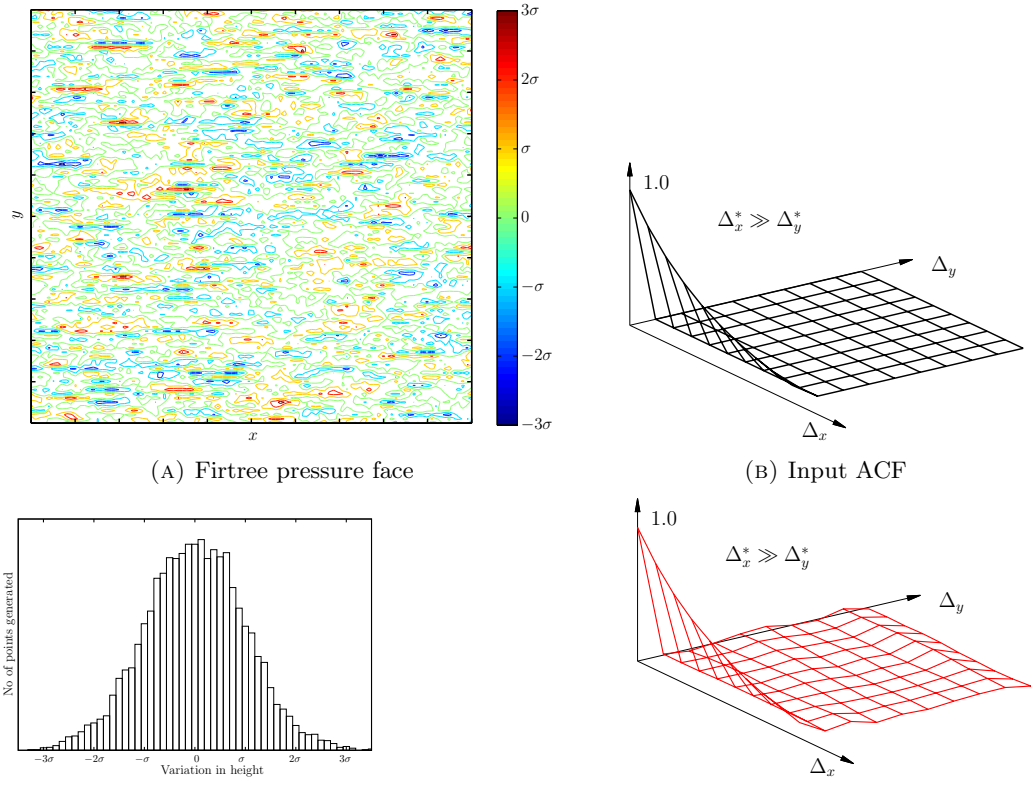

(A) Firtree pressure face

(B) Input ACF

(C) Height distribution function

(D) Generated ACF

FIGURE 3.21: Firtree pressure face A generated using Patir's method

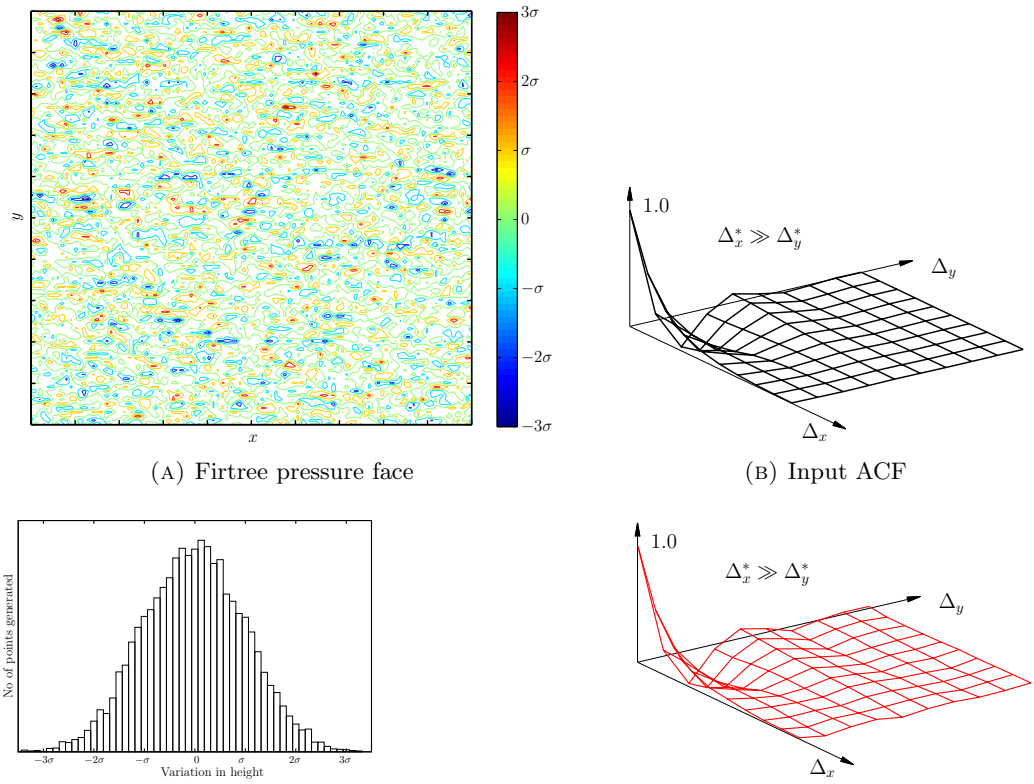

(A) Firtree pressure face

(B) Input ACF

(C) Height distribution function

(D) Generated ACF

FIGURE 3.22: Firtree pressure face B generated using Patir's method

Figure 3.22a are more densely populated as compared to the surface generated using an exponential ACF in Figure 3.21a. Hence, along with the correlation lengths Δ_x^* and Δ_y^* in both directions, the shape of the ACF also has a notable effect on the generated rough surface.

3.4.3 Firtree pressure face generated using Hu and Tonder's method

Using the same ACFs and height distribution function used for Patir's method, Hu and Tonder's method is applied to generate the surface heights. The values of n and m used here are 24 while the surface heights are evaluated at the same number of points $N \times M = 100 \times 100$. Figures 3.23a and 3.24a show the contour plots for the surface heights while Figures 3.23c, 3.23d and 3.24c, 3.24d show the ACFs of the input surface and the generated surface respectively for both cases. It can be seen that the generated ACF is in good agreement with the input ACF in the x direction. As the number of points N and M are increased, the generated ACF will follow the input ACF more closely.

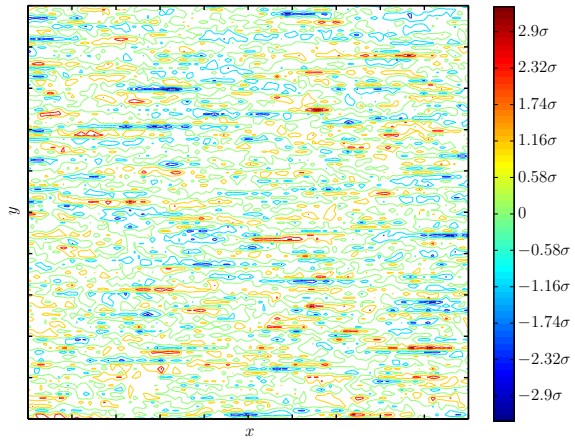

(A) Firtree pressure face

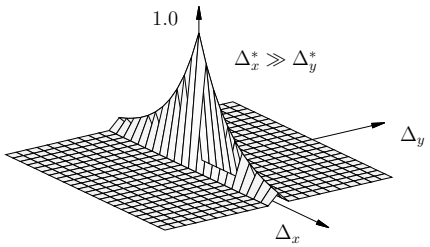

(B) Input ACF

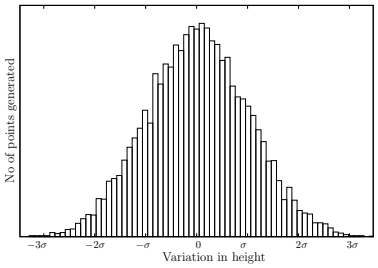

(C) Height distribution function

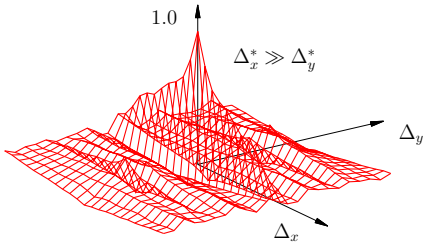

(D) Generated ACF

FIGURE 3.23: Firtree pressure face A generated using Hu and Tonder's method

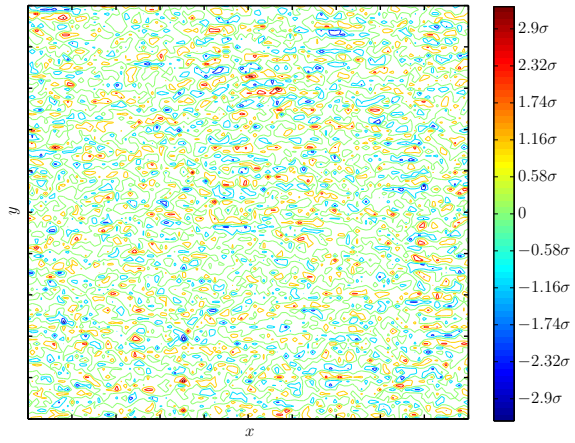

(A) Firtree pressure face

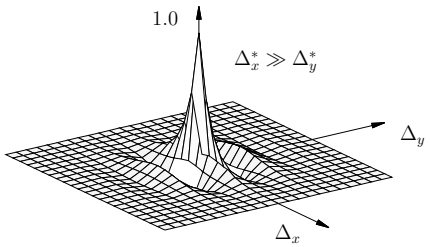

(B) Input ACF

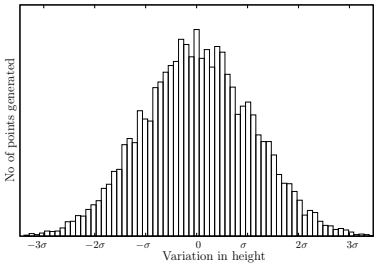

(C) Height distribution function

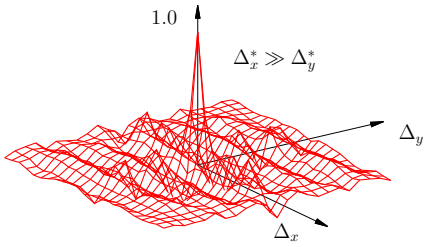

(D) Generated ACF

FIGURE 3.24: Firtree pressure face B generated using Hu and Tonder's method

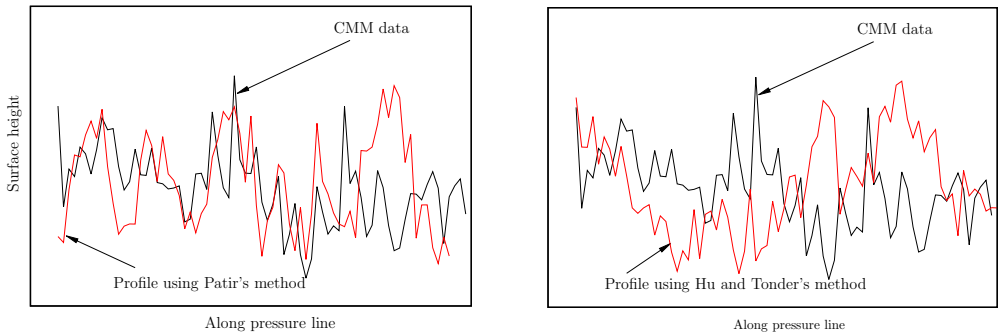

(A) Profile created using Patir's method

(B) Profile created using Hu and Tonder's method

FIGURE 3.25: Profiles generated using Patir's and Hu and Tonder's method with CMM data

The height distribution shown using a histogram in Figures 3.23c and 3.24c is of Gaussian type with mean and standard deviation of the distribution in Figure 3.16. As was observed with the Patir's method, the influence of the shape of the autocorrelation function is clearly visible when the contour plots of surfaces generated using Hu and Tonder's method are compared, Figures 3.23a and 3.24a.

Figures 3.25a and 3.25b compares the CMM data with the surface profile generated using the Patir's and Hu and Tonder's method respectively. Hence, two different methods have been implemented to predict the surface profile on the manufactured disc side pressure face based on the available CMM data.

3.5 Summary

Important properties of a rough surfaces when modelled as a statistical random process are listed. Some of these properties which are useful in generating Gaussian rough surfaces are discussed in more detail. Two methods (i) using linear transformation on random matrices developed by Patir [82] and (ii) 2D digital filters employing Fourier transforms developed by Hu and Tonder [85] to numerically generate rough surfaces for specified height distribution and autocorrelation functions are studied. Comparing both the methods, it can be concluded that Patir's method is more efficient when the size of the ACF matrix is within the limits in order to get good convergence on the solution of the system of nonlinear equations. However, Hu and Tonder's method, although less efficient, can be used to generate a wide range of surfaces with larger ACF matrices. Use of alternative methods like the nonlinear Conjugate Gradient method to evaluate the transformation matrix coefficients may eliminate the convergence issues with Patir's method.

Finally, rough surface height data is generated for the pressure faces on the firtree joints by both methods with the help of the scanned data obtained using a coordinate measuring machine. Selection of a suitable autocorrelation function is required to correctly represent the pressure faces. These numerically generated surfaces can be used in conjunction with CAD and FEA tools to study the effect such roughness parameters have on the performance of the firtree joint.

With this analysis of the measurement data of the firtree joints, in the next chapter the effect these manufacturing variations have on the structural performance of the joint are evaluated. Critical regions that are more severely affected by the manufacturing variations in the firtree joint are identified.

Chapter 4

Effect of Geometric Variation due to Manufacturing on Stresses in Firtree joints

4.1 Introduction

Structural design of an aero engine part component involves minimising the peak resultant stresses and strains while keeping the weight to a minimum. From the structural point of view, a component is required to transfer different kinds of structural loads, generated in working conditions, to its support structure. The stresses and strains experienced by the material used for manufacturing these components are often controlled within elastic limits. In mechanisms where different surfaces of the same part, or of several parts interact or come into contact with each other, the stresses in the neighbourhood of the contact region may enter the plastic range resulting in localised permanent deformations. Such a high magnitude of stress may be acceptable in some applications as long as the plastic deformations are restricted in relatively small regions to keep the stresses in other critical regions of the part component within the elastic range throughout its life. This is one of the most important design criteria an engineer follows while designing a structural component. Hence, it is important to efficiently evaluate the stresses that a component experiences at its critical locations in working conditions.

Analytical solutions to evaluate the stress and strain fields for many benchmark structural problems have been developed. Static stress analysis involves seeking closed-form solutions for the governing partial differential equations obtained by equating all forces at equilibrium. However, many engineering applications involve mechanisms where such closed-form solutions cannot be used directly to obtain the stresses or strains. In such situations, researchers and engineers often use the tools of numerical analysis. Advances

in numerical methods for analysis in engineering have helped analysts to evaluate the field values for problems that cannot be tackled using analytical methods. Numerical methods attempts to evaluate the solutions by reducing a large continuous domain to multiple small discrete domains. The complex geometries involved in real structural engineering applications are discretised into finite individual smaller domains with simpler geometries for which analytical solutions are available. Solutions over such finite domains are then combined to obtain the solution of the original model provided certain assumptions are satisfied.

Methods such as finite element analysis (FEA) [98], boundary element method (BEM) [99], finite difference method [100, 101], finite volume method [102, 103, 104], etc., have been used extensively to obtain field values numerically. From the stress analysis point of view, FEA and BEM are the two numerical methods used most frequently by engineers and researchers. The main difference in the approaches of FEA and BEM is that, in the case of FEA, the whole domain is discretised into multiple finite elements while only the boundary of the domain is discretised in case of the BEM. As a result, in the case of BEM, the dimensions of the problem are greatly reduced, since for a 2D analysis only the line-boundaries need to be discretised while for 3D analyses, the outer surface of the volume is discretised unlike in a FEA where the whole domain is discretised. Hence, as the unknown variables such as the displacements on each node need to be evaluated only on the boundaries of the domain, a much smaller system of equations is obtained compared to the FEA. However, the stiffness matrix obtained using the BEM is fully populated and asymmetric, whereas FEA generates a banded symmetric matrix. When direct solvers are used, the solution time for such fully populated matrices is much longer as compared to banded matrices [99]. For large nonlinear problems, it becomes necessary to use the volume mesh in the numerical analysis, when the advantages of BEM over FEA tend to diminish. The solution time for such problems can be much longer for BEM as compared to the FEA [105]. Furthermore, there are many commercially available finite element software packages such as ABAQUS, ANSYS, Comsol, etc., that have developed into robust tools to perform stress analysis. Due to its ease of use and the wide range of problems for which acceptable results are obtained, FEA has become more popular for analysing complex structural problems. The pre and post processors available today for most FEA packages make the process of setting up the model and then visualising the results fast and easy for the user. Most of the popular FE packages give users the capability of scripting the analysis without using the graphical user interface. This greatly helps in reducing the time for the design optimisation process. Also, most software packages seamlessly integrate with independent Computer Aided Design (CAD) packages helping in automating the entire design process. These factors have made FEA an important tool in solving engineering problems which involve stress analysis.

The firtree joint that is analysed for stresses in this work has a very complicated geometry. The blade disc assembly experiences high centrifugal loads in conjunction with

severe thermal loads which may induce close to yield stresses in the material. The loads travel from blade to disc via contacting surfaces at six different locations. It is difficult to obtain a closed-form expression for the stresses and displacements of such an assembly. Hence, it is essential to make the use of available numerical methods in order to evaluate the stress states in the firtree regions of a blade disc attachment. In this thesis this is done using the finite element analysis.

4.2 Structural behaviour of blade disc attachments

Regions near the blade disc attachments have to experience high localised stresses in order to transfer the high centrifugal and thermal loads by holding the blades in precise locations to ensure the required efficiency is delivered. Under these circumstances, the blade disc attachments have to be designed to sustain such high stresses throughout their life. It is required that the life of such joints be longer than the life of the attached components [25]. It is useful to understand the structural behaviour of a blade disc attachment in order to investigate the important parameters that affect their performance in different aspects.

High pressure turbine discs are driven at rotational speeds of $\approx 10,000$ revs/min. Such speeds induce very high centrifugal loads on the blade disc attachments. Transient conditions are experienced by the rotor during starting and shutdown operations of the engine. Under these conditions the blades undergo variable magnitudes of excitation forces that can result in vibrational response at the fundamental modes of vibration. The stresses that are generated may be high and lead to low cycle fatigue (LCF) problems [106]. Rao [106] suggested that the only way to control these fluctuating high resonant stresses is by dissipating the vibrational energy at such transient resonant conditions. Hence it is desirable, from the vibrational reliability point of view, to reduce the intensity of the magnitude of fluctuating stresses generated. Matveev et al. [107], reported that such energy losses could be obtained via the joints of the blades with the turbine disc to some extent. For a vibrating turbine blade, damping can originate from several mechanisms such as material damping, friction damping at the contact interfaces, gas damping, etc. [106]. Out of these, the friction damping due to the contact between two surfaces is of relevance to this work.

The mathematical modelling of such interfacial damping is a complex problem especially for blade disc attachments like a firtree joint, where six contact pairs of surfaces are active simultaneously. Several researchers have attempted to predict the damping capacity of blade roots [106, 107, 108]. Matveev et al. [108], performed experimental studies on the damping capacity of blade firtree roots by considering the loading parameters such as the tensile centrifugal load, the bending moment in operating conditions and the shearing force. It was reported that the damping capacity increases with bending moment and

as the tensile load decreases. Matveev et al. [108] also suggested that when the spacing on different teeth on the blade side of firtree matches with the disc side, changes in the number of teeth do not affect the damping properties. A similar experimental study was performed on a six toothed composite firtree root, with a pressure angle of 40° by Matveev et al. [107]. Use of the composite firtree root helped in reducing the induced stresses in contact regions which resulted in an increase in the damping capacity of the root. It was also found that decreasing the pressure angle on the firtree joint helped to increase its damping capacity. Rao [106] considered the contact interactions under static and dynamic conditions and studied their effect on the damping capacity analytically. It was found that blade disc attachments of the form of firtree joints provide higher damping capacity as compared to T-roots or dovetail joints. It is suggested that FEA is a useful tool in studying the optimal damping provided by different blade roots.

Petrov and Ewins [109] performed a forced response analysis of bladed disc assemblies by considering the effects of damping and variations in the contact area at the interfaces. The damping due to interaction between surfaces results from the frictional forces caused by small relative motions between the blade and the disc. It was reported that the variation in the contact area in the blade disc attachment affects its stiffness properties and hence the resonance frequencies. A finite element model was used to perform this forced response analysis with special techniques to reduce the computational time. The frequency spectrum for vibration of a bladed disc is dense which makes it unfeasible to prevent the occurrence of resonance. Hence, special devices are used as friction dampers in order to reduce the resonance amplitudes. Petrov [110] analysed an assembly of a bladed disc with friction dampers for forced vibrations by using a finite element model. Special contact friction elements were used in the FE model which allow for friction, stick-slip, and contact separation transitions in contact regions. Hou and Wicks [111] also used 3D finite element analysis to investigate the effect of blade root flexibility on the vibration characteristics of a turbine blade. A validation study with experimental results was done on the FE model. The FE simulation showed that the blade natural frequencies are higher than the results obtained from the experimental study. Avalos et al. [112] studied the forced response of the bladed discs by including variations in the contact interfaces properties. The global matrices for the finite element model for the bladed disc are partitioned into matrices for internal and boundary degrees of freedom. Hence, the variation in mass and stiffness properties on the boundary nodes is included only on those matrices. The uncertainties were introduced using the nonparametric stochastic approach. Larger amplification factors on the blade natural frequencies were obtained when the variation in interface properties is included.

Thus it can be said, that the contact conditions between the surfaces on blade and disc play an important role in contributing to the damping capacity of the joint. Any variation in the contact conditions can affect the response of bladed discs under forced vibration. Although the crowning of blade pressure surfaces aids in locating the contact

area at the required position more accurately than a flat surface, even a slight variation due to manufacturing can induce high stresses near the contact edges [31]. Permanent deformations due to stresses exceeding the elastic limit may have a substantial effect on the contact pressures. High fluctuating stresses in transient and steady state conditions may result in low and high cycle fatigue problems. The tensile stresses in the notch region have to be controlled so that they do not lead to crack nucleation and eventually propagation.

4.3 Stress analysis of blade disc attachments

As is clear from the previous discussion, many researchers have used FEA as a tool to evaluate stresses in the blade disc attachments found in compressors and turbines. However, the literature tends to concentrate more on the analysis of dove-tail joints as opposed to firtree joints although the mechanisms involved in the transfer of the centrifugal loads is the same in both cases. Sinclair and Cormier [113] developed simple physical models to evaluate the stresses in a dove-tail joint which were compared with the results obtained using the finite element method by Sinclair et al. [114]. The evaluation of high peak stresses near the edges of the contact zone in such an attachment is a challenging task when performing stress analysis using FEA. Sinclair et al. [114] proposed a procedure for modelling the contact such that sufficiently fine meshes are obtained which can predict the high stresses near the edges with a comparatively moderate computational effort. Results obtained using the physical model showed good agreement with the FEA results [113]. Charleux et al. [115] used a full-size finite element model of a dovetail joint to assess the frequency response in the case of mistuned blades. The FE model consists of the full disc, with four blades grouped in two and placed diagonally opposite along the circumference of the disc. To reduce the computational time, the FE model is reduced using the Craig & Bampton component modes synthesis method. Charleux et al. [116] proposed a multiharmonic balance method to compute the forced response of bladed discs with friction and contact nonlinearities in the interfaces of the attachment. The numerical results obtained using the FE model of a dovetail joint, when validated with the experimental results showed good correlation with respect to the resonant frequencies, amplitudes and damping capacities of the attachments.

One of the earliest examples of using FEA to perform stress analysis on the firtree joints is reported by Chan and Tuba [117]. They compared the stress distribution of a two dimensional case obtained using FEA with the photoelastic results. It was concluded that the comparison between FEA and the photoelastic results lacked detailed agreement in the field values but they both showed the same trend in the stress contours [117]. In the work reported by Singh and Rawtani [118, 119], the effect of variation in different geometric parameters defining a firtree joint on the stiffness of a firtree joint were studied. In the first part of their work [118], the effect on the stiffness and loads carried by each

tooth is studied by considering a single generalised tooth of a firtree joint while in the second part [119] the same study is performed on the whole firtree joint. Singh and Rawtani [119] gave equations based on equilibrium and equality of relative deformations for a general firtree joint. The computational time is comparatively reduced for solving such equations; also it is reported that for an efficient design, the values of geometric parameters can be different for different teeth of the same blade firtree geometry. Meguid et al. [120] performed two dimensional and three dimensional analyses of the firtree joint to examine the effect of variation in key geometric features such as pressure line lengths, angles and number of teeth on the stress distribution. The results obtained using FEA were validated with the stresses obtained using the photoelastic-stress-freezing technique. It was reported that the results obtained using the two dimensional analysis did not reflect the large stresses observed near the edges perpendicular to the plane of analysis from three dimensional analysis, [120]. Mase et al. [121] performed a linear and nonlinear three dimensional analysis on the firtree joints to extract the peak stresses near contact regions. It was reported that the linear analysis gave reasonably accurate results with a friction coefficient of $\mu = 0.3$.

Finite element models have been used extensively to simulate the fatigue and creep conditions in blade disc attachments to predict their life. Issler and Roos [122] used inelastic finite element analyses to predict life of the firtree joints in low cycle fatigue conditions and compared it with the experimental results. Constitutive laws to reflect static, cyclic, and viscoplastic material behaviour were used in the analysis. It was found that the numerical analysis overestimated the life predictions when compared with the experimental results. It was also reported that life predictions based on maximum principal stresses and strains give more reliable life predictions. Importance should be given to characterise the frictional behaviour on contact interfaces appropriately. Hu et al. [123] performed a similar study where a 3D FE model of turbine firtree section was used to predict the life under combined conditions of creep and fatigue, in order to propose a criteria for withdrawing turbine components from service. A good agreement was observed between the FE results and experimental data. Liu et al. [124] obtained probability distribution functions for the stress and strain levels at critical locations in a turbine disc using FEA for variation in basic parameters such as applied loads, temperatures, geometrical dimensions and material properties. In a similar study, Lu et al. [125] obtained distributions for the stress and strain levels using a FE model of the firtree joint. Rauch and Ross [126] used FE models for two different types of blade disc attachments – a firtree joint used in gas turbine engines and T-shaped blade-shaft-connection of a steam turbine. The notch regions experience complex multiaxial elastic-plastic stresses in working conditions. The accumulated plastic strain after application of cyclic loading was used as a damage parameter in developing a new life assessment method. In another study by Isobe and Nogami [127], a 3D FE model of a dovetail joint was used to evaluate the stress state in the regions surrounding the contact zone including the kinematic material hardening rule. The stress strain hysteresis curve was obtained

by performing the FE simulations until the cyclic behaviour is stabilised. Anandavel and Prakash [128], investigated the effect of three-dimensional bulk loading on the interface in the dovetail joints under resonance conditions. A FE model was used in conjunction with a semi-analytical approach for the computation of wear due to fretting action at the interface. A 3D FE model was used to perform design optimisation on blade disc attachment of double-T root type under lubricated contact conditions by Zhang et al. [129]. As many as twelve design variables were used to optimise the geometry of the root by minimising the maximum equivalent stress. Maharaj et al. [130] used a 2D FE model of a turbine firtree joint to study the creep remnant life of the turbine disc. FE simulation was used to identify the locations of high creep strains and relate them to the deformation values measured experimentally. Significant variations were observed in the contact pressures on the interfaces in firtree region with a loss of contact in some regions during the creep analysis.

Hence, it can be seen that FEA of the blade disc attachment is a common tool used by engineers and researchers to evaluate their structural performances in different aspects. The contact modelling at the interfaces of the attachments is critical in order to have a good confidence in the FE results. Contact interfaces and the regions surrounding them need to be meshed fine enough to allow the FE to simulate the peak stresses accurately. In this work, a FE model created in ABAQUS is used to extract the variations in the stresses in the notch regions of a firtree joint due to the variation in geometry as an effect of the manufacturing process used to produce them.

4.4 Finite element modelling of firtree joints

Limiting the peak tensile stresses in the firtree region is critical for the satisfactory performance of the joint for its designed service life. Since the magnitude of stresses in locations near the contact interfaces is close to the yield stress of the material, any positive variation in these stresses may cause yield of the material and hence affect the life of the joint. The variations in the geometric parameters in the firtree region due to the manufacturing processes should not vary the resultant stresses to an extent when the life of the joint is reduced. Hence, it is useful to evaluate these variations in the stress distribution in firtree section due to such geometric variations. In order to extract this variation, FEA is used in this work to perform the stress analysis on the firtree joints.

4.4.1 Geometry creation

The first step in conducting a finite element analysis is to create an appropriate geometry which is in the format suitable for importing into a FE package. Most FE packages used today, in academia or industry, come with an in-built geometry creation capability.

However, there are limitations over the degree of complexity in geometry that can be achieved with these packages. Moreover, the need to parametrise the geometry to make it suitable for design optimisation purposes makes the creation of geometry an equally important and involved process as setting up the simulations. Geometry creation should be able to provide the designer with a sufficiently large design space to search a geometry optimised for the specific objective. Use of independent packages for geometry creation such as Siemens NX, CATIA, Solidworks, etc., has become common practise today in industry especially for large and complex geometries which are involved in aerospace applications.

The geometry of the firtree section in a blade disc attachment analysed in this work is created in the CAD environment of Siemens NX. The geometry is created in batch mode, to integrate it in an iterative process in conjunction with the FE simulation, with the help of the Open C API capability of Siemens NX [131]. Firtree joints with 2D and 3D parametrised geometries of different degrees of complexities are generated in Siemens NX and then analysed for evaluation of stress distribution in the FEA environment of Dassault Systémes' ABAQUS [132].

4.4.2 Boundary conditions

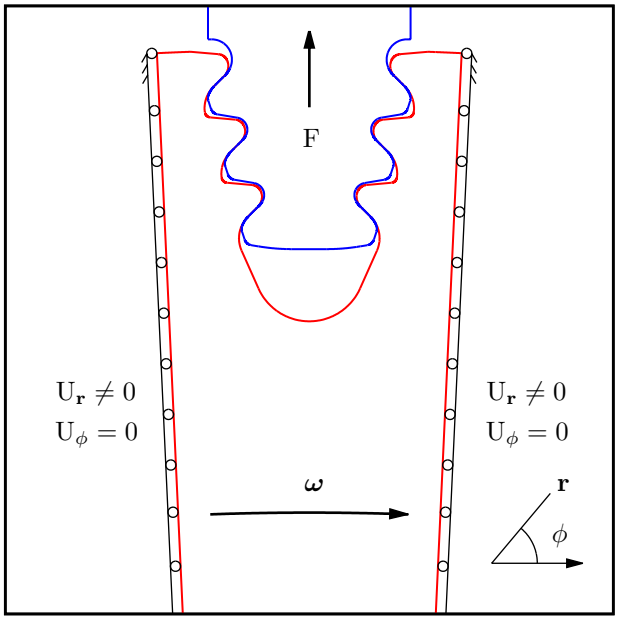

FIGURE 4.1: Free body diagram of blade disc attachment

The 2D and 3D firtree joint geometry created using the Siemens NX Open C API is imported into ABAQUS, to perform a non linear contact elastic analysis within a single disc sector, Figure 4.1. Boundary conditions applied on the cut edges of the disc are such that all points on these edges are free to move in the $r-$direction but restrained in

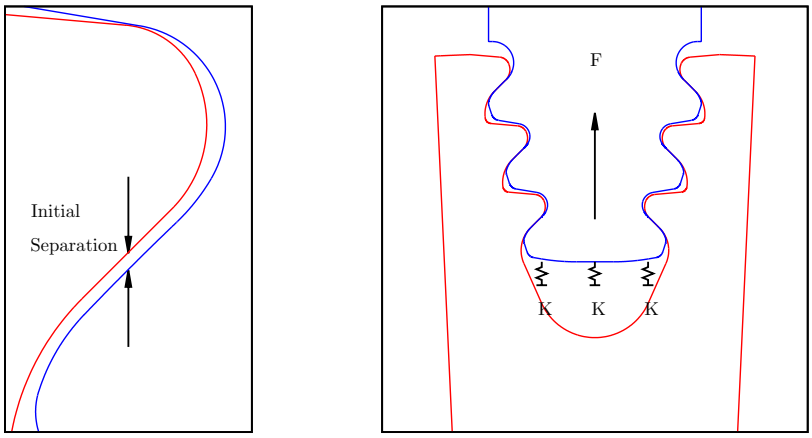

(A) Separation between blade and disc

(B) Springs on blade

FIGURE 4.2: FE assembly

the $\phi-$direction ($U_\phi = 0$) as illustrated in Figure 4.1 (boundary conditions are applied in the polar coordinate system (r, ϕ)). A body force F due to the centrifugal action is applied on the blade which is calculated based on the angular velocity with which the disc is rotating at cruise, ω. Only the centrifugal loads on the blades are considered in this analysis. It is expected that the component of stress tensor in the perpendicular direction to the firtree geometry is less compared to the stresses in its plane and hence plane stress conditions are assumed while performing the 2D stress analysis [120, 26, 133].

While modelling the assembly in the FE environment, the blade was first positioned towards the rotational axis of disc to ensure an initial separation between the pressure faces on the blade and the disc as shown in Figure 4.2a. This is done so that, on application of the load, the ABAQUS solver is able to locate the first point of contact along the pressure faces of the disc and blade. However, since there is no other boundary condition on the blade, the application of any load on the blade will initially result in a singular stiffness matrix for the blade. To overcome this problem very weak springs are located on the blade as shown in Figure 4.2b. The spring stiffness K is selected such that the stresses obtained in the blade, due to these springs before the first contact takes place, are relatively small. Hence, it is ensured that there will be a negligible effect due to the springs on the stress field in the final solution.

4.4.3 Contact modelling in ABAQUS

One of the main functions of a firtree joint is to transfer the centrifugal loads acting on the blade to the disc through the several contacts between pressure faces of blade root and disc rim. While performing a finite element analysis, the contact properties need to be modelled precisely to accurately predict the stress distribution in the firtree section,

especially in the notch regions (the importance of stresses in the notch regions will be discussed in the future sections). Some of the important options for modelling contact between two surfaces in ABAQUS are discussed in the following:

1. Contact algorithm: ABAQUS/Standard provides three different approaches to define a contact (i) general contact, (ii) contact pairs, and (iii) contact elements. Out of these, the first two approaches are relevant from the surface to surface interaction occurring in the firtree joint analysed here. In the case of the firtree joint analysed here, each contact comprise of independent surfaces that belong to two different deformable bodies. The algorithm used to evaluate the contact pressures and areas requires specification of master and slave surfaces. While the general contact algorithm automatically identifies the master and slave surfaces, the approach of contact pairs provides the user with an option to select these surfaces. ABAQUS provides basic guidelines to identify the master and slave surfaces. The surface which is larger or belongs to the stiffer body should be specified as the master surface and the other as a slave surface [134]. Accordingly, in order to make sure that the pressure faces on the disc side firtree are always the master surfaces and that on the blade side are slave surfaces, the approach of contact pairs is used in this work.

2. Finite sliding: There are two sliding formulations available in ABAQUS/Standard – (i) finite sliding and (ii) small sliding. As mentioned in the ABAQUS users manual, small sliding should be used when the relative sliding between the two surfaces is small with respect to the length of elements used on the contact interface. Whereas, interactions when there is a possibility of sliding between the surfaces or separation between the master and slave surfaces a finite sliding formulation is recommended [134]. Hence, a finite sliding formulation is adopted for the analysis performed in this work.

3. Surface-to-surface contact: The surface-to-surface contact formulation is more accurate as compared to the node-to-surface formulation [134], since node-to-surface does not allow slave nodes to penetrate in the master surface. This results to concetrated stresses when they are not expected.

4. Interaction property: The contact between the pressure faces involves transfer of normal and tangential forces from the blade to the disc. To simulate the lubricated state, an appropriate value for friction coefficient (see Section 4.4.4) is used for defining the tangential behaviour of the contacts along with the Penalty formulation method. There are two options for the friction formulation in ABAQUS/-Standard – (i) the Penalty method and (ii) the Lagrange multiplier method. The Penalty method allows the surfaces to slip within elastic limits at load increments when they should stick which may affect the accuracy of evaluation contact pressures. The Lagrange multiplier method allows elastic slip, only when the shear

Side	Flank	Maximum von Mises stress		Maximum tensile stress	
		Lagrange	Penalty	Lagrange	Penalty
	Top	0.903	0.903	0.903	0.903
Left	Middle	0.911	0.911	0.911	0.910
	Bottom	0.999	0.998	0.999	0.999
	Top	0.904	0.904	0.904	0.904
Right	Middle	0.911	0.910	0.911	0.911
	Bottom	1.000	0.999	1.000	0.999

TABLE 4.1: Comparison between the Lagrange and Penalty formulations with respect to maximum von Mises and tensile stress (normalised) in all flanks

stress along the surface exceeds the critical shear stress. The Lagrange multiplier method gives better accuracy in the results but at the cost of adding more degrees of freedom. Hence, the convergence for the Lagrange multiplier method takes longer when compared to the Penalty method [134]. Table 4.1 compares the maximum von Mises stress and maximum tensile stress in all six flanks between the stress analyses performed with the Lagrange and Penalty methods. Since the firtree joint involves simultaneous contact between six different surfaces the computational time required for a Lagrange multiplier method is much longer (CPU time: 19 minutes) than the Penalty method (CPU time: 3 minutes). However, the results obtained using the Penalty formulation are in good agreement with those obtained with the Lagrange formulation. Hence, the Penalty method is adopted for the evaluation of tangential behaviour between the contact interface. The normal behaviour of the contact interaction is specified with the default parameters in ABAQUS/Standard under Penalty method.

4.4.4 Friction

Considerable literature is available for the study of the effect of coefficient of friction while simulating the contact conditions between the pressure faces in the blade disc attachments [130, 120, 26, 135]. While modelling creep in a turbine disc firtree joint, Maharaj et al. [130] suggested a friction coefficient of 0.2 for a surface coated firtree while 0.33 for the non-coated one. It was reported that the variation in the maximum principal stress in the notch regions of the firtree joint is small for a relatively large change in the friction coefficient. Similar results obtained by Chan and Tuba [117], suggested that the initial gap between the pressure faces has a more profound effect on the notch stresses than the friction coefficient. Meguid et al. [120] showed that the value of friction coefficient affects the contact edge peak stresses, while no significant effect was observed on the equivalent stress near the contact regions when the friction coefficient was varied

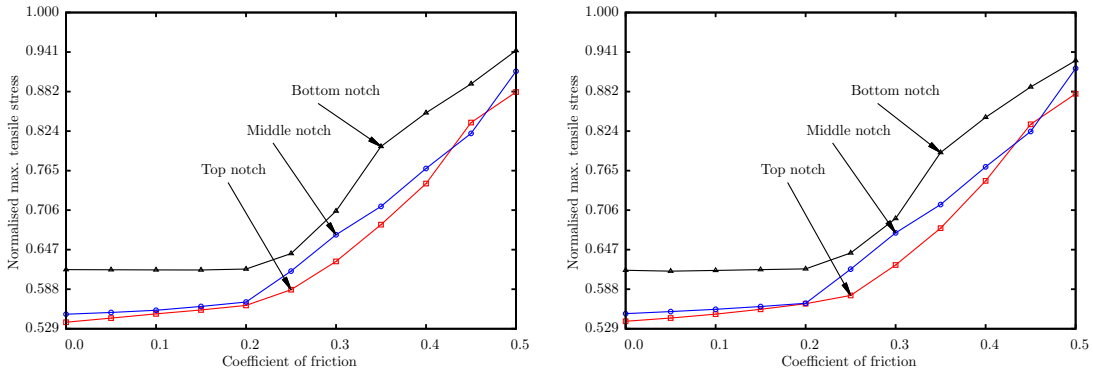

(A) Left side (B) Right side

FIGURE 4.3: Change in notch tensile stress with coefficient of friction

from 0.1 to 0.5. Delhelay [133] also conducted a thermomechanical stress analysis of a firtree joint with varying the coefficient of friction from 0.0 to 0.5. It was observed that higher coefficient of friction results in higher stress magnitudes at the blade disc interface. In another study, Singh and Rawtani [119] reported that the coefficient of friction has no significant effect on the vertical components of the loads carried by different flanks in the firtree joint. In a comprehensive study conducted on the physical and geometrical non-linearities in contact problems of the disc blade attachments, Zboinski [135] used a value of 0.15 as the coefficient of friction while performing a stress analysis on the firtree joint. It was reported that by increasing the friction coefficient, the location of the peak stresses moved towards the contact surfaces. Figure 4.3 shows the change in the maximum tensile stress at all six notch regions when the coefficient of friction is varied from 0.0 to 0.5. It can be seen that the notch stresses do not vary significantly for the values of coefficient of friction less than 0.2, also the magnitude of stresses for friction coefficient values above 0.35 exceed the yield stress of the material. In this study, the variations in the stresses are of more relevance rather than their magnitudes. Hence, to evaluate the contact conditions between the surface coated or lubricated pressure faces of a firtree joint, a lower value of 0.15, also used by Zboinski [135], for the friction coefficient is used in this thesis.

4.4.5 Mesh sensitivity analysis

For the 2D analyses 6 noded quadratic triangular elements are used in this work while for the 3D analyses 20 noded brick elements are used. In order to decide upon the number of elements to be used on the pressure faces or lines, a mesh sensitivity analysis is performed. The percentage change in the maximum principal stress along the pressure line between three different meshes is plotted on Figure 4.4a while Figure 4.4b shows the percentage change in resultant displacement.

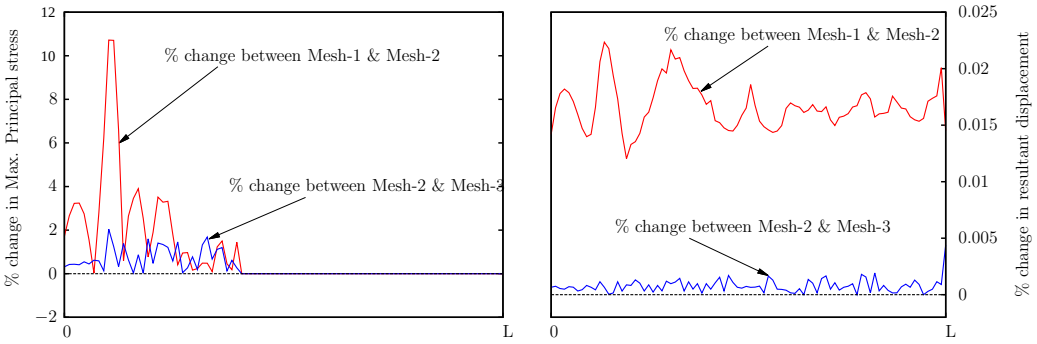

(A) Mesh sensitivity using max. principal stress

(B) Mesh sensitivity using resultant displacement

FIGURE 4.4: Mesh sensitivity analysis

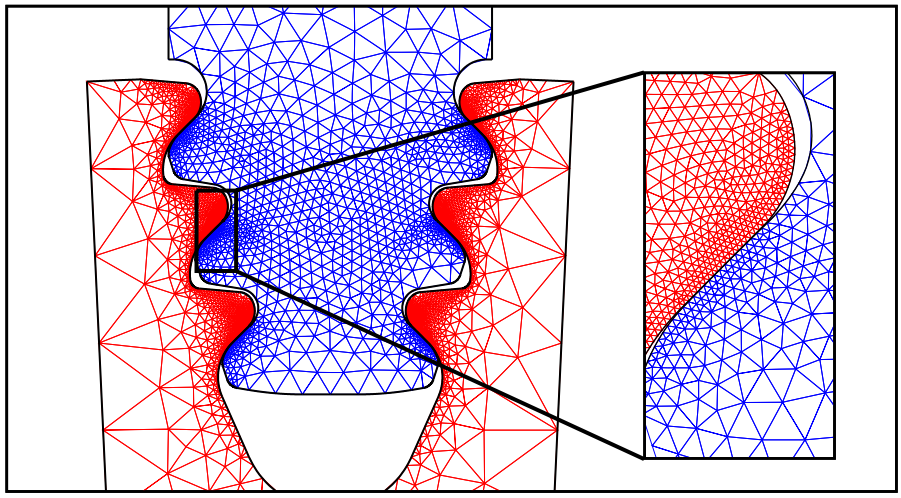

FIGURE 4.5: Typical mesh for 2D firtree geometry

Mesh-1 has 8 elements on the pressure line, while Mesh-2 and Mesh-3 have 30 and 45 elements respectively. It can be observed from Figures 4.4a and 4.4b, that the results obtained using Mesh-2 are in good agreement with the finer mesh, Mesh-3. Hence, Mesh-2 was adopted for all the subsequent 2D stress analyses. A mesh typical of those used for the 2D analysis here is shown in Figure 4.5 while Figure 4.6 show the 3D mesh. A relatively coarse mesh, with 30×26 elements on the pressure face (26 elements along the thickness of the firtree slot), is used for the 3D FE model of the firtree joint on the pressure faces in order to have feasible computational time. The number of elements used for the pressure arcs on the blade firtree are kept constant while changing the number of elements on the pressure lines of the disc firtree.

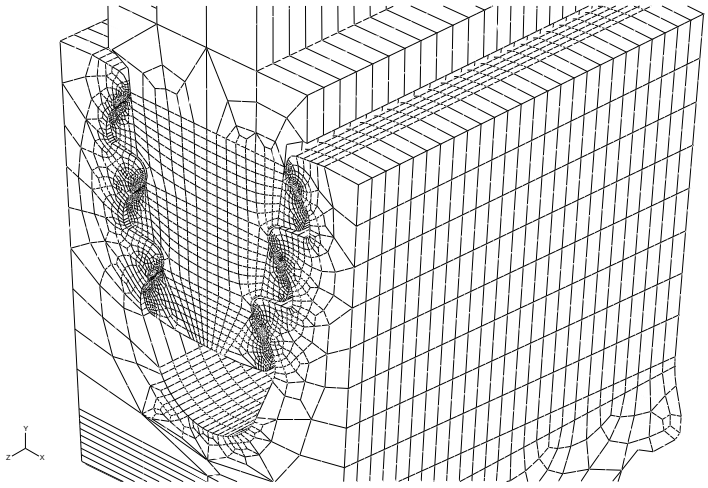

FIGURE 4.6: Typical mesh for 3D firtree geometry

4.4.6 Stress analysis on two- and three-dimensional nominal firtree geometry

Elastic stress analysis is performed on the nominal two- and three-dimensional firtree joint. The variation in the stress distribution due to the changes in geometry will be compared with the stress distribution on the nominal firtree joint. Since the joint involves six different possible contact locations, the load on the blade has to be increased in small increments to guarantee convergence in contact conditions. Any redistribution of stresses due to different contact surfaces getting engaged at different loads will also be captured by using small load increment values. Due to an asymmetric mesh on the part geometries and the weak springs applied at the bottom face of blade firtree part, application of an infinitesimal load can translate or rotate the blade firtree part before first contact is engaged. To protect against this unwanted displacement of blade, additional boundary conditions are applied on the blade part to ensure its movement in the radial direction. The same material is used for both disc and blade parts with properties: Young's modulus $E = 200$ GPa, mass density $\rho = 7.85$ kg/m^3, and Poisson's ratio $\nu = 0.25$. The stress contour plots for von Mises stress in the firtree region for 2D and 3D geometries are shown in Figures 4.7 and 4.8. It can be seen that the stress distribution in the neighbourhood of the pressure surfaces is similar for both 2D and 3D analyses. The slight asymmetry in the contour plot about the firtree centre line is due to the asymmetric mesh generated by ABAQUS. It can be seen from Figure 4.7 that the stress magnitude surrounding pressure lines (1 and 4) near the rim of the disc are less compared to the regions surrounding other pressure lines. This can be explained by the fact that the pressure lines at different flanks at top, middle, and bottom do not share the centrifugal load uniformly [25]. Figures 4.9a and 4.9b show the initial locations of active contact regions on all the six pressure faces on the 3D firtree model. It can be

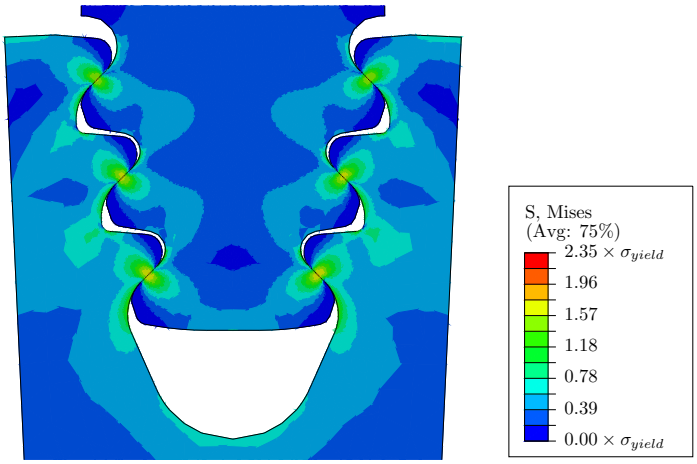

FIGURE 4.7: Contour plot for von Mises stress on a 2D nominal firtree joint

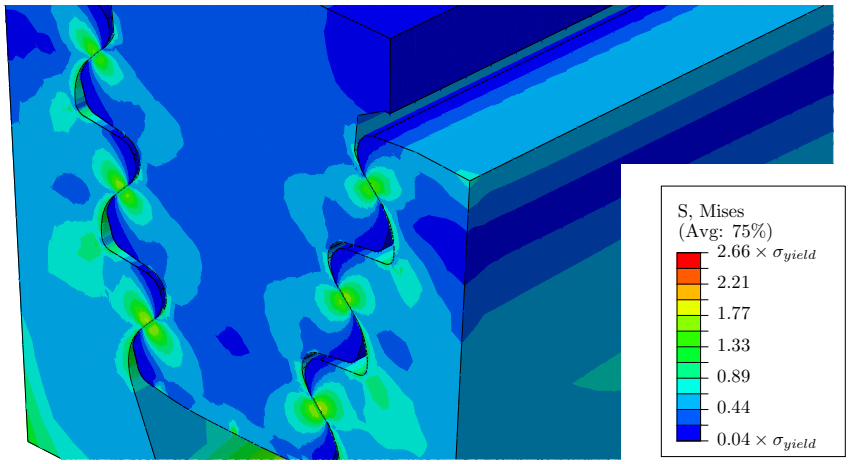

FIGURE 4.8: Contour plot for von Mises stress on a 3D nominal firtree joint

seen that all the six contacts have engaged simultaneously for the same load increment and they are uniformly distributed along the thickness of the firtree joint.

4.5 Effect on stresses due to variation in two dimensional firtree geometry

The tensile stresses or the maximum principal stresses in the notch regions are significant from the blade disc attachment's life point of view. Repetitive application of high centrifugal loads induce fluctuating maximum principal stresses close to the material yield stress. Under the conditions of high and low cycle fatigue, the material in this region may reach the plastic limits due to the hysteresis phenomenon and gradually disintegrate. This may result in nucleation of several micro cracks or in extreme cases macro cracks which could lead to catastrophic effects on the turbine. The fatigue life of a component manufactured from a ductile material depends predominantly on the

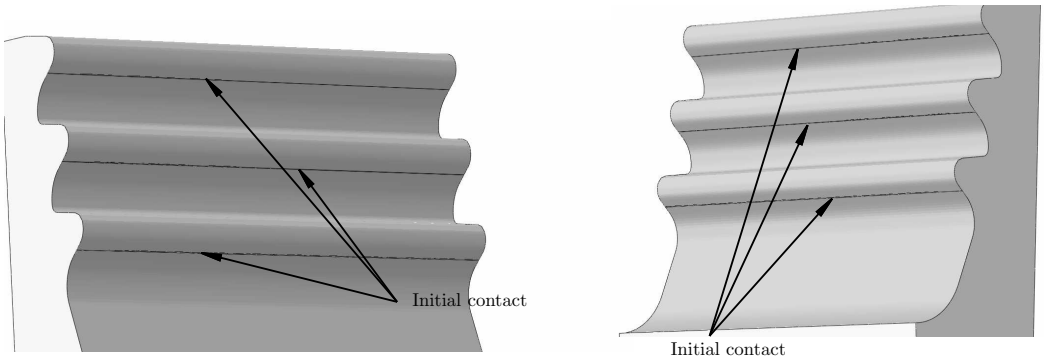

(A) Pressure faces on left side (B) Pressure faces on right side

FIGURE 4.9: Uniform initial contact at same load increment

magnitude of maximum principal stresses[1] it experiences under service conditions [136, 137]. Due to the stringent design requirements on aero engine components weight is reduced to an extent that the working stresses are in the neighbourhood of material's yield stress. Such optimised geometry although resulting in minimised weight often lie close to the constraint boundaries imposing severe restrictions on the variation of stresses in critical regions of the component. It is desirable to restrict the variation in these stresses such that they have minimal effect on the variation of service life of the component.

The variation in geometry extracted from the CMM data in chapter 2 is used in this section to investigate their effect on the stress distribution in notch regions of firtree joints. The variation in the pressure angle is extracted by fitting two different substitute geometries (Figures 2.9 and 2.15). The Fourier transform is used to filter the unwanted data, either by removing high frequency components or high magnitude components. These variations are then included in the firtree geometry with appropriate parametrisation using the Siemens NX Open C API. Figure 4.10 shows the general layout of the process used to study the effect of geometric variations on the stress distribution in the firtree joint. The variation in the angles is included first by having the same variation in angle for all six pressure lines, then separate angles for the top, middle and bottom flanks, and finally six independent angles. To include the surface irregularities, a B-spline is fitted through the FFT-filtered scanned data in Siemens NX.

4.5.1 Same angle on six pressure lines

The variation in nominal pressure angle θ, extracted by fitting curves to the CMM data in section 2.4.1 is used to begin with. The firtree geometry is created using the

[1]Since the industry designs firtree joints for maximum principal stress, the structural performance of the firtree joints is measured with respect to the maximum principal stress in the notch regions in this thesis. Von Mises stress is not relevant to lifing calculations and also it is an artefact of the contact analysis.

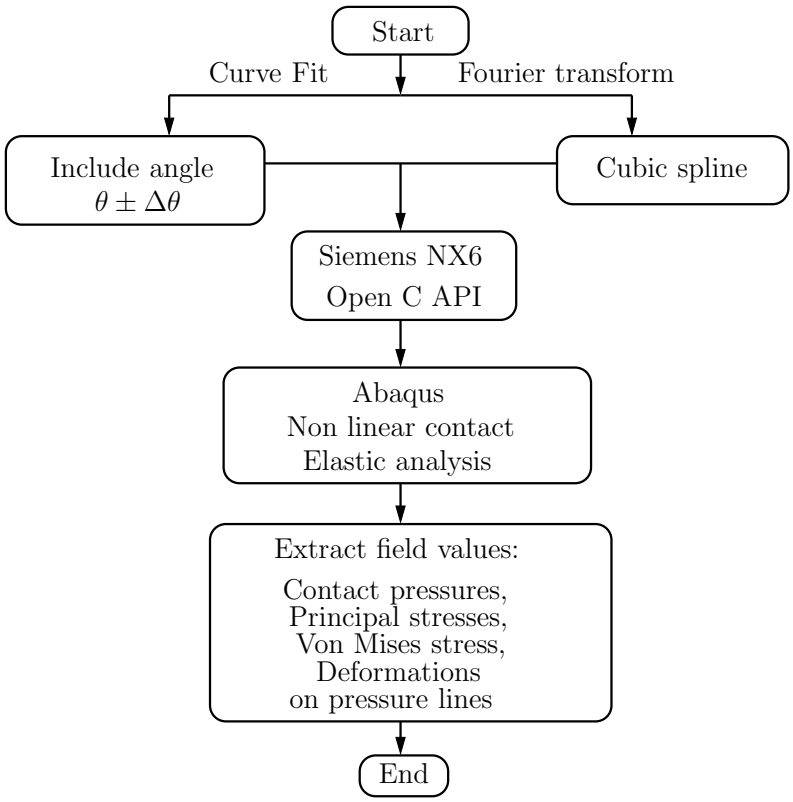

FIGURE 4.10: General layout of the process used to study the effect of geometric variation on stress distribution

pressure angle as the parameter in CAD (Siemens NX6) and analysed in Abaqus 6.9-1 for a centrifugal load on the blade. Field outputs such as contact pressure, principal stresses and von Mises stress are extracted from the region surrounding pressure line 2 as highlighted in Figure 4.5. In Figure 4.11a, both the maximum values of von Mises and maximum notch principal stress (tensile) are plotted on the histogram of Figure 2.13. It is observed that the values of von Mises stress and maximum principal stress[2] vary with a change in the pressure angle in the range $(\theta - \Delta\theta_j)$ to $(\theta - \Delta\theta_m)$ and $(\theta - \Delta\theta_p)$ to $(\theta + \Delta\theta_k)$, Figure 4.11a. Both stresses are approximately constant for a large number of designs (between $(\theta - \Delta\theta_m)$ and $(\theta - \Delta\theta_p)$) with pressure angles slightly less than the nominal angle θ. Any further decrease in the pressure angle from $(\theta - \Delta\theta_m)$, intensifies the maximum von Mises stress. This is also true for maximum principal stress, however the change in magnitude of maximum principal stress is less compared to that of maximum von Mises stress for the same $\Delta\theta$.

The magnitude of maximum von Mises stress for the design with nominal angle θ, is notably higher than the values for the designs with pressure angle in the range $(\theta - \Delta\theta_m)$ to $(\theta - \Delta\theta_p)$. Hence, a better design, with respect to the maximum von Mises stress, can be obtained by reducing the pressure angle by $\Delta\theta$ in the range $\Delta\theta_p$ to $\Delta\theta_m$. Any increase

[2] *Maximum principal stress* refers to the maximum value of the tensile stress in the notch regions and is denoted by $P1$ in this thesis.

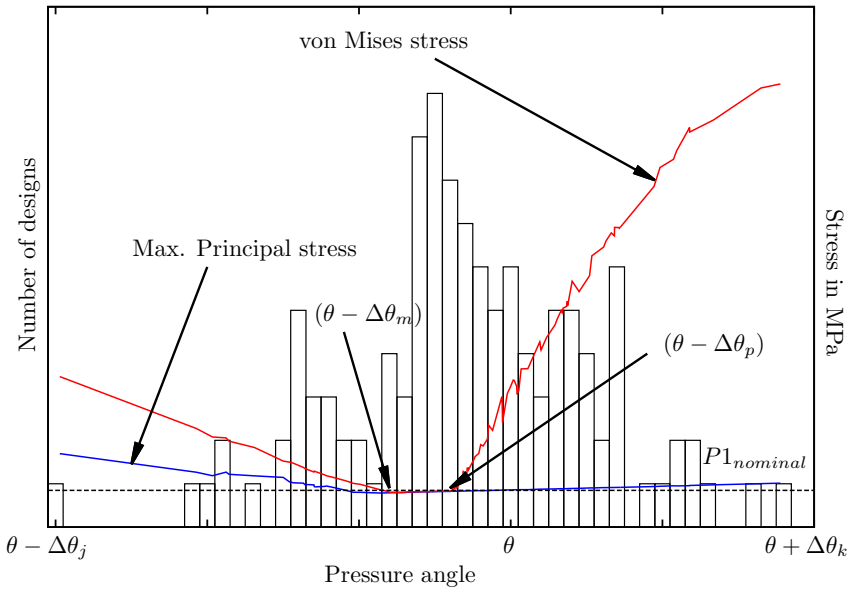

(A) Change in von Mises and maximum principal stress

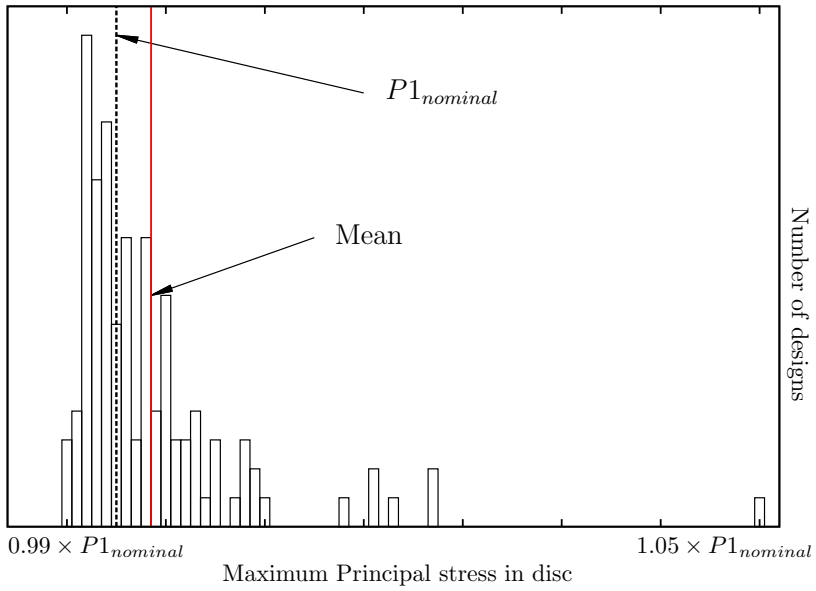

(B) Histogram showing variation in maximum principal stress

FIGURE 4.11: Variation in von Mises and maximum principal stress

in the pressure angle from θ further intensifies the maximum von Mises stress. As compared to the von Mises stress, no substantial variation is observed in the maximum principal stress with increase in pressure angle from θ.

Figure 4.11b shows the variation in the maximum principal stress near the pressure line of the firtree geometry with the help of a histogram. It can be seen that majority of designs have their magnitude of maximum principal stress exceeding the nominal maximum principal stress value. Few designs even have their maximum principal stresses as high as $1.025 \times P1_{nominal}$. The mean of the variation is found to be at $1.003 \times P1_{nominal}$ whereas the standard deviation is 0.67% of $P1_{nominal}$.

4.5.2 Shift in contact area

Figure 4.12 shows the von Mises stress contour plots for three geometries with different $\Delta\theta$s: $\Delta\theta_j, \Delta\theta_m$ and $\Delta\theta_k$. The pressure angle $(\theta - \Delta\theta_m)$ is selected such that the maximum von Mises stress for this design is less than all other designs in Figure 4.11a, whereas pressure angles $(\theta - \Delta\theta_j)$ and $(\theta + \Delta\theta_k)$ are the two extreme designs in Figure 4.11a. The location of the maximum von Mises stress for $\Delta\theta_j$ moves towards the lower end of the pressure line while for $\Delta\theta_k$ the location of maximum von Mises stress is shifted towards the upper end of the pressure line, Figure 4.12. As the pressure angle moves from left to right in Figure 4.11a, the location of maximum von Mises stress moves from bottom to top on the pressure line. The magnitude of maximum von Mises stress in Figures 4.12a and 4.12c is more than its magnitude in Figure 4.12b, since for variations in pressure angle, $\Delta\theta_j$ and $\Delta\theta_k$, the contact region includes contact between the arcs, adjacent to the pressure arc, on the blade firtree and the pressure line on the disc firtree. This shift in contact region can be explained with the help of Figure 4.13. Contact pressures along the pressure surface for the same three designs used in Figure 4.12 are shown here. The shift in contact region is clearly seen as the pressure angle moves from left to right in the figure. The peak contact pressure observed near the bottom end of the pressure line for the design with variation in pressure angle $\Delta\theta_j$, is due to the contact between the arc adjacent to the pressure arc on the blade firtree and the pressure line on the disc firtree, whereas the peak contact pressure near the top end of the pressure line for the design with variation in pressure angle $\Delta\theta_k$ is due to the contact between the arc adjacent to pressure line on the disc firtree and the pressure arc on the blade firtree. Such peak stresses near the edges of contact regions can nucleate cracks, hence reducing the service life of the joint.

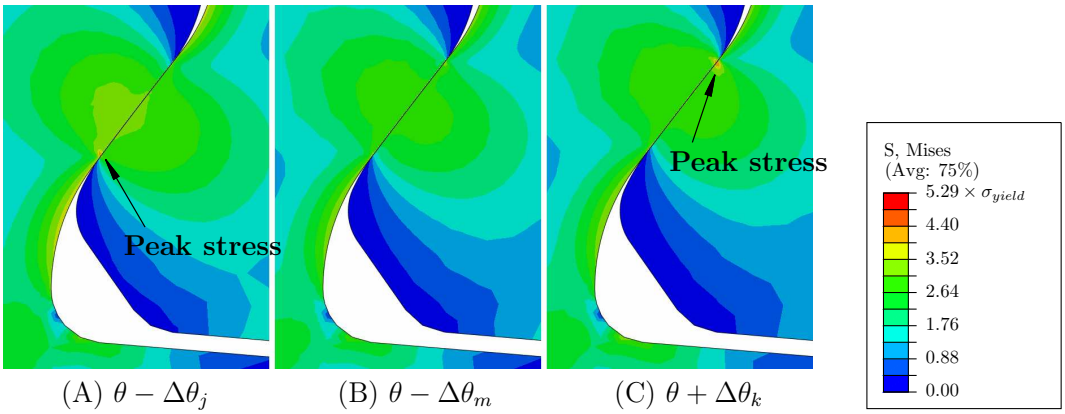

(A) $\theta - \Delta\theta_j$ (B) $\theta - \Delta\theta_m$ (C) $\theta + \Delta\theta_k$

FIGURE 4.12: Effect on von Mises stress near pressure line due to change in pressure angle θ

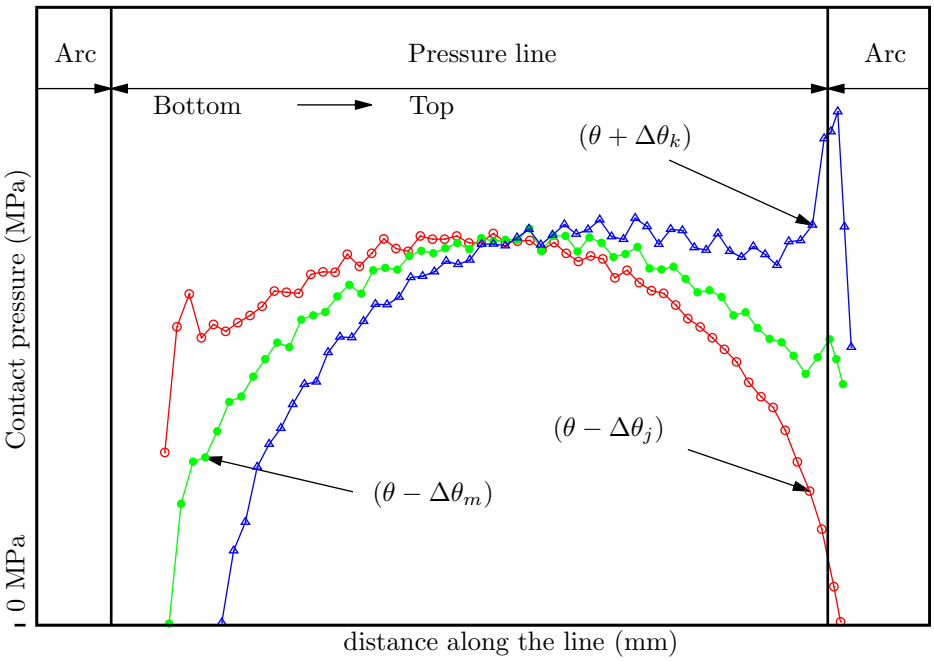

FIGURE 4.13: Shift in contact region across pressure line

4.5.3 Different angles on pressure lines at top, middle and bottom flanks

In this section, the variation in maximum principal stress in the notch regions due to the variation in pressure angles at top, middle, and bottom flanks of a firtree joint is evaluated. The histogram shown in Figure 2.16b is used for the variation in pressure angles which includes 540 angles obtained from 5 firtree slots scanned on 9 discs at their front and rear edges. The 2D parametrised geometry created using Siemens NX Open C API requires values for three parameters as an input $(\theta_1, \theta_2, \theta_3)$. Each parameter represents the angle of two pressure lines at the same distance from the centre of axis of disc rotation. Hence, the angles for pressure lines 1 & 4, 2 & 5, and 3 & 6 are θ_1, θ_2, and θ_3 respectively.

Figure 4.14 shows the variation in pressure angles and maximum principal stresses for three different flanks. For the purpose of comparison, all histograms for angles and stresses are plotted with the same limits on the x and y axes respectively. The magnitude of $P1_{datum}$ is selected such that, the stresses for all the designs analysed in this thesis lie within the range $[P1_{datum}, 1.174 \times P1_{datum}]$. The magnitude of $P1_{nominal}$ in Figures 4.14b, 4.14d, and 4.14f is taken from the stress distribution on the nominal firtree geometry. The mean for the variation in pressure angles for top, middle, and bottom flanks are shifted by -0.09%, -0.07%, and 0.04%, whereas the standard deviations are 0.18%, 0.2%, and 0.21% of the nominal pressure angle, Table 4.2. Although the mean for the pressure angle at the bottom flank is closer to nominal, its standard

deviation is more than the other two flanks. Since the bottom flank is the closest to the axis of rotation, the magnitude of stresses will also be higher compared to the other flanks. This can be seen from Figures 4.14b, 4.14d, and 4.14f which show the variation in maximum principal stresses at the three different flanks. The means of variation in maximum principal stress at top, middle, and bottom flanks are found to be 1.035, 1.043, and 1.141 $\times$ $P1_{datum}$ respectively. Hence, the mean of variation in maximum principal stress in the bottom flank exceeds the values at the top and middle flank. The

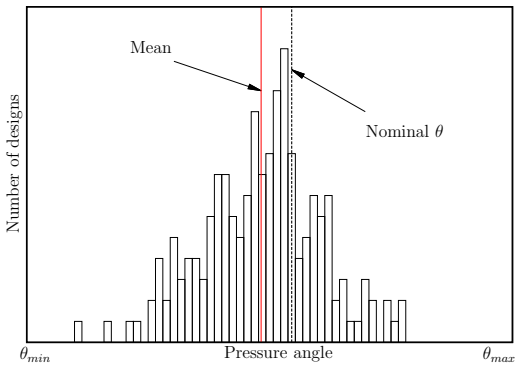

(A) Angle variation for pressure lines 1 and 4 at top flank

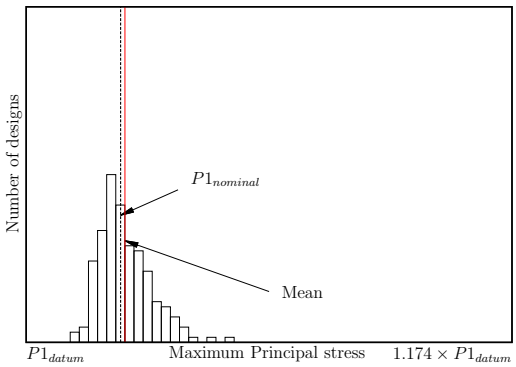

(B) Max. Princ. Stress variation for notches 1 and 4 at top flank

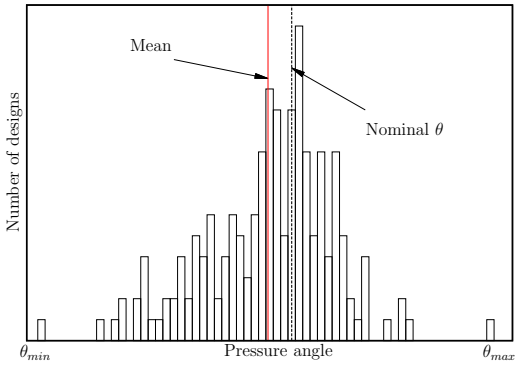

(C) Angle variation for pressure lines 2 and 5 at middle flank

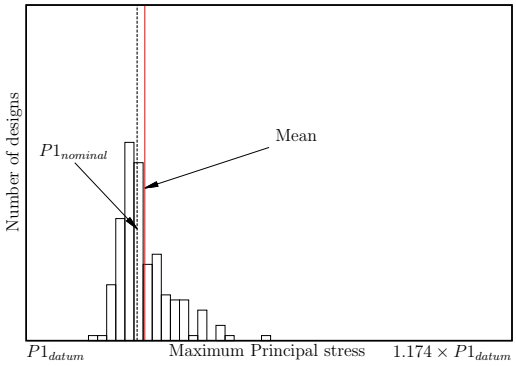

(D) Max. Princ. Stress variation for notches 2 and 5 at middle flank

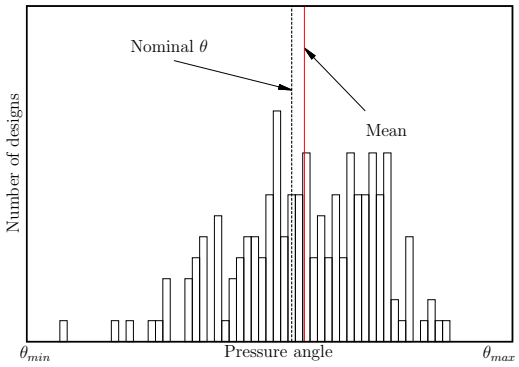

(E) Angle variation for pressure lines 3 and 6 at bottom flank

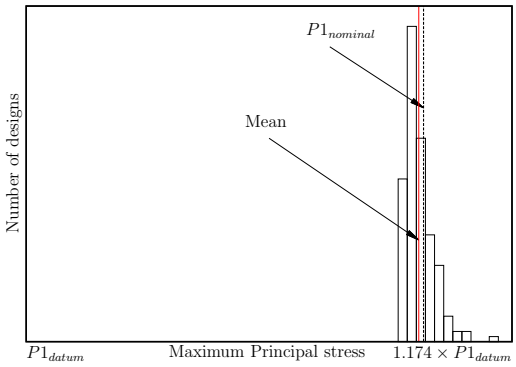

(F) Max. Princ. Stress variation for notches 3 and 6 at bottom flank

FIGURE 4.14: Variation in pressure angles and maximum principal stresses

Flank	Pressure Angle		Maximum Principal stress	
	Mean Shift by % of θ	Std. deviation % of θ	Mean $\times P1_{datum}$	Std. deviation % of $P1_{datum}$
Top	-0.09	0.18	1.035	0.94
Middle	-0.07	0.20	1.043	0.96
Bottom	0.04	0.21	1.141	0.51

TABLE 4.2: Mean and standard deviation for variation in pressure angle and maximum principal stress when same angles are used on the left and right side of the firtree geometry

standard deviation of these stresses for bottom flank is 0.51% which is less than the top and middle flanks with 0.96% and 0.94% of $P1_{min}$ respectively, Table 4.2. Hence, it can be said that although the standard deviation for the bottom flank is less compared to other flanks, the magnitudes of stresses are higher. Designing firtree joints with different pressure angles for the three flanks may result in less variation in the magnitudes of means for variation in maximum principal stress. From Table 4.2, if the mean and standard deviation of the variation in maximum principal stress, for the bottom flank and middle flank respectively, are minimised a design of the firtree joint, that is less sensitive to manufacturing variations, can be obtained.

4.5.4 Six independent pressure angles

The effect on the maximum principal stress is next extracted by varying all six angles simultaneously. The values for angles are selected such that each firtree model represents a scanned firtree joint on the disc either at its front or rear edge. Hence, there are 9 discs $\times$ 5 slots $\times$ 2 edges = 90 designs in total. The means in the variation of pressure angle for the two flanks at the top are shifted by -0.15% and -0.04% of the nominal pressure angle. However, the means for the variation in maximum principal stress in the notch regions at top and middle flanks are observed at 1.038, 1.030 and 1.042, 1.041 $\times P1_{datum}$ respectively, Table 4.3. Whereas, mean for the variation in maximum principal stress at bottom flanks on the left and right sides are at 1.138 and 1.142 $\times P1_{datum}$, Table 4.3. The means of stresses in top two flanks have similar magnitudes however, the mean for variation in the maximum principal stress at bottom flank is rather large. Hence, as in the previous section, it can be concluded that the bottom flank experiences higher stresses compared to the other flanks.

The standard deviations for the variations in the maximum principal stress in the notch regions on the left of the firtree geometry are 0.85%, 0.94%, and 0.86% of $P1_{datum}$ at top, middle and bottom respectively, Figures 4.15b, 4.15d, and 4.15f. While the standard deviations are 0.97%, 1.16%, and 1.09% of $P1_{datum}$ on the right side of the

firtree geometry, Figures 4.16b, 4.16d, and 4.16f. Even though the standard deviations of the variations in pressure angle for the respective flanks are in similar range, Table 4.3, it is observed that the variation in the maximum principal stress for the notch region of the middle flank is more widely spread as compared to the other two flanks. The same trend in the mean and standard deviation of the variation in maximum principal stress is observed as in the previous section. It is seen that the bottom flank is more severely

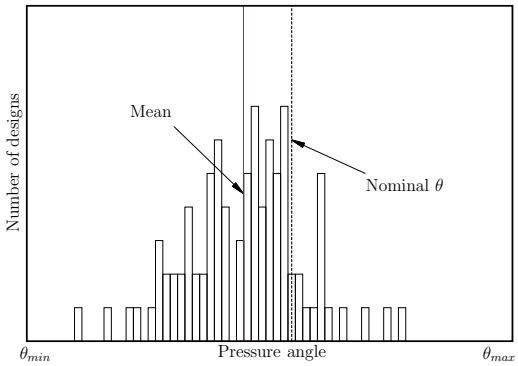

(A) Angle variation for pressure lines 1 at top flank

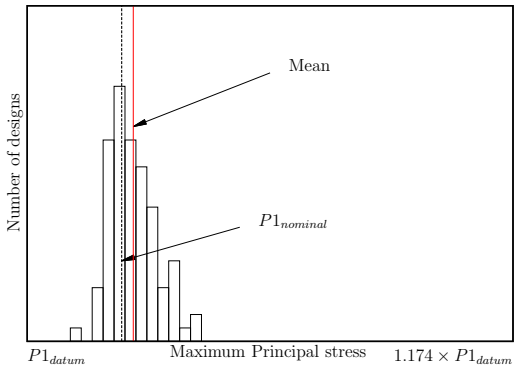

(B) Max. Princ. Stress variation for notches 1 at top flank

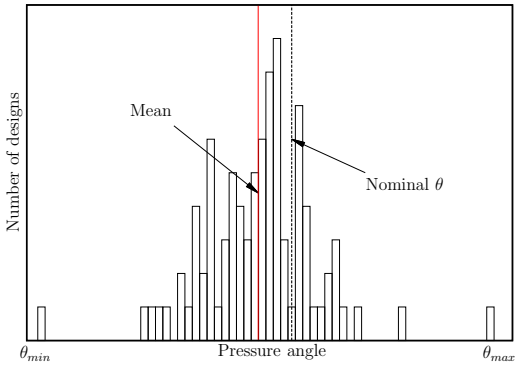

(C) Angle variation for pressure lines 2 at middle flank

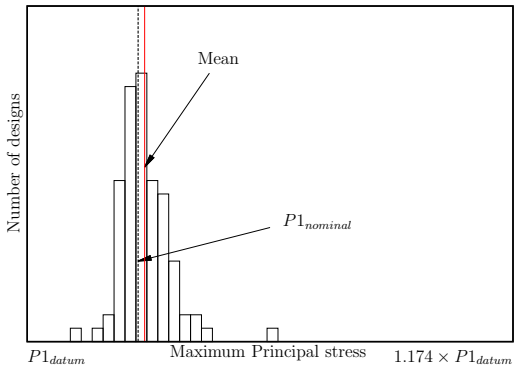

(D) Max. Princ. Stress variation for notches 2 at middle flank

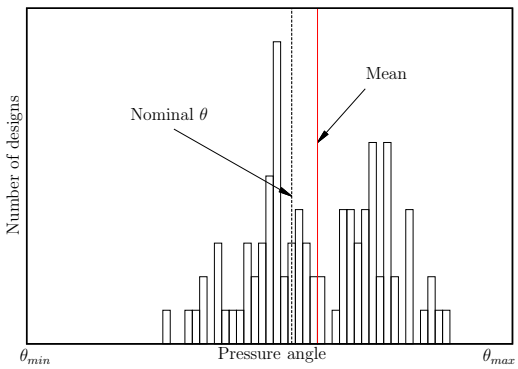

(E) Angle variation for pressure lines 3 at bottom flank

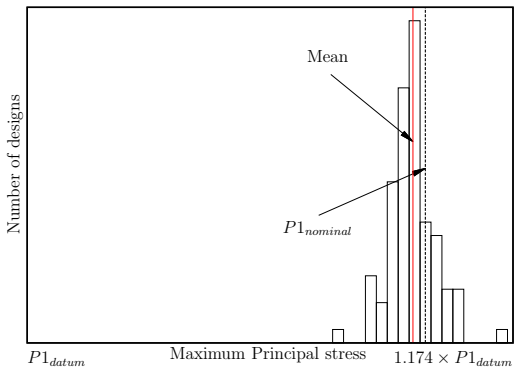

(F) Max. Princ. Stress variation for notches 3 at bottom flank

FIGURE 4.15: Variation in pressure angles and maximum principal stresses on left of firtree

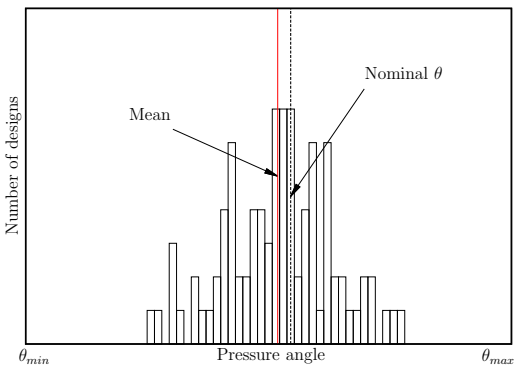

(A) Angle variation for pressure lines 4

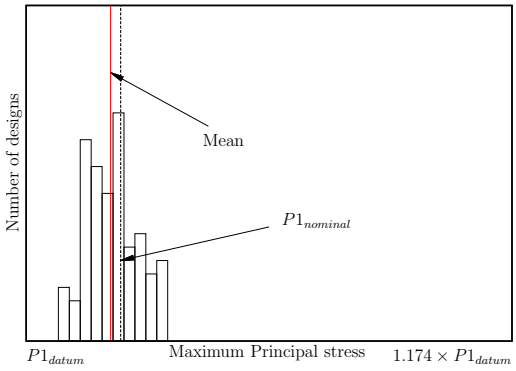

(B) Max. Princ. Stress variation for notches 4

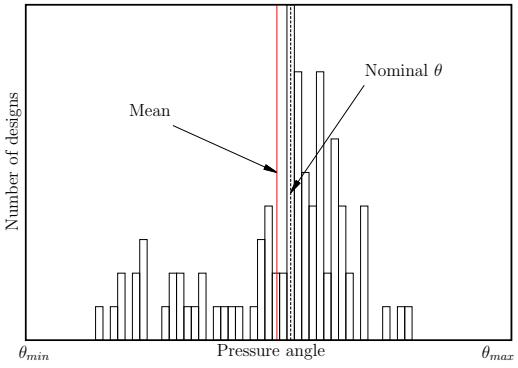

(C) Angle variation for pressure lines 5

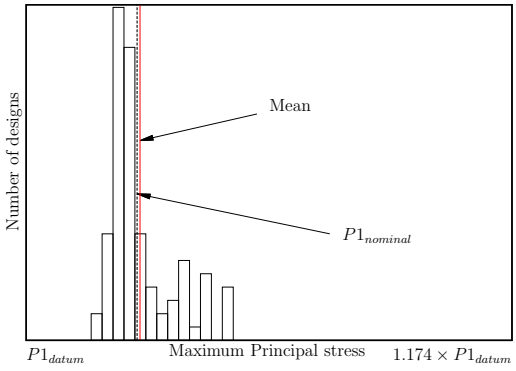

(D) Max. Princ. Stress variation for notches 5

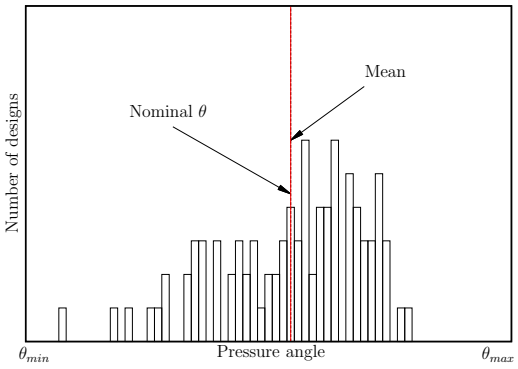

(E) Angle variation for pressure lines 6

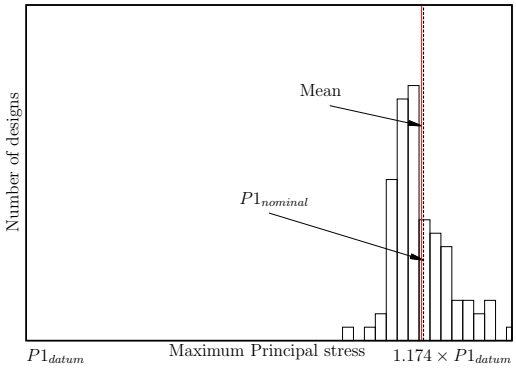

(F) Max. Princ. Stress variation for notches 6

FIGURE 4.16: Variation in pressure angles and maximum principal stresses on right of firtree

stressed as was observed by Vale et al. [138]. Whereas, different pressure faces contacting at different load increments have a relatively more profound effect on the variation in maximum principal stress for the middle flank. These problems could be reduced by having different pressure angles for different flanks, however, this might increase the cost of manufacturing these joints.

Side	Flank	Pressure Angle		Maximum Principal stress	
		Mean Shift by % of θ	Std. deviation % of θ	Mean $\times P1_{datum}$	Std. deviation % of $P1_{datum}$
Left	Top	−0.15	0.18	1.038	0.85
	Middle	−0.10	0.18	1.042	0.94
	Bottom	0.08	0.20	1.138	0.86
Right	Top	−0.04	0.16	1.030	0.97
	Middle	−0.04	0.21	1.041	1.16
	Bottom	0.00	0.22	1.142	1.09

TABLE 4.3: Mean and standard deviation for variation in pressure angle and maximum principal stress when all six angles are different

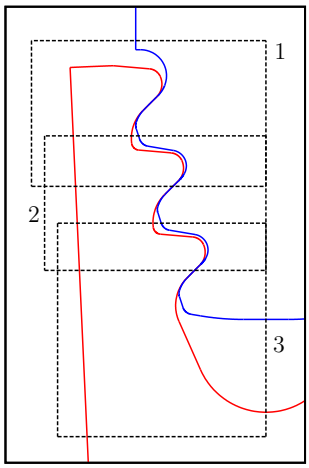

FIGURE 4.17: Reduced firtree FE models

4.5.5 Effect on stresses for reduced models

The contact algorithm has to perform several iterations in order to accurately find the contact locations in case of a multiple contact problem like the firtree joint. Satisfactory evaluation of contact conditions takes considerable computational effort especially when a fine mesh with multiple contact locations is involved. It is therefore worth checking if similar variation in the stress distribution for the full firtree FE model is obtained when reduced FE models, that require considerably less time to attain the contact convergence, are used representing each flank. In this section, the whole firtree FE model with six flanks is reduced to three independent FE models for the top, middle, and bottom flanks as shown in Figure 4.17. Stress analysis is performed under similar boundary conditions with the same material and contact properties. The loadings and the spring stiffnesses are adjusted so as to obtain similar maximum principal stresses in the notch

regions as compared to the nominal firtree geometry with six flanks. To extract the variation in the maximum principal stress in the notch regions, the histograms shown in Figures 4.14a, 4.14c, and 4.14e are used to vary the pressure angles. The magnitudes of stresses obtained in reduced models in the presence of geometric variations may not be comparable with the stresses in the whole firtree model. The objective here is to compare the variation in the stress distribution for the reduced FE models with the whole firtree.

Figures 4.18a, 4.18b, and 4.18c show the variation in maximum principal stresses in the notch regions of the reduced firtree FE models while Table 4.4 lists the mean and standard deviation of angles and stresses for the reduced models. Comparing these histograms with that in Figure 4.14, it can be said that the variation in maximum principal stress differs for the corresponding flanks of the whole firtree model. Although the shift of means of variation in stresses show similar trends at the top and bottom flanks, their standard deviations differ with those obtained from the whole firtree FE analyses, Tables 4.2 and 4.4. The standard deviations are considerably less when the firtree model with multiple contacts is used instead of the single contact models. Hence, it can be concluded that, having multiple contact surfaces, in the blade disc attachment,

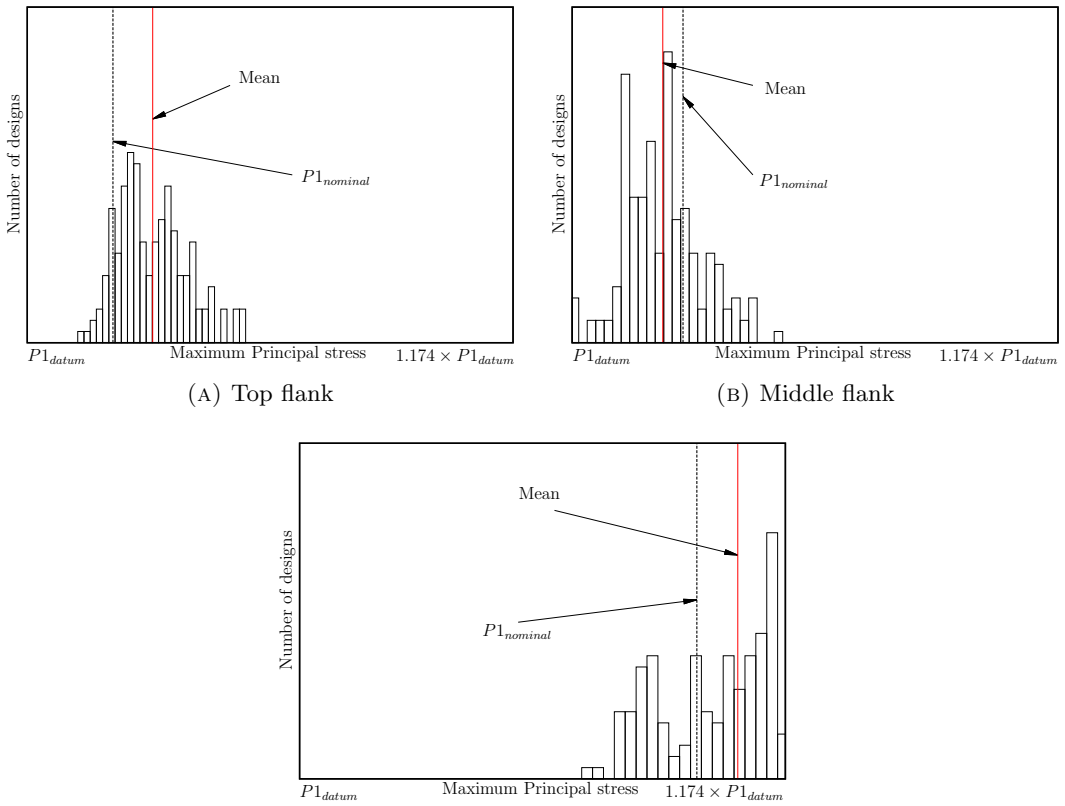

(A) Top flank

(B) Middle flank

(C) Bottom flank

FIGURE 4.18: Variation in maximum principal stresses in notch regions on reduced firtree models

Flank	Pressure Angle		Maximum Principal stress	
	Mean	Std. deviation	Mean	Std. deviation
	Shift by % of θ	% of θ	$\times P1_{datum}$	% of $P1_{datum}$
Top	-0.09	0.18	1.050	1.38
Middle	-0.07	0.20	-1.032	1.39
Bottom	0.04	0.21	1.057	2.40

TABLE 4.4: Mean and standard deviation for variation in pressure angle and maximum principal stress for reduced firtree FE models

reduces the effect of variation in pressure angles on the standard deviation of variation in the stress distribution.

4.5.6 Variation in surface profile

To represent the variation in the surface profile of the pressure faces on the disc firtree, data obtained after filtering noise from the raw scanned data by applying a Fourier transform in section 2.4.2 was modelled in the CAD environment using cubic B-splines. An elastic analysis performed on this model showed several locations on the pressure face where the stresses exceed the elastic limit of the material, Figure 4.19. The mean and standard deviation for variation in the notch stress are listed in Table 4.5. As can be seen the notch stress magnitudes are much higher as compared to those obtained when the pressure line was modelled as a straight line. The high peak stresses observed on the contact region may take the material into its plastic state resulting in permanent localised deformations. With the application of several cycles of loading, such permanent deformations may smoothen the pressure surface. Eventually the pressure surface profile on the disc firtree may follow the shape of pressure surface of the blade firtree resulting in contact between two conforming geometries. Although the resulting contact pressures for conforming geometries are less in magnitude than contact pressures between non

Flank	Maximum Principal stress			
	Left		Right	
	Mean	Std. deviation	Mean	Std. deviation
	$\times P1_{datum}$	% of $P1_{datum}$	$\times P1_{datum}$	% of $P1_{datum}$
Top	1.787	3.56	1.501	2.08
Middle	1.950	2.95	1.812	3.24
Bottom	1.483	3.17	1.623	2.72

TABLE 4.5: Mean and standard deviation for variation in pressure angle and maximum principal stress when pressure lines are modelled as B-splines

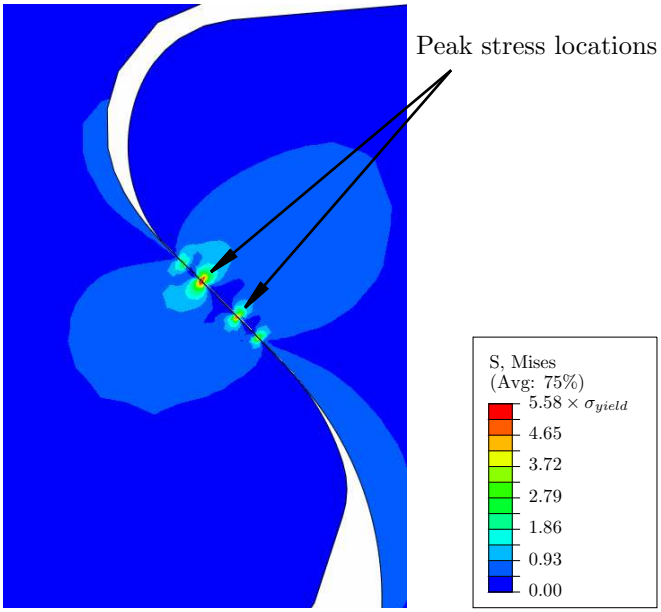

FIGURE 4.19: Von Mises stress near pressure line (the pressure line here represents the waviness as a result of manufacturing)

conforming geometries, the region in which the two bodies come in contact becomes more widely spread, for the same magnitude of load that is transferred through the contact.

4.6 Effect on stresses due to variation in three dimensional firtree geometry

In this section, stress analysis is performed on a parametrised three dimensional firtree joint by including the variation in part geometry due to the manufacturing processes. Creating a two dimensional firtree geometry to include the variation in geometric parameters and the line profile is relatively an easier task. It is more involved to create a three dimensional geometry which can represent the changes in the geometry. Accordingly, a more detailed discussion on geometry creation is essential for the three dimensional case.

4.6.1 Creating a 3D firtree model by including geometric variations

The change in geometry due to the manufacturing processes is first extracted from the CMM data in the form of variation in the pressure angles and non-smooth pressure surface. For a three dimensional firtree joint, the *extrude* feature available in most CAD packages can be used if there are no changes in the geometry along the direction of extrusion. The magnitudes of the pressure angles are obtained by fitting different

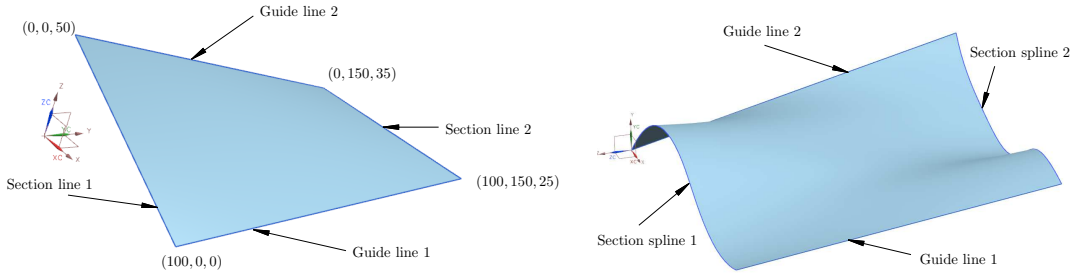

(A) Sweep surface between lines as section curves

(B) Sweep surface between splines as section curves

FIGURE 4.20: Sweep feature in Siemens NX

substitute geometries at front and rear edges of the three dimensional firtree joint. Hence, the extrusion function will not result in a geometry that can represent the change in the pressure angles at front and the rear edges of the firtree joint. Figure 4.20 shows two surfaces created in Siemens NX using a *sweep* feature which can be used for such purposes. It can be seen that both section lines 1 and 2 in Figure 4.20a are in planes parallel to the $x - z$ plane, separated by 150 units. However, the angle these two lines make with the z-axis is different. With the help of the guide lines 1 and 2 Siemens NX creates a *freeform sweep* feature passing through section lines 1 and 2 [139]. Similarly, a sweep surface is created using splines 1 and 2 as the section curves and straight lines as guide curves, Figure 4.20b. This *sweep* feature is used here to create the pressure surfaces on the three dimensional firtree joint using the following steps:

1. Two dimensional parametrised firtree geometries, separated by the thickness of the turbine disc at its rim, are created which can include the variation either in the geometric parameters such as pressure angles, notch radii, etc. or the rough surface profile as a B-spline.

2. Since the number of geometric entities such as lines and arcs is same on both 2D firtree geometries at front and rear, the end points of the corresponding entities are connected by straight lines. These lines are used as guide lines in performing the *sweep* feature on the two 2D firtree sections as shown in Figure 4.21a.

3. Once all the surfaces are created, the solid body of the firtree slot is created using the *sew* feature in Siemens NX, Figure 4.21b.

4. This body is then subtracted from turbine disc sector at its rim as shown in Figure 4.21c which results in the disc side of the 3D firtree geometry, Figure 4.21d.

5. In this work the blade side of the firtree geometry is kept nominal which is created using the *extrude* feature in Siemens NX.

The CMM is used to scan the disc side firtree joint at its front and rear edges. Accordingly, the pressure angles obtained after fitting a substitute geometry are available

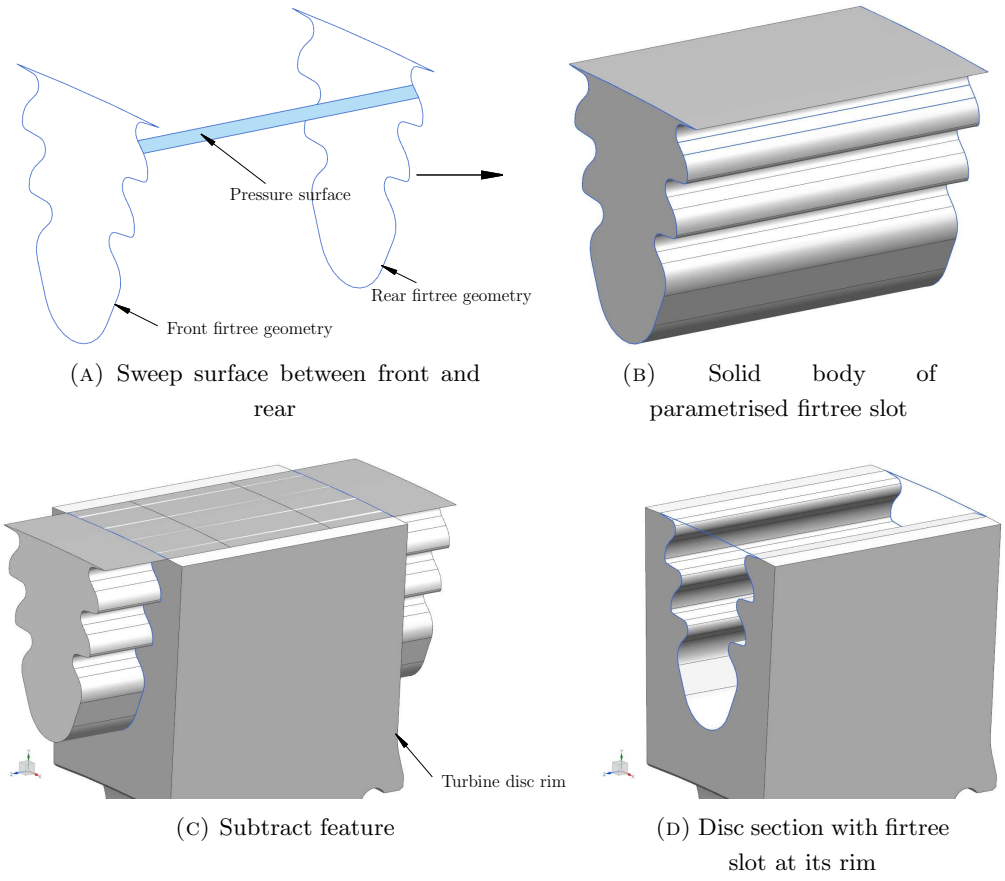

(A) Sweep surface between front and rear

(B) Solid body of parametrised firtree slot

(C) Subtract feature

(D) Disc section with firtree slot at its rim

FIGURE 4.21: Steps in creating parametrised three-dimensional firtree model in CAD

on these two edges. If the firtree joint were scanned at multiple sections from the front edge, variation in geometric parameters such as the pressure angles or notch radii could be included in the 3D analysis by creating multiple 2D firtree geometries as shown in Figure 4.22. However, such data is not available here.

4.6.2 Variation in pressure angle at front and rear edges

To begin with, the three dimensional firtree geometry is created, as discussed in the previous section, by including the variation in the pressure angles at the front and rear edges of the firtree joint. Variation in pressure angles extracted by fitting substitute geometries on CMM data for 45 disc side firtree joints is used to extract the variations in the maximum principal stress at six notch regions. Due to the smooth change in the pressure angle from the front to its rear edge of the firtree joint on all six pressure faces, the centrifugal force may be distributed unevenly along the thickness on the six flanks. Moreover, due to the existence of a twist in the pressure face along the thickness of the disc at its rim, the initial contact may not cover the whole thickness as is observed for the nominal firtree joint, Figure 4.9. Figures 4.23a and 4.23b show the initial locations of active contact regions on all the six pressure faces on the 3D firtree model at the

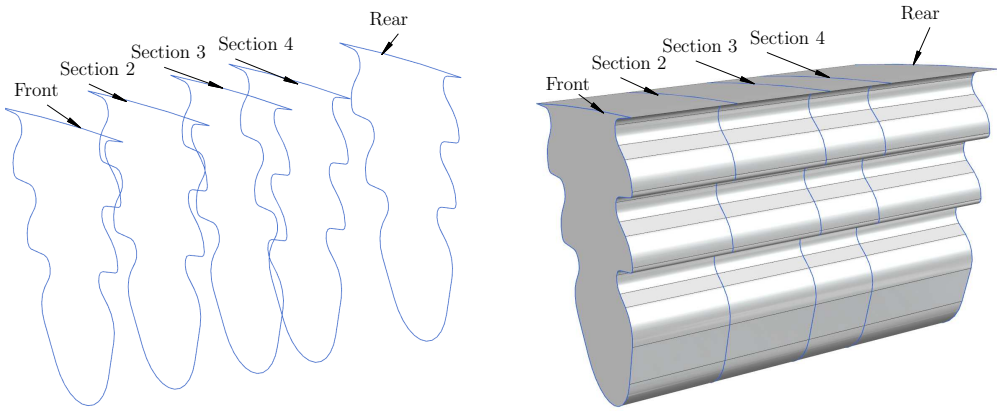

(A) 2D firtree geometries at multiple sections

(B) 3D firtree solid body created using multiple sections

FIGURE 4.22: Construction of 3D firtree slot using multiple sections

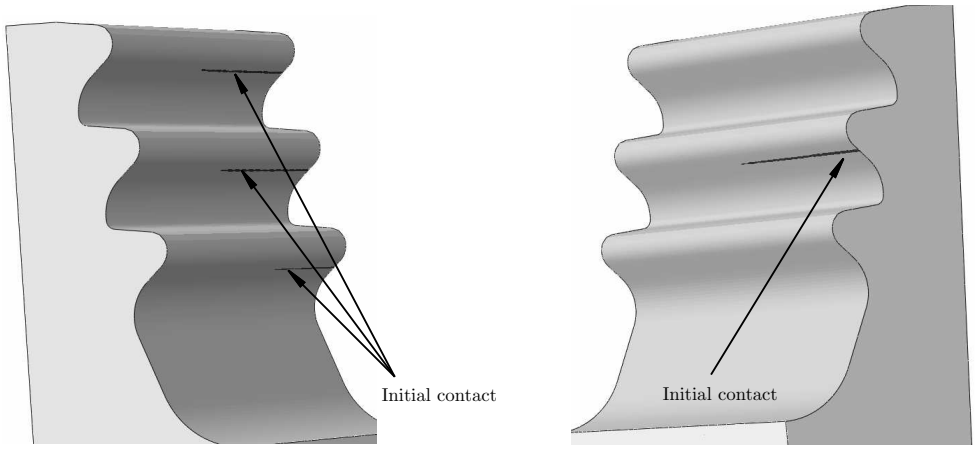

(A) Pressure faces on left side

(B) Pressure faces on right side

FIGURE 4.23: Uneven initial contact at same load increment

same load increment when variation in pressure angles at the front and rear sections is included. It can be seen that the top and bottom flank on the right edge of the firtree joint do not share any centrifugal load, whereas only the regions on the pressure faces near the rear edge on the left side of the firtree geometry contribute in sharing the centrifugal load. This uneven distribution of contact pressures, may induce high magnitude stresses in some regions of the joint. Figures 4.24 and 4.25 show the variation in maximum principal stress in the notch regions, on the left and right side of the firtree joint respectively, due to the variation in pressure angles at front and rear edges. The variation in the pressure angles is plotted using different histograms for the front and rear edges on the firtree joint. The scale on the x-axis for the histograms showing variation in maximum principal stress go from $1.02 \times P1_{datum}$ to $1.42 \times P1_{datum}$. For the purpose of comparing the variation extracted from 2D and 3D stress analyses, the value for $P1_{datum}$ is kept same as in Figure 4.16. The magnitudes of $P1_{nominal}$ shown in the

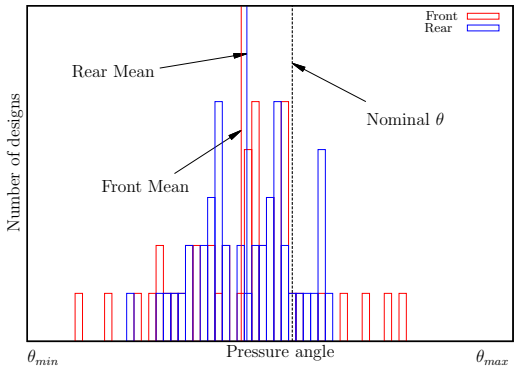

(A) Angle variation for pressure line 1 at top flank

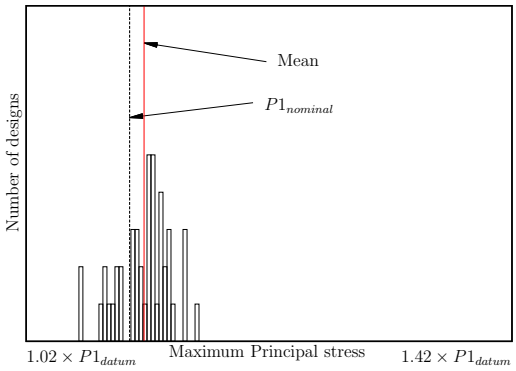

(B) Max. Princ. Stress variation for notch 1 at top flank

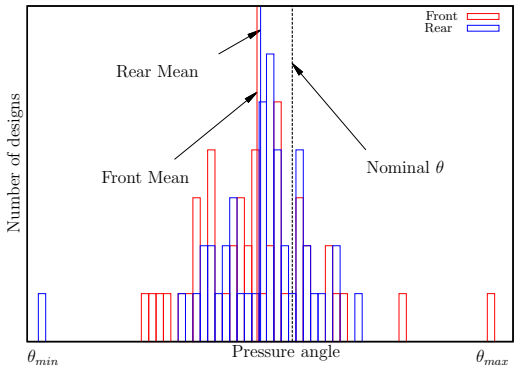

(C) Angle variation for pressure line 2 at middle flank

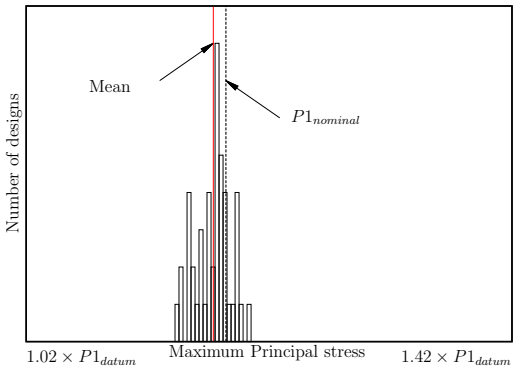

(D) Max. Princ. Stress variation for notch 2 at middle flank

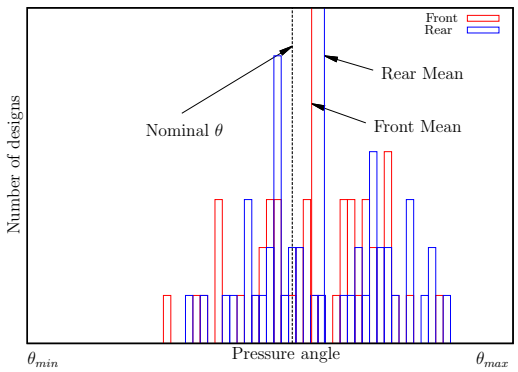

(E) Angle variation for pressure line 3 at bottom flank

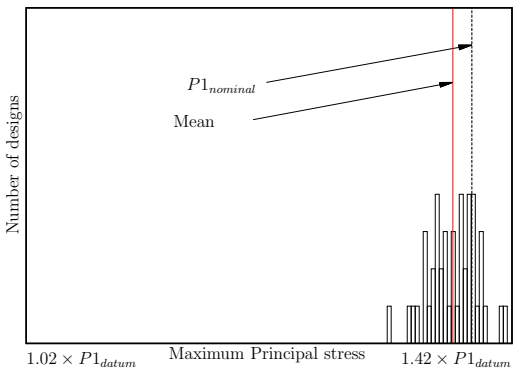

(F) Max. Princ. Stress variation for notch 3 at bottom flank

FIGURE 4.24: Variation in pressure angles and maximum principal stresses in notch regions on the left side of firtree joint

stress histograms are extracted from the stress distribution for respective flanks of the nominal 3D firtree joint. It can be seen that stress analysis on the 3D firtree joint results in higher magnitude stresses as compared to the 2D analysis. Table 4.6 lists the means and standard deviations for the variation in the pressure angle included in this analysis while that of maximum principal stress is listed in Table 4.7. Table 4.7 also show the correlation coefficients between the pressure angles at the front and rear edges of the

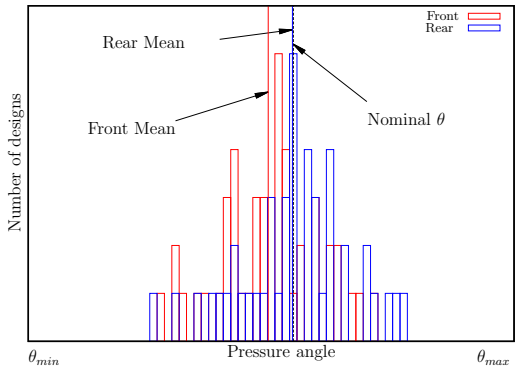

(A) Angle variation for pressure line 4

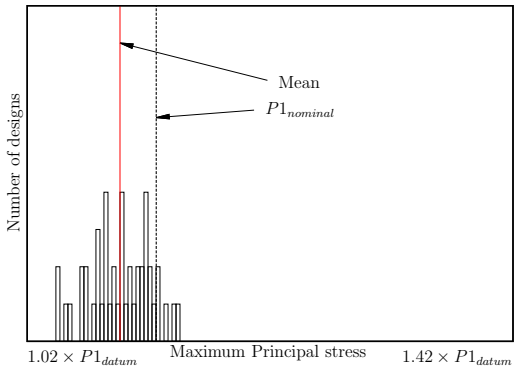

(B) Max. Princ. Stress variation for notch 4

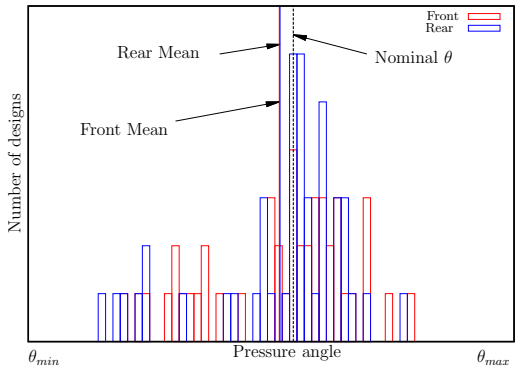

(C) Angle variation for pressure line 5

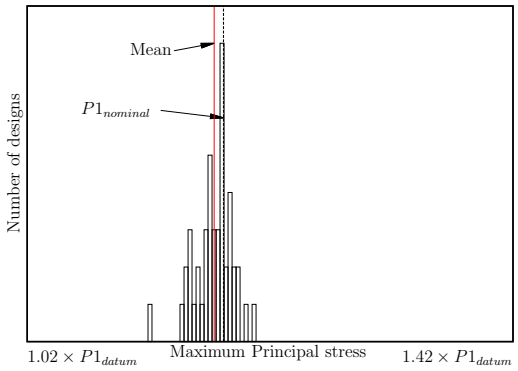

(D) Max. Princ. Stress variation for notch 5

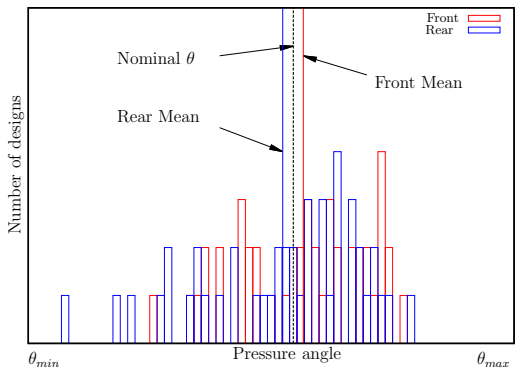

(E) Angle variation for pressure line 6

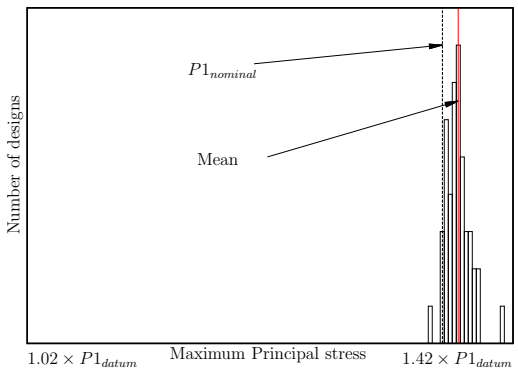

(F) Max. Princ. Stress variation for notch 6

FIGURE 4.25: Variation in pressure angles and maximum principal stresses in notch regions on the right side of firtree joint

firtree joint. The standard deviations for the variation in maximum principal stress in the notch regions for both top flanks (left and right) are higher than the other flanks, Table 4.7. The corresponding correlation coefficients between front and rear pressure angles are 0.28 and 0.20 which are much lower than the coefficients on other flanks. Hence, it can be said that there is larger variation between the pressure angles at the front and rear top flanks which results in larger standard deviations for the maximum

Side	Flank	Pressure Angle			
		Front		Rear	
		Mean Shift by % of θ	Std. deviation % of θ	Mean Shift by % of θ	Std. deviation % of θ
Left	Top	−0.15	0.20	−0.14	0.15
	Middle	−0.11	0.20	−0.10	0.16
	Bottom	0.06	0.19	0.10	0.21
Right	Top	−0.08	0.15	0.00	0.17
	Middle	−0.04	0.22	−0.04	0.21
	Bottom	0.03	0.20	−0.03	0.24

TABLE 4.6: Mean and standard deviation for variation in pressure angle at front and rear of the 3D firtree joint

Side	Flank	Correlation coefficient between front and rear pressure angles r_{FR}	Maximum Principal stress	
			Mean $\times P1_{datum}$	Std. deviation % of $P1_{datum}$
Left	Top	0.28	1.118	2.18
	Middle	0.23	1.174	1.43
	Bottom	0.53	1.369	2.00
Right	Top	0.20	1.097	2.50
	Middle	0.73	1.174	1.54
	Bottom	0.71	1.373	1.02

TABLE 4.7: Mean and standard deviation for variation in maximum principal stress in notch regions of the 3D firtree joint

principal stress in the corresponding notch regions. The standard deviations for the stresses in the bottom flank are relatively less on the left and right sides: 2.00 and 1.02 % of $P1_{datum}$, which also have a larger correlation coefficients: 0.53 and 0.71. Hence, it can be concluded that the standard deviation for variation in the maximum principal stress in the notch regions at the bottom flank tends to decrease as the correlation coefficient between the pressure angles at front and rear edges increase. The correlation coefficient for the left middle flank is less (0.23) while, it takes the maximum value (0.73) on the right side, however their standard deviation in stresses are in a similar range: 1.43 and 1.54 % of $P1_{datum}$.

The 2D analysis showed similar trend in the magnitudes of maximum principal stresses on the three flanks of the firtree joint as seen with the 3D analysis results. The bottom

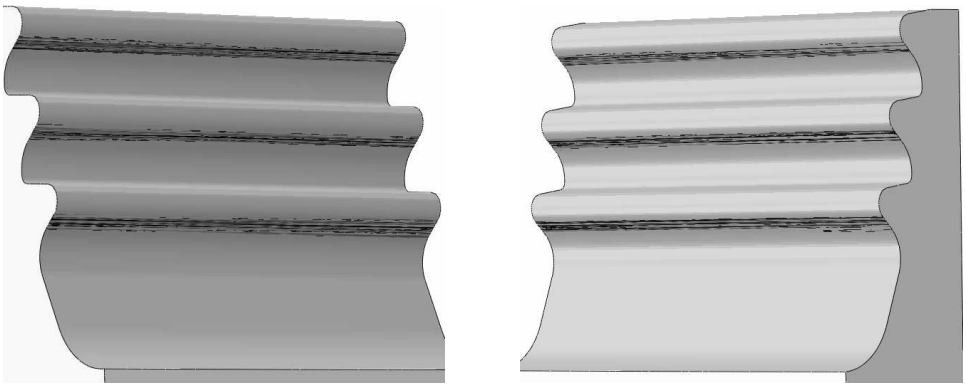

(A) Pressure faces on left side (B) Pressure faces on right side

FIGURE 4.26: Non uniform contact pressures on pressure faces

flank experiences higher stresses compared to the top and middle flanks, with least for the top flank. The 2D analysis cannot, however, reflect the effect of variation in pressure angles at the front and rear edges of the firtree joint on the stress distribution.

4.6.3 Variation in surface profile

Next, the scanned data available after filtering noise using the Fourier transform is included in the geometry by fitting B-splines instead of straight lines at the front and rear edges of the firtree joint. These non-straight edges are again used to create a pressure face using the *sweep* feature in Siemens NX. Figure 4.26 shows the contact locations on six pressure faces of a firtree joint, when they are modelled using *swept* surfaces with cubic splines representing the rough surface profile at the front and rear edges. The CMM is used to scan the firtree slot only at its front and rear edges due to the limitations of placing the CMM probe on the interior of the firtree slot. Hence, no information regarding the surface profile is available away from the firtree slot's edges. It can be seen that the contact pressures are distributed according to the distribution of the asperities on the pressure faces. Since the pressure face is created by sweeping the front edge to the rear edge, the asperities on the surface run along the thickness of the firtree joint. However, high magnitudes of contact pressures are observed resulting in stresses beyond the elastic limit of material in the close vicinity of pressure faces. The stress magnitudes in the notch regions are listed in Table 4.8 which are much higher than previous case. Including an elastic-plastic material and running the stress analysis for several cycles will smoothen the rough surface and a more even distribution of contact pressures may be observed.

4.6.4 Pressure faces as rough surfaces

The *sweep* feature used to create a surface between two edges which can have smooth or rough surface profile needs connecting lines between the edges as their guide lines. Instead of using straight lines as guide lines, surface profiles in the direction of the thickness of the disc can be modelled as splines to serve as guides. However, the designer does not have any control over the surface roughness on the pressure face away from its edges. One way to include this roughness is to edit the nodal coordinates on the pressure faces of an FE model. The numerically generated rough surface in chapter 3 can be used to evaluate the surface heights at predefined locations by providing the same number of points, as the number of nodes on the pressure face, to any of the two methods. Once the surface heights are available, the nodal coordinates for an FE model of a nominal firtree joint can be modified in ABAQUS to represent the rough surface in both orthogonal directions. However, due to the existence of a non-smooth pressure face, the contact algorithm in ABAQUS takes longer to attain convergence.

An elastic stress analysis is performed on one such 3D firtree joint, which has pressure faces with rough profiles on both its orthogonal directions. The surface heights were obtained by using Patir's method with $N \times M = 61 \times 53$ and the exponential ACF shown in Figure 3.19. The value of correlation length in the direction of the thickness of firtree joint is much higher as compared to its value in the orthogonal direction. The mesh that was used while performing this study consisted of same number of nodes on the pressure face as the number of surface heights generated from Patir's method, Figure 4.27. Figure 4.28 shows the contact regions on the six pressure faces at the end of the analysis. It can be seen that the contact pressures are distributed randomly along the pressure faces. An elastic analysis of such model, with contacts between six rough surfaces, results in very high stress magnitudes in the notch regions. It is observed that

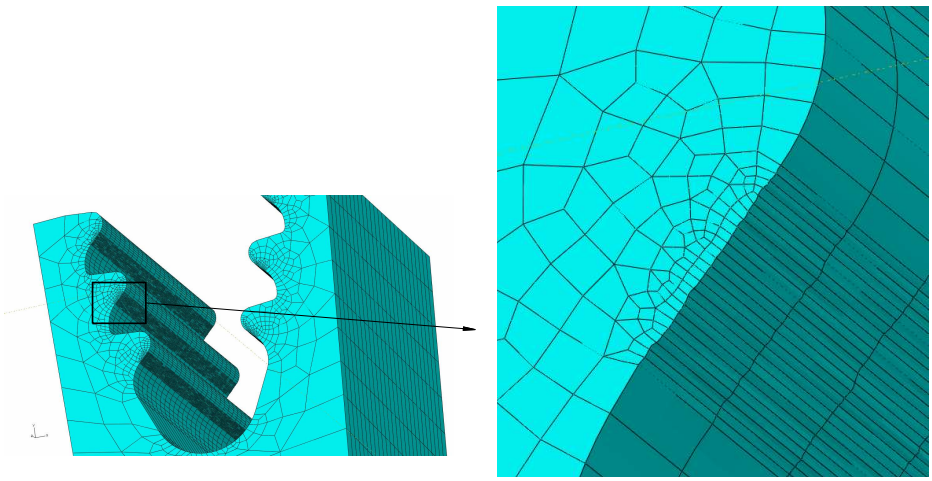

(A) Typical mesh (B) Magnified view of mesh on pressure face with waviness

FIGURE 4.27: Mesh generated by Abaqus

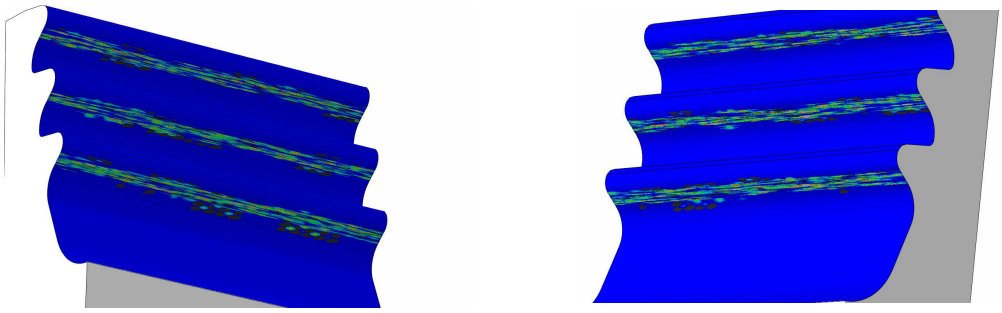

(A) Pressure faces on left side (B) Pressure faces on right side

FIGURE 4.28: Non uniform contact pressures on rough pressure faces

Side	Flank	Maximum principal stress in firtree joint		
		with smooth pressure faces using sweep feature $\times P1_{datum}$	with rough pressure faces using sweep feature $\times P1_{datum}$	with rough pressure faces modifying nodal coordinates $\times P1_{datum}$
Left	Top	1.110	1.446	1.682
	Middle	1.184	1.182	1.708
	Bottom	1.385	1.319	1.633
Right	Top	1.127	1.401	1.571
	Middle	1.182	1.495	1.596
	Bottom	1.360	1.587	1.855

TABLE 4.8: Notch stresses for firtree joints with smooth and rough surface profiles at front and rear edges

the maximum principal stress in the notch regions is affected when the roughness of the pressure faces is included. In order to accurately extract the stress distribution, an elastic-plastic material should be used with a much finer mesh on the pressure faces. However, this may increase the computational time considerably.

Table 4.8 compares the maximum principal stresses observed in the notch regions for all six flanks between the firtree joint with smooth and rough surface profiles (created using the sweep feature or by modifying nodal coordinates) at the front and rear edges. For the purpose of comparison, the magnitude of $P1_{datum}$ is used as in Figure 4.16. It can be seen that the maximum principal stresses are affected considerably when rough surfaces are used instead of smooth surfaces. Since the disc and blade materials are assumed to be elastic while performing the stress analysis, the magnitudes of stresses may not be accurate. Use of an elastic-plastic material, may not intensify the stresses to

these extents, since after several cycles of loading the contact region along the pressure faces will smoothen due to permanent localised deformations.

4.7 Summary

An elastic two- and three- dimensional finite element analysis is performed on the firtree joint to investigate the effect of geometric variation due to the manufacturing processes on the stress distribution. Two methods are used to represent the variation in geometry due to manufacturing. In the first method, the variation in pressure angle θ is used as the parameter to create the manufactured firtree geometry. It is observed that a small decrease in the pressure angle may result in a less sensitive design to the manufacturing variations with respect to the maximum von Mises stress observed near the contact region. Even a small increase in pressure angle by 0.3% can intensify the maximum von Mises stress near contact region by 28% whereas the increase in maximum principal stress is relatively less: 1%. The mean for variation in maximum principal stress in the notch regions for different flanks showed similar trend in 2D and 3D stress analyses. It is observed that the bottom flank attracts higher magnitude stresses as compared to the other flanks. The 2D analyses showed that the standard deviation for the variation in the maximum principal stress in the notch region for the middle flank is higher than for the other two flanks. Although, the 2D analysis resulted in useful information regarding variation in the stress distribution, it cannot highlight the effect of change in geometric parameters between the front and rear edges of the firtree joint. This can be directly observed in case of the 3D analysis, which showed that lower correlation coefficients of pressure angles between front and rear edges affected the stress distribution in the notch regions more severely. Whereas, when the correlation coefficients are higher, the standard deviation in the variation of maximum principal stress tends to decrease.

In the second study, the variation in pressure surface profile is modelled by filtering the noise using a Fourier transform. For both 2D and 3D analysis, the stress distribution for this model showed several locations on the pressure face where stresses higher than the elastic limit of the material are observed. This may result in localised permanent deformations and eventually smoothening of the surface profile. This smoothening of the surface may reduce the intensity of contact pressures across the pressure face and hence the high maximum principal stresses in the notch regions. The roughness of the pressure face is included in the 3D elastic analysis by editing the nodal coordinates on the face to represent the surface roughness evaluated by Patir's method in chapter 3. The contact pressures are distributed randomly on the pressure face as expected. The magnitudes of these contact pressures are higher than that observed in the stress analysis for firtree geometry with smooth pressure faces. These high contact pressures induce peak stresses in the notch regions which are $\approx 9\%$ higher than the yield strength of the material. In order to accurately evaluate the stress distribution in the notch regions for

rough pressure faces, it is essential to include an elastic-plastic material model in the stress analysis. This lies beyond the scope of the current thesis.

Chapter 5

Robust design of firtree joints in the presence of manufacturing uncertainties

5.1 Introduction

Different ways of representing realistic manufacturing variations in geometry while performing the stress analysis on firtree joints were explored in the previous chapter and the effect these variations have on the stress distribution in the firtree region was extracted. The variation in the pressure angle causes a shift in the contact region away from the pressure faces, resulting in variations in the tensile stress in the notch regions. The magnitudes of these notch stresses in the bottom flank are observed to be higher than those in the top and middle flanks. It is essential to incorporate such inherent uncertainties in the design process to minimise the variation in the performance of a component. The main objective of this chapter is to design a firtree joint, in the presence of manufacturing variations, by minimising the notch tensile stresses using a suitable optimisation method.

A firtree joint's main objective is to transfer the centrifugal load from the high pressure turbine blade to the disc via multiple contacting surfaces while holding the blades in precise locations along the rim of the turbine disc. Slight variation in the contact conditions for any or all blade disc joints may give rise to problems of mistuning between the blades, concentrated stresses in the regions in close vicinity to the pressure faces, etc. The critical regions, such as the notch regions and contact edges of the firtree joint experience stresses close to the yield stress of the material. Any positive variation in these resulting stresses during working conditions can take the material into its plastic state. The fluctuating type of loading that is observed in such rotating machines will induce repetitive stresses in these critical regions which may eventually result in low

or high cycle fatigue problems. One of the ways used to improve the firtree joint's resistance against crack initiation and to enhance its life further is by surface treatment methods such as shot-peening [140, 141]. Shot-peening induces residual compressive stresses on the surface layers in order to primarily delay crack initiation and also to retard the crack propagation process. Severe plastic deformation and work hardening along with the compressive stresses are induced onto the surface simultaneously [140]. A stream of small hard spherical shots are impinged on the treated surface which helps in improving its fatigue life [142]. Experiments performed by Hu and Wang [143], on a shot-peened firtree joint under low and high cycle fatigue loading showed improvements in the turbine firtree's life. The results showed an increase in the life of the shot-peened turbine attachment that is 5.23 times longer than that of an unpeened firtree joint.

A firtree joint makes use of multiple contacts between the corresponding surfaces of a blade and disc in performing its job. Multiple contacts increase the surface area hence helping in efficient cooling of the joint as temperatures in the region of 1600°C [2] can be observed in the high pressure turbine regions of an aero engine. The problem of evaluating contact conditions (contact pressures and areas) between two interacting surfaces is a nonlinear one that requires use of iterative algorithms. In mechanisms where more than one contact pair of surfaces are active simultaneously, the evaluation of contact conditions becomes even more challenging. Moreover, the interactions between multiple contacts will affect the stress distribution in the neighbourhood regions. It was seen in the previous chapter that the variation in the stress distribution in the notch regions of a firtree joint with six contact pairs cannot be predicted using a reduced single contact pair FE model with similar geometric, loading and boundary conditions. Different contacts get engaged at different load increments, resulting in the redistribution of stresses amongst different regions of the firtree joint. However, although having multiple contacts helps in reducing the standard deviation for variation in the resulting stresses it will be useful to check if this standard deviation can be further minimised in order to design a firtree joint with higher probability of achieving the expected life. As briefly discussed in chapter 1, reliability-based design optimisation (RBDO) and robust design (RD) are the two more popular methods that incorporate such system uncertainties. The goal here is to minimise the mean and standard deviation (statistical moments) for the variation in the firtree joint's performance in the form of maximum tensile stresses in the notch regions. Robust design principles are most suitable here and hence explored further in order to apply them to the firtree joints.

5.2 Robust design

Conventional design optimisation of engineering components involves evaluation of the effects of changes in the parameter values, defining the part geometry, have on the objective function under specified constraints. More specifically, in an aero engine, the

objective of a design optimisation can be to minimise the cost or the weight of the parts in the presence of constraints. From a structural point of view, the working stresses that a material may experience during its service life should be controlled so as to avoid any catastrophic damage to the structure. Designers make certain assumptions while modelling the in-service conditions in the analysis and design processes. These working conditions along with the manufacturing variations can be the source of many different uncertainties occurring in the system. Such uncertainties may result in variations in the life expectancy of the components which is a critical factor affecting the design of aero engines. Hence, it has become essential to include such uncertainties in the design process of aero engine components.

In particular, the geometric variations emerging as a result of the manufacturing processes are of relevance to this thesis. It is impossible to manufacture an engineering component with precisely the same geometric parameters as specified by the designers. Slight variations in the geometry due to these manufacturing processes are unavoidable. The deterministic design approach does not take into the account these variations or perturbations in the system and hence may result in a design with a degraded performance away from the nominal design. In the case of aero engine components, the parts are optimised for a reduction in weight which can often result in a solution on the boundaries of design constraints. Hence, a small perturbation in the system conditions may significantly affect the performance or violate the design constraints [16]. Such changes in the performance of the design may result in variability in the service life of the component. It is essential from the point of view of the quality of the product, to design it so that the service life of the component shows minimum variation. One of the commonly used methods for tackling such problems is to introduce a *factor of safety* for the constraints in the optimisation. For example, from a structural design point of view, a constraint on the design can be specified by restricting the maximum resultant stress in the part below the yield stress of the material, $\sigma_{max} \leq \sigma_{yield}$. This constraint can be rewritten as $F_s\sigma_{max} \leq \sigma_{yield}$, where F_s is the factor of safety whose magnitude can range from 1.2 to 3, [16]. The choice of the value of factor of safety depends on the specific material and the application for which it is used. It is evident that such a constraint will result in a more conservative design adding to the weight of the component. In aero engine applications where reducing weight is a primary objective, having a high factor of safety is not desirable [16].

5.2.1 Concept of robustness

Robust design is an approach that specifically deals with problems where a design is sought which is less sensitive to the variations in the system, without eliminating the source of variations. This approach of designing a component which performs consistently in the presence of uncertainties was first recognised by Taguchi [144]. He classified

the process of design optimisation into three stages: (i) in *systems design*, a feasible region is defined based on the fundamentals that govern the problem for finding the *optimum* design, (ii) *parameter design* searches for the values of the parameters for which the resulting objective function is optimum, and (iii) *tolerance design* which fine-tunes the optimal solution obtained in the parameter design stage [145, 146]. Of these, the stage of parameter design is of relevance to this thesis. The quality of the designed product depends on several factors, some of them are controllable and the others uncontrollable. In the robust parameter design approach, the controllable factors or variables are chosen such that the required quality is delivered even in the presence of the uncontrollable factors (also known as the noise variables [147]). Taguchi's approach has been used by many researchers to perform design optimisation in various fields [148, 146, 149, 150]. Unal et al. [146] applied Taguchi's method in a propulsion system design optimisation study for an advanced space transportation vehicle. It was reported that Taguchi's method helped in reducing the effort required for the conventional multiparameter full factorial design. Tsai [149] used the case of a steel soaking-pit/rolling-mill plant to demonstrate Taguchi's experiment design in simulation. The use of Taguchi's method reduced the number of experimental trials from 243 to 36 simulation runs for determining the best operating parameters. Khan and Al-Darrab [150] applied the signal-to-noise approach based on the Taguchi's method to determine the optimum levels for factors relating to mobile phone conversation during driving.

Taguchi's method makes use of orthogonal arrays, called the inner and outer arrays, to define the settings for the control and noise factors respectively [16]. At each setting for the control factors, or for each inner array, the effects of the noise variables on the system with these settings are evaluated. The variability in performance is measured by the "signal-to-noise" (SN) ratio for different categories of parameter design problems [16, 151]. Welch et al. [152] used the example of Very Large Scale Integrated (VLSI) circuit design to propose a new method in which the quality characteristics generated by both the control and the noise factors are combined into a single experiment design. It was observed that the number of runs required were reduced considerably as compared to Taguchi's inner-outer arrays model. Shoemaker et al. [153] also used a single experiment or a single array which represented both control and noise factors as proposed by Welch et al. [152]. The conventional approach of separate inner and outer arrays for control and noise variables estimated more control-to-noise factor interactions which are often of higher orders [153].

The concept of robust parameter design can be further explained with the help of Figure 5.1. The horizontal axis represents the change in design parameter x for which the design optimisation is performed and the vertical axis has the objective function $f(x)$ which represents the performance of the design. The variation in the performance for the two designs, due to uncertainty in x, with parameters x_1 and x_2 are shown using red while the variations in the parameters themselves are shown in blue. It is assumed that the

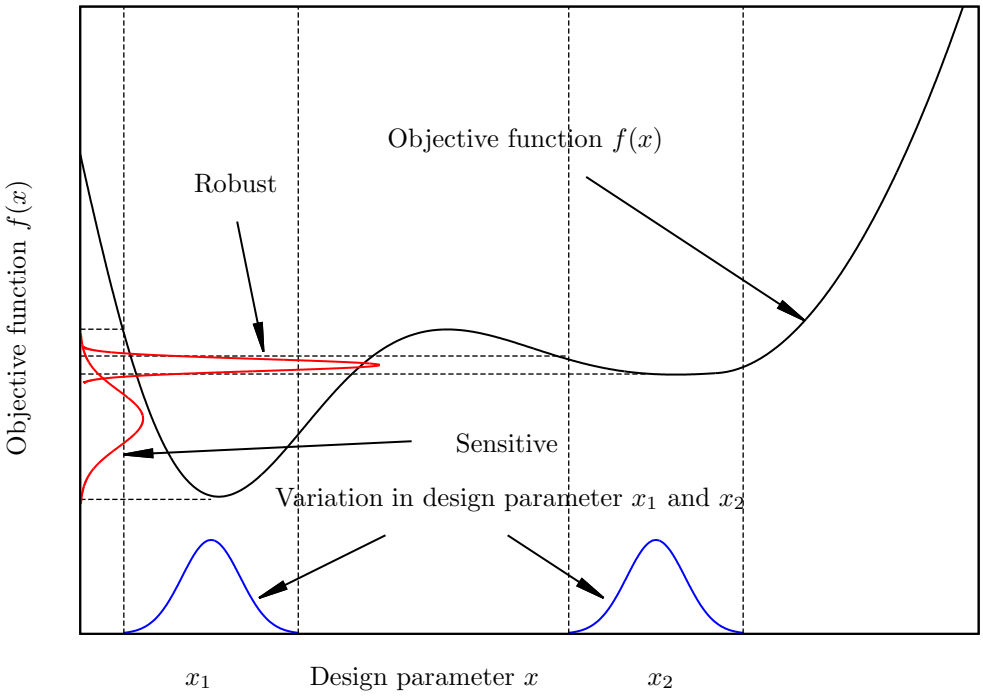

FIGURE 5.1: Robust design concept

variation in x is independent of the value of parameter setting, i.e., the distribution of variation in the parameter value x_i for the i^{th} design is same for all i's. The deterministic design optimisation process with an intent of minimising the objective function will result in a design with parameter value x_1. Although, the mean in the variation of the objective function for design parameter x_1 is less than that for x_2, its performance shows relatively larger variation. Hence, the design with parameter value x_1 is more sensitive compared to the design with parameter value x_2 or it can be said that the second design is more *robust*. Such a robust design can be obtained by minimising the mean and standard deviation for variation in design performance, instead of just its absolute value.

5.2.2 Robust design with multiobjective optimisation

It was observed in the previous example that a robust design can be obtained when the problem is formulated as a biobjective optimisation problem with mean and standard deviation of the performance as the two objectives. Tsutsui and Ghosh [154] used genetic algorithms in finding multiple robust solutions by considering the mean of the performance in the neighbourhood of the design point. Parkinson [155] defined a variability function for the performance measure based on the available uncertainties in the design parameters. An optimisation algorithm was proposed to search for the minimum value of the variability function and validated with a design of a cantilever beam for variability in the tip deflection. Das [156] pointed out that the idea of robust optimisation is to decide upon the trade-off between the 'optimality' and 'robustness' criteria

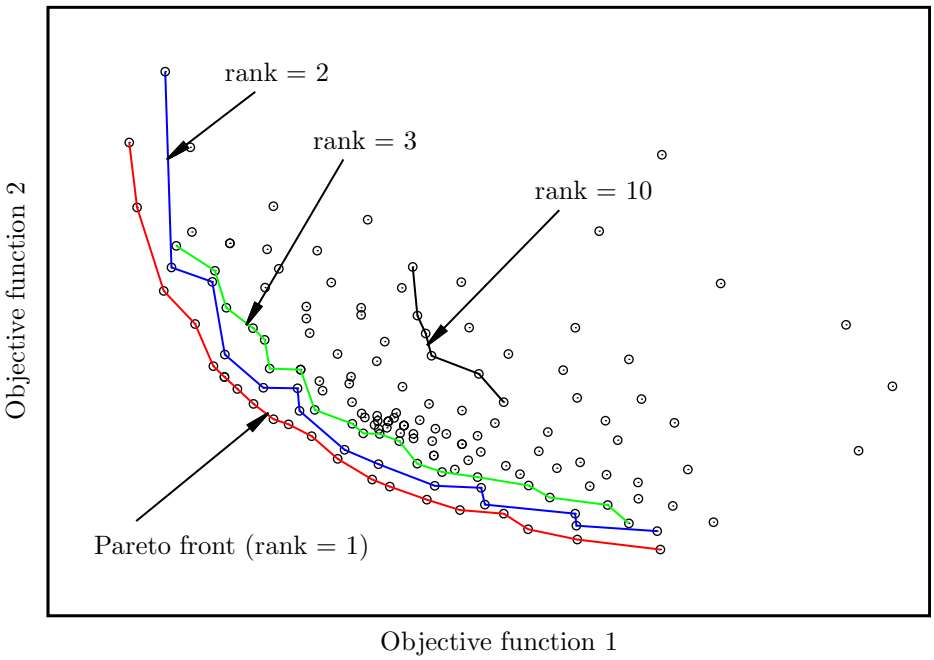

FIGURE 5.2: An example of Pareto curve of two competing objective functions

with the help of Pareto curves, Figure 5.2. These Pareto curves or fronts provide useful information regarding the optimal solutions in the case of a multiobjective optimisation, where the objectives are often competing against each other. Das [156] noted that there can be multiple ways to achieve robustness other than just minimising the mean or the expectation of the design performance. It is possible to define an objective to minimise the worst value of the performance in the presence of uncertainties. Robust optimisation generally searches for a design with a compromise between the two objectives: minimising (i) the mean and (ii) the standard deviation of performance variation making it a biobjective optimisation. Das [156] suggested three different formulations that can be used while performing robust designs[1]:

1. minimising the mean and the standard deviation of performance,
2. minimising the mean and the nominal value of performance[2],
3. minimising the nominal value and the standard deviation of performance.

Many researchers have adopted the mean and standard deviation of the design performance to evaluate robust designs [22, 157, 158, 159, 160, 161]. Gunawan and Azram [157] optimised the design of a simply supported platform with a vibrating motor on its top by minimising the sum of mean and standard deviation for two performance

[1]Here we minimise the performance metrics, but in some problems the mean or nominal performance must be maximised such as when considering component life.

[2]The nominal value of performance is the performance of the component in the absence of any form of uncertainty.

measures: cost and natural frequency. Zang et al. [159] used the robust design approach for a vibration absorber design by considering system uncertainties in the mass and stiffness while Sun et al. [160] presented a multiobjective robust optimisation of crashworthiness designs for a vehicle by adopting a new multiobjective particle swarm optimisation algorithm which removed the requirement of weighted average of combining multiple objectives. As reported by Jin and Sendhoff [162], the tasks of improving the design performance and delivering a better quality product by increasing the robustness are typically conflicting objectives. Hence, it is desirable to evaluate a design in the framework of multiobjective optimisation which leads to the Pareto front that provides the designer with information regarding the stability of the solutions.

5.3 Multiobjective optimisation

As discussed in section 5.2.2 the robust design optimisation problem is generally formulated as a multiobjective optimisation problem where more than one objective exists. For the robust design of the firtree joint, the mean and standard deviation for variation in maximum principal stress in the notch regions are required to be minimised. Several methods are proposed in achieving an optimised solution for multiple objectives that can be broadly classified into classical, i.e. point-by-point search methods and evolutionary, or population based methods. The advantage of working with a population of points, which results in a set of solutions, has made evolutionary methods more popular [163]. Such multiple solutions are known as the Pareto-optimal set of solutions where no one solution is better than any other, i.e., all solutions are *non-dominated* [164]. In an optimisation problem with $q > 1$ objectives, a solution $\mathbf{x}_i$ is said to dominate a solution $\mathbf{x}_j$ if the following two conditions hold true [163]:

1. For all q objectives, solution $\mathbf{x}_i$ is no worse than solution $\mathbf{x}_j$,
2. For at least one objective amongst q objectives, solution $\mathbf{x}_i$ is better than solution $\mathbf{x}_j$.

Accordingly, the goal of multiobjective optimisation is to search for non-dominated sets of solutions, by being as close to the true Pareto-optimal set as possible.

5.3.1 Comparison between classical and evolutionary approaches

The simplest way of approaching a multiobjective optimisation problem is the weighted metric approach. Multiple objectives are combined into a single objective by taking a weighted-sum or weighted deviations from an ideal solution [165, 166]. By selecting

different weights for different objectives, several independent single objective optimisation problems can be solved to obtain a set of solutions which can be said to be non-dominated [163]. However, there are certain drawbacks to this approach as reported by Das and Dennis [167]. The weighted sum approach of solving a multiobjective optimisation problem succeeds in producing the Pareto-optimal set only when the Pareto curve is convex. A common approach is to select evenly spread set of weights for different objectives in order to generate several points in the Pareto-optimal set. Das and Dennis geometrically show that even if the Pareto curve is convex, evenly spread weights do not necessarily produce evenly spread solutions on the Pareto curve. Also, when the Pareto curve is not convex, no single weight will result in a solution that lies on the non-convex part of the Pareto curve [167]. Das and Dennis [168] proposed a new method for generating the Pareto surface which can produce an evenly distributed solution set in the Pareto-optimal set. While solving the multicriteria optimisation, existence of a global minima of the objectives is assumed to be available. A simplex of the convex hull of all the individual minima are searched. Further, the distance between each point from an uniformly distributed set of points on this convex hull towards the origin is maximised to get the optimal solution which could potentially lie on the Pareto curve. Ismail-Yahaya and Messac [169] proposed the normal constraint method for generating a set of evenly spaced solutions on a Pareto frontier which was further improved by Messac et al. [170]. The utopia line/plane which passes through the individual minima for the multiple objectives is evaluated. Thereafter, a constrained optimisation is performed on uniformly distributed points on this plane for one objective while keeping other objectives as constraints.

On the other hand, the evolutionary approach works with a population of solutions hence a single multiobjective evolutionary run may result in a number of Pareto-optimal solutions [54]. The strength Pareto evolutionary algorithm (SPEA2) developed by Zitzler et al. [171] employs an enhanced fitness assignment strategy as compared to its predecessor (SPEA). Comparisons with other evolutionary methods available in the literature such as Pareto-envelope based selection algorithm (PESA) [172], SPEA [173], and the non-dominated sorting genetic algorithm-II (NSGA-II) [174] on various test problems showed that overall, the SPEA2 and NSGA-II have better performance [171]. Shukla and Deb [175] compared the above mentioned, and a few other, classical approaches for solving multiobjective optimisation problems with the evolutionary approach – NSGA-II. It was observed that the classical methods perform well when the problem size is small with a relatively less complex search space. It was also demonstrated that the population-based methods work better for finding a set of well-distributed and well-converged solutions on the Pareto-optimal set. Since NSGA-II is more frequently used for performing an evolutionary multiobjective optimisation as compared to the other population-based methods in the literature [16, 161, 163, 54, 176, 177], it has been adopted for the current problem of robust design optimisation of the firtree joint.

5.3.2 Non-dominated sorting genetic algorithm-II

In 2002, Deb et al. [174] proposed the NSGA-II method which is an improvement over the earlier proposed NSGA by Srinivas and Deb [178]. In the first step, the nondominated members from the population are collected into a set by assigning them a *rank* and an equal score. From the remaining members of the population, a higher ranked set is created consisting of members that dominate the members of the truncated population and again scored equally but with a reduced value. In this way, all the members are sorted into a series of fronts with decreasing ranks. Then the score for every ranked set is reduced with the help of a diversity encouraging sharing mechanism. This transforms the multiple objective problem into a single objective based on the ranks, Figure 5.2. The genetic algorithm is then used to select the new points from the final score [16]. Hence, with every new generation the Pareto front is evolved till no further improvement is obtained.

Three areas over which the NSGA-II is better than its predecessor are (i) computational complexity, (ii) elitism, and (iii) the need of sharing parameter specification. Pareto sets are identified using a fast nondominated sorting algorithm and a crowding comparing operator is used to preserve the diversity in the population [163]. The sharing function that was used in the original NSGA has two difficulties as mentioned by Deb et al. [174]:

1. The sharing parameter chosen to set the extent of sharing affects the performance of the sharing function method in preserving the spread of solutions,
2. The complexity of the sharing function method is $O(N^2)$ since each solution needs to be compared with all other solutions, where N is the size of population.

To overcome these difficulties, Deb et al. [174] used the crowding comparing operator which does not use any parameter for preserving the diversity or the spread among the population members and also results in reduced computational complexity as compared to the NSGA. The overall complexity of the NSGA-II was found to be $O(MN^2)$ where M is the number of objectives as compared to its predecessor which has $O(MN^3)$ [174].

In this work, the mean and standard deviation for the variation in maximum principal stress in the notch regions are minimised in order to obtain a robust design of a firtree joint when the variation in the pressure angles is included. The robust design optimisation may involve evaluating the mean and standard deviation for variation in maximum principal stress on every new design which may require performing FE simulations repetitively for many designs. The computational effort required for such an exercise is often not feasible. To overcome this issue, the use of approximate response surfaces for the mean and standard deviation is made.

5.4 Surrogate modelling

Any optimisation method requires the evaluation of objective functions at multiple design points. This process will not present a problem if the objective functions are available in analytical forms or can be computed cheaply. However, in the case of a firtree joint, in order to minimise the mean and standard deviation for the variation in notch maximum principal stress, FE simulations will be required to run multiple times over a feasible range of pressure angle. Although a single 2D firtree FE simulation requires ≈ 5 minutes on a desktop machine, in order to evaluate the mean and standard deviation several simulations will be required at each pressure angle making it a computationally expensive exercise.

Problems occurring while performing optimisation studies which involve computationally expensive objective function evaluations can be tackled with the help of approximation techniques. The central idea behind such techniques is to represent the true relationship between the design variables $\mathbf{x}$, and the objective function $y = f(\mathbf{x})$ by an approximation $\hat{y} = \hat{f}(\mathbf{x}, \boldsymbol{\alpha})$, where $\boldsymbol{\alpha}$ is a vector of unknown control parameters. These unknown parameters, $\boldsymbol{\alpha}$ are evaluated either by a black-box or physics based approaches [16]. The black-box approach is typically run at a number of pre-selected values of design variables to extract the objective function. Based on these input-output observations, an approximate model is trained by minimising an appropriate loss function. Such approximation models are often referred to as *surrogates* or *metamodels* in the literature [16]. In the context of firtree design, the FE analysis can be considered as a black-box while evaluating a surrogate model for a suitable objective function. Researchers have used different approaches for seeking a surrogate model such as Taylor series approximation, polynomial models, radial basis function models, Gaussian process models, etc. [16, 179]. Out of these, only the Gaussian process modelling approach is discussed here.

The origins of Gaussian Process modelling can be found in the field of geostatics where Krige [180] first developed this method. This method is also referred to as *Krigeage* or more commonly as *Kriging* in the literature [181, 182]. Sacks et al. [183] proposed the use of kriging to build approximations for computer models in 1989. Considerable literature is available where kriging has been used for building surrogate models to perform aerospace design optimisation studies [179, 16]. Simpson et al. [184] used kriging models to replace the second-order polynomial response surfaces for constructing global approximations while performing multidisciplinary design optimisation on an aerospike nozzle. Comparisons made between the two methods showed that kriging resulted in global approximations that were slightly more accurate than the polynomial response surface models. Jeong et al. [185] constructed response surface models based on kriging while performing multiobjective optimisation studies on aerofoil design and position of the flap where the lift-to-drag ratio is maximum. In what follows, a brief description of the formulation for a Gaussian process or kriging predictor is presented.

5.4.1 Formulation of Kriging based surrogate models

Let y be an unknown function which has a functional relationship with q variables $x_1, x_2, \ldots, x_q$. Let $\mathbf{x}$ be a vector containing x_h's ($h = 1, 2, \ldots, q$) such that $\mathbf{x} = [x_1, x_2, \ldots, x_q]^T$. Hence, the true relationship between y and $\mathbf{x}$ can be written as:

$$y = f(\mathbf{x}). \tag{5.1}$$

Suppose that evaluation of the function y at a given $\mathbf{x}$ is computationally expensive and hence is available only at n pre-selected points, $\mathbf{x}^{(1)}, \mathbf{x}^{(2)}, \ldots, \mathbf{x}^{(n)}$. Let $\mathbf{x}^{(i)}$ denote the sampling point i such that $\mathbf{x}^{(i)} = [x_1^{(i)}, \ldots, x_q^{(i)}]^T$ are assumed to be random variables that follow a Gaussian distribution. If the function value at $\mathbf{x}^{(i)}$ is denoted as $y^{(i)}$, it is given as:

$$y^{(i)} = y(\mathbf{x}^{(i)}) = \mu + \epsilon(\mathbf{x}^{(i)}), \quad i = 1, 2, \ldots, n, \tag{5.2}$$

where μ is the mean of the random process and $\epsilon(\mathbf{x}^{(i)})$'s are the normally distributed error terms with zero mean and variance σ^2, [186]. The correlation between the errors at points $\mathbf{x}^{(i)}$ and $\mathbf{x}^{(j)}$ is assumed to be:

$$\text{cor}\left[\epsilon(\mathbf{x}^{(i)}), \epsilon(\mathbf{x}^{(j)})\right] = \exp\left[-d(\mathbf{x}^{(i)}, \mathbf{x}^{(j)})\right], \tag{5.3}$$

where, the special weighted distance $d(\mathbf{x}^{(i)}, \mathbf{x}^{(j)})$ is used as [186]:

$$d(\mathbf{x}^{(i)}, \mathbf{x}^{(j)}) = \sum_{h=1}^{q} \theta_h \mid x_h^{(i)} - x_h^{(j)} \mid^{p_h} \qquad (\theta_h \geq 0, p_h \in [1, 2]). \tag{5.4}$$

In the above equation, θ_h and p_h are the hyperparameters which are tuned using the available input-output data [186]. The parameter θ_h measures the importance or the 'activity' of the variable x_h. The h^{th} variable is said to be active when even for small value of $\mid x_h^{(i)} - x_h^{(j)} \mid$ a large difference is observed in the function values $y^{(i)}$ and $y^{(j)}$. This implies that for a small value of $\mid x_h^{(i)} - x_h^{(j)} \mid$, the correlation between the errors at $\mathbf{x}^{(i)}$ and $\mathbf{x}^{(j)}$ is high. Parameter p_h relates the smoothness in the function in the coordinate direction h, such that when $p_h = 2$ functions are smooth while values near 1 correspond to less smooth functions [186]. From equation 5.3, we can construct an $n \times n$ correlation matrix using the available points:

$$\mathbf{\Gamma} = \begin{bmatrix} \text{cor}\left[\epsilon(\mathbf{x}^{(1)}), \epsilon(\mathbf{x}^{(1)})\right] & \ldots & \text{cor}\left[\epsilon(\mathbf{x}^{(1)}), \epsilon(\mathbf{x}^{(n)})\right] \\ \vdots & \ddots & \vdots \\ \text{cor}\left[\epsilon(\mathbf{x}^{(n)}), \epsilon(\mathbf{x}^{(1)})\right] & \ldots & \text{cor}\left[\epsilon(\mathbf{x}^{(n)}), \epsilon(\mathbf{x}^{(n)})\right] \end{bmatrix}. \tag{5.5}$$

Let $\mathbf{y} = [y^{(1)}, \ldots, y^{(n)}]^T$ denote the vector of output data and $\mathbf{1}$ denote a vector of n ones. The likelihood function can therefore be written as [186]:

$$L = \frac{1}{(2\pi\sigma^2)^{n/2} \mid \mathbf{\Gamma} \mid^{1/2}} \exp\left[\frac{(\mathbf{y} - \mathbf{1}\mu)^T \mathbf{\Gamma}^{-1} (\mathbf{y} - \mathbf{1}\mu)}{2\sigma^2}\right]. \tag{5.6}$$

The dependence of the likelihood function on the hyperparameters is through the correlation matrix $\mathbf{\Gamma}$. It can be seen from Equations 5.4 and 5.6 that the kriging model involves $2q + 2$ parameters, $\mu, \sigma^2, \theta_1, \ldots, \theta_q, p_1, \ldots, p_q$. In order to estimate these parameters, the likelihood function is maximised. To simplify the likelihood function, its natural logarithm is taken as [179]:

$$\ln(L) = -\frac{n}{2}\ln(2\pi) - \frac{n}{2}\ln(\sigma^2) - \frac{1}{2} \mid \mathbf{\Gamma} \mid - \frac{(\mathbf{y} - \mathbf{1}\mu)^T \mathbf{\Gamma}^{-1} (\mathbf{y} - \mathbf{1}\mu)}{2\sigma^2}. \tag{5.7}$$

The estimates of mean μ and variance σ^2 can be obtained by differentiating Equation 5.7 with respect to μ and σ^2 respectively and setting to zero as:

$$\hat{\mu} = \frac{\mathbf{1}^T \mathbf{\Gamma}^{-1} \mathbf{y}}{\mathbf{1}^T \mathbf{\Gamma}^{-1} \mathbf{1}}, \tag{5.8}$$

$$\hat{\sigma}^2 = \frac{(\mathbf{y} - \mathbf{1}\mu)^T \mathbf{\Gamma}^{-1} (\mathbf{y} - \mathbf{1}\mu)}{n}. \tag{5.9}$$

Substitution of these estimates back into Equation 5.7 and removing the constant terms results in a function which is known as the *concentrated ln-likelihood function*, [179]:

$$\ln(L) \approx -\frac{n}{2}\ln(\hat{\sigma}^2) - \frac{1}{2}\ln \mid \mathbf{\Gamma} \mid . \tag{5.10}$$

This function, now depends only on the parameters θ_h and p_h $(h = 1, 2, \ldots, q)$. It is now necessary to find the values of these parameters for which the function in Equation 5.10 attains a maximum value. Differentiating this equation with respect to θ_h does not yield an analytical solution [163]. Instead, iterative numerical optimisation techniques have to be used to obtain the values for these parameters [179, 163, 187]. Once the maximum likelihood estimates (MLE) θ_h, p_h, μ, and σ^2 are calculated, the function value can be predicted at any unobserved point, $\mathbf{x}^*$.

For the design of firtree joints, kriging based response models are constructed for the maximum principal stress in notch regions at various stages while performing the robust design optimisation using the proprietary Rolls-Royce optimisation plug-in OPTIMATv2 which is based on [187, 188].

5.4.2 Validation methods for Kriging based surrogate models

The constructed Gaussian process (or Kriging) model needs to be validated to ensure the accuracy of the model before using it for the optimisation process. If the output data, $y^{(i)}$ is available at a sufficiently large number of points $\mathbf{x}^{(i)}$ (testing data) other than the input or training points, the constructed model can be validated by evaluating the prediction error obtained as the difference between the predicted and the actual function values at these testing points. However, such testing output data may increase the computational cost in case of a high-fidelity black-box system. To overcome this problem, Jones et al. [186] proposed a procedure called the 'standardized cross-validated residual' (SCVR)

which uses the same training points, used to construct the model, in order to validate it. Cross-validation involves constructing a new kriging model by leaving out one point, from the available training data, and then calculating the posterior mean and variance at the left-out point. If a large number of training points are available, an m-fold cross-validation procedure can be used. From the available n training points, p roughly equal subsets are created by randomly selecting m points for each subset. Then instead of leaving out one point, an m-fold subset is left-out and a kriging model is constructed on the remaining training points. As in the leave-one out cross-validation procedure, the constructed model is validated by comparing the predicted values at each point of the left-out subset with their actual function values [179].

5.5 Surrogate model based optimisation

Sections 5.3 and 5.4 gave a brief account of optimisation and surrogate modelling methods which are the two important tools that are used in this thesis while performing the robust design optimisation on firtree joints. As mentioned by Mack et al. [189] surrogate-based optimisation frameworks consider the global view of the characteristics of the design space while searching for the optimum solution. They also enable the user to update the design of experiments (DOE) and characterise tradeoffs between multiple objectives. Mack et al. [189] demonstrated the use of response surface-based models while performing a multicriteria optimisation of a radial turbine for an expander cycle-type liquid rocket engine. In addition to giving a global perspective of the design problem, surrogate models also can be used in capturing the local changes in the performance by having denser sampling in those regions. Surrogate models can be used while performing optimisation using trust-region methods, [16]. An overview of steps involved in optimisation assisted by surrogate models is presented by Keane and Nair [16]. Such frameworks can be adopted when the objective functions and the constraints are computationally expensive to evaluate and when the goal is to obtain a near optimal solution by limiting the computational effort. A straightforward way to tackle this issue is to replace the expensive functions with computationally cheap functions obtained by constructing surrogate models and perform the optimisation study, with an initial guess $\mathbf{x}_0$, on these approximate response functions. The optimal solution $\hat{\mathbf{x}}^*$ obtained from these cheap functions will not be the true optimal solution $\mathbf{x}^*$. When the true performance is checked at the solution $\hat{\mathbf{x}}^*$, there could be three possible scenarios [16]:

1. performance at $\hat{\mathbf{x}}^*$ is satisfactory,
2. performance at $\hat{\mathbf{x}}^*$ is better as compared to the performance at $\mathbf{x}_0$, but further improvement is desired for the design requirements,
3. performance at $\hat{\mathbf{x}}^*$ is poorer as compared to the performance at $\mathbf{x}_0$.

For the first case, the designer would perform experiments and simulations at $\hat{\mathbf{x}}^*$ and confirm that the performance of this design is satisfactory. In case of the second and third outcomes, the designer would further update the surrogate model using the values of the objective functions and constraints at $\hat{\mathbf{x}}^*$ and perform another optimisation on the updated surrogate model. This process, when carried out iteratively for long enough may result in good results with respect to the accuracy of the final surrogate model being used. Kriging response surface methods were used in conjunction with the Monte Carlo approaches while evaluating the mean and standard deviation of the performance of a gas turbine compressor blade section in the presence of uncertainties arising from deviations during working conditions and manufacturing processes by Keane [190]. Advanced surrogate modelling approaches such as cokriging, where a Monte Carlo simulation was performed on the response surfaces obtained by combining results from varying fidelities, were implemented successfully in performing robust design optimisation by Keane [161]. With this background, a kriging based surrogate modelling approach along with the NSGA-II optimisation algorithm is used here to search for a firtree design whose performance with respect to notch stresses is more robust in the presence of manufacturing variations.

5.6 Robust design of firtree joints

A robust design optimisation study on the firtree joint requires efficient evaluation of the mean and standard deviation for the variation in maximum principal stress in the notch regions. Evaluation of these quantities via Monte Carlo simulation will require thousands of simulations in the neighbourhood of a single design point making it a computationally expensive exercise. Hence, kriging based surrogate models are constructed to replace the FE simulations of the firtree joint. In the sections to follow, a multiobjective optimisation is performed on the firtree joint by combining the tools of Gaussian process modelling and NSGA-II.

The steps involved in performing a robust design optimisation on the firtree joint are:

1. Select the upper and lower bounds, θ_{Up} and θ_{Lo}, of the pressure angle based on the feasibility of geometry creation.

2. Select N design points θ_i, where $(i = 1, 2, \ldots, N)$, evenly distributed in the range of probable pressure angles. These points represent the initial design of experiments (DOE) for the optimisation.

3. Based on the variation in pressure angles obtained by fitting substitute geometries on the CMM data in Chapter 2, extract the mean μ_θ and standard deviation σ_θ in the pressure angles. Select M points based on a suitable sampling strategy, θ_{ij} where $(j = 1, 2, \ldots, M)$, around each design point θ_i chosen in Step 2 in the range

$[(-3\sigma_{\theta,i} + \mu_{\theta,i}), (3\sigma_{\theta,i} + \mu_{\theta,i})]$[3]. Run M firtree FE simulations at these θ_{ij}'s (input data) for each design point θ_i and extract the maximum principal stress (output data) in the notch regions.

4. Construct N independent kriging models[4] from M input-output training data. Validate the surrogate models using the leave-out one cross-validation approach.

5. Evaluate N means $\mu_{P1,i}$, and standard deviations, $\sigma_{P1,i}$, in maximum principal stress ($P1$) by performing Monte Carlo simulation on the N kriging models constructed in Step 4.

6. Construct separate kriging models for the mean and standard deviation for maximum principal stress based on N θ_i (input data) and $\mu_{P1,i}$, $\sigma_{P1,i}$ (output data). Hence, the approximate response models for the mean and standard deviation for $P1$ in notch regions are obtained.

7. Obtain a Pareto-optimal set of pressure angles by performing a multiobjective optimisation, using the NSGA-II algorithm, by minimising the mean and standard deviation (μ_{P1} and σ_{P1}) for variation in maximum principal stress in notch regions using the surrogate models constructed in Step 6. It should be noted here that the Pareto-optimal set hence obtained is a predicted one, i.e., its accuracy is as good as the accuracy of the kriging models.

8. To improve the quality of the kriging models an update process is essential at this stage. Accordingly, five evenly spaced solutions in the design space, for pressure angles, known as *infill points*, are selected from the Pareto set obtained in Step 7. These pressure angles are then added to the initial N DOE points and the same procedure is repeated to obtain an improved Pareto-optimal set of pressure angles. This process is repeated till no improvement in the response surface models for μ_{P1} and σ_{P1} can be obtained or if the computational budget is reached. Figure 5.3 shows the optimisation methodology with the help of a flowchart.

In the following sections, this optimisation methodology is employed on firtree joints in two different cases with respect to variation in pressure angle on different flanks. In the first case, the variation (uncertainty) in pressure angle for all six flanks is kept same (perfect correlation). To demonstrate the robust optimisation cycle, every step is explained in detail for this case. The second case is more realistic with independent pressure angles on the six flanks. Only the results obtained at the end of last optimisation cycle are discussed in detail.

[3]The three sigma rule is adopted which assures that 99.7% of the designs lie within three times the standard deviation beyond either side of the mean.

[4]Instead of constructing N different Kriging models, two global models for $P1$ for left and right bottom notch regions could be constructed. However, it is assumed here that the response values at design points are uncorrelated. Also, by constructing local Kriging models it is expected that the evaluated mean and standard deviation would be more accurate as compared to running Monte Carlo simulations on the global model which becomes a trade-off between accuracy and the computational effort.

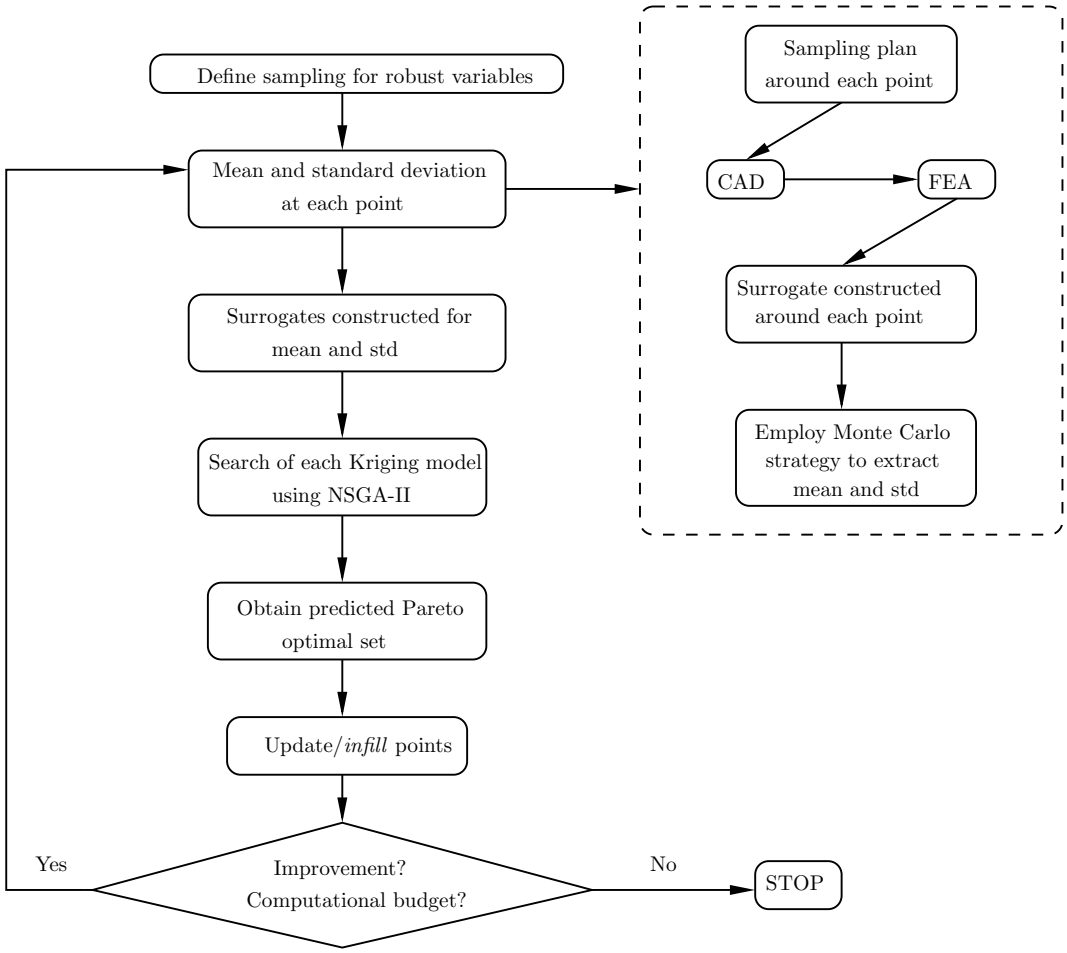

FIGURE 5.3: Flow chart detailing the optimisation methodology adopted in this chapter

5.6.1 Same variation on all six pressure angles

As a first step, the lower and upper bounds for the pressure angle, as a robust design variable, are selected so that all the designs in this range are feasible. Accordingly θ_{Lo} is found to be $0.91 \times \theta_{nominal}$ while θ_{Up} is $1.07 \times \theta_{nominal}$. The variation in the pressure angles extracted by fitting substitute geometries for all six flanks are used in this section, Figure 2.13. The mean and standard deviation are found to be $\mu_\theta = 99.96\%$ of $\theta_{nominal}$ and $\sigma_\theta = 0.21\%$ of $\theta_{nominal}$. N evenly spaced θ_i are selected within the bounds $[\theta_{Lo}, \theta_{Up}]$ ($N = 8$) that represent the initial design of experiments (DOE) points. The starting geometry is selected with a pressure angle of θ_4. Next, for each θ_i, $M = 10$ evenly spaced one-dimensional points are selected as explained in Step 3 in the range $[(-3\sigma_{\theta,i} + \mu_{\theta,i}), (3\sigma_{\theta,i} + \mu_{\theta,i})]$ where

$$\mu_{\theta,i} = 99.96\% \text{ of } \theta_i, \qquad \sigma_{\theta,i} = 0.21\% \text{ of } \theta_i.$$

For each θ_i, at M values of pressure angles, which represent the DOE for constructing the respective kriging models, two-dimensional firtree geometries are created which are

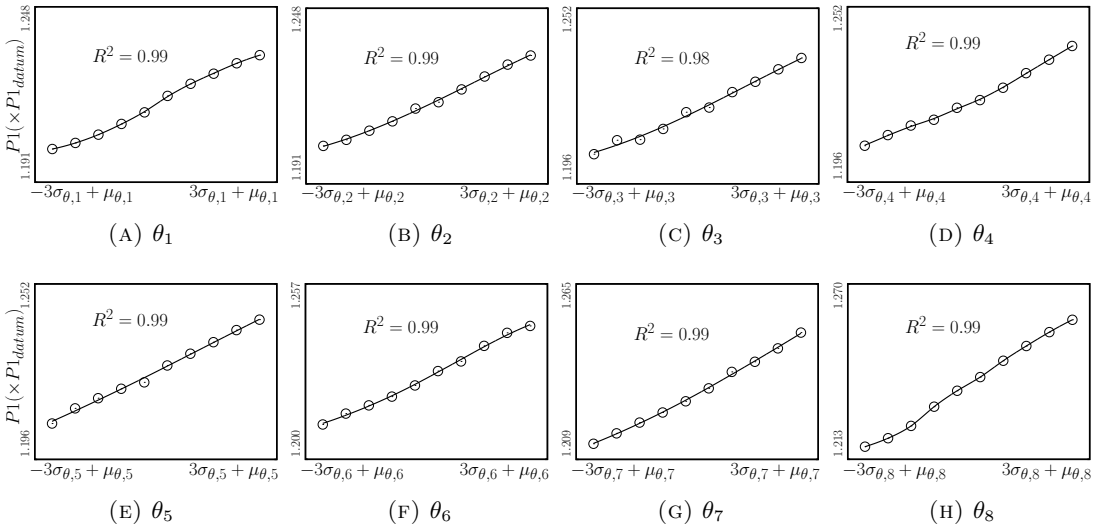

(A) θ_1 (B) θ_2 (C) θ_3 (D) θ_4

(E) θ_5 (F) θ_6 (G) θ_7 (H) θ_8

FIGURE 5.4: N kriging based surrogate models

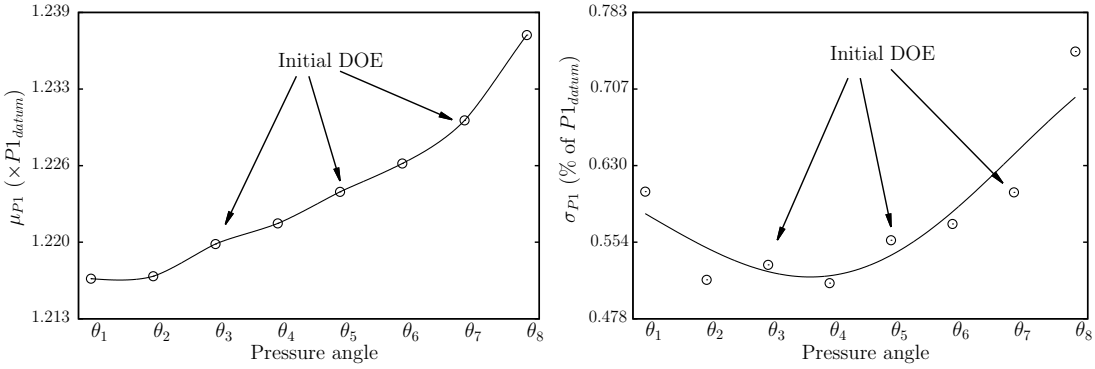

(A) Kriging model for μ_{P1} (B) Kriging model for σ_{P1}

FIGURE 5.5: Kriging based surrogate models for μ_{P1} and σ_{P1}

further analysed for stresses in the notch regions using FEA. N surrogate models are constructed using M input (variations in pressure angle) and output (variations in maximum principal stress in notch regions) data, Figure 5.4. For the purpose of comparison, the value for $P1_{datum}$ is taken from Figure 4.14.

It should be noted here that while changing the pressure angles on the disc side of the firtree joint from $\theta_{i,1}$ to $\theta_{i,10}$, the magnitude of pressure angle on the blade side was kept constant, i.e., θ_i. Also, since the magnitude of stresses are higher in the bottom flank as compared to the top and middle flank, kriging models are constructed only on the maximum principal stress in the notch regions for the bottom flank. It is expected that minimising the mean for variation in notch tensile stress only for the bottom flank will minimise the means for variation in maximum principal stress for the other two flanks. For each θ_i, the mean and standard deviation $(\mu_{P1,i}, \sigma_{P1,i})$, for maximum principal stress $P1$ are evaluated by performing Monte Carlo simulation on the N kriging models shown in Figure 5.4.

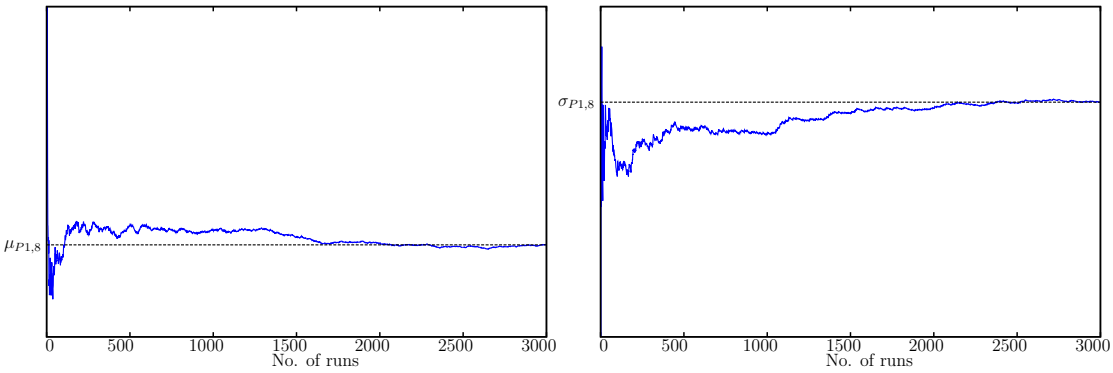

(A) $\mu_{P1,8}$ (B) $\sigma_{P1,8}$

FIGURE 5.6: Monte Carlo convergence for μ_{P1} and σ_{P1}

Separate kriging based surrogate models are constructed based on input (θ_i) and output ($\mu_{P1,i}, \sigma_{P1,i}$) data as shown in Figure 5.5. The convergence in mean and standard deviation while performing Monte Carlo simulation for θ_8 is shown in Figure 5.6. It is observed that the kriging model constructed for the mean shows better accuracy as compared to that of standard deviation of maximum principal stress, Figure 5.5. Due to

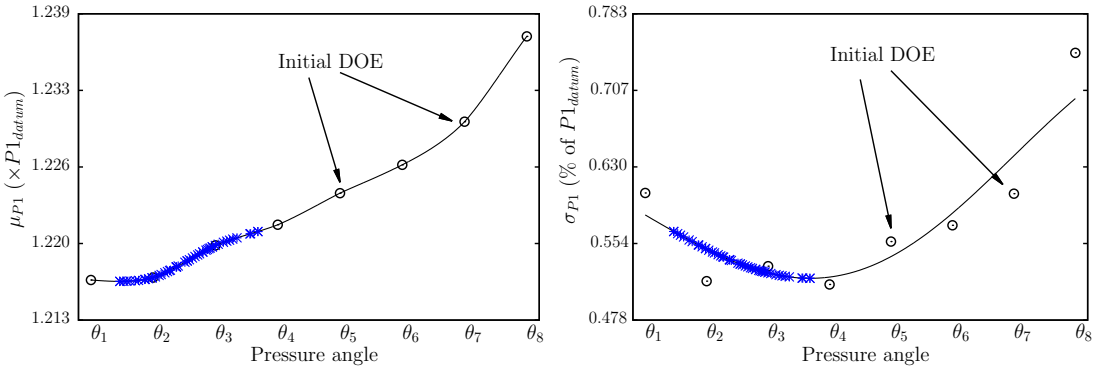

(A) Kriging model for μ_{P1} (B) Kriging model for σ_{P1}

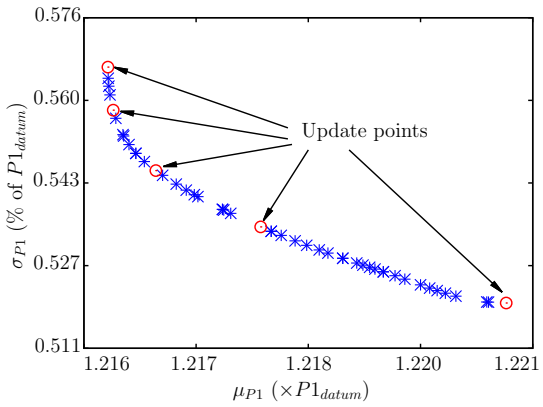

(C) Predicted Pareto-optimal set of solutions

FIGURE 5.7: Results from NSGA-II after first iteration

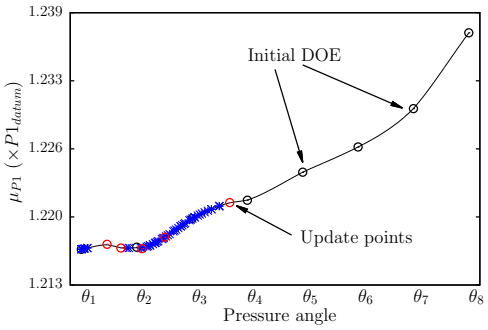

(A) Kriging model for μ_{P1}

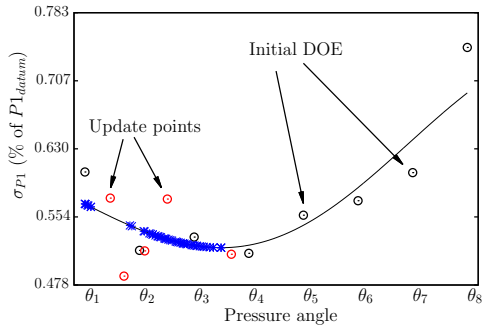

(B) Kriging model for σ_{P1}

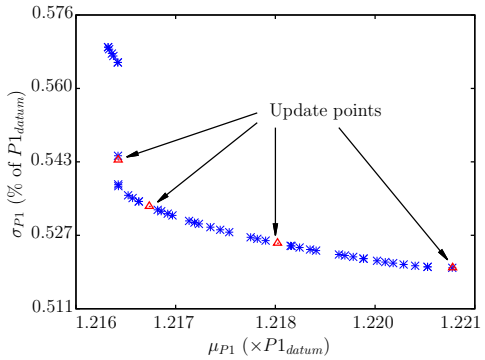

(C) Predicted Pareto-optimal set of solutions

FIGURE 5.8: Results from NSGA-II after second iteration

the presence of noise in the evaluation of standard deviation σ_{P1}, a regression constant λ is adjusted while constructing the kriging model to obtain a more feasible approximation of the true variation σ_{P1} [191]. However, both kriging models capture the general trend of the variation in mean and standard deviation within the range of θ_i.

A biobjective optimisation is performed to minimise μ_{P1} and σ_{P1} with the help of NSGA-II. A population size of 50 with a maximum of 100 generations are used while setting up the NSGA-II routine. The predicted Pareto-optimal set obtained as a result of the optimisation is as shown in Figure 5.7c. Figures 5.7a and 5.7b show the location of all the points from the Pareto-optimal set on the kriging models for the mean and the standard deviation for maximum principal stress, μ_{P1} and σ_{P1}. Figure 5.7c also highlights the five points that are selected as the update points. The pressure angles corresponding to these points are added to the initial DOE θ_i's resulting in a set of $N+5$ pressure angles.

Two more similar optimisation update iterations were performed. The predicted Pareto fronts and the kriging models used for the optimisation for the second and third iterations are shown in Figures 5.8 and 5.9. It can be seen from the kriging model for the standard deviation of maximum principal stress constructed after including the update points from the first iteration, that there is not much improvement in the accuracy as compared to the kriging model used for first iteration. However, as in the first iteration, the kriging

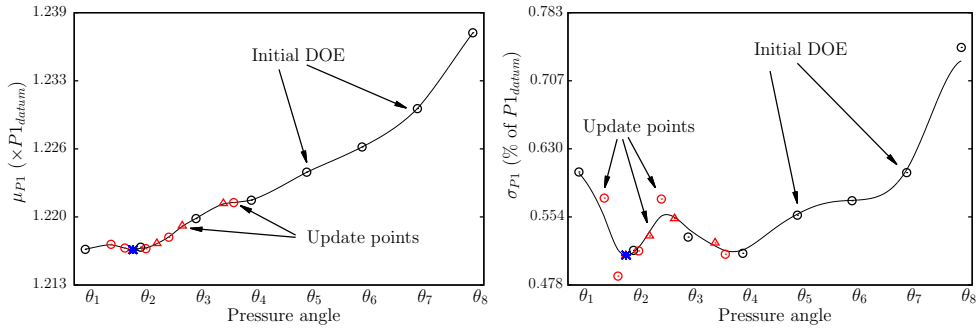

(A) Kriging model for μ_{P1}

(B) Kriging model for σ_{P1}

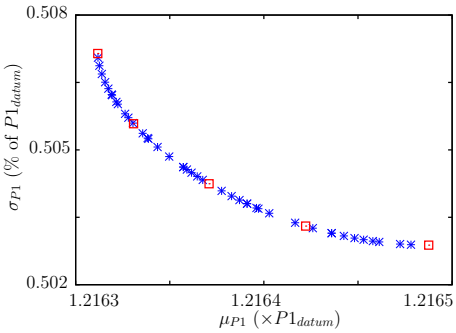

(C) Predicted Pareto-optimal set of solutions

FIGURE 5.9: Results from NSGA-II after third iteration

model manages to reflect the general trend of the variation in standard deviation but fails to reflect the local changes between θ_1 and θ_3.

When the update points extracted from the Pareto front obtained at the end of the second iteration are included, the kriging model for the standard deviation follows the input data more closely. The kriging models for mean of variation in maximum principal stress shows good accuracy for both second and third iterations. Figure 5.10 shows the Pareto-optimal sets of pressure angles obtained at the end of all the three iterations. After every iteration, the Pareto front moves towards the origin showing an improvement with respect to both the objectives. At the end of the third iteration, all solutions in the Pareto-optimal set are seen to be clustered in the neighbourhood region of θ_2, Figures 5.9a and 5.9b. It is observed that the mean for variation in maximum principal stress near θ_1 is similar to that near θ_2. However, the standard deviation at θ_1 is 15.4% larger than the standard deviation at θ_2 and hence, the pressure angles near θ_1 are ignored in the final Pareto-optimal set of solutions.

It can be observed from Figure 5.10 that if the firtree joint is designed with the pressure angle set as 92.86% of $\theta_{nominal}$, the mean of the variation in maximum principal stress is reduced by 0.37% as compared to the mean at $\theta_{nominal}$. A reduction of 4.95% in standard deviation for variation in maximum principal stress is also observed at 92.86% of $\theta_{nominal}$ as compared to the standard deviation at $\theta_{nominal}$. Although, a larger reduction can be

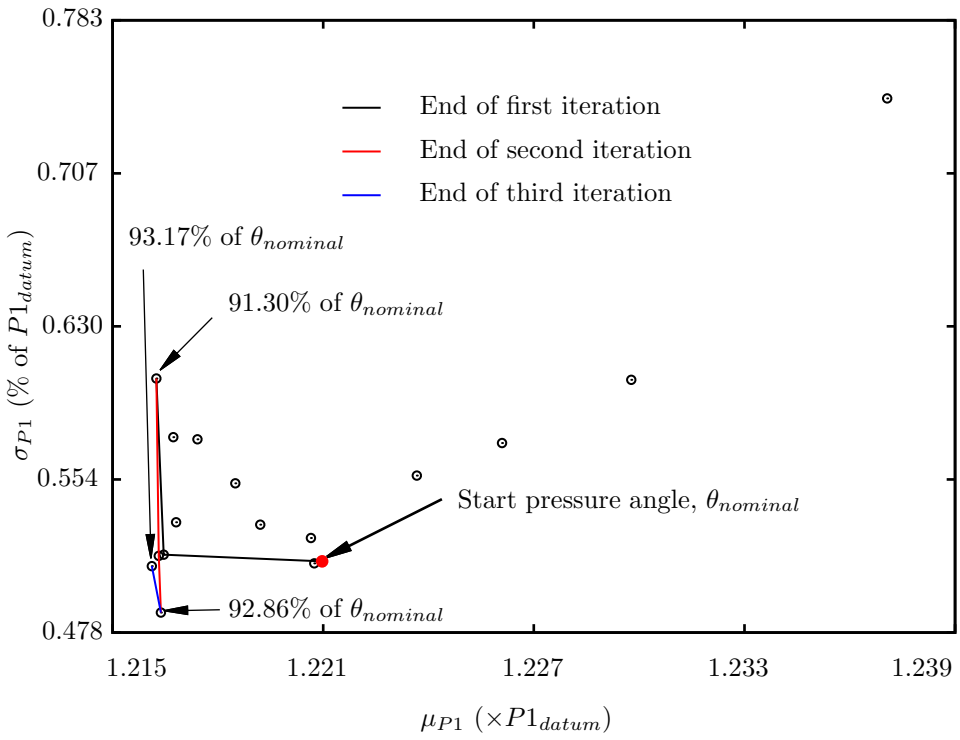

FIGURE 5.10: Pareto fronts at the end of each iteration using actual FE evaluations

obtained in the mean, μ_{P1} with 93.17% of $\theta_{nominal}$, no substantial improvement in the standard deviation, σ_{P1} is obtained.

Thus, with the help of the above example, a robust design optimisation process is demonstrated on a two-dimensional firtree joint. While performing this study, it is assumed that the variation observed on different pressure angles is same for all the six flanks. In practise, however, the variations in all six pressure angles are independent of each other as was shown in the previous chapter. The magnitudes of standard deviations for the variation in maximum principal stresses due to six independent pressure angles is also higher as compared to the standard deviation in the case of all six flanks having the same variation. This is due to the non-uniform distribution of centrifugal loads between the six flanks. As a result pressure lines/faces on different flanks come into contact at different load increments affecting the standard deviation.

5.6.2 Independent variation on each pressure angle

The same lower and upper bounds for the robust design variable, i.e. the pressure angle are used in this section,

$$\theta_{Lo} = 0.91 \times \theta_{nominal}, \quad \theta_{Up} = 1.07 \times \theta_{nominal}.$$

$N = 5$ evenly spaced initial design of experiments (DOE) points are selected with $\theta_3 = \theta_{nominal}$ as the starting pressure angle. For each θ_i, the variation has to be included in the

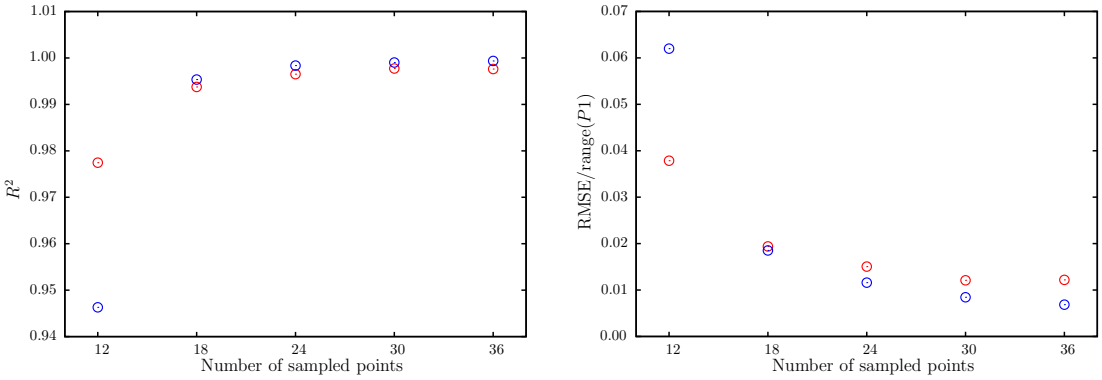

(A) Correlation coefficient R^2 (B) Normalised RMSE

FIGURE 5.11: R^2 and normalised RMSE for $P1$ at bottom left (blue) and bottom right (red) flank of firtree joint

firtree geometry such that, all pressure angles on the six flanks are independent of each other. The variations for each pressure angle extracted in the previous chapter (Table 4.3) are used here. Hence, a six dimensional surrogate model needs to be constructed for every θ_i. In the previous example, $M = 10$ points were selected to construct the N one dimensional kriging models. However, in this study, to construct a sufficiently accurate kriging model, the number of input-output training data, M, has to be evaluated before building the surrogates.

Kriging models, constructed at $\theta_3 = \theta_{nominal}$, with increasing number of six dimensional input data generated using a space-filling sampling strategy are compared. Two separate kriging models are constructed for the maximum principal stress, $P1$, experienced by the firtree joint in the bottom left and right notch regions. The correlation coefficient R^2 and normalised root mean square error (RMSE) for the kriging prediction are shown in Figure 5.11. It can be seen that both the kriging models show that there is limited improvement in the R^2 and RMSE values when the number of sampling points is increased beyond 30. The results obtained from the 2D firtree FE simulations conducted on the pressure angles extracted from the CMM data in the previous chapter (Figures 4.15, 4.16 and Table 4.3) can be used here to compare with the kriging model based predicted results.

The maximum principal stress $P1$ extracted from these simulations (actual values) are compared with the predicted values based on the kriging models constructed on a sampling plan of 30 six dimensional points in Figure 5.12. It can be seen, that the kriging model predicts the response of maximum principal stress with sufficiently good accuracy. Hence, a space-filling sampling plan with $M = 30$ points has been adopted here to construct the kriging models for $P1$ at the bottom left and right notch regions.

As in the previous example, 10 kriging based surrogate models are constructed here for the maximum principal stress at bottom left and right notch regions for $N = 5$, θ_i's. The mean and standard deviation, $\mu_{P1,i}$ and $\sigma_{P1,i}$, are calculated by performing Monte Carlo simulation with $20,000$ runs on these kriging models. Four separate surrogate models

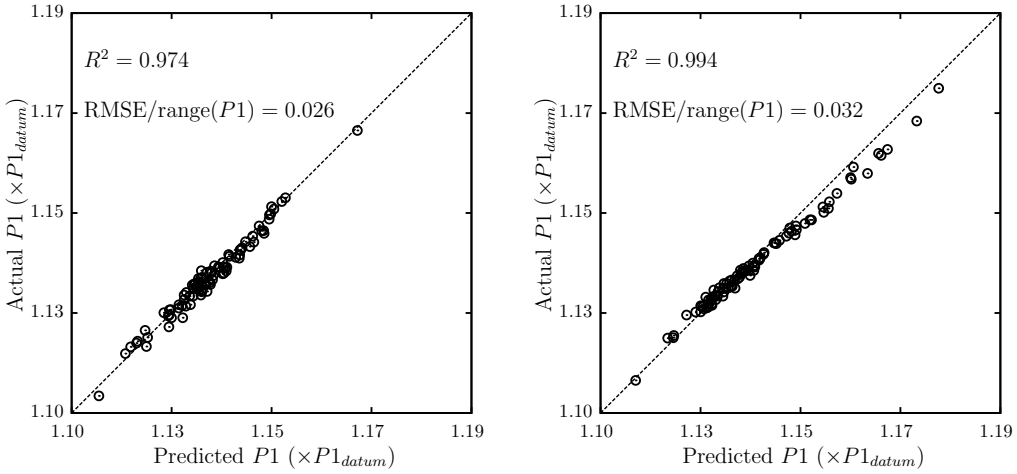

(A) Bottom left notch (B) Bottom right notch

FIGURE 5.12: Kriging model (with 30 sampled points) validation: Actual vs predicted $P1$

are constructed using two sets (bottom left and right notches) of input (θ_i) and output ($\mu_{P1,i}$ and $\sigma_{P1,i}$) data providing four objective functions. NSGA-II with population size of 50 is implemented for a maximum of 100 generations while minimising these four objectives in order to obtain the predicted Pareto front. Five uniformly spaced update points are extracted from this Pareto front and the same process is repeated two more times. The R^2 and RMSE/range($P1$) for all 15 design points are listed in Table 5.1. The four surrogate models constructed at the end of the third iteration of optimisation are shown in Figure 5.13. It can be seen that the kriging models are able to extract the general trend in the variation for all four objective functions. The magnitudes of mean and standard deviation for variation in the right bottom flank are observed to be higher than on the left bottom flank of the firtree joint. This observation corresponds with the results obtained in the previous chapter shown in Table 4.3. It was reported earlier, that the magnitudes for mean and standard deviation for variation in angles on the left side flanks are lower as compared to the right side flanks. Accordingly, it can be concluded that this asymmetric variation in pressure angles on the either sides of the firtree joint raises the stress magnitudes on the notches to the right side of the firtree joint hence resulting in higher magnitudes of the mean and standard deviations for stresses in right bottom notch region. The magnitude of mean, μ_{P1}, intensifies with any further increase of design angle from $\theta_{nominal}$ (θ_3 in Figure 5.13a), whereas it reduces on both bottom notches when the design angle is reduced. However, the standard deviation, σ_{P1}, shows no significant change for pressure angles below θ_3. As with the mean, a rise in the magnitude of standard deviation is observed for a design angle greater than θ_4 on both bottom flanks of the firtree joint.

It was shown in Figure 4.13, that one of the reasons for the scatter in stress magnitudes in the notch regions is due to the shift of the contact area away from the pressure lines or faces. The contact area can be controlled to stay within the pressure face, by maximising

Optimisation cycle	Design point	Kriging based surrogate models			
		Bottom left		Bottom right	
		R^2	RMSE / range($P1$)	R^2	RMSE / range($P1$)
Initial DOE	θ_1	0.999	0.009	0.998	0.012
	θ_2	0.998	0.011	0.999	0.009
	θ_3	0.999	0.010	0.999	0.005
	θ_4	0.998	0.009	0.999	0.009
	θ_5	0.999	0.007	0.999	0.006
Update points after first iteration	θ_6	0.998	0.010	0.999	0.009
	θ_7	0.999	0.010	0.997	0.014
	θ_8	0.999	0.008	0.998	0.011
	θ_9	0.998	0.012	0.999	0.006
	θ_{10}	0.999	0.008	0.999	0.011
Update points after second iteration	θ_{11}	0.962	0.038	0.957	0.030
	θ_{12}	0.998	0.013	0.999	0.009
	θ_{13}	0.996	0.016	0.999	0.010
	θ_{14}	0.999	0.009	0.999	0.004
	θ_{15}	0.997	0.015	0.999	0.007

TABLE 5.1: R^2 and RMSE/range($P1$) obtained after cross-validation on $(N+5+5)\times 2$ Kriging models using leave-one-out strategy

the length of the pressure face. The length of the pressure line at θ_5 is found to be 0.76 times the length at θ_3, but the radii of the pressure arc on the blade side for both the designs are same. However, although the length of the pressure line for design with θ_1 is 1.23 times that of pressure line at θ_3, the standard deviation σ_{P1} is in the same range for both the designs, Figure 5.13b. Hence, a design with maximum length of the pressure line may not always perform better.

The Pareto fronts at the end of every optimisation cycle are shown in Figure 5.14. A designer can use such curves to select a design that is suitable for the particular problem. For example, in Figure 5.14, if the standard deviation, σ_{P1}, is more critical for both the bottom notch regions then design with pressure angle θ_{15} can be selected. However, the mean, μ_{P1}, at design with pressure angle θ_6 is less in both bottom notch regions. The design with pressure angle $\theta_1 = 0.91 \times \theta_{nominal}$ performs better than other designs with respect to the mean μ_{P1} on the left bottom notch while $\theta_7 = 0.96 \times \theta_{nominal}$ can be considered as a trade-off between μ_{P1} and σ_{P1} at the left bottom notch. If only the standard deviation σ_{P1} needs to be minimised, design with $\theta_{15} = 1.02 \times \theta_{nominal}$ performs better than other designs for both side notches. Whereas the design with a pressure angle $\theta_6 = 0.94 \times \theta_{nominal}$ has better performance with respect to the μ_{P1} at both notches.

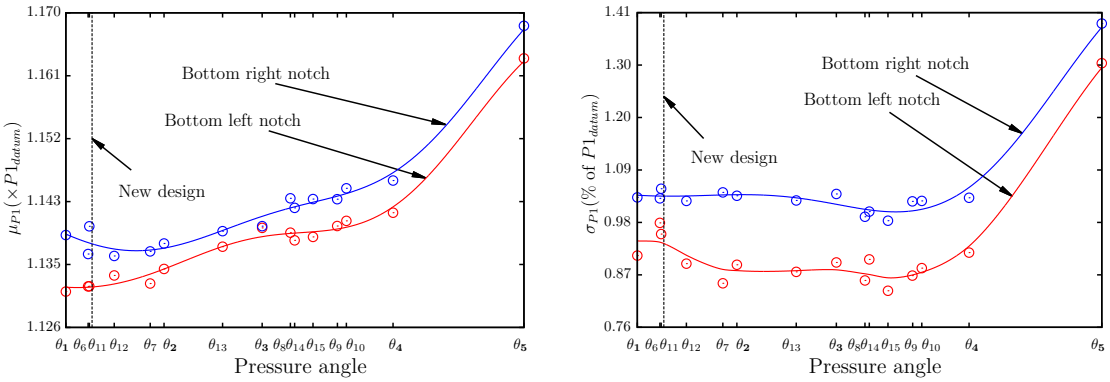

(A) μ_{P1} (B) σ_{P1}

FIGURE 5.13: Kriging models with input output data for mean and standard deviation of maximum principal stress at bottom left and right flanks of firtree joint

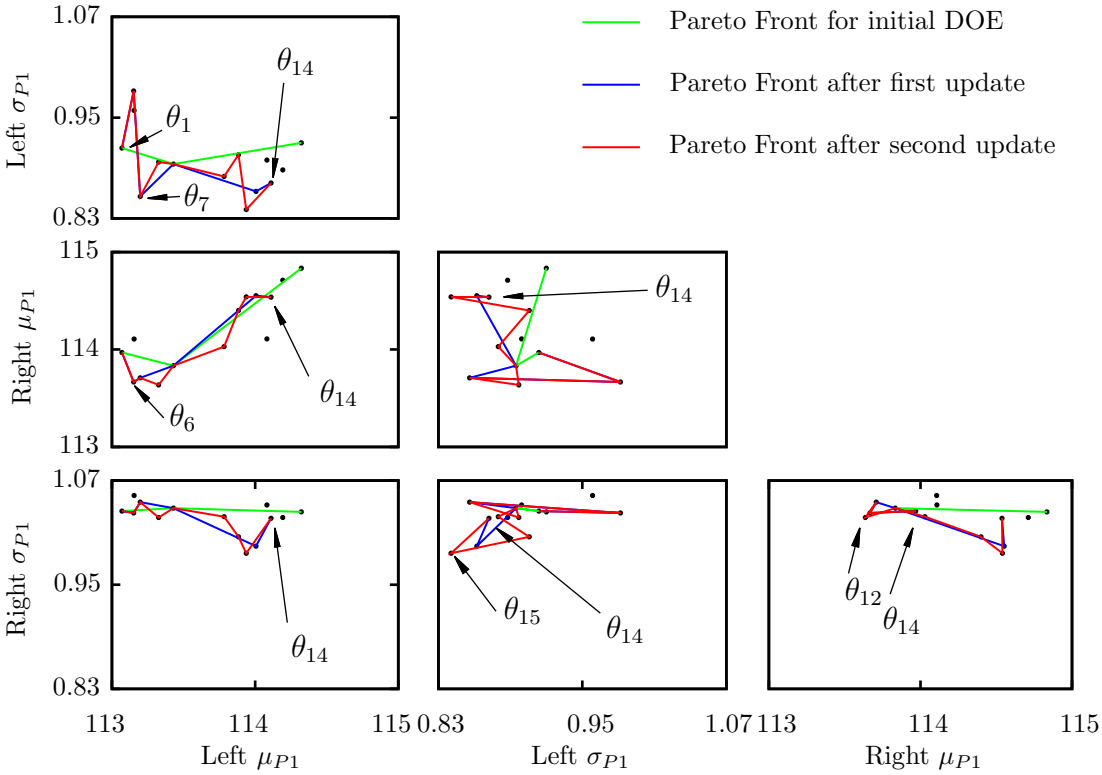

FIGURE 5.14: Pareto fronts for all combination of objective functions (All values are % of $P1_{datum}$, θ_3 is the starting geometry)

If only the variation in the right bottom notch is considered, $\theta_{12} = 0.95 \times \theta_{nominal}$ has better performance with respect to μ_{P1} and σ_{P1} compared to the other designs. Hence, it can be seen that such curves, obtained from the non-dominated sets of solutions from an optimisation on multiple objectives, can be used to select a suitable design by considering the existing trade-offs between different objectives. The magnitudes of the mean μ_{P1} on both the notch regions are minimum for a pressure angle of $0.94 \times \theta_{nominal}$. However, since the standard deviation remain relatively constant, a firtree joint with a pressure

angle that is $\approx 6\%$ lower than $\theta_{nominal}$ is found to be more robust in the presence of manufacturing variations.

Alternatively, the designer can use a plot as shown in Figure 5.15 which shows the values of objective functions for each design on the Pareto front in Figure 5.14. The designs plotted in green are on the Pareto front after performing optimisation on the initial DOE, whereas designs in blue and red are on the Pareto fronts after first and second updates respectively. It is seen from the figure that the performance of designs improve as the surrogate models are updated with infill points. Figure 5.16 shows the distribution of maximum principal stress at the bottom left and right notches for designs with $\theta_{nominal}$ and $0.94 \times \theta_{nominal}$ for the variation in pressure angle obtained from scanning real disc side firtree joints. It is assumed that the variation in the pressure angle for the new design is the same as that for the original design. It is observed that the mean for variation in $P1$ is reduced in both left and right bottom notch regions. However, it should be noted here that these statistical moments are evaluated based on a limited number of data and that these are not the true mean and standard deviation. Table 5.2 compares the mean and standard deviation in $P1$ for all six flanks for the new design with the old design. A reduction in the magnitude of mean μ_{P1} is observed in the new design for all the six notch regions. Although the standard deviation σ_{P1} is reduced at the top and bottom flanks, σ_{P1} for the middle flanks at both left and right sides show a rise for the new design as compared to that for the old design. However,

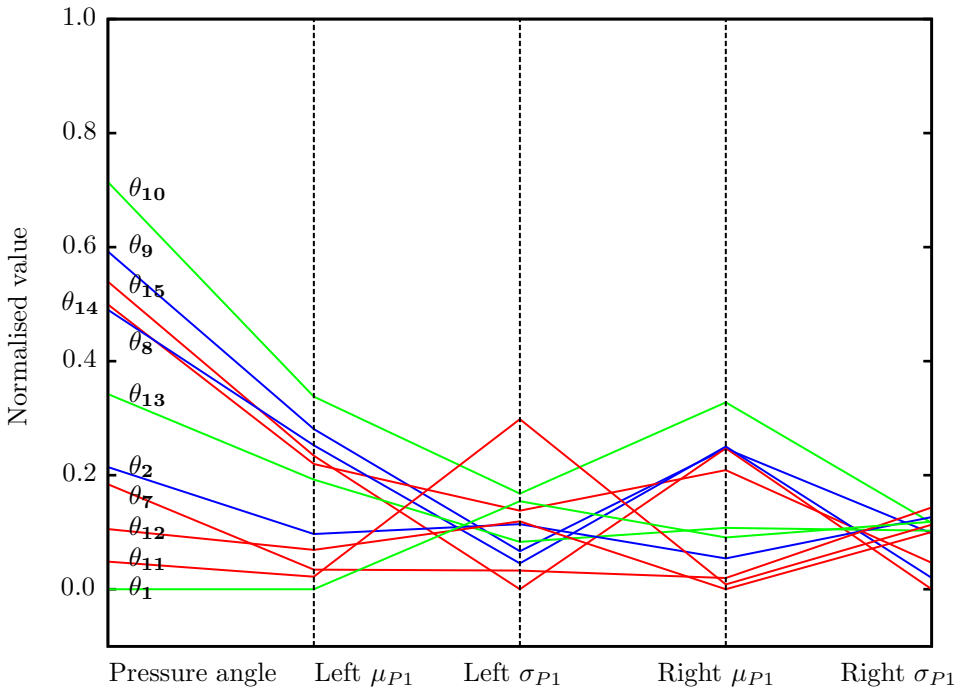

FIGURE 5.15: Parallel axis plot for four objectives and one design variable (green designs from initial DOE, blue designs from first update, and red designs from second update Pareto fronts)

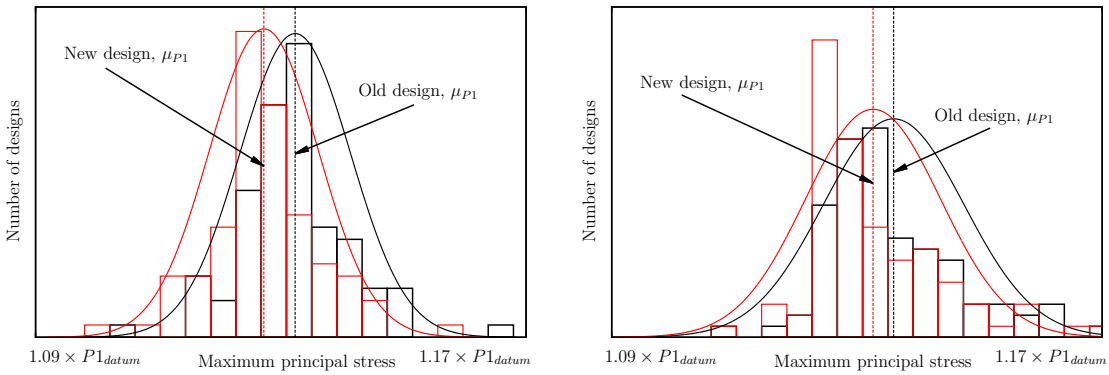

(A) Bottom left notch (B) Bottom right notch

FIGURE 5.16: Old design compared with the new design

Side	Flank	Max. principal stress for old design		Max. principal stress for new design	
		Mean $\times P1_{datum}$	Std. deviation % of $P1_{datum}$	Mean $\times P1_{datum}$	Std. deviation % of $P1_{datum}$
Left	Top	1.038	0.85	1.020	0.83
	Middle	1.042	0.94	1.026	0.98
	Bottom	1.138	0.86	1.133	0.84
Right	Top	1.030	0.97	1.014	0.94
	Middle	1.041	1.16	1.023	1.19
	Bottom	1.142	1.09	1.138	1.05
Average		1.072	0.98	1.059	0.97

TABLE 5.2: Comparison between old and new design with mean and standard deviation for variation maximum principal stress

since the magnitudes of stresses at the bottom flank are higher than the other two flanks and the average values of these statistical moments show improvement (Table 5.2), it can be said, that the new design is more *robust* against the manufacturing variations as compared to the old design with respect to the tensile stress in the bottom notch regions.

Only the angle that the pressure line makes with the vertical axis is considered as design variable while performing this robust optimisation. Other parameters, such as length of the pressure face, fillet radii may also have an effect on the notch stresses. An optimisation study with these geometric parameters as the design variables in addition to the pressure angle, may result to different values for the pressure angle.

5.7 Summary

A multiobjective optimisation is performed on the firtree joint based on robust design principles by taking the pressure angle as the robust design parameter. The bottom flank attracts higher stresses compared to the other two flanks on the firtree joint considered here. Hence, the mean and standard deviation for variation in maximum principal stress at the left and right notches for the bottom flank form the objective functions for the optimisation. The variation in the pressure angle extracted by fitting substitute geometries using available scanned data on real disc side firtree joints are used. To evaluate the mean and standard deviation, a large number of two-dimensional finite element analyses are required to be performed on the firtree joints. The computational effort required to perform such an optimisation directly is not feasible. In order to overcome this problem, the use of surrogate models based on Gaussian process modelling (Kriging) is explored. It is seen that the approximate models are able to extract the trend in the objective functions with fewer number of FE simulations. The non-dominated sorting genetic algorithm-II is implemented on the surrogate models of the objective functions. Five equally spaced points are selected from the predicted Pareto front to further update the surrogate models twice. Based on the non-dominated set of solutions, a new design for the firtree joint, with the pressure angle reduced by 6%, is proposed which shows improvements over the old design with respect to the variation in maximum principal stress at the bottom notches. The new design lowers the means μ_{P1} by $\approx 0.5\%$ at the bottom notch regions and the standard deviation is reduced by $\approx 3\%$. However, the standard deviation σ_{P1} at the middle flank tends to increase for the new design. Since, the magnitudes of stresses in the bottom notches are higher as compared to the other two notch regions, the variation in the bottom notch stresses will affect the firtree joint's performance more than the variation in the top and middle notch stresses. Hence, a new design for the firtree joint is obtained as a result of robust design optimisation that is less sensitive to manufacturing variations.

Chapter 6

Conclusions and future work

While designing an engineering component, engineers specify tolerances on different geometric entities such that the manufacture of those parts of the component should lie within these tolerances. For components used in an aero engine the tolerance requirements are very stringent. A slight variation in any of the geometric entities may affect the performance of the component. It is observed in this work that even though the manufactured components follow the tolerance requirements, a variation within the bounds of tolerances can still affect the performance of such components. For example a tolerance on an edge is usually specified in a way such that each point on the edge should lie within an envelope (a rectangle in case of a straight edge). However, although all points on that edge lie within the envelope, the orientation of that edge can have a slight variation. In mechanisms where the orientation of edges or faces have to be precise for their desired functioning, such small variations can result in undesirable scatter in their performance.

The disc blade attachment which is found in an aero engine turbine or compressor is one such component. Pairs of surfaces in contact are used in order to transfer the large centrifugal loads through the joint between the blade and the disc at several locations. A slight variation in the orientation of the faces (pressure faces) of the blade or the disc where they come into contact can affect the stress distribution in the joint and hence its service life. The blade disc attachments are designed such that their service life is greater than that of the attached blade or the disc in order to ensure that the joint does not fail before the blade or the disc. It is desirable to design these components so that they show reduced variation in their life expectancy in the presence of system uncertainties.

6.1 Conclusions

In this work the firtree joint found between a blade and the disc of an aero engine high pressure turbine is used to study the effect of manufacturing variations in geometry on

the stress distribution in the joint. The firtree joint that is analysed here involves six pressure faces along which the contact takes place simultaneously. Pressure faces for the firtree on the disc are made of straight lines in two dimensions while the pressure faces are arcs on the blade side firtree. Sample firtree joints were scanned using a coordinate measuring machine on five uniformly distributed slots along nine different disc rims. The work done here can be divided into four sections: (i) extraction of variation in geometry due to manufacturing from CMM data on disc firtrees, (ii) extraction of the roughness defining parameters from the CMM data and their use while generating non-smooth machined surfaces numerically, (iii) assessing the effect of geometric variation on the stress distribution in the firtree region, and (iv) design of firtree joints in the presence of manufacturing uncertainty based on robust optimisation principles.

6.1.1 Extracting geometric variation

Two methods have been used to extract the variation in geometry due to manufacturing:

1. **Minimising the RMS error**: A coordinate measuring machine was used to scan the firtree slots on the high pressure turbine disc rims. Two separate geometries were fitted to this cloud of points by minimising the root mean square error of the normal distance between a scanned point and the nominal geometry. The first substitute geometry, consisting of a straight line (representing the pressure line) along with two adjoining tangential arcs, is fitted to the scanned data. Selecting the adjoining arcs ensured that all of the points from the scanned data that represent the pressure line were included while extracting the substitute geometry. The orientation of these pressure lines is of importance in this thesis, i.e. the angle these lines make with the vertical axis: the pressure angle. It was observed from the variation of the pressure angle that approximately 61% of the pressure lines were manufactured with an angle less than the nominal angle. The second substitute geometry includes the bottom edge of the flank in addition to the pressure line and two tangential arcs between these two lines. The variation in the included angle for each flank, extracted as a result of fitting this substitute geometry to the scanned data, showed that majority of the designs have included angles greater than the nominal value. However, the variation of pressure angles extracted from this geometry showed similar results as with the first substitute geometry, with approximately 57% designs having angles less than the nominal pressure angle. Hence, it can be said that the pressure lines are manufactured with higher precision as compared to the bottom line of the flanks. The standard deviations in the pressure angle were observed to be 0.222% and 0.206% of the nominal pressure angle for variation extracted from the two substitute geometries, respectively. The correlation coefficients for the pressure angles between front and rear edges of the firtree slots were found to be 0.44 and 0.53 for each of the substitute geometries.

This leads to a variation in the twist between the front and rear pressure angles with a standard deviation of 0.198% of the nominal. Such twist angles may affect the contact conditions between the pressure faces on disc and blade sides and hence the stress distribution in the firtree joints. It was also observed that the fillets with smaller radii are manufactured with higher precision as compared to the fillets with larger radii.

2. **Fourier transform**: The data scanned using the CMM includes noise in the form of closely spaced irregularities which may have originated due to the measuring machine itself or due to foreign particles sticking to the surface that was being scanned. It is essential to filter this noise from the raw data to accurately extract the variation in surface profile that may have a functional relationship with the characteristic dimension of the part. It was shown that such unwanted closely spaced irregularities can be filtered out with the help of a Fourier transforms. The surface profile was represented in its frequency domain, from which the components of the frequency representing noise were eliminated. From this truncated frequency spectrum, a surface profile was regenerated by applying an inverse Fourier transform to give a smooth variation in geometry. A method based on the root mean square value of the generated surface profile was used to select the cut-off frequency. It was observed that the profile generated after filtering the high frequency components, corresponding to this cut-off frequency, maintained the smooth variation along the pressure line while removing the closely spaced irregularities.

6.1.2 Numerical generation of non-nominal surfaces

Manufacturing processes cannot produce engineering components with perfectly smooth surfaces. While performing analysis and design on such components, it is often assumed that the surfaces do not possess any deviations from their nominal dimensions. However, in mechanisms where such engineering surfaces interact with each other, the unevenness that define the manufactured surface profile may affect their performance. To include such real surfaces in the analysis, information regarding the height and spatial distribution is required at a sufficiently large number of points on these surfaces. Coordinate measuring machines can be used to collect such information, however, the time and cost required may not be feasible to measure all manufactured surfaces. Hence, numerically generating surfaces with the same height and spatial distribution as that of a few measured surfaces which belong to the same family of surfaces can be useful. Two such methods based on linear transformation of random matrices and Fourier series based digital filters, developed by Patir [82] and Hu and Tonder [85] respectively, were applied while generating pressure surfaces on the disc firtree slots. It was observed that both methods were able to generate similar rough surfaces for a given height and spatial distribution (autocorrelation function). While applying Patir's method it was observed

that for larger dimensions of the autocorrelation matrix, advanced methods are required for solving the nonlinear equations to achieve convergence. Hu and Tonder's method was found to handle relatively large matrices with better efficiency in generating rough surfaces as compared to the Patir's method. Two different analytical functions were fitted on the measured autocorrelation function (ACF) along with a Gaussian height distribution function. Although the same ratio of correlation lengths in orthogonal directions was used, two independent rough surfaces were obtained with two different autocorrelation functions. Hence, in addition to the correlation lengths, selection of appropriate analytical functions that represents the ACF of the surfaces is important.

6.1.3 FEA of the firtree joint to include geometric variation

Two- and three-dimensional finite element analysis of the firtree joint was performed in Abaqus 6.9-1. The material used for the blade and the disc was elastic and plane stress conditions were assumed for the two dimensional analysis. A parametric geometry of the firtree was created using the Open C API in the CAD environment of Siemens NX. This geometry was further imported in the FEA environment to perform an axisymmetric stress analysis with centrifugal load on the blade. The analysis was started by shifting the blade towards the disc axis, hence adding a uniform initial gap between the pressure faces on the disc and blade side of the nominal firtree joint. The parametrisation used for creating the firtree joint was able to represent the variation due to the manufacturing process in different ways: variation in the pressure angles and representing the waviness of the pressure lines by B-spline curves. While creating the three dimensional parametrised firtree geometry, the *sweep* feature in Siemens NX was used to include changes in the geometry between the front and rear edges. The sweep feature is unable to represent the unevenness of the pressure surface away from its edges. Instead, the nodal coordinates on the pressure surface in the FE model were modified to represent the roughness as obtained through Patir's method. The variation in the maximum tensile stress in the firtree notch regions was extracted by including variation in the geometry using these firtree parametrisations. The important observations made from this exercise are listed below:

1. **Variation in notch stresses from 2D stress analysis**: Variation in the pressure angles obtained by fitting a substitute geometry to the CMM data was used to evaluate the effect on the stress distribution in the firtree region. It was observed that the maximum von Mises stress in the region surrounding the pressure lines is minimum for angles slightly less than the nominal pressure angle. The contact region between the pressure faces on the blade and the disc firtree shifts as the pressure angles vary. Due to this shift in the location of the contact region, the contact pressure near the contact edges intensify which raises the von Mises stress beyond the material yield limit in that region. Such fluctuating peak stresses near

the contact edges, may nucleate a crack and further propagate it resulting in a catastrophic failure. The stresses were also observed to vary in the notch regions when the variation in pressure angles was included in the analysis. It was observed that the stress magnitudes in the notch regions closer to the disc axis are higher as compared to the other flanks. The mean maximum principal stress for the bottom notch is $\approx 10\%$ larger than that for the top and middle notch regions. However, the standard deviation in the maximum principal stress in the notch region for the middle flank was found to be $\approx 15\%$ higher. The magnitude of stresses on the right side of the firtree joints were found to be higher than that on the left side, due to pressure angle values being slightly larger on the right side. Another observation was that the standard deviation for variation in the notch stresses is affected more severely when variation in angles on individual flanks is independent of variation on the remaining flanks. Also the variation in the notch stresses obtained for reduced models of firtree flanks did not conform with the variation extracted from the whole firtree model. Hence, it can be concluded that different pressure faces coming into contact at different load increments have an important influence on the stress distribution in the notch regions.

2. **Effect of surface waviness from 2D stress analysis**: B-splines were fitted through the filtered CMM data in Siemens NX to represent the waviness on the manufactured pressure face. The linear elastic stress analysis of this geometry showed several locations on the pressure face where high von Mises stresses are observed due to the unevenness of the surface profile. These peak stresses exceed the yield limit of the material and hence would result in permanent localised deformations. With the application of a cyclic loading with an elastic plastic material, the surface profile of the pressure face on the disc may follow the profile of pressure face on the blade. Due to these peak stresses in contact regions, the stresses in the notch regions are also affected. However, the stress magnitudes in the notch regions are not found to be less affected. The use of an elastic-plastic material model in the stress analysis may provide more useful information regarding the variation in notch stresses when the waviness on the pressure face is included in the stress analysis.

3. **Variation in notch stresses from 3D stress analysis**: Although the three-dimensional stress analysis on the firtree joints showed similar trends in the variation of notch stresses, the magnitudes of stresses were observed to be $\approx 18\%$ higher in all notch regions as compared to the two-dimensional analysis. The 2D analysis, moreover cannot highlight the effect of change in geometric parameters at the front and rear edges which was observed from the 3D analysis. It was seen that when the variation in the pressure angles is included in the 3D analysis, the initial contact regions are not uniformly distributed over the pressure faces. This non-uniform contact due to the manufacturing variations in the firtree geometry

can have a considerable effect on the variation in notch stresses. Higher standard deviations were observed in the variation for notch stresses for lower correlation coefficients $(0.20, 0.28)$ of pressure angles between the front and rear edges. It was also observed that when the correlation coefficients are higher $(0.71, 0.73)$, the standard deviation in the variation of maximum principal stress tends to reduce. The standard deviations extracted from the 3D analysis are considerably higher than those observed from the 2D analysis with higher magnitudes on the top flank where the correlation coefficients were less than other two flanks. Hence, the variation in such geometric parameters between the front and rear edges also needs to be considered in the design process.

4. **Effect of surface roughness from 3D stress analysis**: An elastic stress analysis on the 3D firtree joints was performed by including the unevenness on pressure surfaces by two methods. As was observed with the 2D analysis, high von Mises stresses were observed in the contact regions which exceeded the elastic limit of the material.

The computational time required for the 3D analysis on the firtree joint was much higher ($\approx$ 15 hours) than the 2D stress analysis ($\approx$ 5 minutes). Due to the six contact pairs being active simultaneously, the load must be applied in small increments to achieve convergence in the contact conditions. In order to perform any optimisation study on the firtree joint, stress analysis is required to be performed iteratively for a large number of designs. The computational time required for such an exercise with the 3D analysis is not generally feasible. However, the variation in notch stresses extracted from 2D and 3D analyses showed similar trends, hence the 2D analysis can be used for the robust design optimisation on the firtree joint.

6.1.4 Robust design of firtree joints

An optimisation was performed on the firtree joints based on robustness principles in the presence of variations in geometry due to the manufacturing processes. The angle a pressure face makes with the vertical axis was used as the robust design variable while minimising the mean and standard deviation for variation in maximum principal stress in the notch regions. Since the magnitudes of stresses in the bottom notch regions are higher compared to the other notches, only the variation in notch stresses at the bottom flank were considered during the optimisation. Four objective functions comprising of means and standard deviations for variation in stress for both bottom notch regions were minimised. Even though the 2D stress analysis on the firtree joint takes $\approx$ 5 minutes on a desktop machine, multiple runs are required in order to evaluate the statistical moments using Monte Carlo methods. Hence, the use of surrogate models to replace the objective functions was explored. The Kriging methodology of approximating the expensive objective functions was used in this thesis and the non-dominated sorting

genetic algorithm-II (NSGA-II) was implemented with a population size of 50 for maximum 100 generations in order to obtain the predicted Pareto fronts. Five equally spaced points from this set of optimal solutions were used to update the response surfaces and this procedure was repeated three times.

Approximate response surfaces for the maximum principal stress in the bottom notch regions were constructed using 30 points based on a space-filling sampling strategy. It was observed that the magnitudes of mean and standard deviation for variation in stresses on the bottom right notch were greater than that on the bottom left notch. This could be due to the larger shift in the mean of pressure angles on the left side of the firtree joint as compared to the right side. A consistent decrease in the mean μ_{P1} was observed when the pressure angle was varied. However, the standard deviation σ_{P1} does not show considerable change for design angles below the original pressure angle. Both the mean and the standard deviation tend to intensify with any increase in the pressure angle. As the pressure angle is increased, the length of the pressure line decreases. Hence for similar loading conditions, the contact regions are more susceptible to shifting on to adjoining arcs, affecting the variation in the notch stresses more severely.

A firtree joint with a pressure angle that is 6% smaller than the original value is found to be less sensitive to the manufacturing variations with respect to the notch stresses. The mean for variation in maximum principal stress was reduced by 0.44% and 0.35% at the bottom left and right notches of the proposed design as compared to the old design while a reduction of 2.38% and 3.8% was observed in the standard deviation respectively. The new design also performed better with respect to the mean for notch stresses at the top and middle flanks. Although the standard deviation showed a slight rise for the notch stress in the middle flank the magnitudes of stresses were lower by 11% compared to the bottom notch.

In summary, the main contributions of this thesis are listed below:

- The variation in the manufactured geometry of a disc side firtree joint has been extracted from the CMM data using two different methods: curve fitting and Fourier transform. By assuming the surface heights on a machined surface to be a random process, new surfaces belonging to the same family of surfaces have been generated.
- The variation in the geometry due to the manufacturing process is related to the tensile stresses in the notch regions. The results showed that the bottom notch regions experience higher stresses as compared to the top and middle notch regions and hence the variation in the stresses at the bottom notch regions is critical.
- A surrogate model assisted design optimisation has been performed on the firtree joint based on the robustness principles by minimising the mean and standard deviation of maximum principal stress in the bottom notch regions with the pressure

angle as the design variable. The variations in the pressure angle extracted from the measured data on the manufactured disc side firtree slots have been used.

6.2 Future work

Further work could be carried out in the areas of extraction of geometric and roughness parameters from the CMM data. Research could also look into reducing the time involved in solving the contact conditions by the ABAQUS which contributes to most of the computational effort required in performing any optimisation on such a component. A few recommendations for future work in these areas are listed below:

1. The CMM is used to scan the disc side firtree geometries at the front and rear edges of the slot. Variation only on the disc side firtree joints was considered, whereas the blade side geometry was assumed to be nominal throughout this thesis. The variation in the blade side geometry will also have an effect on the stress distribution. A similar study could be carried out by including the variation in important geometric parameters defining the blade side firtree geometry such as the pressure arc radius, their lengths, orientations, notch radii, etc.

2. It was shown in chapter 2, that a considerable and inconsistent variation is observed in the fillet radii at different flanks (see Figures 2.19a and 2.20). It was also seen that the stresses intensify near the contact edges due to the shift in contact regions beyond the pressure faces. Accordingly, the effect these variations in the fillet radii, length of pressure faces, etc. have on the stress distribution will provide further information which would be useful while designing a firtree joint.

3. The roughness parametrisation requires information regarding the height distribution and the autocorrelation functions of the machined surfaces. The CMM data that was available during this work consisted of point coordinates randomly distributed in narrow strips along the front and rear edges of the firtree joints. Two assumptions were made while generating new surface profile data: (i) the points along the narrow strips at both edges are uniformly distributed and (ii) an exponential autocorrelation function with relatively larger correlation length along the thickness of the firtree slots compared to the correlation length along the narrow strips. Measuring the pressure faces with a constant sampling frequency in both orthogonal directions over the surface would provide useful information in order to generate rough surfaces more accurately.

4. The material model used for the blade and the disc in this work is a linear elastic material. However, it was shown that the stresses near the contact regions exceed the yield stress of the material, hence the use of an elastic-plastic material model would help in extracting the permanent localised deformations along the pressure lines with the application of cyclic loading.

5. 2D stress analysis on the firtree joints with smooth pressure lines take around 5 minutes on a desktop machine while the analysis with non-smooth pressure lines take much longer. The 3D analysis with rough surfaces took almost 15 hours of computational time. With every increment of load, contact conditions must be evaluated simultaneously in six contact pairs requiring substantial computational effort. For the non-smooth pressure lines, a finer mesh is required which makes this stress analysis even more expensive. Several researchers have proposed algorithms to evaluate contact pressures and areas when two non-smooth surfaces interact with each other [59, 66, 192]. However, most of these methods consider a single pair of contacting surfaces while solving the nonlinear equations. Further work could look into implementing these methods for multiple simultaneous contacts in conjunction with the FEA to provide a faster and reasonably accurate solution.

6. It is known that the machined surfaces of the firtree joint are shot-peened in order to enhance their fatigue life. Shot-peening induces residual compressive stresses on the surfaces which help in reducing the resultant tensile stresses in working conditions and hence retard the crack nucleation and propagation process. The magnitudes of maximum principal stress in the notch regions, as a result of these compressive stresses, will reduce. However, the variation observed in these notch stresses may not be affected due to the shot-peening process. The FE model that was used in this thesis did not account for these residual compressive stresses. A stress analysis including the effects of the shot-peening process could be used to compare the variation observed in the notch regions with the results available from this thesis.

7. The pressure lines in the firtree geometry analysed here are inclined at an angle with the vertical axis along which the centrifugal load is applied. Hence, at the contact interface, the load that is transferred can be transformed in two orthogonal components. Since normal and tangential forces are transferred across each contact interface, the contact region along each pressure line will be divided into *stick* and *slip* regions. Due to the cyclic nature of loading, these stick and slip regions shift along the contact interface which is the main factor affecting the wear of the material due to the fretting fatigue. A lifing model based on the fretting fatigue phenomenon could be used to predict the available life of the firtree joint which could then be used in the optimisation process.

8. The robust design optimisation performed on the firtree joint in this thesis involved minimising the statistical moments of the maximum principal stress in the bottom notch regions. Hence, four objective functions were minimised in searching for an optimum firtree joint design. It was observed that the new design showed a higher standard deviation in the notch stress at the middle flank. Including the mean and standard deviation for notch stresses in top and middle flank will result in a twelve objective optimisation which may provide a different design. Also, only the

pressure angle was considered as a design variable. The radius of the fillet will have an effect on the tensile stresses in the notch regions. Also, it was seen in this work that peak stresses are observed near the contact edges due to the contact zone shifting away from the pressure line. Hence, the fillet radii, pressure line lengths, and other related geometrical parameters could be included in the robust design optimisation as design variables.

9. The performance of the firtree joint was measured with respect to the maximum magnitude of the tensile stress in the notch regions which is located at some nodal point on the FE mesh. Such a performance measure will introduce noise in the objective function. Hence, to avoid such noise, instead of using maximum principal stress in the notch region, the J-integral (commonly used to characterise an advancing crack) could be used as an objective function.

10. It was seen that the interface properties between the blade and the disc in such joints play an important role in contributing to the damping capacity of the blade-disc assemblies. Previous studies performed on evaluating the damping capacities include the variations in the form of gaps between the pressure faces. The FE models created in this work, represent the variations due to manufacturing processes more accurately. The static analysis of the three dimensional firtree joint takes approximately 15 hours of computational time. However, a modal analysis in conjunction with model reduction methods will yield the frequency response with much lesser computational effort. Hence, such FE models could be used to assess the effect of manufacturing variations on the damping capacity of the bladed-discs.

Appendix A

Patir's method

A.1 Newton method to evaluate coefficients of transformation matrix

The nonlinear system of equations 3.8,

$$R_{pq} = \sum_{k=1}^{n-p} \sum_{l=1}^{m-q} A_{kl} A_{k+p,l+q}$$

can be rewritten as,

$$\mathbf{a^{b+1}} = \mathbf{a^b} - \left[\mathbf{J^b}\right]^{-1} \mathbf{f}(\mathbf{a^b}) \qquad \mathbf{b} = 0, 1, \ldots \tag{A.1}$$

where the coefficient matrix $[A_{kl}]$ is represented as $\mathbf{a}$ such that,

$$\mathbf{a} = [A_{11}\ A_{12}\ A_{13}\ \ldots\ A_{1m}\ A_{21}\ A_{22}\ A_{23}\ \ldots\ A_{nm}]^{\mathrm{T}}$$

and the $\mathbf{f}$ is written as,

$$\mathbf{f} = [f_{00}\ f_{01}\ f_{02}\ \cdots\ f_{0,m-1}\ f_{10}\ f_{11}\ f_{12}\ \cdots\ f_{n-1,m-1}]^{\mathrm{T}}$$

where f_{pq} is given by,

$$f_{pq} = \sum_{k=1}^{n-p} \sum_{l=1}^{m-q} A_{kl} A_{k+p,l+q} - R_{pq}$$

and the Jacobian matrix, $\mathbf{J^b}$, has components,

$$J^{\mathbf{b}}_{rs} = \frac{\partial f_{pq}}{\partial A^{\mathbf{b}}_{ij}} = A^{\mathbf{b}}_{i+p,j+q} + A^{\mathbf{b}}_{i-p,j-q}$$

where,

$$r = pm + q + 1$$

$$s = (i-1)m + j$$

To solve the equations, an initial approximation for the coefficient vector $\mathbf{a^0}$ is required, which can be obtained by [82],

$$A_{ij}^{\mathbf{0}} = sc_{ij}$$

where,

$$c_{ij} = \frac{R_{i-1,j-1}}{(n-i+1)(m-j+1)}$$

and,

$$s^2 = \frac{R_{00}}{\sum_{i=1}^{n}\sum_{j=1}^{m} c_{ij}^2}$$

$i, j, p, q, k,$ and l are defined as in Section 3.3.2. Convergence is said to have reached when the norm $||\mathbf{a^{b+1}} - \mathbf{a^b}|| = \mathbf{0}$.

Bibliography

[1] Mattingly, J. D., Heiser, W. H., and Pratt, D. T., 2002. *Aircraft Engine Design*, Second ed. American Institute of Aeronautics and Astronautics, Inc.

[2] *The Jet Engine*. Rolls-Royce, 2006.

[3] Kerrebrock, J., 1977. *Aircraft Engines and Gas Turbines*, First ed. The MIT Press.

[4] Samareh, J. A., 1999. "A Survey of Shape Parameterisation Techniques". In AIAA/CEAS/ICASE/NASA-LaRC International Forum on Aeroelasticity and Structural Dynamics Conference.

[5] Song, W., and Keane, A. J., 2004. "A study of shape parameterisation methods for airfoil optimisation". In 10th AIAA/ISSMO Multidisciplinary Analysis and Optimization Conference, pp. 2031–2038.

[6] Castonguay, P., and Nadarajah, S., 2007. "Effect of shape parameterization on aerodynamic shape optimization". In 45th AIAA Aerospace Sciences Meeting and Exhibit, pp. 8–11.

[7] Hicks, R. M., and Henne, P. A., 1978. "Wing design by numerical optimisation". *Journal of Aircraft,* ***15***(7), pp. 407–412.

[8] Sobieczky, H., 1999. "Parametric airfoils and wings". *Notes on Numerical Fluid Mechanics,* ***68***, pp. 71–88.

[9] Mousavi, A., Castonguay, P., and Nadarajah, S., 2007. "Survey of shape parameterization techniques and its effect on three-dimensional aerodynamic shape optimization". In 18th AIAA Computational Fluid Dynamics Conference, pp. 25–28.

[10] Connolly, P. E., 2009. "CAD software industry trends and directions". *Engineering Design Graphics Journal,* ***63***(1), pp. 26–33.

[11] Kang, Z., 2005. "Robust design optimization of structures under uncertainties". PhD thesis, Institut für Statik und Dynamik der Luft- und Raumfahrkonstruktionen Universität Stuttgart.

[12] Mourelatos, Z. P., 2006. "A methodology for trading-off performance and robustness under uncertainty". *Journal of Mechanical Design,* ***128***, pp. 856–863.

[13] Kuschel, N., and Rackwitz, R., 2000. "Optimal design under time-variant reliability constraints". *Structural Safety,* ***22***, pp. 113–127.

[14] Rackwitz, R., 2001. "Reliability analysis – a review and some perspectives". *Structural Safety,* ***23***, pp. 365–395.

[15] Kaymaz, I., and McMahoan, C. A., 2005. "A response surface method based on weighted regression for structural reliability analysis". *Probabilistic Engineering Mechanics,* ***20***, pp. 11–17.

[16] Keane, A. J., and Nair, P. B., 2005. *Computational approaches for aerospace design*, First ed. John Wiley & Sons, Ltd.

[17] Brujic, D., Ristic, M., Mattone, M., Maggiore, P., and Poli, G. P. D., 2010. "CAD based shape optimisation for gas turbine component design". *Structural and Multidisciplanry Optimization,* ***41***, pp. 647–659.

[18] Thakur, N., Keane, A. J., and Nair, P. B., 2011. "Robust design of turbine blades against manufacturing variability". *International Journal of Reliability and Safety,* ***5***(3/4), pp. 420–436.

[19] Beyer, H.-G., and Sendhoff, B., 2007. "Robust optimisation – A comprehensive survey". *Computer methods in applied mechanics and engineering,* ***196***, pp. 3190–3218.

[20] Taguchi, G., 1986. *Introduction to Quality Engineering.* Tokio, Japón: Asian Productivity Organization.

[21] McAllister, C. D., and Simpson, T. W., 2003. "Multidisciplinary robust design optimization of an internal combustion engine". *Transactions of the ASME: Journal of Mechanical Design,* ***125***, pp. 124–130.

[22] Kumar, A., Keane, A. J., Nair, P. B., and Shahpar, S., 2006. "Robust design of compressor blades against manufacturing variations". In Proceedings of IDETC/-CIE 2006.

[23] Thakur, N., Keane, A. J., and Nair, P. B., 2008. "Capture of manufacturing uncertainty in turbine blades through probabilistic techniques". In Proceedings: Association for Structural and Multidisciplinary Optimization in the UK (ASMO-UK).

[24] Du, X., and Chen, W., 2000. "Towards a better understanding of modelling feasibility robustness in engineering design". *Journal of Mechanical Design,* ***122***, pp. 385–394.

[25] Sawyer, J. W., 1976. *Sawyer's Gas Turbine Engineering Handbook*, Second ed. Gas Turbine Publications.

[26] Kanth, P. S., 1998. "2D & 3D analysis of fir-tree joints in aeroengine discs". Master's thesis, University of Toronto.

[27] Qin, F., Chen, L., Li, Y., and Zhang, X., 2006. "Fundamental frequencies of turbine blades with geometry mismatch in fir-tree attachments". *Transactions of the ASME,* ***128***, pp. 512–516.

[28] Singh, M. P. "Probabilistic estimation of the effect of dimensional tolerance for turbine/compressor blade attachment".
http://www.dresser-rand.com/techpapers/tp021.pdf.

[29] Rao, J. S., 1998. "Application of fracture mechanics in the failure analysis of a last stage steam turbine blade". *Mechanism and Machine Theory,* ***33***(5), pp. 599–609.

[30] Witek, L., 2006. "Failure analysis of turbine disc of an aero engine". *Engineering Failure Analysis,* ***13***, pp. 9–17.

[31] Arrieta, H. V., Wackers, P., Dang Van, K., Constantinescu, A., and Maitournam, H., 2003. "Modelling attempts to predict fretting-fatigue life on turbine components". In RTO-AVT Specialists Meeting on "The Control and Wear in Military Platforms".

[32] James, M. N., 2011. "Residual stress influences on structural reliability". *Engineering Failure Analysis,* ***18***, pp. 1909–1920.

[33] Barella, S., Boniardi, M., Cincera, S., Pellin, P., Degive, X., and Gijbels, S., 2011. "Failure analysis of a third stage gas turbine blades". *Engineering Failure Analysis,* ***18***, pp. 386–393.

[34] Farhangi, H., and Moghadam, A. A. F., 2007. "Fractographic investigation of the failure of second stage gas turbine blades". In 8th International Fracture Conference, Istanbul, Turkey, pp. 577–584.

[35] Song, W., 2002. "Shape optimization of turbine blade firtrees". PhD thesis, University of Southampton.

[36] Song, W., Keane, A., Rees, J., Bhaskar, A., and Bagnall, S., 2002. "Turbine blade fir-tree root design optimisation using intelligent cad and finite element analysis". *Computers & Structures,* ***80***(24), pp. 1853–1867.

[37] Zhang, M., Zhang, Q., Zheng, L., and Zhang, D., 2013. "Research on three-dimensional structure optimization for fir-tree root and rim of turbine blad with complex damping structure". *Applied Mechanics and Materials,* ***312***, pp. 55–59.

[38] Zhou, Q., Zhang, M., Chen, H., and Xie, Y., 2013. "Design optimization for fir-tree root of turbine blade considering manufacturing variations". *Applied Mechanics and Materials,* ***694***, pp. 2733–2737.

[39] Saliby, E., 1990. "Descriptive sampling: a better approach to Monte Carlo simulation". *Journal of the Operational Research Society,* ***41***(12), pp. 1133–1142.

[40] Dowling, M. M., Griffin, P. M., Tsui, K. L., and Zhou, C., 1997. "Statistical issues in geometric feature inspection using coordinate measuring machines". *Technometrics,* ***39***(1), pp. 3–16.

[41] Carbone, V., Carocci, M., Savio, E., Sansoni, G., and Chiffre, L. D., 2001. "Combination of a vision system and a coordinate measuring machine for the reverse engineering of freeform surfaces". *The Internation Journal of Advanced Manufacturing Technology,* ***17***, pp. 263–271.

[42] Zhang, G., Veale, R., Charlton, T., Borchardt, B., and Hocken, R., 1985. "Error compensation of coordinate measuring machines". *Annals of the CIRP,* ***34***(1), pp. 445–448.

[43] Yan, Z., Yang, B., and Menq, C., 1999. "Uncertainty analysis and variation reduction of three dimensional coordinate metrology. Part 1: geometric error decomposition". *Internation Journal of Machine Tools & Manufacture,* ***39***, pp. 1199–1217.

[44] Summerhays, K. D., Henke, R. P., Baldwin, J., Cassou, R. M., and Brown, C. W., 2002. "Optimizing discrete point sample patterns and measurement data analysis on internal cylinderical surfaces with systematic form deviations". *Precision Engineering,* ***26***, pp. 105–121.

[45] Brown, C. W., 1992. "Dimensional inspection techniques for sample-point measurement technology". *Precision Engineering,* ***14***(2), pp. 110–111.

[46] Shunmugam, M. S., 1986. "On assessment of geometric errors". *International Journal of Production Research,* ***24***(2), pp. 413–425.

[47] Capello, E., and Sameraro, Q., 2001. "The harmonic fitting method for the assessment of the substitute geometry estimate error. Part I: 2D and 3D theory". *International Journal of Machine Tools & Manufacture,* ***41***, pp. 1071–1102.

[48] Weckenmann, A., Eitzert, H., Garmer, M., and Weber, H., 1995. "Functionality-oriented evaluation and sampling strategy in coordinate metrology". *Precision Engineering,* ***17***(4), pp. 244–252.

[49] Choi, W., Kurfess, T. R., and Cagan, J., 1998. "Sampling uncertainty in coordinate measurement data analysis". *Precision Engineering,* ***22***, pp. 153–163.

[50] Murthy, T. S. R., and Abdin, S. Z., 1980. "Minimum zone evaluation of surfaces". *International Journal of Machine Tool Design and Research,* ***20***, pp. 123–136.

[51] Capello, E., and Semeraro, Q., 2000. "Harmonic fitting approach for plane geometry measurements". *International Journal of Advanced Manufacturing Technology,* ***16***, pp. 250–258.

[52] Sinclair, G. B., and Cromier, N. G., 2002. "Contact stresses in dovetail attachments: Alleviation via precision crowning". *Journal of Engineering Gas Turbines and Power,* ***125***, pp. 1033–1041.

[53] MATLAB R2010B HELP. *The MathWorks Inc.*

[54] Thakur, N., 2010. "Probabilistic Manufacturing Variability Quantification from Measurement Data for Robust Design of Turbine Blades". PhD thesis, University of Southampton.

[55] Press, W. H., Teukolsky, S. A., Vetterling, W. T., and Flannery, B. P., 1992. *Numerical Recipes in C*, Second ed. Cambridge University Press.

[56] Bensmail, H., Golek, J., Moody, M. M., Semmes, J. O., and Haoudi, A., 2005. "A novel approach for clustering proteomics data using bayesian fast fourier transform". *Bioinformatics,* ***21***(10), pp. 2210–2224.

[57] Moore, D. F., 1975. *Principles and applications of tribology*, First ed. Pergamon Press.

[58] Greenwood, J. A., and Williamson, J. B. P., 1966. "Contact of nominally flat surfaces". *Proceedings of the Royal Society of London. Series A. Mathematical and Physical Sciences,* ***295***(1442), pp. 300–319.

[59] Liu, G., Wang, Q., and Lin, C., 1999. "A survey of current models for simulating the contact between rough surfaces". *Tribology Transactions,* ***42***(3), pp. 581–591.

[60] Ciulli, E., Ferreira, L. A., Pugliese, G., and Tavares, S. M. O., 2008. "Rough contacts between actual engineering surfaces part I. Simple models for roughness description". *Wear,* ***264***, pp. 1105–1115.

[61] Pugliese, G., Tavares, S. M. O., Ciulli, E., and Ferreira, L. A., 2008. "Rough contacts between actual engineering surfaces part II. Contact mechanics". *Wear,* ***264***, pp. 1116–1128.

[62] Thwaite, E. G., 1984. "Measurement and control of surface finish in manufacture". *Precision Engineering,* ***6***(4), pp. 207–217.

[63] Liu, G., Zhu, J., Yu, L., and Wang, Q. J., 2001. "Elasto-plastic contact of rough surfaces". *Tribology Transactions,* ***44***(3), pp. 437–443.

[64] Nayak, P. R., 1971. "Random process model of rough surfaces". *Journal of Lubrication Technology,* ***93***, pp. 398–407.

[65] Nayak, P. R., 1973. "Random process model of rough surfaces in plastic contact". *Wear,* ***26***(3), pp. 305–333.

[66] Bhushan, B., 1998. "Contact mechanics of rough surfaces in tribology: multiple asperity contact". *Tribology letters,* ***4***(1), pp. 1–35.

[67] Ao, Y., Wang, Q. J., and Chen, P., 2002. "Simulating the worn surface in a wear process". *Wear,* ***252***(1), pp. 37–47.

[68] Sellgren, U., Björklund, S., and Andersson, S., 2003. "A finite element-based model of normal contact between rough surfaces". *Wear,* ***254***, pp. 1180–1188.

[69] Kogut, L., and Etsion, I., 2003. "A finite element based elastic-plastic model for the contact of rough surfaces". *Tribology Transactions,* ***46***(3), pp. 383–390.

[70] Ardito, R., Corigliano, A., and Frangi, A., 2010. "Finite element modelling of adhesion phenomena in MEMS". In 11th International Conference on Thermal, Mechanical & Multi-Physics Simulation, and Experiments in Microelectronics and Microsystems (EuroSimE), 2010, IEEE, pp. 1–6.

[71] Reeves, M. J., 1985. "Rock surface roughness and frictional strength". *International journal of Rock Mechanics and Mining Sciences & Geomechanics Abstracts,* ***22***(6), pp. 429–442.

[72] Grasselli, G., Wirth, J., and Egger, P., 2002. "Quantitative three-dimensional description of a rough surface and parameter evolution with shearing". *International journal of Rock Mechanics and Mining Sciences,* ***39***(6), pp. 789–800.

[73] Thomas, T. R., 1981. "Characterization of surface roughness". *Precision Engineering,* ***3***(2), pp. 97–104.

[74] Dong, W. P., Sullivan, P. J., and Stout, K. J., 1992. "Comprehensive study of parameters for characterizing three-dimensional surface topography I: Some inherent properties of parameter variaton". *Wear,* ***159***, pp. 161–171.

[75] Dong, W. P., Sullivan, P. J., and Stout, K. J., 1993. "Comprehensive study of parameters for characterizing three-dimensional surface topography II: Statistical properties of parameter variation". *Wear,* ***167***, pp. 9–21.

[76] Dong, W. P., Sullivan, P. J., and Stout, K. J., 1994. "Comprehensive study of parameters for characterising three-dimensional surface topography III: Parameters for characterising amplitude and some functional properties". *Wear,* ***178***, pp. 29–43.

[77] Dong, W. P., Sullivan, P. J., and Stout, K. J., 1994. "Comprehensive study of parameters for characterising three-dimensional surface topography IV: Parameters for characterising spatial and hybrid properties". *Wear,* ***178***, pp. 45–60.

[78] Thomas, T. R., and Rosén, B. G., 2000. "Determination of the optimum sampling interval for rough contact mechanics". *Tribology International,* ***33***, pp. 601–610.

[79] Peklenik, J., 1967-68. "New developments in surface characterization and measurements by means of random process analysis". *Proceedings of the Institution of Mechanical Engineers,* ***182***, pp. 108–126.

[80] Box, G. E. P., and Jenkins, G. M., 1970. *Time series analysis forecasting and control*, First ed. Holden-Day.

[81] Thomas, T. R., 1982. *Rough Surfaces.* Longman London.

[82] Patir, N., 1978. "A numerical procedure for random generation of rough surfaces". *Wear,* ***47***, pp. 263–277.

[83] Elson, J. M., and Bennett, J. M., 1995. "Calculation of the power spectral density from surface profile data". *Applied Optics,* ***34***(1), pp. 201–208.

[84] Duparré, A., Ferre-Borrull, J., Gliech, S., Notni, G., Steinert, J., and Bennett, J. M., 2002. "Surface characterization techniques for determining the root-mean-square roughness and power spectral densities of optical components". *Applied Optics,* ***41***(1), pp. 154–171.

[85] Hu, Y. Z., and Tonder, K., 1992. "Simulation of 3-d random rough surface by 2d digital filter and fourier analysis". *International Journal of Machine Tools and Manufacture,* ***32***(1), pp. 83–90.

[86] Whitehouse, D. J., and Archard, J. F., 1970. "The properties of random surface of significance in their contact". *Proceedings of the Royal Society of London. Series A. Mathematical and Physical Sciences,* ***316***, pp. 97–121.

[87] Manesh, K. K., Ramamoorthy, B., and Singaperumal, M., 2010. "Numerical generation of anisotropic 3D non-Gaussian engineering surface with specified 3D surface roughness parameters". *Wear,* ***268***, pp. 1371–1379.

[88] Bakolas, V., 2003. "Numerical generation of arbitrarily oriented non-Gaussian three-dimensional rough surfaces". *Wear,* ***254***, pp. 546–554.

[89] Watson, W., and Spedding, T. A., 1982. "The time series modelling of non-Gaussian engineering processes". *Wear,* ***83***, pp. 215–231.

[90] Whitehouse, D. J., 1983. "The generation of two dimensional random surfaces having a specified function". *CIRP Annals-Manufacturing Technology,* ***32***(1), pp. 495–498.

[91] Wu, J.-J., 2000. "Simulation of rough surfaces with fft". *Tribology International,* ***33***, pp. 47–58.

[92] Wu, J.-J., 2004. "Simulation of non-gaussian surfaces with fft". *Tribology International,* ***37***, pp. 339–346.

[93] Thomas, T. R., Rosén, B. G., and Amini, N., 1999. "Fractal characterization of the anisotropy of rough surfaces". *Wear,* ***232***, pp. 41–50.

[94] Ling, F. F., 1990. "Fractal, engineering surfaces and tribology". *Wear,* ***136***, pp. 141–156.

[95] Majumdar, A., and Tien, C. L., 1990. "Fractal characterization and simulation of rough surfaces". *Wear,* ***136***, pp. 313–327.

[96] Mack, C. A., 2013. "Generating random rough edges, surfaces, and volumes". *Applied Optics,* ***52***(7), pp. 1472–1480.

[97] Chilamakuri, S. K., and Bhushan, B., 1998. "Contact analysis of non-gaussian random surfaces". *Proceedings of the Institution of Mechanical Engineers, Part J: Journal of Engineering Tribology,* ***212***(1), pp. 19–32.

[98] Zienkiewicz, O. C., and Taylor, R. L., 1977. *The finite element method.* McGraw-hill, London.

[99] Aliabadi, M. H., 2002. *The Boundary Element Method Volume 2: Applications in Solids and Structures.* John Wiley & Sons, Ltd.

[100] Smith, G. D., 1993. *Numerical solution of partial differential equations: finite difference methods*, Third ed. Oxford University Press.

[101] Thomas, J. W., 1995. *Numerical partial differential equations: finite difference methods.* Springer Verlag.

[102] Demirdžić, I., and Martinović, D., 1993. "Finite volume method for thermo-elasto-plastic stress analysis". *Computer Methods in Applied Mechanics and Engineering,* ***109***, pp. 331–349.

[103] Fainberg, J., and Leister, H.-J., 1999. "Finite volume multigrid solver for thermo-elastic stress analysis in anisotropic materials". *Computer Methods in Applied Mechanics and Engineering,* ***137***, pp. 167–174.

[104] Demirdžić, I., Horman, I., and Martinović, D., 2000. "Finite volume analysis of stress and deformation in hygro-thermo-elastic orthotropic body". *Computer Methods in Applied Mechanics and Engineering,* ***190***, pp. 1221–1232.

[105] Banerjee, P. K., and Butterfield, R., 1981. *Boundary Element Methods in Engineering Science.* McGraw-Hill Book Company (UK) Limited.

[106] Rao, J. S., 1991. *Turbomachine Blade Vibrations*, First ed. New Age International Publishers.

[107] Matveev, V. V., Chaikovskii, B. S., and Shpak, D. E., 1977. "Study of the damping capacity of a turbine blade fir-tree fixing with a composite root". *Strength of Materials,* ***9***(12), pp. 1485–1489.

[108] Matveev, V. V., Chaikovskii, B. S., Kovalev, M. S., and Rzhavin, L. N., 1973. "Effect of design features and loading conditions on damping capacity of a turbine blade fir-tree root". *Strength of Materials,* ***5***(10), pp. 1228–1233.

[109] Petrov, E. P., and Ewins, D. J., 2006. "Effects of damping and varying contact area at blade-disk joints in forced response analysis of bladed disc assemblies". *Journal of Turbomachinery,* ***128***, pp. 403–410.

[110] Petrov, E. P., 2008. "Explicit finite element models of friction dampers in forced response analysis of bladed disks". *Transactions-ASME: Journal of Engineering Gas Turbines and Power,* ***130***(2), pp. 022502–1–022502–11.

[111] Hou, J., and Wicks, B. J., 2002. Root flexibility and untwist effects on vibration characteristics of a gas turbine blade. Tech. rep., DTIC Document.

[112] Avalos, J., Mignolet, M. P., and Soize, C., 2009. "Response of bladed disks with mistuned blade-disk interfaces". *Proceedings of ASME Turbo Expo 2009: Power for Land, Sea and Air,* ***6***(Pts A and B), pp. 1–9.

[113] Sinclair, G. B., and Cormier, N. G., 2002. "Contact stresses in dovetail attachments: Physical modeling". *Journal of Engineering for Gas Turbines and Power,* ***124***, pp. 325–331.

[114] Sinclair, G. B., Cormier, N. G., Griffin, J. H., and Meda, G., 2002. "Contact stresses in dovetail attachments: Finite element modeling". *Transactions of the ASME,* ***124***, pp. 182–189.

[115] Charleux, D., Gibert, C., Thouverez, F., Lombard, J. P., and Dupeux, J. "Analysis of a bladed disk with friction in blade attachments".

[116] Charleux, D., Gibert, C., Thouverez, F., and Dupeux, J., 2006. "Numerical and experimental study of friction damping in blade attachments of rotating bladed disks". *International Journal of Rotating Machinery,* ***2006***, pp. 1–13.

[117] Chan, S. K., and Tuba, I. S., 1971. "A finite element method for contact problems of solid bodies". *International Journal of Mechanical Sciences,* ***13***, pp. 627–639.

[118] Singh, G. D., and Rawtani, S., 1982. "Fir tree fastening of turbomachinery blades – I". *International Journal of Mechanical Sciences,* ***24***(6), pp. 377–384.

[119] Singh, G. D., and Rawtani, S., 1982. "Fir tree fastening of turbomachinery blades – II". *International Journal of Mechanical Sciences,* ***24***(6), pp. 385–391.

[120] Meguid, S. A., Kanth, P. S., and Czekanski, A., 2000. "Finite element analysis of fir-tree region in turbine discs". *Finite Element Analysis and Design,* ***35***, pp. 305–317.

[121] Mase, M., Kaneko, Y., Kobayashi, T., Fujita, K., and Kadoya, Y. Ikeda, S., 1992. "Root and groove contact analysis for steam turbine blades". *Japan Society of Mechanical Engineers International Journal,* ***35***(4), pp. 508–514.

[122] Issler, S., and Roos, E., 2003. "Numerical and experimental investigations into life assessment of blade-disc connections of gas turbines". *Nuclear Engineering and Design,* ***226***, pp. 155–164.

[123] Hu, D., Wang, R., and Hou, G., 2013. "Life assessment of turbine components through experimental and numerical investigations". *Journal of Pressure Vessel Technology,* ***135***, pp. 024502–1–024502–6.

[124] Liu, C. L., Lu, Z. Z., Xu, Y. L., and Yue, Z. F., 2005. "Reliability for low cycle fatigue life of the aeronautical engine turbine disc structure under random environment". *Materials Science and Engineering: A,* ***395***, pp. 218–225.

[125] Lu, Z. Z., Liu, C. L., Yue, Z. F., and Xu, Y. L., 2005. "Probabilistic safe analysis of the working life of a powder metallurgical turbine disc". *Materials Science and Engineering: A,* ***395***, pp. 153–159.

[126] Rauch, M., and Roos, E., 2008. "Life assessment of multiaxially cyclic loaded turbine components". *Fatigue & Fracture of Engineering Materials & Structures,* ***31***(6), pp. 441–451.

[127] Isobe, N., and Nogami, S., 2009. "Micro-crack growth behaviour and life in high temperature low cycle fatigue of blade root and disc joint for turbines". *International Journal of Pressure Vessels and Piping,* ***86***, pp. 622–627.

[128] Anandavel, K., and Prakash, R. V., 2011. "Effect of three-dimensional loading on macroscopic fretting aspects of an aero-engine blade-disc dovetail interface". *Tribology International,* ***44***, pp. 1544–1555.

[129] Zhang, M., Zhang, D., and Xie, Y., 2012. "Design optimization for double-t root and rim of turbine blade with three-dimensional finite element method". *Applied Mechanics and Materials,* ***215–216***, pp. 239–243.

[130] Maharaj, C., Morris, A., and Dear, J. P., 2012. "Modelling of creep in inconel 706 turbine disc fir-tree". *Materials Science & Engineering: A,* ***558***, pp. 412–421.

[131] Siemens NX. `http://www.plm.automation.siemens.com/en_gb/products/nx/`. [Online; accessed 19-June-2013].

[132] Dassault Systémes' ABAQUS. `http://www.3ds.com/products/simulia/portfolio/abaqus/`. [Online; accessed 19-June-2013].

[133] Delhelay, D. S., 1999. "Nonlinear finite element analysis of the coupled thermo-mechanical behaviour of turbine disc assemblies". Master's thesis, University of Toronto.

[134] Help documentation. *SIMULIA Abaqus 6.9*.

[135] Zboinski, G., 1995. "Physical and geometrical non-linearities in contact problems of elastic turbine blade attachments". *Proceedings of the Institution of Mechanical Engineers, Part C: Journal of Mechanical Engineering Science,* ***209***(4), pp. 273–286.

[136] Mackenzie, A. C., Hancock, J. W., and Brown, D. K., 1977. "On the influence of state of stress on ductile failure initiation in high strength steels". *Engineering Fracture Mechanics,* ***9***(1), pp. 167–188.

[137] Hancock, J. W., and Mackenzie, A. C., 1976. "On the mechanisms of ductile failure in high-strength steels subjected to multi-axial stress-states". *Journal of the Mechanics and Physics of Solids,* ***24***(2), pp. 147–160.

[138] de Oliveira, V., da Costa Villar, G., and Menzes, J. C., 2012. "Methodology for structural integrity analysis of gas turbine blades". *Journal of Aerospace Technology and Management,* ***4***(1), pp. 51–59.

[139] NX 6 Help Library. *Siemens NX*.

[140] Tian, J. W., Dai, K., Villegas, J. C., Shaw, L., Liaw, P. K., Klarstrom, D. L., and Ortiz, A. L., 2008. "Tensile properties of a nickel-base allow subjected to surface severe plastic deformation". *Materials Science and Engineering A,* ***493***, pp. 176–183.

[141] Dong, J., Liu, W., Ding, W., and Zou, J., 2011. "Surface characteristics and high cycle fatigue performance of shot peened magnesium alloy ZK60". *Journal of Metallurgy,* ***2011***, pp. 1–9.

[142] Bouraoui, C., Sghaier, R. B., and Fathallah, R., 2009. "An engineering predictive design approach of high cycle fatigue reliability of shot peened metallic parts". *Materials and Design,* ***30***, pp. 475–486.

[143] Hu, D., and Wang, R., 2013. "Combined fatigue experiments on full scale turbine components". *Aircraft Engineering and Aerospace Technology,* ***85***(1), pp. 4–9.

[144] Taguchi, G., Tung, L. W., and Clausing, D., 1987. *System of experimental design: engineering methods to optimize quality and minimize costs*, Vol. 1. UNIPUB-/Kraus International Publications New York.

[145] Trosset, M. W., 1997. "Taguchi and robust optimisation". *Rapport technique, Rice University*, pp. 1–10.

[146] Unal, R., Stanley, D. O., and Joyner, C. R., 1993. "Propulsion system design optimization using the taguchi method". *IEEE Transactions on Engineering Management,* ***40***(3), pp. 315–322.

[147] Robinson, T. J., Borror, C. M., and Myers, R. H., 2004. "Robust parameter design: A review". *Quality and Reliability Engineering International,* ***20***, pp. 81–101.

[148] Kurt, U., and Onbilgin, G., 2009. "Design and optimization of axial flux permanent magnet synchronous machines using taguchi approach". In International Conference on Electrical and Electronics Engineering, 2009. ELECO 2009., IEEE.

[149] Tsai, C.-S., 2002. "Evaluation and optimisation of integrated manufacturing system operations using taguch's experiment design in computer simulation". *Computers & Industrial Engineering,* ***43***(3), pp. 591–604.

[150] Khan, Z. A., and Al-Darrab, I. A., 2010. "Taguchi techniques-based study on the effect of mobile phone conversation on drivers' reaction time". *International Journal of Quality & Reliability Management,* ***27***(1), pp. 63–77.

[151] Nair, V. N., Abraham, B., MacKay, J., Box, G., Kacker, R. N., Lorenzen, T. J., Lucas, J. M., Myers, R. H., Vining, G. G., Nelder, J. A., Phadke, M. S., Sacks, J., Welch, W. J., Shoemaker, A. C., Tsui, K. L., Taguchi, S., and Wu, C. F. J., 1992. "Taguchi's parameter design: A panel discussion". *Technometrics,* ***34***(2), pp. 127–161.

[152] Welch, W. J., Yu, T.-K., Kang, S. M., and Sacks, J., 1990. "Computer experiments for quality control by parameter design". *Journal of Quality Control,* ***22***(1), pp. 15–22.

[153] Shoemaker, A. C., Tsui, K. L., and Wu, C. F. J., 1989. "Economical experminetation methods for robust parameter design". In Fall Technical Conference, American Society of Quality Control, Houston, TX.

[154] Tsutsui, S., and Ghosh, A., 1997. "Genetic algorithms with a robust solution searching scheme". *IEEE Transactions on Evolutionary Computation,* ***1***(3), pp. 201–208.

[155] Parkinson, D. B., 1997. "Robust design by variability optimization". *Quality and Reliability Engineering International,* ***13***(2), pp. 97–102.

[156] Das, I., 2000. "Robustness optimization for constrained nonlinear programming problems". *Engineering Optimization,* ***32***, pp. 585–618.

[157] Gunawan, S., and Azarm, S., 2005. "Multi-objective robust optimization using a sensitivity region concept". *Structural Multidisciplinary Optimization,* ***29***, pp. 50–60.

[158] Park, G.-J., Lee, T. H., Lee, K. H., and Hwang, K. H., 2006. "Robust design: An overview". *AIAA Journal,* ***44***(1), pp. 181–191.

[159] Zang, C., Friswell, M. I., and Mottershead, J. E., 2005. "A review of robust optimal design and its application in dynamics". *Computers & Structures,* ***83***, pp. 315–326.

[160] Sun, G., Li, G., Zhou, S., Li, H., Hou, S., and Li, Q., 2011. "Crashworthiness design of vehicle by using multiobjective robust optimization". *Structural Multidisciplinary Optimization,* ***44***, pp. 99–110.

[161] Keane, A. J., 2012. "Cokriging for robust design optimization". *AIIA Journal,* ***50***(11), pp. 2351–2364.

[162] Jin, Y., and Sendhoff, B., 2003. "Trade-off between performance and robustness: An evolutionary multiobjective approach". In Evolutionary Multi-Criterion Optimization, Springer, pp. 237–251.

[163] Pant, S., 2012. "Multidisciplinary and multiobjective design optimisation of coronary stents". PhD thesis, University of Southampton.

[164] Deb, K., 2001. *Multi-objective optimization using evolutionary algorithms*, Vol. 16. Wiley.

[165] Kim, I. Y., and De Weck, O. L., 2006. "Adaptive weighted sum method for multiobjective optimization: a new method for Pareto front generation". *Structural and Multidisciplinary Optimization,* ***31***(2), pp. 105–116.

[166] Kim, I. Y., and De Weck, O. L., 2005. "Adaptive weighted-sum method for bi-objective optimization: Pareto front generation". *Structural and Multidisciplinary Optimization,* ***29***(2), pp. 149–158.

[167] Das, I., and Dennis, J. E., 1997. "A closer look at drawbacks of minimizing weighted sums of objectives for Pareto set generation in multicriteria optimization problems". *Structural Optimization,* ***14***, pp. 63–69.

[168] Das, I., and Dennis, J. E., 1998. "Normal-boundary intersection: A new method for generating the Pareto surface in nonlinear multicriteria optimization problems". *SIAM Journal on Optimization,* ***8***(3), pp. 631–657.

[169] Ismail-Yahaya, A., and Messac, A., 2002. "Effective generation of the pareto frontier using the normal constraint method". In AIAA 40th Aerospace Sciences Meeting and Exhibit.

[170] Messac, A., Ismail-Yahaya, A., and Mattson, C. A., 2003. "The normalized normal constraint method for generating the Pareto frontier". *Structural and Multidisciplinary Optimization,* ***25***, pp. 86–98.

[171] Zitzler, E., Laumanns, M., and Thiele, L., 2001. "SPEA2: Improving the strength Pareto evolutionary algorithm". *Eidgenössische Technische Hochschule Zürich (ETH), Institut für Technische Informatik und Kommunikationsnetze (TIK).*

[172] Corne, D. W., Knowles, J. D., and Oates, M. J., 2000. "The pareto envelope-based selection algorithm for multiobjective optimization". In Parallel Problem Solving from Nature PPSN VI, Springer, pp. 839–848.

[173] Zitzler, E., and Thiele, L., 1999. "Multiobjective evolutionary algorithms: A comparative case study and the strength pareto approach". *IEEE Transactions on Evolutionary Computation,* ***3***(4), pp. 257–271.

[174] Deb, K., Pratap, A., Agarwal, S., and Meyarivan, T., 2002. "A fast and elitist multiobjective genetic algorithm: NSGA-II". *IEEE Transactions on Evolutionary Computation,* ***6***(2), pp. 182–197.

[175] Shukla, P. K., and Deb, K., 2007. "On finding multiple pareto-optimal solutions using classical and evolutionary generating methods". *European Journal of Operational Research,* ***181***(3), pp. 1630–1652.

[176] Kumar, A., Keane, A. J., Nair, P. B., and Shahpar, S., 2006. "Robust design of compressor fan blades against erosion". *Journal of Mechanical Design,* ***128***, pp. 864–873.

[177] Atiquzzaman, M., Liong, S.-Y., and Yu, X., 2006. "Alternative decision making in water distribution network with NSGA-II". *Journal of Water Resources Planning and Management,* ***132***(2), pp. 122–126.

[178] Srinivas, N., and Deb, K., 1994. "Multiobjective optimizationg using nondominated sorting in genetic algorithms". *Evolutionary computation,* ***2***(3), pp. 221–248.

[179] Forrester, A., Sóbester, A., and Keane, A., 2008. *Engineering Design via Surrogate Modelling*, First ed. Wiley.

[180] Krige, D. G., 1951. "A statistical approach to some basic mine valuation problems on the witwatersrand". *Journal of Chemical, Metallurgical and Mininng Society of South Africa,* ***52***(6), pp. 119–139.

[181] Cressie, N., 1990. "The origins of Kriging". *Mathematical Geology,* ***22***(3), pp. 239–252.

[182] Matheron, G., 1963. "Principles of geostatics". *Economic Geology,* ***58***, pp. 1246–1266.

[183] Sacks, J., Williams, W. J., Mitchell, T. J., and Wynn, H. P., 1989. "Design and analysis of computer experiments". *Statistical science,* ***4***(4), pp. 409–423.

[184] Simpson, T. W., Mauery, T. M., Korte, J. J., and Mistree, F., 2001. "Kriging models for global approximation in simulation-based multidisciplinary design optimization". *AIAA journal,* ***39***(12), pp. 2233–2241.

[185] Jeong, S., Murayama, M., and Yamamoto, K., 2005. "Efficient optimization design method using kriging model". *Journal of Aircraft,* ***42***(2), pp. 413–420.

[186] Jones, D. R., Schonlau, M., and Welch, W. J., 1998. "Efficient global optimization of expensive black-box functions". *Journal of Global Optimization,* ***13***, pp. 455–492.

[187] Toal, D. J. J., Bressloff, N. W., Keane, A. J., and Holden, C. M. E., 2008. "Kriging hyperparameter tuning strategies". *AIAA Journal,* ***46***(5), pp. 1240–1252.

[188] Toal, D. J. J., Bressloff, N. W., Keane, A. J., and Holden, C. M. E., 2011. "The development of a hybridized particle swarm for kriging hyperparameter tuning". *Engineering optimization,* ***43***(6), pp. 675–699.

[189] Mack, Y., Goel, T., Shyy, W., and Haftka, R., 2007. "Surrogate model-based optimization framework: A case study in aerospace design". In *Evolutionary Computation in Dynamic and Uncertain Environments*. Springer, pp. 323–342.

[190] Keane, A. J., 2009. "Comparison of several optimization strategies for robust turbine blade design". *Journal of Propulsion and Power,* ***25***(5), pp. 1092–1099.

[191] Forrester, A. I. J., Keane, A. J., and Bressloff, N. W., 2006. "Design and analysis of "noisy" computer experiments". *AIAA journal,* ***44***(10), pp. 2331–2339.

[192] Jackson, R. L., and Green, I., 2006. "A statistical model of elasto-plastic asperity contact between rough surfaces". *Tribology International,* ***39***(9), pp. 906–914.